ADVANCED ELECTRIC PROPULSION RESEARCH

prepared for

NATIONAL AERONAUTICS AND SPACE ADMINISTRATION

GRANT NGR06-002-032

REPORT NO. 5

SPACE PROPULSION PROGRAM

ENERGY CONVERSION PROGRAM

COLLEGE OF ENGINEERING

COLORADO STATE UNIVERSITY

FORT COLLINS, COLORADO

FACILITY FORM 602

N67-36941 (ACCESSION NUMBER)

N67-36949 (THRU)

278 (PAGES)

1 (CODE)

CR-88419 (NASA CR OR TMX OR AD NUMBER)

28 (CATEGORY)

MER 67-68WRM-8

SEMI-ANNUAL REPORT

For the period January 1, 1967 to June 30, 1967

ADVANCED ELECTRIC PROPULSION RESEARCH

Prepared for

NATIONAL AERONAUTICS AND SPACE ADMINISTRATION

July 1967

Grant NGR06-002-032

Technical Management

George Pfannebecker
Nuclear Electric Systems Division
Office of Advanced Research Technology
NASA Headquarters
Washington, D. C. 20546

Prepared by: William R. Mickelsen

W. R. Mickelsen, principal investigator
Professor of Mechanical Engineering
and Professor of Electrical Engineering
Engineering Center
Colorado State University
Fort Collins, Colorado 80521

CONTENTS

SUMMARY i

ADVANCED CONCEPTS IN ELECTRIC PROPULSION 1.1 ✓

PARTICLE CHARGING BY ELECTRON BOMBARDMENT 2.1 ✓

ELECTROTHERMAL THRUSTERS IN THE ATEP SYSTEM 3.1 ✓

FUNDAMENTAL PLASMA PROCESSES IN ELECTRON-BOMBARDMENT-THRUSTER IONIZATION CHAMBERS 4.1 ✓

NEUTRAL-ATOM SPEED MEASUREMENT IN AN IONIZATION CHAMBER 5.1

APPROXIMATE METHODS IN MISSION ANALYSIS 6.1 ✓

ALUMINUM COLLOID FORMATION BY HOMOGENEOUS NUCLEATION IN A SUPERSONIC NOZZLE 7.1 ✓

A DIRECT-CONVERSION DEVICE USING THERMALLY ACCELERATED, CHARGED, COLLOIDAL PARTICLES 8.1 ✓

THE PRODUCTION OF CHARGED-PROTEIN MOLECULES BY ELECTROSTATIC SPRAYING 9.1 ✓

FACILITIES AND EQUIPMENT 10.1

SUMMARY

This semi-annual report contains detailed descriptions of research done in the period 1 January 1967 to 30 June 1967. The research is reported in sections, and the salient features of each section are summarized in the following paragraphs.

1. Advanced Concepts in Electric Propulsion.

This AIAA paper (No. 67-426) is reproduced here in entirety for the record. At present a condensed version of this paper is being prepared for publication in the Journal of Spacecraft and Rockets.

It is pointed out in the paper that the relative merits of auxiliary electric propulsion systems may be judged in terms of:

a. capability of operation at a high enough specific impulse for the ΔV requirement of the satellite mission
b. reduction or elimination of power conditioning
c. reduction or elimination of power drawn from the solar-cell array
d. capability of precision thrust vectoring.

Criteria a. and c. are related in the sense that a particular combination of specific impulse and power will provide minimum propulsion system weight for a given mission ΔV.

Flight-prototype electric propulsion systems, experimental thruster systems, and advanced concepts are discussed in the paper, and this discussion can be summarized in terms of the four criteria:

		high specific impulse	no power-conditioning	low solar-cell power	thrust vectoring
flight prototype	resistojet		✓	✓	
	contact-ion	✓			✓
	electron bombardment	✓			?
experimental	charged-particle	✓		✓	✓
	MPD	✓	✓		
	SPET	✓		✓	
advanced concepts	isotope-heated contact	?✓		?✓	?✓
	plasma separator	?✓	?✓	?✓	?
	ACCENT	?✓	?✓	?✓	?✓

In considering this tabulation, it must be remembered that the advanced concepts have not been reduced to practice as yet and there might be unanticipated problems encountered in their development. Furthermore, some shortcomings of flight-prototype auxiliary propulsion systems might be overcome in the future.

Solar-electric spacecraft may be the first application of primary electric propulsion. Planetary-orbiter and fly-by missions have optimum specific impulse in the 2000-3000 second range when solar-electric propulsion is used. Flight-prototype electric thrusters are heavy and inefficient in this range of specific impulse, so a compromise toward a higher (off-optimum) specific impulse must be made. Even with this compromise, flight-prototype thrusters will cause propulsion system weights to be two or three times as great as the weight of the solar-cell array alone.

Advanced concepts such as the plasma-separator and the charged-particle thrusters have promise of much improved efficiency in the 2000-4000 second range of specific impulse, but these advanced concepts would require power conditioning. The MPD thruster advanced concept would not require power conditioning, but has promise of improved efficiency at power levels considerably greater than would be used by solar-electric spacecraft.

Propellant consisting of spent tankage (from boosters) and/or biowaste would do much towards improving the performance of primary electric propulsion systems at low specific impulse. Charged-particle electrostatic thruster concepts appear to be one direction to follow in utilization of spent tankage and biowaste. Another possible approach is that of increasing the specific impulse of electrothermal thrusters by power addition to the supersonic nozzle flow. Combinations of nuclear-rocket and electric-rocket principles, or even electric augmentation of the radioisotjet are possible embodiments of the ATEP system advanced concept. Systems such as these might not require power conditioning.

2. Particle Charging by Electron Bombardment

Theoretical estimates have been made of the discharge voltage and the electron/particle ratio in charging chambers for aluminum particles. Discharge voltage might be from tens to hundreds of volts, depending on the physical state of the particles. Electron/particle ratios for cross-beam electron flow are very high, so that electron-containment fields will be required in the charging chamber presently being designed.

3. Electrothermal Thrusters in the ATEP System

Power addition to supersonic streams has been examined with the Crocco relations. It is concluded that power addition to supersonic streams may be a feasible method for increasing the specific impulse of electrothermal thrusters. The Crocco-relation analysis shows that power addition should begin at the nozzle throat, but this analysis cannot provide the optimum power-addition profile.

A fully-optimized analysis is being prepared at present. Theoretical calculations with this analysis will be done for conditions appropriate to electric-power augmentation of the radioisojet and to nuclear-rocket/electric-rocket combinations.

4. Fundamental Plasma Processes in Electron-Bombardment Ionization Chambers

Data from the literature have been used to determine the probability of ionization of neutral atoms during traversal of the ionization chamber. Preliminary results of this analysis indicate that cesium neutral atoms would have a somewhat lower probability of ionization during traversal of the chamber centerline than mercury neutral atoms, if both have the same neutral-atom temperature (e.g., wall temperature). If the lower-voltage cesium discharge produces lower neutral-atom speeds than the higher-voltage mercury discharge, then this observation might be reversed. More comprehensive calculations of this kind are expected to provide more definitive conclusions.

5. Neutral-Atom Speed Measurement in an Ionization Chamber

The importance of neutral-atom speed to the ionization process has prompted an experiment to measure neutral-atom speed in an operating thruster. An electron-bombardment thruster has been received (on July 14, 1967) on loan from the Jet Propulsion Laboratory, and is being installed in the vacuum chamber at present. Instrumentation for neutral-atom speed measurement has been designed and fabricated.

6. Approximate Methods in Mission Analysis

The characteristic length has been used as the basis for an approximate method in analyzing solar-electric, hyperbolic-boost, missions. Good agreement has been found with results from high-precision analyses done elsewhere. Further comparisons are being made.

7. Aluminum Colloid Formation by Homogeneous Nucleation in a Supersonic Nozzle

Preliminary estimates indicate that condensation of aluminum vapor should be feasible.

8. A Direct-Conversion Device Using Thermally Accelerated, Charged, Colloidal Particles

This preliminary analysis has outlined some general features of this high-voltage direct-current energy-conversion concept.

9. The Production of Charge Protein Molecules by Electrostatic Spraying

Theoretical studies indicate that electrostatic spraying of liquid-solid mixtures of biowaste may be possible. Experimental apparatus has been assembled for investigation of this charged-particle thruster concept. Various liquids are presently being electrostatically sprayed with this experimental apparatus.

ADVANCED CONCEPTS IN ELECTRIC PROPULSION*

by William R. Mickelsen**

Colorado State University
Fort Collins, Colorado

N67-36942

SUMMARY

Electric propulsion is achieving a competitive status for some satellite and space missions. Beyond the present status there are a number of advanced concepts that have promise of higher performance, and consequently a broader applicability to space propulsion. Most of these concepts have features which avoid or diminish fundamental limitations of existing thrusters, and in addition have important advantages in compatibility with the overall spacecraft system.

Auxiliary propulsion systems for attitude and position control of satellites and spacecraft must meet exacting requirements for thrust magnitude and direction, and must be compatible with the power supply. Advanced concepts with promise of high performance in meeting these requirements include electron-bombardment, radioisotope-heated contact-ion, plasma-separator, plasma, and colloid thrusters. Conceptual design of ACCENT, a complete auxiliary propulsion system, is reported for the first time.

MPD, ALPHA, and new electrostatic thruster concepts promise significant improvements in the competitive status of solar-electric primary propulsion. These thruster concepts also appear to be directly compatible with low-voltage power from future nuclear turboelectric, thermionic, or MHD powerplants. Colloid thruster concepts have demonstrated considerable progress, but will require very high-voltage power.

Future concepts under study are the ATEP system which combines principles of nuclear rockets and electric propulsion, and electric thrusters that utilize biowaste and spent booster tank material as propellant.

---

* This review was carried out under NASA Grant NGR06-002-032, Electric Thruster Systems, OART.

**Associate Fellow, AIAA; Professor of Mechanical Engineering and Electrical Engineering.

INTRODUCTION

Electric propulsion has received a considerable research and development effort in the past 10 years. This research and development effort has produced electric propulsion systems that are now ready for use in space missions[1-5]. Beyond the present status there are a number of advanced concepts in electric propulsion that have promise of higher performance[6], and consequently a broader applicability to space propulsion. It is the purpose of this paper to review these advanced concepts and to compare their potential performance with the performance of existing flight-prototype electric propulsion systems.

Most of the advanced concepts have features that avoid or diminish fundamental limitations of existing thrusters. For example, conventional electrostatic thrusters have a low thrust per unit area at lower values of specific impulse. This limitation on the performance of conventional electrostatic thrusters is due to the fundamental laws of space charge flow. Two of the advanced concepts have features that diminish the fundamental limitation of space charge. In one of the advanced concepts, charged particles are used which are much more massive than atomic ions thereby providing much greater thrust density. The other advanced concept employs very closely spaced electrodes, thereby greatly reducing the space charge and allowing operation at reasonably high thrust densities and low specific impulse.

Some of the advanced concepts have important advantages in compatibility with the overall spacecraft system. For example, two of the advanced concepts would be operated with the direct output from solar-cell arrays in contrast to existing flight-prototype ion thrusters which require complex power conditioning to change the direct current solar cell power into high-voltage d.c. power. In another advanced concept which is suitable for auxiliary propulsion, a high-voltage d.c. power source is an integral part of the thruster system, thereby eliminating the need for solar cells.

As a part of the comparison between the various thruster types and concepts it is desirable to denote their state of realism. Three general classifications are used in this paper:

1. "Flight-prototype" refers to extensively tested complete systems that are based on well-known technology throughout, and that are ready for starting on a flight program.
2. "Experimental" refers to electric thruster systems that are fairly well tested in laboratory-prototype form, with

a number of man years of research and development, and in which all of the basic principles have been demonstrated.

3. "Advanced concept" is an electric propulsion system that is based on demonstrated principles, which has not been operated as a laboratory prototype.

Classification of the various thruster systems into these three categories is based on published information, and on past experience in the field of electric propulsion.

POWER FOR ELECTRIC PROPULSION

At the present time solar-photovoltaic cells are the favored source of power for electric propulsion. No serious difficulty is anticipated in using solar cells to power small electric thrusters for auxiliary propulsion[2]. Solar-cell power for primary propulsion appears to be practical, at least for spacecraft as large as unmanned interplanetary probes[7,8].

The solar intensity in space at Earth distance from the sun is about 1.4 kilowatts/sq. meter. Solar-cell efficiencies are less than 10%, so a solar array will deliver about 100 watts of electric power per sq. meter of array area. One of the most demanding tasks for auxiliary propulsion is the north-south station keeping of synchronous satellites. A continuously operating thruster operated at a level of about 350 micropounds could perform the north-south station keeping function, and such a thruster requires about 100 watts of electric power. For this application of auxiliary electric propulsion, a solar array of about three feet by three feet would provide all the power needed. Such an application of solar cells is certainly within the state of the art.

The SERT-II spacecraft will have 1.5 kilowatts of solar-cell power. At this power level the solar array will have to be about 10 sq. meters in area, which is about 10 feet by 10 feet. Design studies and some laboratory-prototype experience indicate that solar arrays with power levels as high as 50 kilowatts are feasible[8,9].

Solar-cell arrays at power levels below 100 watts have specific weights of about 150 lb/kwe. This value of specific weight is used in this paper for comparing system weights of the various types of auxiliary electric propulsion. The design studies[8,9] of multi-kilowatt solar-cell arrays predict specific weights as low as 40 lb/kwe as shown in Figure 1. The specific weights shown in Figure 1 for the multi-kilowatt range are sufficiently low to make solar-electric propulsion attractive for space probe missions[10].

Solar-cell arrays have several disadvantages in some mission applications[11]. Solar-cell arrays in the 100 watt range and above must be packaged during boost, and unfolded after boost. The array must be sun-oriented, which introduces considerable mechanical complexity in most missions. In those missions where a substantial amount of time is spent in the planet shadow, batteries must be provided for energy storage, which results in very large increases in system weight[12].

The radioisotope thermoelectric generator is a potential power source for electric propulsion. Specific weight of the RTG used in the Transit satellites is about 1000 lb/kwe. Because of this very high specific weight, RTG's probably could be used only for auxiliary electric propulsion in the 10 watt range. If nuclear safety requirements can be relaxed in the future then the RTG may have a lower specific weight which would allow application to auxiliary propulsion at higher power levels. For those missions where a large fraction of time is spent in the planet shadow, it may well be that RTG's will prove superior to the solar-cell-battery system. Another potential application for the RTG is that of auxiliary-propulsion power at great distances from the sun.

Radioisotope Brayton-cycle powerplants are being considered for the MORL mission[13,14]. A powerplant such as this might provide 3 kwe of power to operate electric thrusters for attitude control and to overcome drag in the MORL flight. The design of this powerplant is based on existing technology, but until a laboratory prototype is operated, it must remain an advanced concept.

Nuclear turboelectric, nuclear thermionic, and nuclear MHD powerplants must all be placed in the advanced concepts category, since complete systems including the reactor have not been operated to date. However, the technology of these systems is progressing rapidly enough to warrant some degree of optimism[15-18]. There can be no doubt that nuclear-electric powerplants with sufficiently low specific weights for primary propulsion missions will become a reality in the future. Until that future date when nuclear electric powerplants become a reality, those wishing to apply electric propulsion to space missions have but two alternatives: (a) to be content with solar-cell arrays, and perhaps the RTG in some instances or (b) conceive and develop new and unique electric powerplants that can surpass the solar-cell array in performance.

POWER-CONDITIONING AND CONTROLS

Most electrostatic thrusters and some plasma thrusters require high-voltage d.c. electric power. Typical solar-cell arrays have an output of 28 volts d.c. Because of the mismatch in voltage between the powerplant and the electric thruster, power-conditioning is usually a necessary part of the electric propulsion system.

It will be shown later that power conditioning can be a significant fraction of the total propulsion system weight. The power conditioning and controls weights shown in Figure 2 are representative of the present state-of-the-art for flight-prototype systems. The weight of 5 lbs at 27 watts of output power from the power conditioning is the total weight of the flight-prototype power conditioning for a 14 micro-pound electrostatic thruster[19]. The weights shown in Figure 2 above 1000 watts are taken from a flight-prototype power conditioning and controls system designed for primary solar-electric propulsion[8]. The controls weight is about 0.5 pounds, so the power conditioning accounts for nearly all of the weight. This is not too surprising because the power conditioning consists of a large number of components in a d.c./a.c. inverter, a transformer stage, and a a.c./d.c. rectifier stage.

Power losses in the power conditioning can result in very appreciable increases in system weight, because these losses increase the size and weight of the electric powerplant. The power conditioning and controls efficiency of 65% at 27 watts of output power is representative of values encountered in a 14 micro-pound electrostatic thruster system[19], but it is possible that this efficiency would be improved. The efficiencies of 92% and better above an output power of 1000 watts are taken from a flight-prototype design intended for primary solar-electric propulsion[8].

In addition to the weight and power losses caused by the power conditioning and controls, this subsystem also introduces a very much greater complexity to the total electric propulsion system. For example, the power conditioning and controls for the 14 micro-pound electrostatic thruster has more than 1000 critical components. The ramifications to system reliability are clearly of major importance. It is self-evident that a truly optimum design will be achieved only when the electric thruster can operate directly from the powerplant output with a bare minimum of power conditioning, with very simple control circuitry, and low-weight power cables.

AUXILIARY ELECTRIC PROPULSION

Electric propulsion systems are well suited for a number of auxiliary propulsion functions which include:

satellite station-keeping
satellite attitude control
satellite drag cancellation
satellite orbit changes
other programmed maneuvers
mid-course control of spacecraft attitude

Some of these thrusting functions, particularly in very long duration missions, are so demanding that it appears that electric propulsion will be the only satisfactory system.

An excellent example of the potential application of electric propulsion is the station-keeping and attitude-control of synchronous satellites[2]. A typical electric propulsion system design for the synchronous satellite is shown in Figure 3. Approximate ΔV requirements for the synchronous satellite mission are:

north-south station-keeping	180 ft/sec/yr
east-west station-keeping	7 ft/sec/yr
attitude-control	13 ft/sec/yr

For a 2000-pound satellite these ΔV's correspond to a total impulse of about 12,000 lb-sec/yr. Propellant weight is related to total impulse and specific impulse as follows:

$$W_{pr} = \dot{w}t = \frac{Ft}{I} \tag{1}$$

where W_{pr} is the propellant weight, $\dot{w}$ is the propellant weight flow rate, t is the thrusting time, Ft is the total impulse, and I is specific impulse. For example, a propulsion system with a specific impulse of 100 seconds would require 100 pounds of propellant per year of mission time. If the synchronous satellite were intended to have a lifetime of 5 years, then one-fourth of the total satellite weight would be propellant. Electric propulsion systems have specific impulses of the order of 1000 seconds so that the propellant requirement can be greatly reduced.

Electric power required by the thruster is related to thrust and specific impulse:

$$P = \frac{g_c F I}{2\eta} \tag{2}$$

where P is the electric power input to the thruster in watts, g_c is the gravitational conversion factor of 9.806 meters/sec^2, F is the thrust in newtons, I is the specific impulse in seconds, and η is the thruster efficiency. Because of the high specific weight of solar-cell arrays as shown in Figure 1 it is most advantageous to operate the electric thrusters at low thrust levels but for long thrusting times. In this way the power required by the thruster can be minimized, and the combination of low thrust and low thrusting time can still satisfy the total impulse requirements. For the continuous thrusting mode of operation shown in Figure 3, the thrust levels for a 2000-pound synchronous satellite are:

north-south station-keeping	350 micro-pounds
east-west station-keeping	14 micro-pounds

There are exceptions to the continuous-thrust mode of operation, for example a continuous flow of electric power for the solar-cell array could be stored in capacitors. When sufficient energy is accumulated in the capacitors the energy can be discharged to the electric thruster thereby producing repetitive impulse bits each having a thrust level much higher than the values listed above. In both of these modes of operation the power level of the solar-cell array is minimized, and in this way the weight of the total system is also kept to a minimum.

Total weight of the electric propulsion system is simply the sum of the weights of the components:

$$\begin{aligned} W_{ps} &= W_{th} + W_{pc} + W_{pr} + W_{pp} \\ &= W_{th} + W_{pc} + \frac{Ft}{I} + \alpha P \end{aligned} \tag{3}$$

where W_{th} is the weight of the thruster system including the thruster, the propellant feed, and the propellant tank; W_{pc} is the weight of the power conditioning and control system such as shown in Figure 2; W_{pr} is the propellant weight, and W_{pp} is the electric powerplant weight. For a fixed thrust F and total impulse Ft there will be a value of specific impulse that will result in a minimum total system weight. Since the weight of the power conditioning and controls, and the specific weight of the powerplant, are both functions of the power, and since the power depends on specific impulse and thruster efficiency, and further since the thruster efficiency depends on both specific impulse and thruster size, the procedure for finding the optimum specific impulse is not straightforward. However, the weight breakdown expressed by equation (3) is instructive in comparing different types of electric propulsion systems, and will be used for that purpose herein.

Flight-Prototype Electric Propulsion Systems

There are three types of electric propulsion systems that can be considered ready for use in a flight program. These systems are all powered by solar-cell arrays and can be distinguished by the type of thruster: resistojet, contact-ion electrostatic thruster, and electron-bombardment electrostatic thruster. All components of these systems are derived from well-known technology[20]. Furthermore, each of the thruster types has been duration tested for many thousands of hours in ground vacuum facilities. As a final accreditation for the flight-prototype status, experimental models of all three of the thruster types have been flown in space.

Resistojets. The present status of flight-prototype resistojet systems is described in detail in another paper at this symposium[21], so the discussion here will be brief. A conceptual diagram of a resistojet is shown in Figure 4. Electric power is used to resistance-heat surfaces over which the propellant flows. The heated propellant is then expanded thermodynamically through a conventional exhaust nozzle. In principle, a specific impulse of about 1000 seconds should be possible using hydrogen as the propellant.

Because of the high tank weights required for long-term storage of liquid hydrogen, liquid ammonia is used[12]. The ammonia is vaporized and dissociated so that the propellant is a mixture of nitrogen and hydrogen gas. In the micro-pound thrust range the ammonia resistojet has achieved specific impulses of 175 to 250 seconds. These relatively low values of specific impulse appear to be due to the relatively moderate temperatures achieved so far, and the very small nozzle throat size which causes considerable loss due to slip flow.

A resistojet with a specific impulse of 200 seconds would require about 56 pounds of propellant to accomplish the north-south station keeping of a 2000-pound satellite for only one year. As will be shown in the following sections the weight of resistojet systems is much greater than flight-prototype ion thruster systems for performing such missions as the synchronous satellite. However the resistojet in the micro-pound range may find use in important functions such as the inversion maneuver for gravity-gradient stabilized satellites[2]. Resistojets in the micro-pound thrust class have important advantages for moderate total-impulse missions; the electric power required is less than 10 watts, the resistance heater can be designed to operate directly from the solar-cell array output power, and the resistojet itself is very simple and rugged. Thrust vectoring probably would have to be accomplished by a mechanical gimbal.

At higher thrust levels the resistojet has much better performance. For instance at a thrust level of 0.1 lb. a specific impulse of 840 seconds has been obtained with hydrogen propellant. Resistojets of about 0.1 lb. would be well suited for the drag cancellation propulsion function on manned orbiting laboratories[13,14]. The low power/thrust of resistojets would be particularly suitable for this application because power will probably be limited in such vehicles. The resistojet has another very important advantage in the manned orbiting laboratory mission. When the environmental control life support system is operating in the electrolysis mode, then hydrogen and carbon dioxide would be available for propellant in the resistojet. The quantities of these gasses would be sufficient to satisfy the mission requirements. If the resistojet could be used with such biowaste propellants, then only fresh water resupply would be required.

Typical performance of flight-prototype resistojets is summarized in Table I. Propulsion times of 1000 and 10,000 hours are used here for purposes of comparison with the other types of auxiliary electric propulsion systems. As noted above the high weight of resistojet systems for long propulsion times is due to the low values of specific impulse that have been obtained with resistojets in the micro-pound thrust range. This poor performance for long propulsion times is in contrast to the superior performance of resistojets for those missions where propulsion times of the order of 100 hours are required.

Contact-ion thrusters. Research and development of the contact-ion thruster began as early as 1957, and since then a major effort has been expended to bring this thruster type to the flight-prototype stage. The contact-ion thruster has tens of thousands of hours of duration testing in ground vacuum facilities, and has been flown in space.

Principles of operation of the contact-ion thruster are illustrated in the conceptual diagram of Figure 5. Cesium propellant moves from the storage tank to the vaporizer and flow control by capillary flow. The cesium vapor at several torr pressure flows through the porous tungsten ionizer and is ionized as it leaves the ionizer. This contact ionization process proceeds with nearly 100% effectiveness when the ionizer is maintained at 1150 to 1350°K. The ionizer is maintained at a voltage ϕ_{net} above space potential and the accelerator electrode is maintained at a voltage below space potential to prevent electron backstreaming. The cesium ions are accelerated through the electrostatic field and emerge at high exhaust velocity from the thruster. The ion exhaust beam must be neutralized with electrons which are supplied from the neutralizer filament. Very efficient heat shielding must be used to prevent excessive heat loss from the ionizer.

Mass flow rate in the ion exhaust beam is proportional to the ion current. Exhaust velocity of the ions is proportional to the square root of ϕ_{net}. Because of space charge in the acceleration region, the ion current density is limited to a maximum value which depends on the voltage ϕ_A and the accel length. The thrust per unit exhaust area can be written in terms of the voltages and the accel length:

$$\frac{F}{A} = K \left(\frac{\phi_{net}}{\phi_A} \right)^{1/2} \frac{\phi_A^{\ 2}}{L^2} \qquad (4)$$

where F/A is the thrust per unit area, and the constant K depends somewhat on the geometry of the space charge flow. For precision ion optics the accel length cannot be much less than the ionizer width. Fabrication difficulties have prevented accel lengths of less than a few millimeters, so that the accelerator voltages must be in the kilovolt range in order to provide a reasonably high value of thrust density[22]. For this reason electrostatic ion thrusters require much power conditioning to convert the low voltage power from solar-cell arrays.

Electrostatic acceleration of ions in the contact-ion thruster provides a simple means for precision thrust vectoring. By applying potential differences to segments of the accelerator electrode, or to electrodes downstream of the accelerator electrode, the ion beam may be deflected in a manner similar to a cathode ray tube[23,24]. A microthruster with segmented electrodes is shown in Figure 6. Precision thrust vectoring has been amply demonstrated throughout at 32° cone angle.

Complete flight-prototype contact-ion microthruster systems[19,25] (except for solar-cell arrays) are shown in Figures 7 and 8. Thruster systems such as these are intended for the east-west station keeping and the attitude control functions of synchronous satellites illustrated in Figure 3. A contact-ion thruster[25] suitable for the north-south station keeping function is shown in Figure 9. Performance characteristics of the 14 micro-pound and the 300 micro-pound thrusters are listed in Tables II and III, respectively.

Electron-bombardment thrusters. Research and development on electron-bombardment thrusters started in about 1960 with the conception of the Kaufman mercury-propellant electron-bombardment thruster[26] at NASA/Lewis. Many of the design principles of the original Kaufman thruster are still used today, but there have been a number of new concepts developed which have led to cesium-propellant electron-bombardment microthrusters[27] having excellent performance.

Although some of the basic mechanisms important to the operation of electron-bombardment thrusters are not well understood, the basic technology of all components is well in hand. Electron-bombardment thrusters have been duration tested for many tens of thousands of hours in ground vacuum facilities. The most successful space flight test was accomplished with the original Kaufman thruster. The SERT-II flight tests to be flown in the near future will have electron-bombardment thrusters in the propulsion system. There is no doubt that the electron-bombardment thruster stands today in the flight-prototype classification.

Principles of operation of the cesium-propellant electron-bombardment microthruster are shown in Figure 10. Cesium propellant flows by capillary action to the cesium vaporizer and flow control. Cesium vapor then flows through the feed tube to the auto-cathode. The auto-cathode is equipped with a heater needed only in starting the thruster. The cesium covers the surface of the auto-cathode thereby enhancing the thermonic emission of electrons needed for the discharge in the ionization chamber proper. Electrons from the auto-cathode are attracted toward the anode, which is about 8 volts above cathode potential. The cylindrical-shell permanent magnet produces a solenoidal magnetic field which tends to keep the electrons in the ionization volume until they have had collisions. The ionization potential of cesium is about 3.5 ev, so the electrons have sufficient energy to produce a nearly fully ionized plasma in the chamber. The chamber and screen grid are maintained at a voltage ϕ_{net} above space potential, and the accelerator electrode is maintained at a voltage below space potential. The electrostatic field between these electrodes causes a curved plasma sheath to form upstream of each of the holes in the screen grid. Ions are extracted from the plasma through this sheath and then accelerated out through the holes in the accelerator electrode to form ion exhaust beams. Electrons emitted from the neutralizer filament enter each of the ion exhaust beams to neutralize the positive space charge.

Thrust density of the electron-bombardment thruster is limited by the accelerator voltages and the accel lengths in the same manner as the contact-ion thruster, as expressed by equation (4). Flight-prototype electron-bombardment thrusters have accel lengths of several millimeters, so ϕ_{net} must be in the kilovolt range in order to achieve a reasonably high thrust density. Power conditioning is required to convert the low voltage power from the solar-cell arrays to the high-voltage power required by the electron-bombardment thruster.

Flight-prototype electron-bombardment microthrusters[27] are shown in Figure 11. Chamber diameters of these thrusters are from 0.5 to 5.3 inches, and the thrusters cover a thrust range from 10 to 6700 micro-pounds. Performance characteristics of a 370 micro-pound thruster are listed in Table IV.

Summary of flight-prototype electric thruster systems. Total system weights of the flight-prototype electric thruster systems are summarized in Figures 12 and 13; these figures are for propulsion times of 1000 and 10,000 hours respectively. A propulsion time of 10,000 hours corresponds to a mission time of somewhat over 1 year for the synchronous satellite illustrated in Figure 3. From inspection of Figure 12 it is evident that the resistojet is superior with respect to total system weight for short missions, but the electrostatic ion thruster systems become competitive when propulsion time reaches about 2000 hours. For a propulsion time of 10,000 hours the 500 micro-pound resistojet listed in Table I has a total system weight of 136 pounds, which is about 3 times as heavy as electrostatic ion thruster systems at that thrust level, as shown in Figure 13. On the basis of these total system weight comparisons it is evident that the resistojet electric propulsion system is superior for short missions, while the electrostatic ion thruster systems are superior for long auxiliary propulsion missions.

Other factors are also important in the choice of the electric propulsion system. The resistojet can operate directly from a solar-cell array power output, and therefore requires a minimum of power conditioning and controls. A typical power conditioning subsystem for the electrostatic ion thruster has more than 1000 critical components; such a large number of critical components is bound to drastically affect the reliability of the electrostatic ion microthruster system. In this respect the electrostatic ion thruster system can be competitive with the resistojet system only if adequate reliability of power conditioning is conclusively proven.

Another important factor for many missions is the capability for precision thrust vectoring. The contact-ion electrostatic thruster possesses this capability. Precision thrust vectoring might be possible for the electron-bombardment microthruster, but it is unlikely that precision thrust vectoring can be developed for the resistojet by any other means than mechanical gimballing.

Total power requirement may be an important consideration in some satellite designs, so power level is shown in Figures 12 and 13. The resistojet has a marked advantage in this regard.

The performance characteristics of the flight-prototype electric propulsion systems described here are firm, and form an excellent basis for judging the relative merits of the experimental thruster systems and the advanced concepts to be described in the following sections.

Experimental Thruster Systems

There are three thruster types judged to be in the experimental thruster category; charged-particle electrostatic thrusters (colloid thrusters), magnetoplasmadynamic thrusters (MPD thrusters), and solid-propellant electric thrusters (SPET systems). All of these experimental thrusters have received a considerable amount of research and development effort. Laboratory prototypes of each of these thrusters have been operated for hundreds of hours in ground vacuum facilities. Although the basic mechanisms important to the operation of each of the thruster types are not completely understood, performance measurements have been made with a sufficient degree of confidence to allow a fairly reliable evaluation.

Colloid thrusters. Colloid electrostatic thrusters have been advocated for some time as being potentially superior to any other type of electric thruster[28,29]. In the past few years a liquid-spray charged-particle electrostatic thruster[30] has been developed to a status of excellent experimental performance.

Principles of operation of the liquid-spray charged-particle electrostatic thruster are illustrated by the conceptual diagram in Figure 14. In the laboratory prototype the glycerol propellant is forced under pressure to flow into hollow needles with 0.014 inch outside diameter and 0.004 inch inside diameter. The glycerol propellant contains an additive such as H_2SO_4 or NaI to control the electrical conductivity of the fluid. When the liquid reaches the end of the tube, it is exposed to a strong electric field. The forces exerted on the liquid surface at the needle tip include surface tension, the feed pressure, and the electric pressure produced by the field. In a manner not yet well understood an unstable liquid is produced from which charged multimolecular droplets are ejected continuously. The charged droplets are then accelerated in the electrostatic field through the accelerator electrode aperture where electrons are added to the exhaust beam to neutralize the positive space charge.

Although the charged particles have a spectrum of charge/mass, the spectral width is fairly narrow so that the power loss is only about 10 to 30 percent due to the velocity distribution in the exhaust beam. The width of the charge/mass spectrum is somewhat independent of the specific impulse, and appears to be more a function of the geometry of the needle tips and of the uniformity of the needle bore. The mean value of the mass/charge can be controlled by adjusting the mass flow rate and the voltage between the needles and the extractor electrode, and by adjusting the electrical conductivity of the propellant and the type of additive used in the propellant. Charge/mass ratios of from 200 to 10,000 coulombs/kilogram have been obtained experimentally; these values of charge/mass correspond to specific impulses of 140 to 1000 seconds respectively with a ϕ_{net} of 6000 volts.

There has been some difficulty with erosion of the needle tips, normally because of electric discharges. Even in the absence of needle tip erosion a gradual decrease in performance has been observed in some tests of 100 hours or more in duration. This gradual degradation in performance appears to be due to either deposits of material at the needle tip, or condensation of organic material on the extractor and the needle.

Estimated performance characteristics of the liquid-spray charged-particle electrostatic microthruster are listed in Table V. This estimate is based on published data[30], and in addition a neutralizer of 1.1 watts and a vaporizer of 2.0 watts are included in the 3.5 watts for the thruster system. (The vaporizer is assumed to supply the pressure in the feed system). These system weights are compared with the performance of flight-prototype ion thrusters in Figure 15.

An estimate of system weights for a 37-needle experimental thruster is also shown in Figure 15, based on published data[30]. The 37-needle thruster operates at a total current of 300 micro-amperes, a charge/mass ratio of 4000 coulomb/kg, a specific impulse of 680 seconds, and a thrust of 115 micro-pounds. The 37-needle thruster data have been extrapolated in Figure 15 to a thrust level of 345 micro-pounds to illustrate possible future performance.

A large part of the estimated system weight at 345 micro-pounds of thrust is propellant weight, so if a propulsion time of only 1000 hours were required, the total system mass would be 12.4 pounds at this thrust level. This weight is less than that of flight-prototype resistojet system described previously, so it appears that the charged-particle electrostatic microthruster may become competitive with the resistojet system for short propulsion-time missions.

From inspection of Figure 15 it is evident that the charged-particle experimental microthruster will be competitive with flight-prototype ion thrusters if adequate durability of the experimental thruster can be demonstrated in the future. However, for missions with propulsion times of more than 10,000 hours, it is clear that the charged-particle electrostatic thruster system weight will become higher than the flight-prototype ion thruster system weight, unless the specific impulse of the charge-particle thruster can be substantially increased by further research and development.

An important feature of the charged-particle electrostatic thruster is the low power consumption. By comparison of Figures 13 and 15 it is evident that the flight-prototype ion thrusters require much more power than the charged-particle electrostatic thruster, and this is true even if the specific impulse of the charged-particle electrostatic thruster is increased in the future. The fundamental reason for the higher power consumption of flight-prototype ion thrusters is simply that they are very inefficient. In the contact-ion thrusters large amounts of power are lost by radiation and conduction from the extremely hot ionizer. In the electron-bombardment thrusters it appears that a great amount of power is lost by recombination of ions on the inner walls of the thruster chamber. In the charged-particle electrostatic thruster the only appreciable power loss is in the vaporizer, the neutralizer, and the exhaust velocity distribution. If the charged-particle electrostatic thruster can be developed to a flight-prototype status then it might be possible to supply the moderate power requirements of this thruster with radioisotope thermoelectric generators. For vehicles and missions where solar cells are awkward or impossible the low power consumption of the charged-particle electrostatic thruster could be a significant advantage.

Solid propellant electric thrusters (SPET). The SPET microthruster[31] is an unusual concept in which a thin film of propellant is exploded by the passage of a sudden discharge of electrical energy. The exhaust velocity of the resulting plasma can be augmented by electromagnetic acceleration. The name of this concept is by way of analogy to restartable solid propellant rockets.

Principles of operation of SPET are illustrated in Figure 16. Capillary flow carries the propellant to a slot connecting two electrodes. When a capacitor containing electrical energy of about 1 joule is discharged across the two electrodes the sudden addition of electrical energy explodes and ionizes the propellant which can be further accelerated by the parallel rail arrangement. The normal mode of operation is one pulse every two seconds.

One of the difficulties encountered in the development of SPET has been the formation of hard deposits of certain constituents of the organic propellants. It is reported that a non-organic propellant has been found which has appropriate characteristics for explosion by electrical energy addition. Duration tests have been conducted with as many as 3.65×10^6 pulses. There are 31.5×10^6 seconds per year, so these duration tests are equivalent to about 0.1 year at the rate of 1 pulse per second. Data[31] from this duration test are listed in Table VI.

If the SPET experimental microthruster can be developed further to have a durability of one year then it could provide about one tenth of the total impulse required for the attitude control of the 2000-pound synchronous satellite illustrated in Figure 3. If still further development is possible, and the SPET system is scaled up to the equivalent of 14 micro-pounds of thrust, then the input power to the thruster would be 10 watts. This would bring the SPET microthruster to a competitive status with the flight-prototype contact-ion microthruster performance listed in Table II. Scaling up to this thrust level involves the release of about 10 joules of electrical energy per pulse; whether the release of this much energy into the propellant film can be accomplished without damage to the thruster is a question that still must be answered.

Another difficulty encountered in the development of the SPET microthruster is the lifetime of the switching tube. Cold cathode thyratrons have been used so far, but these have a life of only about 200,000 pulses, which is a far from adequate durability.

On the basis of this information it must be concluded that a considerable amount of development remains to be done before the SPET microthruster can achieve a flight-prototype status.

MPD thrusters. Electromagnetic acceleration of plasmas has been the subject of much research since the early days of electric propulsion. Two rationales have often been quoted for this research effort, one being that the plasma thruster has promise of a high thrust per unit area compared with the ion thrusters, and the other being that the plasma thruster can operate on low-voltage power. High thrust per unit area is not a particularly important advantage for microthrusters, but operation with low-voltage power may be a significant advantage.

For a number of years a magnetoplasmadynamic (MPD) thruster has been under development at the NASA/Lewis Research Center[32,33]. Principles of operation of this MPD thruster are shown in Figure 17. A propellant such as argon flows into a hollow cathode where it is ionized by electron bombardment. The major portion of the propellant enters the chambers through the anode feed tubes and is ionized in the discharge that exists between the cathode and the anode. A strong axial magnetic field is maintained by the permanent magnets and the electromagnets. Field strength at the cathode is about 500 gauss and is about 250 gauss at the exhaust aperture. Thrust is generated by the expansion of the hot plasma in the magnetic nozzle. The discharge voltage ranges from 100 to 200 volts, depending on the operating conditions.

In earlier versions of the MPD thruster the magnetic field was produced by electromagnets entirely. Because of poor heat rejection the electromagnets overheated after about 15 minutes of operation; electromagnet power was 300 watts at a coil temperature of 600°C. In the EM-PM MPD thruster illustrated in Figure 17 a cylindrical permanent magnet around the hollow cathode generates a significant fraction of the total magnetic field. With this combination of permanent magnet and electromagnets, the electromagnet power has been reduced by 50%, but as a consequence the thruster weight has been increased significantly by the addition of the permanent magnet. Performance characteristics of this experimental microthruster[33] are listed in Table VII.

Estimated total system weights of the experimental MPD microthruster are compared in Figures 18 and 19 with weights of flight-prototype ion thruster systems. For missions with propulsion time of 1000 hours the experimental MPD microthruster system would be 2 or 3 times heavier than the flight-prototype ion thruster systems. Even if the electromagnet power were eliminated entirely the MPD microthruster system would not be competitive. The same remarks can be made for the comparative status of the experimental MPD microthruster in missions with propulsion times of 10,000 hours. On these grounds, it must be concluded that the EM-PM MPD thruster does not have much promise of having lower system weights than the flight-prototype ion thruster systems.

Improvement of performance of this thruster would probably have to be accomplished with propellants other than argon. The estimated system weights listed in Table VII do not include weight penalties associated with the use of gaseous propellants. From inspection of Figure 19 it is clear that a tankage of 50 to 100% would seriously increase the total system weight of the MPD microthruster for missions with propulsion times of the order of 10,000 hours. In principle, propellants such as the alkali metals could be used in the MPD microthruster, and these propellants would have much lower tank weights.

A potential advantage of the MPD microthruster is the elimination of power conditioning with resulting reliability due to simplicity. Realization of this advantage must await the development of flight-qualified solar-cell arrays[11] that can operate at output voltages of 100 to 200 volts. Until such solar power is available, the EM-PM MPD thruster cannot be considered a serious competitor, and even then the MPD thruster performance would have to be improved significantly.

Advanced Concepts

There are three advanced concepts in auxiliary propulsion that appear to have great promise of much better performance than the flight-prototype ion thruster electric propulsion systems. These are the radioisotope-heated contact-ion microthruster, the plasma-separator microthruster, and the ACCENT system. All three of these advanced concepts are based on the demonstrated principles, but have not yet been operated as laboratory prototype thrusters. In fact, the feasibility of all components of these advanced concepts has been demonstrated in laboratory experiments. There are a number of other advanced concepts such as the ELM (exploded liquid metal) thruster, the REPPAC (pulsed plasma accelerator) thruster, pulsed vacuum-arc microthruster, etc. None of these are included in the present review because of the lack of sufficient information to establish their feasibility or potentiality.

Radioisotope-heated contact-ion microthrusters. A major fraction of the power requirements for contact-ion thrusters is consumed by the ionizer heater. The porous-tungsten ionizer[34] must be maintained at $1150^{\circ}K$ for an ion current density of 1 milliampere/cm^2 and $1350^{\circ}K$ for an ion current density of 10 milliampere/cm^2. Because of radiation and conduction heat transfer a considerable amount of power must be used to maintain the ionizers at these temperatures. It appears possible, in principle at least, to use radioisotope heating of ionizers instead of the electrical heating that is presently used in flight-prototype contact-ion microthrusters.

The relative merit of various radioisotopes as ionizer heaters can be estimated by calculating the size of a solid cylinder of the radioisotope that would be required to maintain the ionizer at the temperatures quoted above. If the heat transfer from the solid cylinder of radioisotope is assumed to be radiation heat transfer alone, then the cylinder diameter is related to the temperature by the following expression:

$$D = 23.1\varepsilon(1 + 1/2\ L/D)(V/\dot{Q})(T/1000)^4 \qquad (5)$$

where D is the cylinder diameter in cm, L is the cylinder in cm, ε is the emittance, $V/\dot{Q}$ is the volume per unit power in cm^3/watt, and T is the equilibrium temperature of the cylinder in $^{\circ}K$. For example the following cylinder diameters would be required to bring four candidate radioisotope cylinders to the temperatures of $1200^{\circ}K$ and $1400^{\circ}K$ respectively:

	Pm-147	Pu-238	Cm-242	Po-210
for T = $1200^{\circ}K$;D,cm	40	18	.08	.06
for T = $1400^{\circ}K$;D,cm	73	34	.15	.11

From this simple calculation it is evident that the low power densities of promethium-147 and plutonium-238 would require high quality thermal insulation design if they were to be used as ionizer heaters. From the viewpoint of power density, curium-242 and polonium-210 are far superior. However, both Cm-242 and Po-210 are alpha particle emitters, so a void fraction of about 10 would be required to accomodate the evolution of helium gas. Incorporation of the helium receiver volume into the ionizer heater structure will introduce mechanical and heat-transfer problems.

Power requirements for the various components of the flight-prototype contact-ion microthrusters are listed in Table VIII. For the 14 micro-pound microthruster, the ionizer heater requires 7.6 watts which corresponds to a solar cell power of 11.7 watts which in turn corresponds to about 1.8 lb. of solar-cell array. From this it is clear that radioisotope heating of 10 micro-pound thrusters will save only a small amount of total system weight. For the 300 micro-pound microthruster, about 7 lb. of solar-cell array could be saved. From inspection of Figures 12 and 13 it is evident that a 7 lb. reduction in total system weight is appreciable.

On the basis of this cursory examination of the merits of radioisotope heating of ionizers it may be concluded that significant weight reductions could be attained if the radioisotope containment and helium-gas-receiver vessels can be developed to a reliable and lightweight status. It is expected that the technology being developed for radioisojets[35] will have much bearing and usefulness in radioisotope heating of ionizers. The promethium-147 heater capsule in the radioisojet has already attained operating temperatures of 1280°K. In the static heat transfer environment of ionizer heating, and with improved thermal insulation, it is possible that promethium-147 could become an adequate heater for contact-ion microthrusters at low ion current densities. Since promethium-147 is a beta particle emitter and has only a small radiation intensity, it has operational advantages over the alpha particle emitting radioisotope. Further theoretical analysis and experimental development is needed before the feasibility of radioisotope heating of ionizers can be established conclusively. Additional work will be worthwhile because of the potential reductions in system weight in the several hundred micro-pound thrust range.

Plasma separator thruster. Some experimental work has been done which establishes the performance of the critical components of the plasma-separator thruster concept. Although this concept has not been operated as a complete thruster the components appear to be fully compatible, and their measured characteristics offer promise of a high performance thruster[36].

Principles of operation of the plasma-separator microthruster concept are illustrated in Figure 20. Propellant is vaporized and flows through a hollow cathode. The surfaces of the hollow cathode are very hot to insure copious thermionic emission of electrons, and this emission is further enhanced if the propellant is an alkali metal, which lowers the work function of the cathode surface. Electrons are attracted to the anode which is at a potential about 10 volts above the cathode. Nearly complete ionization of the propellant occurs in the cathode and nozzle region; this ionization is accomplished with a small amount of power because of the high density of the propellant vapor in the hollow cathode. (In contrast, ionization in the Kaufman electron-bombardment thruster occurs at a much lower density). The nearly fully ionized plasma formed in the hollow cathode expands rapidly through the nozzle and the expansion region; this expansion occurs quickly so there is negligible recombination. The portion of the total ion flow reaching the separator electrode is extracted from the plasma and accelerated electrostatically to the desired exhaust velocity. The peripheral flow of ions is condensed on the cone and returned to the feed system for another pass through the hollow cathode. This design should reduce wall losses and raise the propellant utilization at the cost of a small increase in power. By virtue of special design and operating conditions of the accelerator electrodes, all of the ions approaching the separator electrode are extracted and accelerated into the exhaust beam.

Performance characteristics of the hollow-cathode plasma source have been established with extensive experimental measurements[36]. The electric power consumption of the hollow-cathode plasma source is about one-tenth of the electric power consumption in the Kaufman electron-bombardment ionization chamber. (As reported in another paper[37] at this symposium a hollow cathode is being used in the SERT-II thruster and has resulted in considerable improvement in performance). The total-throughput ion optics of the accelerator system has received sufficient experimental investigation to verify the concept. Although recycling of propellant has not been demonstrated in a thruster, the principles of recycling have been firmly established in alkali-metal heat-pipe experiments. On the basis of these facts it is concluded here that the plasma-separator concept is a valid and realistic thruster design.

Adaptation of the plasma-separator concept to the microthrust regime, and the possibility of operating this thruster directly from the output of the solar-cell arrays is presently under study[38]. The standard output voltage from solar-cell arrays is 28 volts d.c. When mercury or cesium ions are accelerated through a potential drop of 28 volts, their final velocities are very low, which results in very low specific impulses. The alkali metals potassium, sodium, and lithium are much lighter than cesium and would produce satisfactorily high specific impulse in a 28-volt accelerator. Since propellants such as these would also lower the work function of the hollow cathode surface, it is reasonable to expect that the high performance of the hollow-cathode plasma source would be preserved.

With a low accelerator voltage, the thrust density will be small unless the accel length, L, can be made very small as shown by equation (4). For acceleration of lithium, sodium, and potassium through 28 volts, the thrust density is reasonably high if the accel length is about 0.010 inch. Accel lengths of less than 0.040 inch were considered to be impractical until some excellent work in West Germany on accelerator structures was reported[39] in early 1966. This work shows that a solid dielectric insulator could be sandwiched between the separator electrode and the accelerator electrode. Electrode systems such as this have been tested[40] on a mercury electron-bombardment thruster and have been found to be satisfactory. These tests were of comparatively short duration, and it has not been established whether adequate durability could be obtained using mercury propellant and several hundred volts in the accelerator (in order to obtain a reasonable value of specific impulse with mercury).

Since the lighter alkali metals are being considered for propellants in the plasma-separator microthruster, the accelerator voltage can be much less than for mercury propellant, perhaps as low as 28 volts d.c. The threshold for sputtering in most ion/target-metal combinations is about 20 e.v.; and since most of the charge-exchange ions will have energies considerably less than the total voltage in the accelerator, then it may be concluded that a 28-volt accelerator system will have essentially no sputtering problem. With the problem of sputtering being eliminated by low-voltage operation, there should be no problem with accelerator electrode durability.

Estimates have been made of the potential performance of the plasma-separator microthruster concept; these estimates[38] are based on the experimental performance of the hollow-cathode plasma source. Experimental data for the hollow-cathode plasma source have all been obtained with cesium propellant. It is assumed in the estimated performance calculations that the power consumption in the hollow-cathode plasma source is proportional to the first ionization potential of the propellant, so that the plasma source performance is lower for the other alkali metals than it is for cesium. It is also assumed in the estimate that only 60% of the plasma issuing from the hollow cathode arrives at the separator electrode, while the other 40% must be recirculated. With these conservative assumptions, the estimated performance of this microthruster system is shown in Figures 21 and 22.

It is important to note that the estimated performance in Figures 21 and 22 is for an accelerator voltage of only 28 volts d.c. If 100 volts d.c. were available from the solar-cell array, then the specific impulse with each of the propellants shown in the figures would be doubled, thereby reducing the propellant requirements by 50%. In addition the power requirements would be reduced at each thrust level, thereby reducing the weight of the solar-cell array. Estimated total system weights with 100-volt solar-cell arrays is shown in Figure 23.

Even with only 28 volts d.c. accelerating voltage, the hypothetical plasma-separator microthruster system appears to have promise of much better performance than the flight-prototype ion microthruster systems. If the output voltage of the solar-cell arrays can be raised to 100 volts, then the hypothetical plasma-separator thruster has promise of much superior performance. It should be pointed out again that operation of microthrusters directly from the solar-cell array output would eliminate the need for the very complex power conditioning with its more than 1000 critical components. The potential advantages of this microthruster concept should be just cause for further development work.

The ACCENT system. The ACCENT system is a totally new concept and is still in the early stages of development[41]. This advanced concept is an autogenetically-controlled-cesium-electro-nuclear-thruster system. All of the components of the ACCENT system have a basis in well-established experimental fact. In addition, a great deal of the technology of contact-ion thrusters is utilized.

Principles of operation of ACCENT are shown in Figure 24. Cesium propellant flows from the reservoir through a long feed tube to the conventional porous tungsten ionizer. After being ionized at the exit of the porous tungsten ionizer, the cesium ions are accelerated through a potential difference to the desired exhaust velocity. A radioisotope ionizer heater is shown in the diagram in Figure 24, but it should be noted that the heating of the ionizer could also be accomplished with electric power from solar cells or from a radioisotope thermoelectric generator incorporated into the nuclear electrogenerator of ACCENT.

High-voltage d.c. electric power is provided by a radioisotope electrogenerator, and does not involve any power conditioning. High-energy beta particles are emitted from a thin film of radioisotope that covers the surface of the inner cylinder. Those beta particles having sufficient energy will travel to the outer cylinder thereby generating a negative charge on the outer cylinder. The daughter atoms left behind on the inner cylinder have a positive charge thereby raising the potential of the inner cylinder with respect to the outer cylinder. Movement of the beta particles from the inner cylinder to the outer cylinder through the adverse potential difference produces the electric power for acceleration of the cesium ions. For small microthrusters the cesium ion beam will be a thin beam so that charge neutralization will not be required locally in the cesium ion exhaust beam; therefore only current neutralization is required and these neutralizing electrons can be emitted from any place in the system. Radioisotope electrogenerators have been operated successfully as long ago as 1913 by Mosely, so that all components of the ACCENT system have an experimentally established feasibility.

Radioisotopes of interest have end-point energies of 200,000 ev or more, so the accelerator voltage will be limited only by electric breakdown problems. Experience with conventional ion thrusters has shown that 10,000 volts accelerator potential is practical. With such large accelerator voltages the specific impulse will be well above 10,000 seconds. Thrust in the ACCENT system can be terminated instantaneously with a simple shunt current.

Preliminary estimates of the total system weight of ACCENT are shown in Figures 25 and 26. The potential performance exhibited by these preliminary calculations indicate that the ACCENT concept is of definite interest for further development.

PRIMARY ELECTRIC PROPULSION

Many applications of electric propulsion for primary thrust have been suggested and studied. These missions include:

a. drag cancellation and attitude control of manned orbiting laboratories.

b. orbit changing of satellites, including raising from low parking orbit to synchronous orbits.
c. geocentric and planetocentric mapping mission.
d. interplanetary probes, including fly-by, orbiters, and landers.
e. solar probes, including out-of-the-ecliptic and near-solar (0.1 AU) missions.
f. lunar ferries
g. manned interplanetary round trips

Many of these missions depend on future development in nuclear-electric powerplants, but many others appear to be possible with solar-photovoltaic powerplants. The potentialities of performing some of these missions with existing electric propulsion systems are treated in other papers at this symposium[37,42].

The second portion of the review will examine advanced concepts in electric propulsion and compare their potential performance with that of flight-prototype electric propulsion systems. Definitions of flight-prototype, experimental, and advanced concepts, are those given in the INTRODUCTION.

Electric Propulsion System Performance Criteria

Criteria for electric propulsion system performance have been established in previous papers and are as follows:

1. high thruster efficiency
2. capability for variable specific impulse throughout the mission (existing thrusters do not have this capability)
3. low weight of the total electric propulsion system
4. adequate durability
5. adequate reliability
6. ease of packaging in booster vehicle
7. compatibility with the spacecraft.

The degree to which an electric propulsion system can meet these performance criteria should be a valid basis for the comparison of various systems.

Thruster efficiency has a marked effect on the total weight of the propulsion system, which in turn affects the payload capacity of the electric spacecraft. Power and propellant losses in the thruster may be made up by increases in power conditioning and powerplant size, so the specific weight α^*_{ps} of the overall propulsion system can be expressed as follows[43]:

$$\alpha^*_{ps} = \alpha_{pp} + \alpha^*_{c} + \alpha^*_{th} + (W_o/P_{j,eff})\,\Delta(W_{pay}/W_o)_{P/M} \qquad (6)$$

where the specific weights α^* have the dimensions of lb/kwj; $P_{j,eff}$ is the effective jet power which accounts for all power and propellant losses; the subscripts are pp for powerplant, c for power conditioning and controls, th for thruster system; W_{pay} is payload weight; and W_o is the initial weight of the total spacecraft. The last term in equation (6) is the penalty for non-optimum matching of propulsion system to the spacecraft, ie, there is an optimum value of $W_o/P_{j,eff}$ for each mission and α^*_{ps}. The last term is neglected in the present analysis. Starred quantities in equation (6) denote effective values, which are greater than the physical specific mass of the subsystem:

$$\alpha^*_c = \alpha_c + \alpha_{pp} \left[(1 - \eta_c)/\eta_c \right] \tag{7}$$

$$\alpha^*_{th} = \alpha_{th} + \left[\alpha_c + (\alpha_{pp}/\eta_c)\right] \left[(1 - \eta_{th})/\eta_{th} \right]$$
$$+ W_{tank}/P_{j,eff} + (W_o/P_{j,eff}) \Delta (W_{pay}/W_o)_I \tag{8}$$

for example, α_c is the weight of the power conditioning and controls subsystem divided by the electric power output from that subsystem, ie, $\alpha_c = W_c/P_c$. Sub-system efficiences are η_c for the power conditioning and controls, and η_{th} for the electric thruster. The last term in equation (8) accounts for non-ideal specific impulse programs; since nearly all electric thruster types discussed herein can operate only at a constant specific impulse, this last term will be neglected in this analysis.

Propellant tank weight W_{tank} can be expressed in terms of the tankage fraction k, the weight flow rate $\dot{w}$ of propellant and propulsion time t, and in turn the weight flow rate is $\dot{w} = F/I$, and finally the thrust is $F = (2\, P_{j,eff})/(g_c I)$, so that:

$$W_{tank}/P_{j,eff} = (2kt)/(g_c I^2) \tag{9}$$

Specific weight of the propellant tank is shown in Figure 27 for a propulsion time of one year, and for a range of tankage fraction k and specific impulse I.

Equations (6) to (9) provide the means for evaluating the first three performance criteria. The remaining criteria 4.-7. cannot be evaluated with simple and straightforward analyses. Qualitative trends in thruster durability have been discussed[22], but firm evaluations of durability can only be obtained with long duration tests of the complete system under realistic environmental conditions. Reliability studies have been performed[44], but a firm evaluation of reliability must also depend on long duration tests. Electric spacecraft, particularly those with large solar-cell arrays, will have significant problems associated with the packaging into the payload shroud of booster rockets. The relative difficulty of such packaging will be reflected in the total weight of the electric propulsion system, and in the reliability of the system. Compatibility with the spacecraft is a performance criteria that will depend to a large degree on the nature of the other spacecraft subsystems; for example, there is some concern at present regarding the deposition of exhaust material from electric rockets onto the solar-cell array and the possibility of degradation of solar cell performance as a result of this deposition. For the purposes of this survey, a propulsion system specific weight α^*_{ps} will be used as the main criterion for comparing different types of electric propulsion. Wherever possible the other criterion will be discussed.

Flight Prototype Systems

Small versions of primary electric propulsion systems have been flown in short space flights. One of these flights was ballistic with about 45 minutes in space[45], and the electric thruster was powered with chemical batteries. Another flight was orbital, and the electric thruster was powered with a thermoelectric powerplant[46].

There are two types of electric thrusters that are in the flight-prototype category. Both of these types have been ground tested in vacuum facilities in duration runs of from 4000 to 8000 hours without servicing of any kind. The experience gained in these development programs provides a firm basis for embarking on the SERT-II flight program, which is described in more detail in another paper[37] at this symposium. Details of the SERT-II thruster are also given in that paper. A brief description of flight-prototype thrusters is included here to provide a performance standard against which experimental thrusters and advanced concepts can be compared.

Kaufman thruster. The Kaufman thruster, developed at the NASA/Lewis Research Center, is the original concept of electron-bombardment thrusters.

Principles of operation of this thruster are similar to those described previously for the electron-bombardment thruster shown in Figure 10. The Kaufman thruster differs from that shown in Figure 10 in that mercury is used as the propellant, and an oxide-coated cathode is used instead of the auto-cathode. The magnetic field may be generated by either electromagnets or permanent magnets. In the Kaufman thruster the discharge voltage is between 30 and 40 volts, and the accelerator voltage is somewhat greater than for cesium thrusters because of the higher mass of the mercury ion.

Durability of the Kaufman thruster is limited by erosion of the accel electrode, and by erosion of the oxide cathode[22]. Erosion of the accel electrode is a result of charge-exchange ions sputtering away the electrode material. The charge-exchange ions are formed by collisions between neutral atoms and mercury ions being accelerated in the space between the screen grid and the accelerator electrode. The erosion rate can be kept within acceptable limits by reducing the current density of mercury ions, or by reducing the neutral atom efflux from the ionization chamber. Reduction of the neutral atom efflux requires higher power in the discharge, thereby lowering the thruster efficiency. Reduction of the ion current density has little effect on thruster efficiency but does result in a lower exhaust jet power density. Thruster weight depends essentially on the exhaust area, so the specific weight of the thruster is higher when the exhaust jet power density is reduced.

Erosion of the oxide cathode is caused by ions falling from the discharge onto the cathode surface and sputtering away the cathode material. The discharge voltage in the Kaufman thruster is well above the sputtering threshold (which is about 20 ev), but this is not a problem in the cesium electron-bombardment thruster. Adequate durability of the oxide cathode in the Kaufman thruster has been attained with a spring mechanism that continuously replenishes the oxide cathode surface inside of the discharge chamber[47].

Cesium electron-bombardment thruster. This thruster[48] has been developed at Electro-Optical System, Inc., and features the cesium auto-cathode in addition to many of the basic design concepts of the original Kaufman thruster. The cesium discharge operates at about 8 volts, which is well below the sputtering threshold, so there is no problem of cathode durability. However, charge-exchange ion erosion of the accel electrode still occurs. The charge-exchange cross section for cesium is much higher than for mercury, but the discharge power in the cesium electron-bombardment thruster is considerably less than in the Kaufman thruster, so the discharge power can be increased in order to reduce the neutral atom efflux and still maintain a higher thruster efficiency than the Kaufman thruster. Because of the lower mass of cesium ions, accelerator voltages are lower than in the Kaufman thruster, so the ion current density must be increased in order to attain the same exhaust jet power density as that of the Kaufman thruster. This higher ion current density requires still more discharge power in order to further reduce the neutral atom efflux. When all of these effects are accounted for, the cesium electron-bombardment thruster has a higher performance than the Kaufman thruster.

Summary of flight-prototype thrusters. As noted previously, mechanical limitations to electrode spacing results in the need for accelerator voltages of several thousand volts in order to obtain an adequately high value of ion current density. In addition, the value of ϕ_{net} must be such that the exhaust velocity has a value commensurate with the required specific impulse. Values of ϕ_{net} are shown in Figure 28 for a number of atomic-ion propellants. From this figure it is clear that cesium and mercury propellants will require power conditioning when operated from solar-cell powerplants. For power levels above 6 kilowatt, the specific weight of power conditioning[8] is about 6 lb/kwe. Specific weights for solar-cell powerplants are given in Figure 1. These specific weights for power conditioning and controls, and for solar-cell powerplants, are used here to obtain performance comparisons of the various thruster types.

Specific weight of an electric propulsion system with the Kaufman thruster[47] is shown in Figure 29. The various subsystem specific weights are shown, as expressed by Equations (6) to (9). When propulsion systems with a specific weight of about 100 lb/kwj are used in missions such as the Mars orbiter-lander, the optimum specific impulse lies in the range from 3000 to 4000 seconds. In this specific impulse range of interest, it is evident from Figure 29 that the Kaufman thruster would cause the total propulsion system to be more than twice as heavy as the solar-cell powerplant alone. The major portion of this increased weight is due to the inefficiency of the Kaufman thruster in the lower range of specific impulse. An appreciable amount of weight is due to the thruster itself, and this is a consequence of the smaller values of ϕ_{net} in the lower range of specific impulse. In preparing Figure 29 it was assumed that the ion current density remained constant at the highest value possible for satisfactory durability of the accel electrode.

The cesium electron-bombardment thruster[48] has an improved performance compared with the Kaufman thruster as shown in Figure 30. It is assumed in this analysis that the cesium propellant tankage can be as low as that for mercury. There has been some question about this point, but it seems reasonable that cesium could be cooled below its melting point during the boost phase, and in this way the high-g forces could be largely absorbed by the solid cesium.

From this brief summary of flight-prototype electric propulsion systems it is clear that the electric thruster is responsible for more than one-half of the total propulsion system weight in a specific impulse range of interest for solar-electric spacecraft. This large weight penalty caused by the electric thruster is contrary to the expectations of many during the last decade. There can be no doubt that electric thrusters are far from meeting their full potential, and that much remains to be done to improve the efficiency of electric thrusters, and to reduce their physical specific weight. It is notable that even with this primitive level of performance, electric propulsion could provide more payload and/or faster trip times than conventional chemical rockets. As electric propulsion systems are improved in the future, this superiority will become even greater.

Experimental Thrusters

At the present time there are two electrostatic ion thrusters that can be considered in the experimental thruster category. Both of these have been operated for several hundreds of hours in ground vacuum facilities, with all components being fairly realistic.

Resistojets and arc-jets might be construed to fall into the experimental thruster category for a limited class of missions having very short propulsion times. Resistojets and arc-jets have been operated with propellants such as hydrogen and ammonia, but these propellants require tankage of at least 25%, and since the resistojet and arc-jet operate at specific impulse below 1000 seconds, reference to Figure 27 indicates that these thruster types are not suitable for primary propulsion in most missions.

The original Kaufman thruster has mercury vapor for propellant, and employs an oxide-coated cathode. An alternate to the oxide-coated cathode has been conceived and tested with very promising results. This alternative is the liquid pool cathode in which liquid mercury propellant is fed directly to the discharge chamber and the liquid surface acts as the cathode. Performance of the liquid-mercury-cathode electron-bombardment thruster[6,49] has been found to be superior to both the Kaufman thruster and the cesium electron-bombardment thruster. However, this experimental thruster has not yet been operated in a laboratory prototype having realistic components. For this reason, the LMC electron-bombardment thruster is not compared with the flight-prototype thrusters in this paper.

The other experimental thruster is an electron-bombardment thruster with mercury vapor propellant. This thruster is being developed for the SERT-II flight, and is described more completely in another paper[37] at this symposium. The SERT-II thruster represents a synthesis of a number of concepts that have been found to have merit. The basic configuration of the discharge chamber and accelerator system is similar to the original Kaufman thruster. The SERT-II thruster features a hollow cathode, a highly divergent magnetic field, and a screen grid with 70% open area. Only a small fraction of the propellant flows through the hollow cathode and the remainder enters the discharge chamber at other places. With these improvements, the performance of the SERT-II thruster is about the same as that of the cesium electron-bombardment thruster, as shown in Figure 31. Many man-years of research and development have been invested in the three thrusters shown in Figure 31. Whether significantly improved performance can be obtained with these thrusters is a moot question.

Advanced Concepts

There are a number of advanced concepts in electric propulsion presently being investigated in various laboratories. All of these concepts have promise of reducing or avoiding fundamental limitations of the thrusters discussed in the preceeding sections. Each of these advanced concepts are discussed in the following sections, and a prognosis is offered wherever possible.

High-power electron-bombardment thrusters. Large electric spacecraft of the future will require jet power levels of hundreds of kilowatts, or even megawatts, for primary propulsion[50]. The flight-prototype and the experimental thrusters discussed previously have jet powers of the order of 1 kilowatt. From a systems standpoint the prospect of hundreds or thousands of thruster modules on a single spacecraft is not attractive. For this reason, high-power single modules of the Kaufman thruster have been designed and operated as feasibility demonstrations. A fifty-centimeter anode-diameter Kaufman thruster[51] installed in a vacuum chamber is shown in Figure 32. This thruster has a jet power of as high as 30 kilowatts, and complete performance measurements have been made in the specific impulse range from about 8000 to 10,000 seconds. A 150-cm Kaufman thruster with a jet power of about 200 kilowatts is presently being tested in the same facility. The successful operation of these two large thruster modules appears to be an adequate demonstration of basic feasibility in the 8000 - 10,000 second specific impulse range.

Efficiency of the 30-kilowatt thruster is about 90% in the specific impulse range from 8000 to 10,000 seconds, so the total propulsion system specific weight is much less than that for systems in the lower specific impulse range with 1-kilowatt thruster modules. Total system specific weight with the 30-kilowatt thruster is compared with the 1-kilowatt thruster systems in Figure 33. It should be noted that when lighter weight powerplants become available, then the effective specific weights associated with thruster and power conditioning efficiencies will become smaller than those shown in Figure 33.

The large size of the 50-cm and 150-cm Kaufman thrusters is possible primarily because a larger spacing, L, between the screen grid and the accel electrode can be used. With the higher accelerator voltages at specific impulses approaching 10,000 seconds, the spacing can be as large as 1-cm and still maintain an adequately high ion current density as indicated by Equation (4). In addition, the higher values of ϕ_{net} for specific impulses of 8000 to 10,000 seconds increases the jet power density. In the lower range of specific impulse, ϕ_{net} is much smaller so that the accelerator electrodes must have much smaller spacing in order to maintain an adequate ion current density. Thermal stresses cause warping of the screen-grid and the accel-electrode plates which prevents practical operation of thrusters much larger than 20-cm anode diameter in the lower range of specific impulse.

The 30-kilowatt and 200-kilowatt Kaufman thruster modules offer concrete evidence that arrays of such thrusters for megawatt-level electric spacecraft could fit within the payload shroud of booster rockets without any special problems in packaging. However this is only true in the specific impulse range near 10,000 seconds. If lightweight powerplants can be developed in the future, then most missions in the solar system[43] would demand a specific impulse in the neighborhood of 10,000 seconds. This generalization is valid for constant thrust operation in which there is always a significant penalty in payload. Variable thrust operation, which is the ideal case, would require much lower specific impulse for the earth-escape phase and for the initial portion of the heliocentric-transfer phase. It is also important to note that lunar ferry missions will require specific impulse in the 2000 to 4000 second range. For these reasons, it is of great interest to develop electric thrusters having a high exhaust-jet power density in the low specific impulse range. It does not appear that the electron-bombardment thruster can achieve high power density at low specific impulse without radical departures from the existing design concepts.

Plasma thrusters. In plasma thrusters the gaseous or vapor propellant is first ionized and then accelerated with a combination of magnetic and electric fields. A host of schemes and concepts have been examined in the past decade and most of these have proven not of interest for electric propulsion for various fundamental reasons. Of those concepts still remaining, the MPD thruster has the best performance and appears to be of the most interest for future research and development[52]. The MPD thruster operates with direct current power at 100 to 200 volts so that direct coupling to nuclear-electric powerplants with the Rankine cycle or with thermionic diodes should be possible, thereby eliminating power conditioning. Another advantage of the MPD thruster is a much greater exhaust-jet power density than is possible with electron-bombardment thrusters. Although the electromagnetic acceleration of the plasma propellant has appreciable power losses (in contrast to the loss-free acceleration process in electrostatic thrusters) it is possible in principle that this accelerator loss can be made negligibly small. To have high thruster efficiency, the MPD thruster must also have a small ionization power in comparison to jet power. For example, if the exhaust energy of the propellant ions is 100 ev and if the ionization power is 10 ev/ion, then the thruster power efficiency would be about 90%. Thruster efficiency is the product of power efficiency and propellant utilization efficiency, so nearly all the propellant atoms would have to be ionized and accelerated to the same exhaust velocity in order to have a high thruster efficiency. It is hoped that these stringent demands can be met in the future, but at present the performance of the MPD thrusters is much lower than that of electron-bombardment thrusters.

The basic processes in plasma thrusters are very complex and are not fully understood at present. Much of the research on these thrusters must be done experimentally. Laboratory experiments have been carried out with thruster concepts operated in the kilowatt power range. At these low power levels the magnetic field needed for the acceleration process must be largely supplied by external electromagnets. As the power level is increased, the electric currents in the thruster become much larger so that self-induced magnetic fields are generated. It is expected that MPD thrusters with power levels in the hundreds of kilowatts will have high enough self-induced magnetic fields to eliminate the need for external magnetic fields. Reduction or elimination of electromagnet power would do much to improve the efficiency of MPD thrusters. In addition it is expected that the high current levels would also improve the efficiency of the ionization and acceleration processes. Although thruster durability has not been investigated as yet, experiments with high current thrusters has shown no visible erosion of the cathode; and this is thought to be due to the strong self-induced magnetic field around the cathode which protects the cathode surface from ion impingement. In principle at least, the acceleration process can be accomplished without appreciable impingement of ions on the anode.

MPD thruster designs can be classified in terms of steady-state or pulsed mode operation. The ALPHA thruster[53] is an example of the steady-state type. This thruster has an efficiency of 50% at a specific impulse of 5000 seconds and a linear decrease in efficiency at lower values of specific impulse. Pulsed mode MPD thrusters are also being investigated[54] with the expectation that higher currents can be developed than with the steady-state type. Most of the plasma thruster experiments have been done with argon or xenon gas propellants, but in some recent work lithium[53] and cesium propellants have been used with success. In the light of the tankage specific weights shown in Figure 27, high density propellants will have to be used if the MPD thruster system is to have good performance at low specific impulse.

In summary, interest in plasma thruster research and development is continuing with the hope that high thruster efficiency can be achieved, particularly in the low specific impulse range of interest. Potential advantages of the MPD thruster are elimination of power conditioning, and high exhaust jet power density.

Radioisotope-heated contact-ion thrusters. Improved exhaust-jet power density is possible with contact-ion thrusters. Neutral-atom efflux can be less than 1%, and allowable ion current density may be 5 to 10 times as great as in electron-bombardment thrusters. Adequate accel electrode durability has been demonstrated[55] with ion current densities as high as 170 amp/m^2. With a ϕ_{net} of 1000 volts, corresponding to a specific impulse of 4000 seconds, the exhaust jet power density for such a thruster is 170 kwj/m^2.

As mentioned previously, the contact ionizer must be maintained at high temperature (1400°K for 170 amp/m^2), and there is a great amount of heat loss by radiation and conduction from the ionizer. Because of this heat loss, the contact-ion thruster has been plagued with a lower efficiency than the Kaufman or cesium electron-bombardment thrusters. Radioisotope heating of the contact ionizer would relieve the powerplant of the ionizer-heating function, thereby greatly improving the thruster efficiency.

Using the Hughes strip-beam contact-ion thruster shown in Figure 9 as an example, total system specific weights can be estimated for a radioisotope-heated version of this thruster. For the purposes of this estimate, plutonium-238 has been selected because of the long half-life (90 yr.), fairly high power density (3.9 watt/cm^3), and good availability (30 kwt/yr by 1970). A disadvantage of plutonium-238 is that a large void fraction must be provided to contain the helium evolved in the decay process. Based on the quoted performance of the strip-beam contact-ion thruster[55], the sub-system parameters are[56]:

$$\eta_{th} = \left[1 + (50/\phi_{net}) \right]^{-1} \qquad (10)$$

which accounts for estimated vaporizer, neutralizer, and accelerator drain powers, and:

$$\alpha_{th} = 12{,}400/\phi_{net} \qquad (11)$$

in lb/kwj at j = 170 amp/m^2, and:

$$\dot{Q}/P_{j,eff} = 870/\phi_{net} \qquad (12)$$

where the ionizer heat loss per unit area is $\dot{Q}/A = 150$ kwt/m^2 at j = 170 amp/m^2.

Specific weight of a hypothetical propulsion system based on the preceeding discussion is shown in Figure 34. This estimate suggests that radioisotope-heating of the contact thruster ionizer might result in performance superior to that of the electron-bombardment thruster systems. Whether this potential performance can be realized depends on a number of factors. For example, the necessity for a large void fraction to contain the helium gas might result in greater thruster weights than used in the present estimate. Another important factor is the availability of radioisotopes. As shown by equation (12) the thermal power required for the radioisotope heater is roughly equal to the jet power of the thruster. Jet powers needed for an electric spacecraft such as the Mars orbiter-lander are about 10 kwj, so that about one-third of the annual production of plutonium-238 in 1970 would be required for one spacecraft. When test and back-up systems are included, it is possible that the entire annual production would be required, which is probably out of the question. Even though production of radioisotopes will be much greater in the future, radioisotope-heated contact-ion thrusters will probably not be attractive for extensive application to high-power electric spacecraft missions.

Plasma-separator thruster. Another advanced concept that holds promise for higher jet power density is a scaled-up version of the plasma separator thruster discussed previously in the section on auxiliary electric propulsion. If accelerator structures with thin separating insulators can be developed to a reliable status with acceptably low leakage current, then the very small spacing L between electrodes would allow very high ion current densities even with the low accelerator voltages encountered in the lower range of specific impulse.

Further analysis should be done to determine whether the charge-exchange ion erosion of the accel electrode is small enough at low accelerator voltages to allow high ion current densities. If such analyses indicate a reasonable degree of feasibility, then an experimental program on large plasma-separator thrusters could go forward with confidence.

Potential propulsion system specific weights with the plasma-separator thruster are shown in Figure 35. The plasma-separator thruster does not have any electromagnets or permanent magnets, so the thruster weight was assumed to be 5 lb. which is about one-half of the weight of comparable sized electron-bombardment thrusters. Furthermore the peak ion current density arriving at the separator electrode was assumed to be 60 amp/m^2 which is about the value presently used in electron-bombardment thrusters. If further investigation shows that much higher ion current densities can be tolerated at the low voltages in the lower specific impulse range, then the thruster physical specific mass could be considerably reduced, particularly in the lower range of specific impulse. In addition, the exhaust-jet power density would be substantially improved. For the hypothetical 15-cm diameter thruster shown in Figure 35, the total ion current was assumed to be 0.6 amperes. At a specific impulse of 2130 seconds the value of ϕ_{net} is 300 volts, so the power density at that low specific impulse is only 10 kwj/m^2 which is an order of magnitude lower than the exhaust jet power density quoted previously for the contact-ion thruster. With an exhaust-jet power density of 10 kwj/m^2, a 1 megawatt array of such thrusters would cover an area of 100 square meters which is too large to fit into the payload shroud of even the largest boosters. From such simple considerations, it is clear that much higher ion current density must be achieved before the plasma-separator thruster can be considered for primary propulsion in high-power spacecraft.

Mission analysis has shown that electric propulsion may have great advantages for propulsion of unmanned spacecraft in the heliocentric transfer portion of the mission profile. For this application total jet power is in the tens of kilowatts. At these power levels, only a few square meters of exhaust jet area would be required even though the power density is only 10 kwj/m^2. The potential capability of plasma-separator thruster to operate at very low voltages is of special interest for solar-electric spacecraft. For example, with ϕ_{net} equal to 100, 200, 300 volts the specific impulse with potassium propellant would be

2280, 3940, and 5090 seconds, respectively. Direct coupling of a potassium-propellant plasma-separator thruster to a high-voltage solar-cell array would eliminate the weight and complexity of power conditioning equipment. The advantages of direct coupling have been extolled in the preceeding text.

The potentially superior performance of the plasma-separator thruster should be adequate incentive for continued study of this advanced concept. An important facet of this continued study should be the development of thin-insulator accelerator structures with unsupported spans large enough to allow practical operation of high-power thruster modules in the lower range of specific impulse.

Space-charge-sheath thruster. If electrons can be constrained to remain in, or flow through, the accelerator region then the positive space charge of the ions could be reduced or cancelled by the negative space charge of the electrons. By this means, very large ion current densities should be possible, thereby providing high exhaust jet power densities even at low accelerator voltages. The space charge sheath thruster[57] shown in Figure 36 represents an attempt to reduce the space charge limitation on exhaust jet power density. Cesium propellant flows through the ring-shaped porous-tungsten ionizer and these ions are accelerated through the potential difference between the ionizer and space. Electrons are emitted from filaments around the outer diameter of the ionizer ring and are attracted toward the ionizer by a potential difference. A radial magnetic field of several thousand Gauss is maintained between the inner and outer pole pieces, and this magnetic field together with the axial electric field causes the electrons to travel around the ionizer surface in cycloidal paths. The dimensions of the cycloid are a function of the cyclotron radius of the electrons, and the cyclotron radius is roughly a measure of the accel length, L, of the ion acceleration process. With a strong magnetic field the electron cyclotron radius will be small which in principle will allow very high ion current densities. Further downstream other electrons are emitted from filaments surrounding the ion beam and these electrons enter the ion beam to neutralize the space charge in the exhaust.

This advanced concept has been operated successfully but only limited experimental measurements have been published. There has been no analysis published of the flight performance parameters required to judge the potential merit of the concept. In the discussion of plasma thrusters it was noted that external magnetic fields impose a severe weight penalty, and this will be an important factor in evaluating the merit of the space charge sheath electric thruster.

Charged-particle electrostatic thrusters. The liquid-spray charged-particle electrostatic thruster discussed previously in AUXILIARY ELECTRIC PROPULSION is also a potential candidate for primary propulsion. The efficiency of this thruster in the lower range of specific impulse is much higher than electron-bombardment thrusters. Exhaust-jet power from each needle is simply the product of ϕ_{net} and the current of charged particles from that needle. Successful operation of this thruster has been attained with needle currents as high as 13 microamperes with charge/mass ratios from 400 to 9000 coulomb/kilogram. With the 9000 coulomb/kilogram charged particles the ϕ_{net} is from 38,000 to 340,000 volts in the specific impulse range from 2000 to 6000 seconds respectively. Therefore the power per needle in this range of specific impulse is from 0.5 to 4.5 watts. For an electric spacecraft with 10 kilowatts of jet power, roughly 2000 needles would be required, which is a staggering number. The physical size of a liquid-spray charged-particle thruster array for primary propulsion will depend on the needle spacing. A needle spacing of 1 cm appears feasible, and this would provide an exhaust-jet power density of about 10 kwj/m^2 which would be adequate for solar-electric propulsion of unmanned spacecraft. For megawatt level spacecraft, a spacing of a few millimeters would be required to attain a reasonably high exhaust-jet power density.

There has been some question raised about the durability of charged-particle electrostatic thrusters[58]. A charged particle of 9000 coulomb/kg has a mass of 10,000 amu, and with an energy of 100,000 ev, can be expected to cause considerable impact damage. Even with an exceedingly small amount of charge-exchange between charged and neutral particles, accel electrode durability could be a severe problem. The two-hundred-hour tests performed so far with the liquid-spray charged-particle thruster are not long enough to stand as sufficient evidence of durability. In the absence of other means for demonstrating durability, resort must be made to duration tests of several thousand hours in order to establish durability.

In conclusion, the excellent performance of laboratory prototype liquid-spray charged-particle thrusters is sufficient grounds for a continuing program of research and development.

ADVANCED ELECTRIC PROPULSION RESEARCH

A number of fundamental limitations and shortcomings of electric thrusters have been pointed out in the preceeding text. Some of these are presently receiving attention in basic research programs. Because of their possible importance to future trends in electric propulsion, these basic research programs are discussed briefly in the following sections.

ATEP System

One of the shortcomings of the resistojet is the very low specific impulse which has been obtained from these thrusters so far. A part of the reason for this low specific impulse is the limited temperatures that have been achieved so far in the heaters. Another important factor is the frozen-flow loss, first from dissociation, and then from ionization at higher temperatures. The ATEP system[56] is a possible means for obtaining higher specific impulse with electrothermal thrusters, and also may be of some benefit to plasma thrusters and electrostatic thrusters.

Fundamental concepts of the ATEP system are shown in Figure 37. Instead of entering directly into the electric thruster, propellant is first passed through the prime thermal power source and then enters the electric thruster at a fairly high temperature. Propellant vapor is then expanded thermodynamically through a supersonic nozzle to a velocity v_n. After leaving the nozzle, the propellant is further accelerated to the exhaust velocity v_j by electrical means. In applying the ATEP system concept to the resistojet, acceleration from v_n to v_j would be accomplished by addition of heat to the supersonic stream by some means involving electric power. By use of a contoured nozzle and by an axial variation of heat addition, it is hoped that the static temperature of the vapor stream can be kept down to levels where dissociation and ionization are negligible. Theoretical studies of the addition of heat to supersonic streams for this purpose are presently being done[56].

Analyses[56] have shown that the ATEP system concept might double the exhaust jet power density of electrostatic thrusters operating at specific impulse in the 1000 to 2000 second range. A study of the application of the ATEP system concept to plasma thrusters is planned for the future[56]. It is notable that the thermal heating of propellants before entry into the electric thruster has been considered for the resistojet electric propulsion system intended for possible use in MORL missions.

Preliminary mission analysis[56] has shown that the ATEP system might provide considerable increases in the payload capacity of electric spacecraft. This is primarily due to significant reductions in the specific weight of the total propulsion system because the thermodynamic cycle inefficiency is avoided to some degree by thermal power addition in the first part of the propellant acceleration process. In other words, the ATEP system can be thought of as a combination of nuclear rocket and electric rocket principles. Payload mass fractions for the ATEP system are compared with those for conventional electric propulsion system in Figure 38. The parameter β is a measure of the difficulty of the mission and the specific weight of the total propulsion system. Fast missions and/or long-distance missions have higher values of β. Solar-electric propulsion systems will also have large values of β, even for comparatively easy missions, because of the high specific weight of such propulsion systems. From inspection of Figure 38 it is clear that the ATEP system offers very significant payload increases for the higher values of β. Potential improvements in electric spacecraft performance such as illustrated here offer motivation for basic research to investigate the fundamental feasibility of the ATEP system.

Charged-Particle Electrostatic Thrusters

The most crucial problem facing electrostatic thruster development is attainment of a sufficiently high exhaust-jet power density in the lower range of specific impulse. Of course, thruster efficiency also must be high in the lower range of specific impulse. Exhaust-jet power density is limited by three factors:

a. Space-charge-limited current density.
b. Break-down limited electric field strength.
c. Charge-exchange-erosion limited current density.

The first two of these limits are illustrated in Figure 39 where maximum exhaust-jet power density is plotted against v/g_c for a fixed accel length L, and for several propellant types. From examination of this figure it is evident that electrostatic thrusters with atomic-ion propellants cannot have adequately high exhaust-jet power densities unless the accel length, L, is much smaller than 2 mm. Electrostatic accelerator systems with very thin insulation between the electrodes might provide such small accel length, but the complete practicality of accelerator systems with very small accel length can be established only after more research and development.

With accelerator systems having accel lengths of several millimeters or even centimeters, it is clear that charged-particle propellants could provide much higher exhaust-jet power densities than atomic-ion propellants. In fact, the power densities shown to be possible in Figure 39 are more than adequately high even for megawatt class electric spacecraft. If such power densities can be achieved with charged-particle thrusters, then the plasma thrusters could no longer claim a unique potential advantage of high exhaust-jet power density.

For the reasons described above, charged-particle electrostatic thrusters are of interest. The liquid-spray charged-particle thruster discussed previously will depend on very close needle spacing or on much higher needle currents to provide high power density. Another possible charged-particle thruster[56] is one in which the particles are formed by nucleation from the vapor state with subsequent charging by electron attachment or bombardment. A number of propellant types have been successfully used in homogeneous nucleation experiments, and it appears possible that nearly any kind of vapor can be used in producing sub-microscopic particles by homogeneous nucleation. With this omnivorous capability in mind, propellant sources such as spent components of spacecraft and biowaste can be considered.

Propellant from spent tankage. Chemical rocket propellant tanks are expected to be made of aluminum because of the superior fracture resistance of aluminum at cryogenic temperatures. Aluminum melts at 932°K and has a reasonably high vapor pressure at temperatures below 2000°K, so with a high-temperature reactor on board aluminum might be a suitable propellant for charged-particle thrusters.

Improvement in mission performance that would result from the utilization of spent booster tankage has been analyzed[56]. Payload gains by using spent tanks from booster rockets can be quite large, depending on the difficulty of the electric spacecraft mission. The greatest increase in payload would occur if all of the electric spacecraft propellant were obtained from spent booster tankage. These payload gains are shown in Figure 40, and as explained in a previous section, the parameter β is a measure of mission difficulty and propulsion-system specific mass. For the more ambitious missions (large β) the payload gain with spent-tankage as propellant is very great. Payload gains such as shown in Figure 40 are much greater than those that could be obtained from many other improvements to electric thrusters. These potential payload gains provide much incentive and justification for research on charged-particle thrusters that can employ aluminum vapor as propellant.

Aluminum particle formation by homogeneous nucleation. The feasibility of formation of aluminum particles by homogeneous nucleation with subsequent charging by electron bombardment or attachment is presently being investigated. A theoretical analysis based on the Frenkel theory of nucleation is being developed. With the aid of this theory, supersonic nozzles are being designed and fabricated for experimental operation.

Aluminum-oxide particle formation by vapor-phase chemical reaction. Another possible method for particle formation is by chemical reaction, in particular the chemical reaction between aluminum vapor and oxygen and/or water vapor. With aluminum available from spent tankage, the oxidant would be available from open-cycle life maintenance systems. Experimental equipment is presently being assembled to investigate the feasibility of particle formation by this method.

Liquid-spray charged-particle formation from biological wastes. There are a number of organic macromolecules having molecular weights in the range of interest for charged-particle thrusters. Several possibilities exist for utilizing biowastes for propellant, for example organic molecules might form the central kernel for liquid drops, thereby promoting a more uniform size of droplets in the electrostatic spraying process. Experimental equipment is presently being assembled to study the feasibility of this advanced concept.

CONCLUDING REMARKS

Electric propulsion is ready to take a useful part in a number of space missions. With solar-cell powerplants, electric thrusters of several types offer significant advantages over all other forms of propulsion for satellite station-keeping and attitude control. There are a number of experimental thrusters and advanced concepts that have promise of even better performance, so it may be expected that electric propulsion will become even more useful in the future. Present flight-prototype electric propulsion systems are rather complex, being composed of thousands of critical components in the power conditioning subsystem. Simplicity usually is synonymous with reliability, and this implies that the advanced concepts that can be directly coupled to the powerplant are of the most interest for continued research and development. With a firm flight-ready status, and with definite potential for great improvement, the future of auxiliary electric propulsion systems is sure to grow in importance and scope.

Primary electric propulsion has been greatly hampered in the past by lack of a suitable powerplant. Through the efforts of certain managers of the national electric propulsion program and some groups in the electric propulsion community, a well-thought-out plan has been initiated for the development of solar-electric propulsion systems. All indications are that solar-electric propulsion, when used in the heliocentric portions of the mission, can greatly increase the payload of unmanned interplanetary spacecraft. Further, all indications are that the development of flight-ready solar-electric propulsion systems will be accomplished swiftly and surely. Success in this program should place electric propulsion firmly on the roster of practical space propulsion systems.

The review of primary electric propulsion has called attention to the need for efficient, electric thrusters that can operate in the specific impulse range from 2000 seconds and up with a high exhaust-jet power density at module power levels of 10,000 to 100,000 kilowatts. Plasma thrusters are believed to have the potential capability for meeting these requirements. At present, the efficiency of plasma thrusters in the lower range of specific impulse is much too low to be competitive with electrostatic thrusters. Processes inside the plasma thruster are very complex, so much work is being done to gain a better understanding of these processes, which hopefully will lead to greatly improved performance of the plasma thruster. Improvements in electrostatic thrusters are also expected. At present electrostatic thrusters are notably lacking in exhaust-jet power density in the lower range of specific impulse. Two approaches have promise of overcoming this disadvantage. The first of these is an atomic-ion thruster with very closely spaced accelerator electrodes that can operate directly from powerplant outputs of a few hundred volts. The second advanced concept is charged-particle thrusters wherein high exhaust-jet power densities and high efficiencies are very likely to be attained at low specific impulse.

National programs in electric propulsion have been in existence for a mere decade. Electric thrusters were once a laboratory curiosity but in a matter of a few years have come to be ready for space applications. Much has been accomplished, but much more remains to be discovered in electric propulsion. This is particularly true in the area of power for primary electric propulsion. So far, electric propulsion has been constrained to the use of powerplants that are not fundamentally suitable for this purpose. There are two alternatives: either electric thrusters may be developed that are specifically suited to existing concepts in electric power generation, or new electric power generation concepts must be conceived and developed that are directly compatible with ideal forms of electric thrusters.

Not so long ago electric propulsion suffered outrageous jibes about long extension cords. Today electric propulsion stands ready to perform tasks in satellite missions that cannot be done by less sophisticated propulsion systems. The not too distant future may find the "argosies of magic sails"[59] propelled with electrically charged sands of Mars, and given a little more time, with stardust.

References

1. Ernstene, M. P.: Progress and Prospects of Electrical Propulsion. AIAA Paper No. 66-830. November, 1966.

2. Lazar, J., and Mullin, J. P.: A Review of the Role of Electric Propulsion. AIAA Paper No. 66-1025. November, 1966.

3. Moeckel, W. E.: Status of Electric Thrusters. AIAA Paper No. 66-1024. November, 1966.

4. Brewer, G. R.: Ion Propulsion Is Ready for Application. AIAA Paper No. 66-1026. November, 1966.

5. John, R. E.: Current Status and Potentialities of Electrothermal and Electromagnetic Propulsion Systems. AIAA Paper No. 66- November, 1966.

6. Mickelsen, W. R.: Future Trends in Electric Propulsion. AIAA Paper No. 66-595. June, 1966.

7. Stearns, J. W., and Kerrisk, D. J.: Solar-Powered Electric Propulsion Systems - Engineering and Applications. AIAA Paper No. 66-576. June, 1966.

8. Solar Powered Electric Propulsion Program. Program Summary Report, JPL Contract No. 951144. Hughes Aircraft Company SSD 60374R. December, 1966.

9. Fabrication Feasibility Study of a 20 Watt per Pound Solar Cell Array. Final Report, JPL Contract 951132. The Boeing Company D2-23942-5. November, 1965.

10. Ritchie, D., Toms, R., and Menetrey, W.: Potentials of Solar Power for Electric Propulsion. AIAA Paper No. 66-210. March, 1966.

11. Krausz, A., Luft, W., and Bauer, P.: Solar Cell Power Systems for Electric Propulsion. AIAA Paper No. 66-891. November, 1966.

12. Tobias, I. I.: A Resistojet System for Attitude Control of Unmanned Earth Satellites. AIAA Paper No. 66-225. March, 1966.

13. Goodman, M.: Advanced Low-Thrust Propulsion Systems for Station Keeping and Stability Control of the NASA Manned Orbital Research Laboratory (MORL): Resistojets and Radioisotope Thrusters. AIAA Paper No. 66-226. March, 1966.

14. Goodman, M.: Low-Thrust Propulsion for the MORL. Journal of Spacecraft and Rockets. February, 1967.

15. Milligan, H. H., and Brandes, D. J.: Development Status of the Closed-Brayton Cycle Power Conversion System. AIAA Paper No. 66-889. November, 1966.

16. Zipkin, M.: Alkali Metal Rankine Cycle Power Systems for Electric Propulsion. AIAA Paper No. 66-890. November, 1966.

17. Rosa, R. J.: A High-temperature MHD Rankine Cycle. AIAA Paper No. 66-892. November, 1966.

18. Davis, J. P.: Thermionic Reactor Systems for Space Propulsion. AIAA Paper No. 67-51. January, 1967.

19. Worlock, R. M., Ramirez, P., Jr., Ernstene, M. P., and Beasly, W. E., Jr.: A Contact Ion Microthruster System. AIAA Paper No. 67-80. January, 1967.

20. Anderson, J. R., and Cybulski, R. J.: Status and Application of Low Thrust Electric Propulsion Systems. AIAA Paper No. 66-578. June, 1966.

21. White, A.: Electrothermal Microthrust Systems. AIAA Paper No. 67-423. July, 1967.

22. Mickelsen, W. R., and Kaufman, W. R.: Status of Electrostatic Thrusters for Space Propulsion. NASA TN D-2172. May, 1964.

23. Anderson, J. R., and Work, G. A.: Ion Beam Deflection for Thrust Vector Control. AIAA Paper No. 66-204. March, 1966.

24. Eilenberg, S. L., Caplinger, E., and Worlock, R. M.: Applications and Characteristics of Ion Thrusters in the Micro to Millipound Range. AIAA Paper No. 66-212. March, 1966.

25. Anderson, J. R., and Thompson, S. A.: Development and Long-Life Performance of Ion Engines for Satellite Control. AIAA Paper No. 66-234. March, 1966.

26. Kaufman, H. R.: An Ion Rocket with an Electron-Bombardment Ion Source. NASA TN D-585. 1961.

27. Sohl, G., Fosnight, V. V., Goldner, S. J., and Speiser, R. C.: Cesium Electron Bombardment Ion Microthrusters. AIAA Paper No. 67-81. January, 1967.

28. Hunter, R. E.: Theoretical Considerations of Non-Uniformly Charged Expellant Beams. ARL TN 60-138. October, 1960.

29. Mickelsen, W. R.: Electric Propulsion for Space Flight. Aerospace Engineering. November, 1960.

30. Cohen, E., and Huberman, M. N.: Research on Charged Particle Electrostatic Thrusters. Technical Report AFAPL-TR-66-94. September, 1966.

31. LaRocca, A. V.: Solid Propellant Electrical Thrusters for Attitude Control and Drift Correction of Space Vehicles. AIAA Paper No. 66-229. March, 1966.

32. "Another Plasma Jet" Industrial Research, p. 32. May, 1967.

33. Johansen, A. E., Bowditch, D. N., and Burkhart, J. A.: Experimental Performance of a Low-Power MPD Arc Thrustor. AIAA Paper No. 67-50. January, 1967.

34. Shelton, H., and Hall, D. F.: Program of Analytical and Experimental Study of Porous Metal Ionizers. Vol. I. NASA CR-54694. January, 1967.

35. Viventi, R., and Isley, W. C.: Design and Demonstration of a Radioisojet. AIAA Paper No. 67- . July, 1967.

36. Free, B. A., and Mickelsen, W. R.: Plasma Separator Ion Thruster Development. AIAA Paper No. 66-598. June, 1966.

37. Kerrisk, D. J., and Kaufman, H. R.: Primary Propulsion: Current Technology. AIAA Paper No. 67-424. July, 1967.

38. Free, B. A.: unpublished analysis. The General Electric Company, Evendale, Ohio, April, 1967.

39. Löb, H.: Entwicklungsstand des Gießener Ionentriebwerkes. Paper No. 66-003. DGRR-Symposium Elektrishe Raum-Antriebe. Sonnenberg/Harz (West Germany). February, 1966.

40. Margosian, P. M.: Preliminary Tests of Insulated Accelerator Grid for Electron-Bombardment Thrustor. NASA TM X-1342. February, 1967.

41. Preliminary Design Study of the ACCENT System. Monthly Progress Report for period 3 April 1967 to 3 May 1967, NASA Contract NAS5-10366. The DANE Company. May, 1967.

42. Lazar, J., and Peko, P. E.: Potential Applications for Electric Propulsion. AIAA Paper No. 67-422. July, 1967.

43. Mickelsen, W. R.: Performance Parameters for Electric-Propulsion Systems. Journal of Spacecraft and Rockets. February, 1966.

44. Molitor, J. H., Berman, P., Seliger, R. L., and Olson, R. N.: Design of a Solar-Electric Propulsion System for Interplanetary Spacecraft. AIAA Paper No. 66-214. March, 1966.

45. Cybulski, J., Shellhammer, D. M., Lovell, R. R., Domino, E. J., and Kotnik, J. T.: Results from SERT I Ion Rocket Flight Test. NASA TN D-2178. March, 1965.

46. Wilson, R. F., and Dieckamp, H. M.: What Happened to SNAP-10A? Astronautics and Aeronautics. October, 1965.

47. Reader, P. D.: Durability Tests of Mercury Electron-Bombardment Ion Thrusters. AIAA Paper No. 66-231. March, 1966.

48. Sohl, G., and Speiser, R. C.: Life Testing of Electron Bombardment Cesium Ion Engines. AIAA Paper No. 66-233. March, 1966.

49. King, H. J., Eckhardt, W. O., Ward, W., and Knechtli, R. C.: Electron-Bombardment Thrusters Using Liquid-Mercury Cathodes. AIAA Paper No. 66-232. March, 1966.

50. Mickelsen, W. R., and MacKay, J. S.: Interplanetary Flight with Electric Propulsion. Astronautics and Aeronautics. January, 1965.

51. Reader, P. D.: Experimental Performance of a 50-centimeter Diameter Electron-Bombardment Ion Rocket. AIAA Paper No. 64-689. August, 1964.

52. John, R. R., Bennett, S., and Jahn, R. G.: Current Status of Plasma Propulsion. AIAA Paper No. 66-565. June, 1966.

53. Jacobs, P. F., Moore, R. A., and Prichard, R. W.: Diagnostic Measurements in an Alkali Plasma Hall Accelerator. AIAA Paper No. 67-46. January, 1967.

54. Clark, K. E., and Jahn, R. G.: The Magnetoplasmadynamic Arcjet. To be published in Astronautica Acta. 1967.

55. Zimmerman, R. L., Garvin, H. L., McKee, W. E., and Kami, S.: Development of Multistrip Cesium Contact Thrustors. AIAA Paper No. 66-235. March, 1966.

56. Mickelsen, W. R.: Advanced Electric Propulsion Research. Annual Report for the period January to December, 1966, NASA Grant NGR06-002-032. January, 1967.

57. Meyer, Rudolph X.: A Space-Charge-Sheath Electric Thrustor. AIAA Paper No. 66-927. January, 1967.

58. Mickelsen, W. R.: Colloid-Particle Electrostatic Thrusters. Raumfahrtforschung, Heft 4. Oktober-Dezember, 1966.

59. Lord Tennyson, Alfred: Locksley Hall.

Table I. - Performance characteristics of AVCO flight-prototype resistojet microthrust propulsion system

thrust, micro-pounds	500
propellant	ammonia
tankage	25%
specific impulse, sec	175
power, watts	7

propulsion time, hrs.	1,000	10,000
thruster system, lb.	4.8	28.6
controls, lb.	.5	.5
propellant, lb.	10.6	106.
solar-cell array, lb.	1.1	1.1
TOTAL SYSTEM WEIGHT, lb.	17.0	136.2

Table II. - Performance characteristics of EOS flight-prototype contact-ion microthrust propulsion system.

thrust, micro-pounds	14
propellant	cesium
specific impulse, sec	6700
ϕ_{net}, volts	3000
power to thruster system, watts	12.3
power to conditioner, watts	18.9

propulsion time, hrs.	1,000	10,000
thruster system, lb.	2.5	2.5
power conditioning and controls lb.	5.0	5.0
propellant, lb.	.007	.07
solar-cell array, lb.	2.8	2.8
TOTAL SYSTEM WEIGHT, lb.	10.3	10.4

Table III. - Performance characteristics of Hughes flight-prototype contact-ion microthrust propulsion system.

thrust, micro-pounds	300
propellant	cesium
specific impulse, sec.	5000
ϕ_{net}, volts	1420
power to thruster, watts	69
power to conditioner, watts	105

propulsion time, hrs.	1,000	10,000
thruster system, lb.	5.0	5.0
power conditioning and controls, lb.	5.5	5.5
propellant, lb.	.2	2.2
solar-cell array, lb.	15.7	15.7
TOTAL SYSTEM WEIGHT, lb.	26.4	28.4

Table IV. - Performance characteristics of EOS flight-prototype electron-bombardment microthrust propulsion system (2.5 in. chamber diameter).

thrust, micro-pounds	370
propellant	cesium
specific impulse, sec	4680
ϕ_{net}, volts	2000
power to thruster system, watts	85
power to conditioner, watts	128

propulsion time, hrs.	1,000	10,000
thruster system, lb.	2.0	2.0
power conditioning and controls, lb.	5.9	5.9
propellant, lb.	.3	3.0
solar-cell array, lb.	19.2	19.2
TOTAL SYSTEM WEIGHT, lb.	27.4	30.1

Table V. - Estimated performance characteristics of TRW liquid-spray charged-particle electrostatic microthrust propulsion system

thrust, micro-pounds	20
propellant	glycerol
specific impulse, sec	700
ϕ_{net}, volts	5000
power to thruster system, watts	3.5
power to conditioner, watts	5.4

propulsion time, hrs.	1,000	10,000
thruster system, lb.	2.0	2.0
power conditioning and controls, lb.	5.0	5.0
propellant, lb.	.1	1.1
solar-cell array, lb.	.8	.8
TOTAL SYSTEM WEIGHT, lb.	7.9	8.9

Table VI. - Performance data for the SPET experimental microthrust propulsion system.

number of pulses in duration test	3.65×10^6
equivalent operation time at 1 pulse/sec	0.1 year
total impulse per pulse	1.4 micro-pound-sec
equivalent specific impulse	3300 sec
efficiency	10%
total impulse per year at 1 pulse/sec	44 lb-sec/yr
equivalent thrust level	1.4 micro-pound
power input to thruster	1 watt

Table VII. - Estimated performance characteristics of an experimental EM-PM MPD microthrust propulsion system with argon propellant.

thrust, micro-pounds	241	406	727
specific impulse, sec.	400	800	1600
power to thruster discharge, watts	92	125	241
electromagnet power	300	300	300

406 micro-pound thruster propulsion system

propulsion time, hrs.	1,000	10,000
thruster system*, lb.	11	11
controls, lb.	.5	.5
propellant, lb.	1.8	18.3
solar-cell array, lb.	63.9	63.9
TOTAL SYSTEM WEIGHT, lb.	77.2	93.7

*thruster system component weights:

thruster, feed lines, and tank, lb.	2
electromagnet coils	3
permanent magnet	6
	11

Table VIII. - Power requirements for contact-ion microthrusters.

thruster type	EOS	Hughes
thrust, micro-pounds	14	300
ion beam, watts	1.48	29.8
electrode drain, watts	.08	.2
vaporizer, watts	2.0	3.0
neutralizer, watts	1.1	6.0
sub total	4.66	39.0
ionizer heater, watts	7.66	30.0
total power to thruster	12.3	69.0

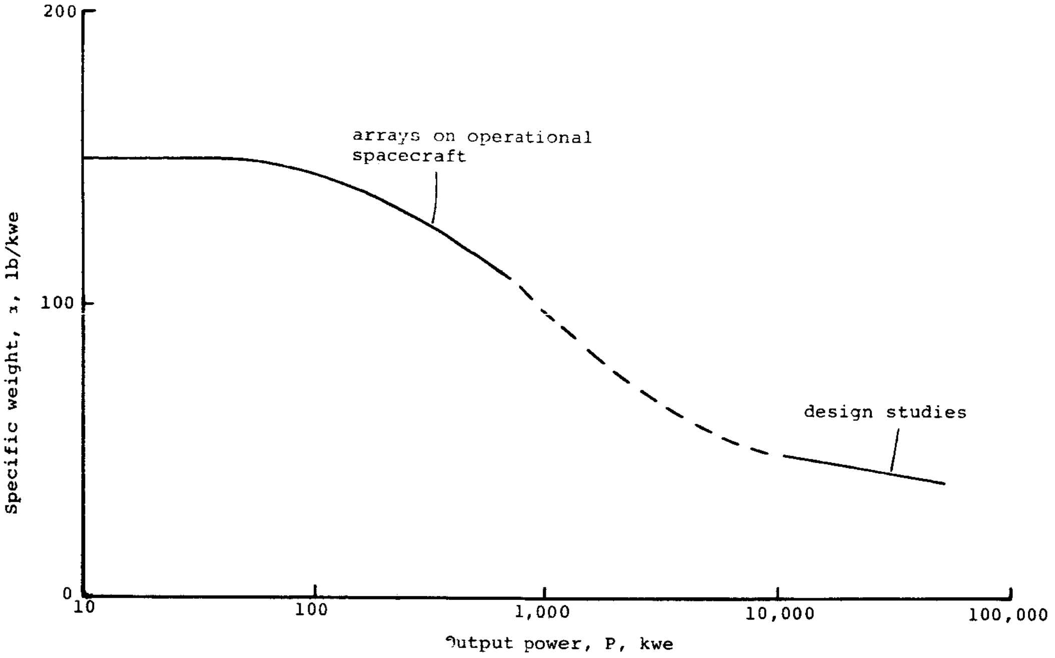

FIG. 1 - Solar-cell array specific weight at 1 A.U.

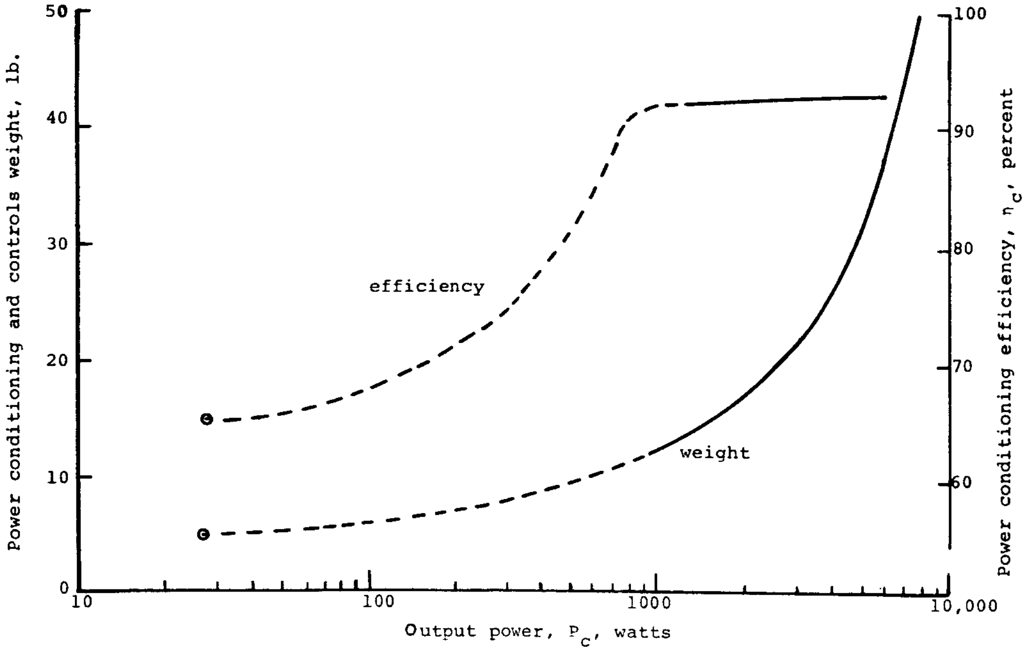

FIG. 2 - Power conditioning and control system weight and efficiency.

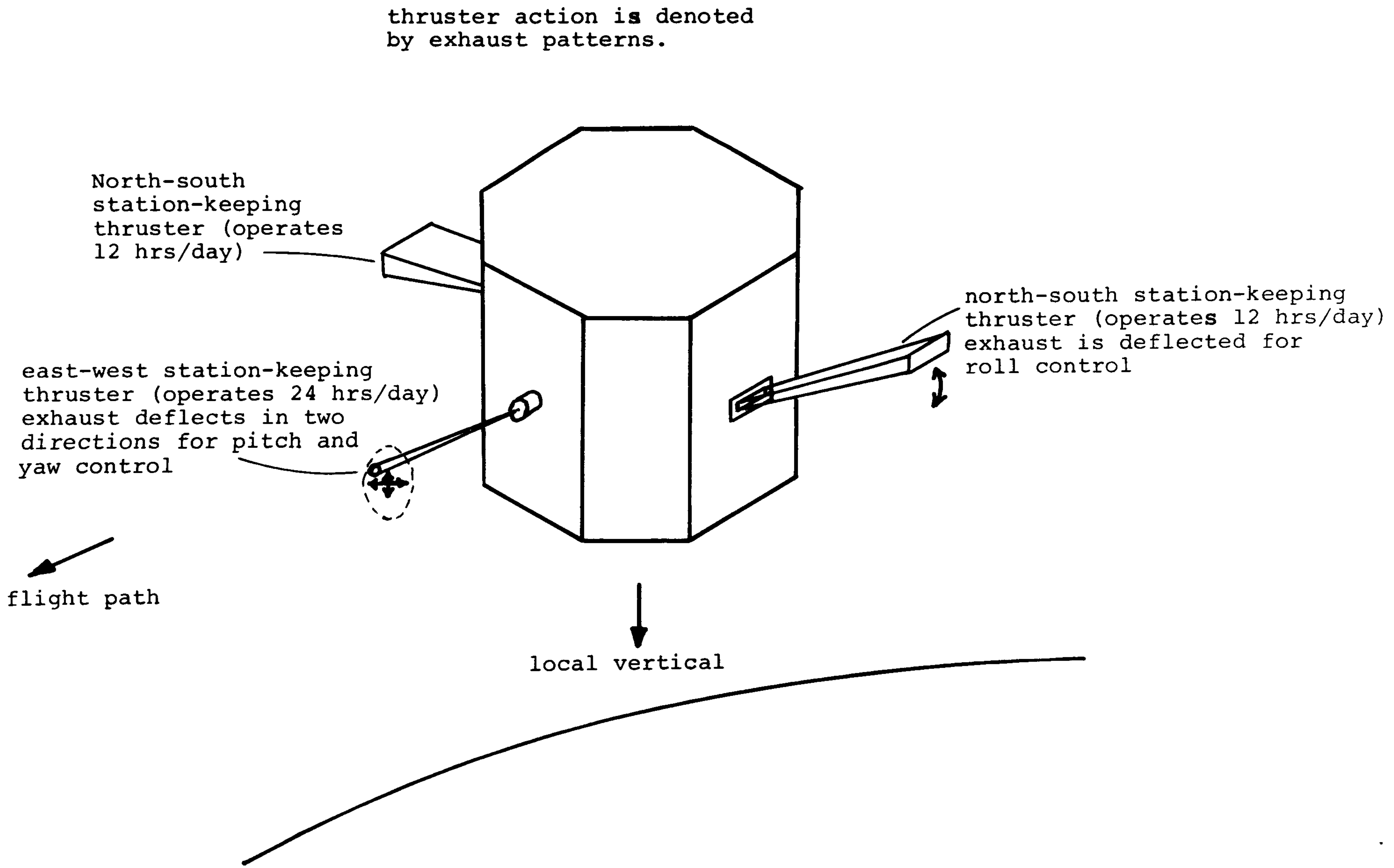
thruster action is denoted
by exhaust patterns.
North-south
station-keeping
thruster (operates
12 hrs/day)
north-south station-keeping
thruster (operates 12 hrs/day)
exhaust is deflected for
roll control
east-west station-keeping
thruster (operates 24 hrs/day)
exhaust deflects in two
directions for pitch and
yaw control
flight path
local vertical

FIG. 3 - Electric propulsion system for station-keeping and attitude-control
f synchronous satellites

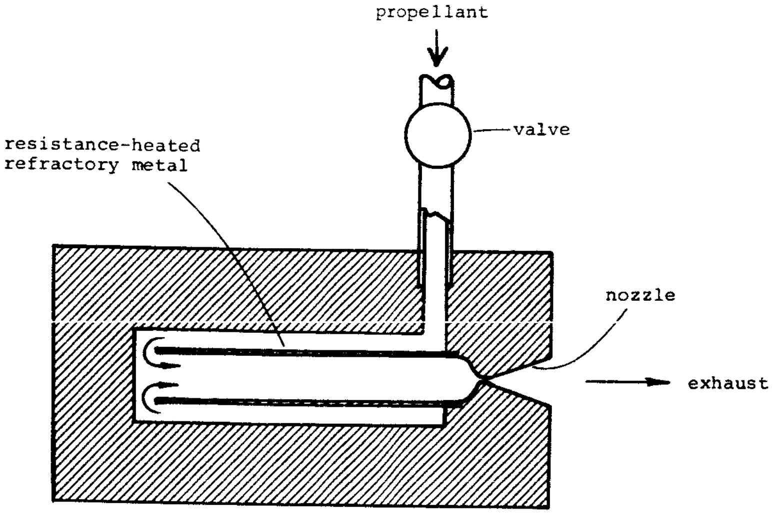
propellant
valve
resistance-heated refractory metal
nozzle
exhaust

FIG. 4 - Conceptual diagram of resistojet.

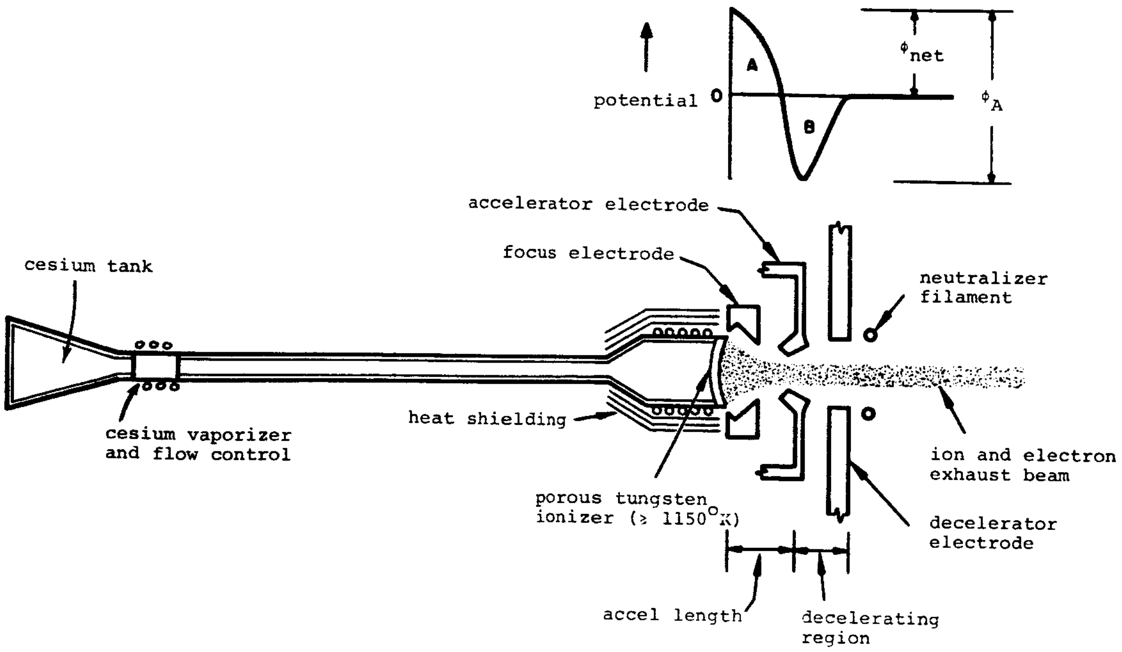
potential
0
A
B
ϕ_{net}
ϕ_A
accelerator electrode
focus electrode
cesium tank
neutralizer filament
cesium vaporizer and flow control
heat shielding
ion and electron exhaust beam
porous tungsten ionizer (≥ 1150°K)
decelerator electrode
accel length
decelerating region

FIG. 5 - Conceptual diagram of contact-ion thruster.

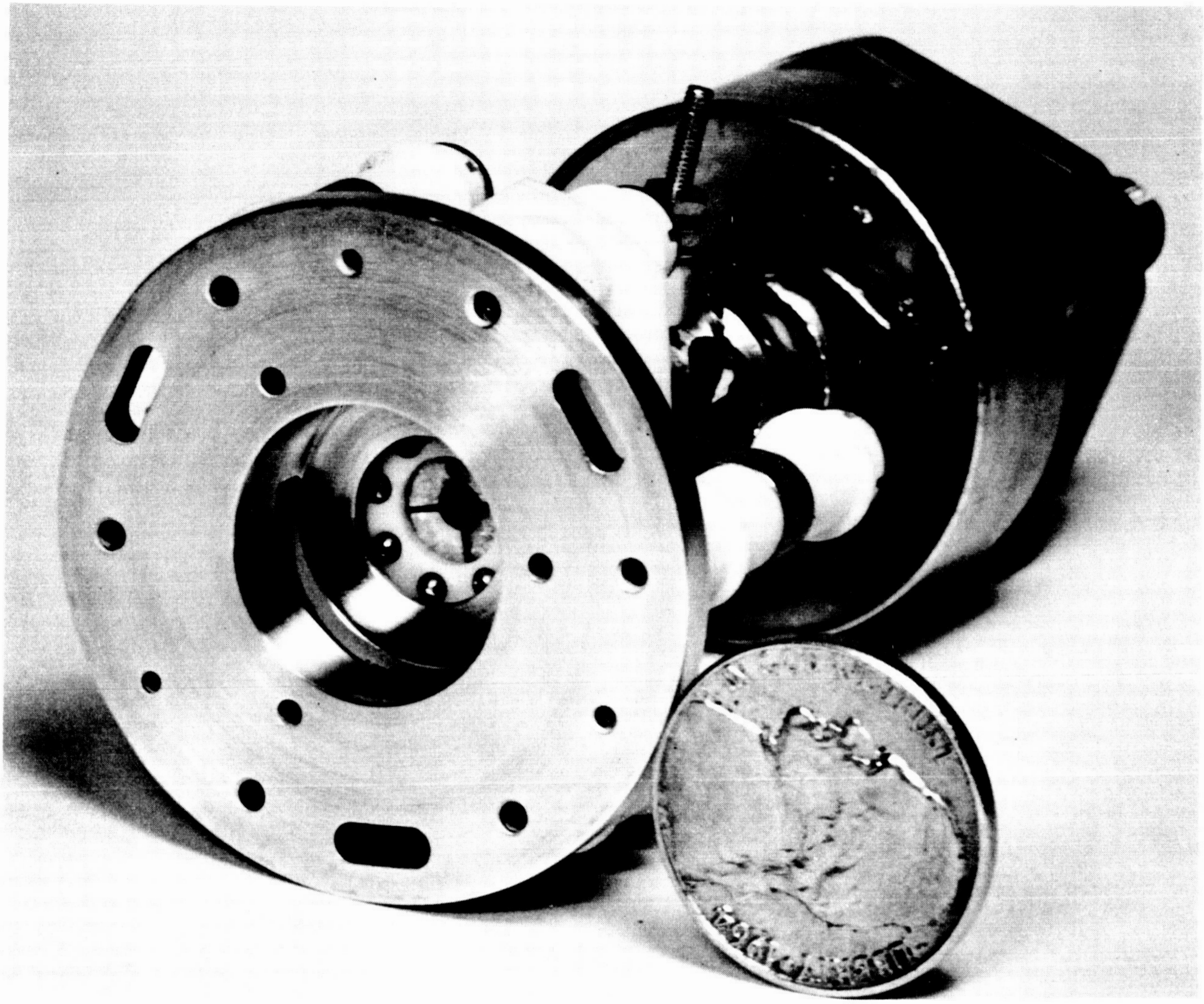

FIG. 6 - Segmented electrodes for precision exhaust-beam vectoring in flight-prototyp contact-ion microthruster. Courtesy of Hughes Research Laboratories, Malibu California.

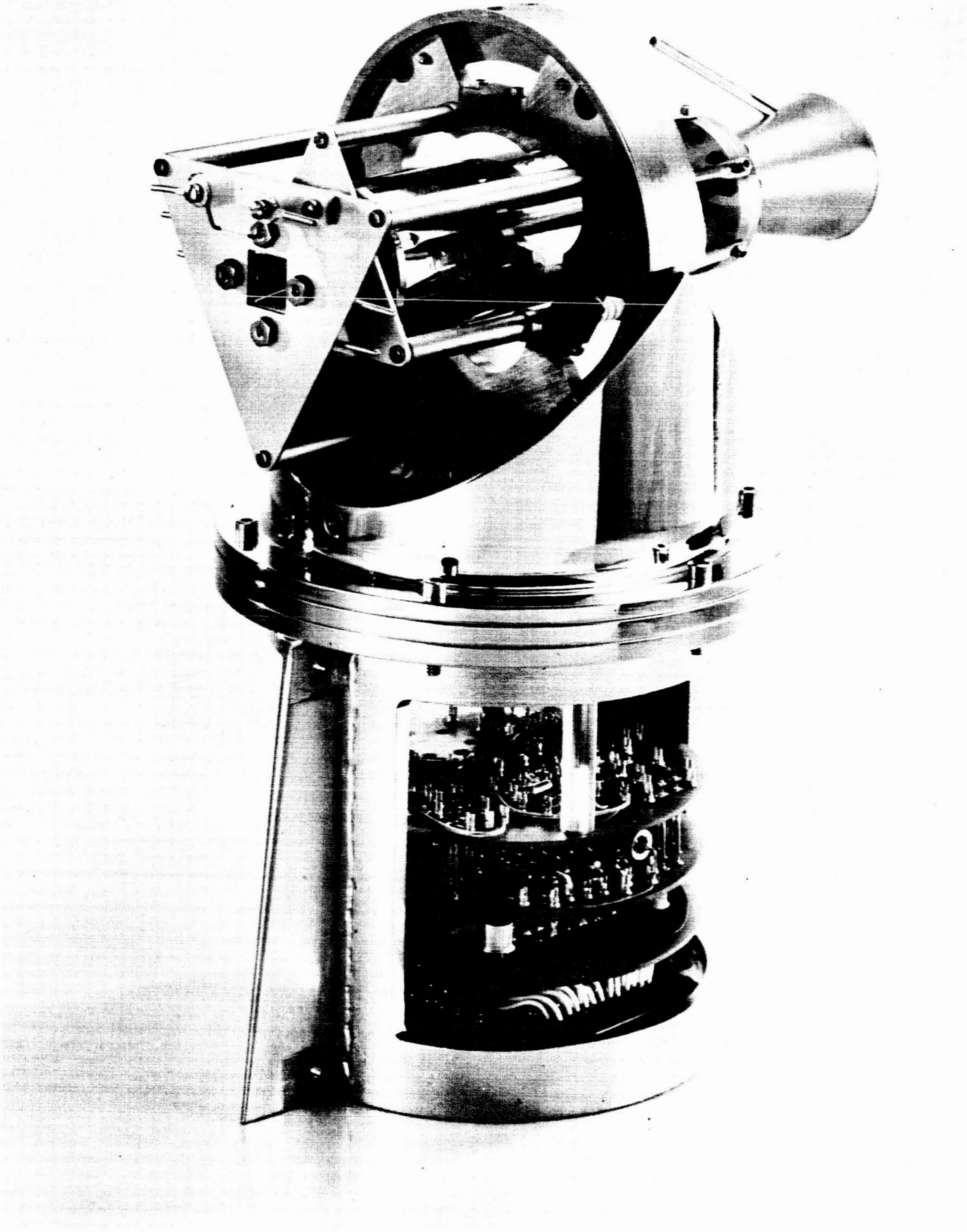

FIG. 7 - Flight-prototype contact-ion microthruster system. Thrust: 14 micro-pounds. Courtesy of Electro-Optical Systems, Inc., Pasadena, California.

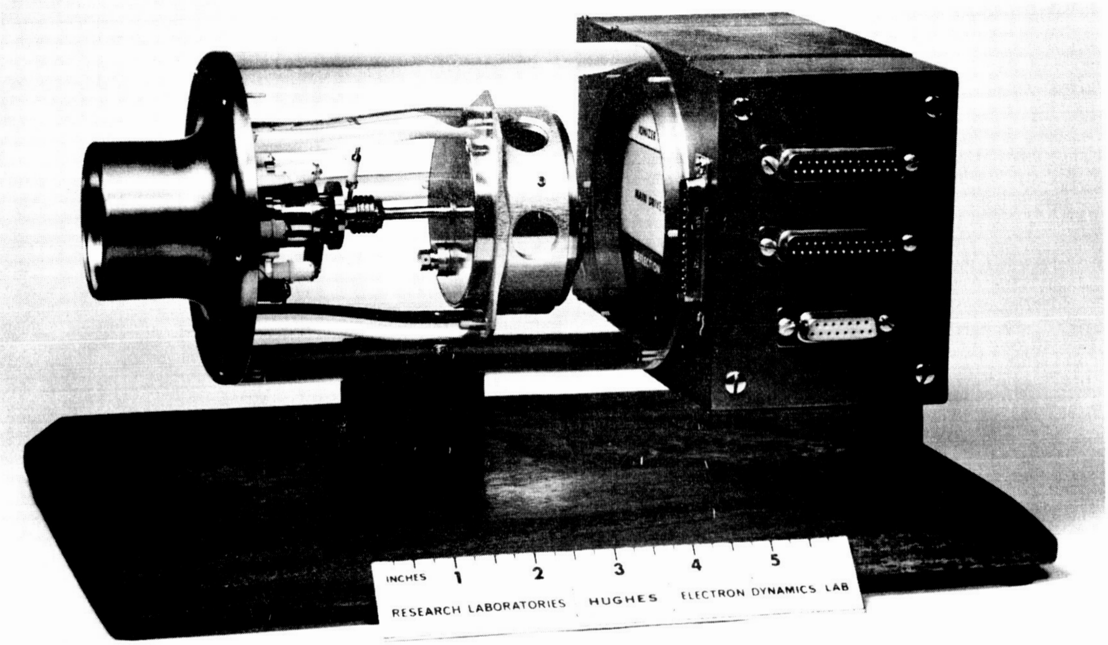
INCHES
1
2
3
4
5
RESEARCH LABORATORIES
HUGHES
ELECTRON DYNAMICS LAB
IONIZER
MAIN DRIVE

FIG. 8 - Flight-prototype contact-ion microthruster system. Thrust: 20 micro-pounds. Courtesy of Hughes Research Laboratories, Malibu, California.

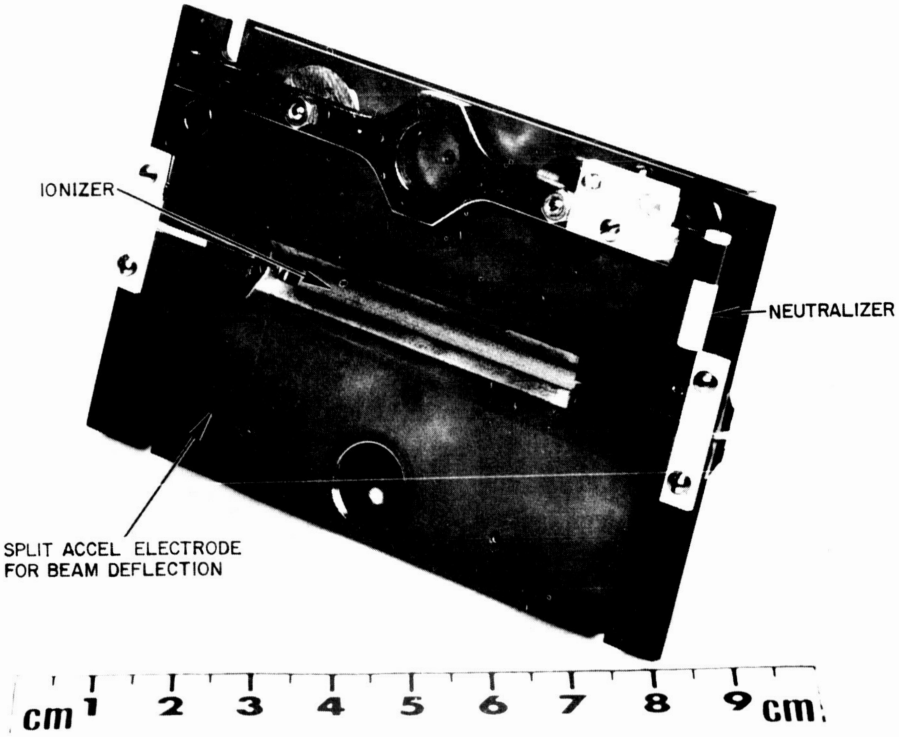
IONIZER
NEUTRALIZER
SPLIT ACCEL ELECTRODE
FOR BEAM DEFLECTION
cm 1 2 3 4 5 6 7 8 9 cm

FIG. 9 - Flight-prototype contact-ion microthruster. Thrust: 300 micro-pounds. Courtesy of Hughes Research Laboratories, Malibu, California.

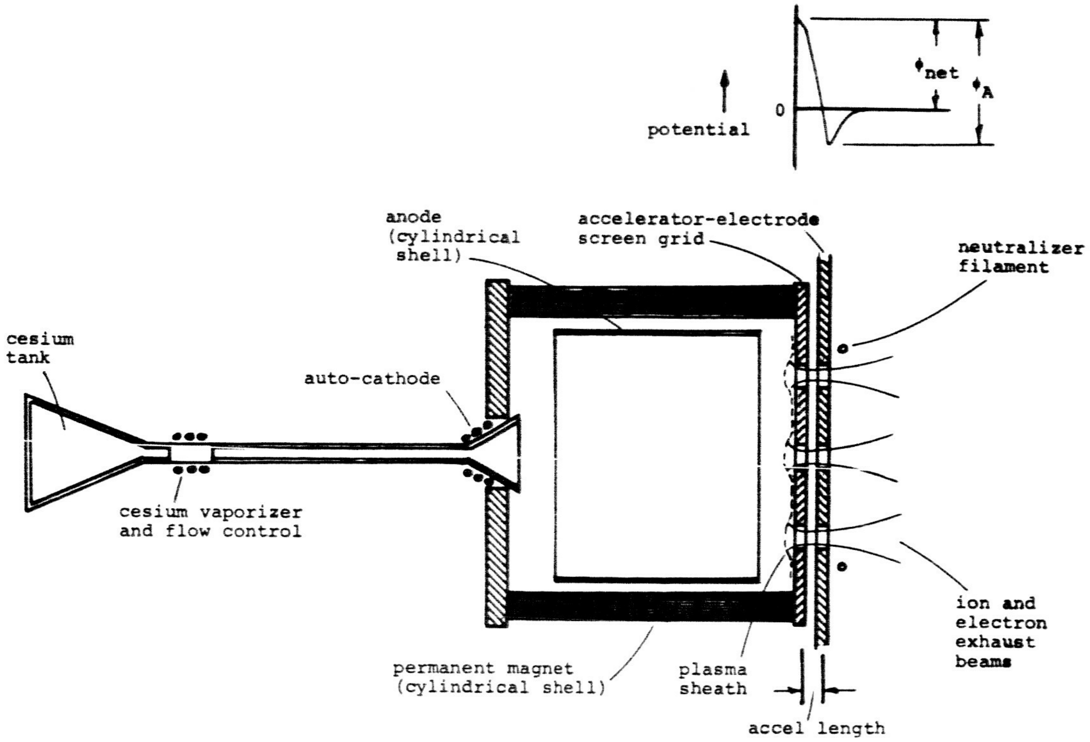
potential
0
φnet
φA
anode
(cylindrical
shell)
accelerator-electrode
screen grid
neutralizer
filament
cesium
tank
auto-cathode
cesium vaporizer
and flow control
ion and
electron
exhaust
beams
permanent magnet
(cylindrical shell)
plasma
sheath
accel length

FIG. 10 - Conceptual diagram of electron-bombardment thruster.

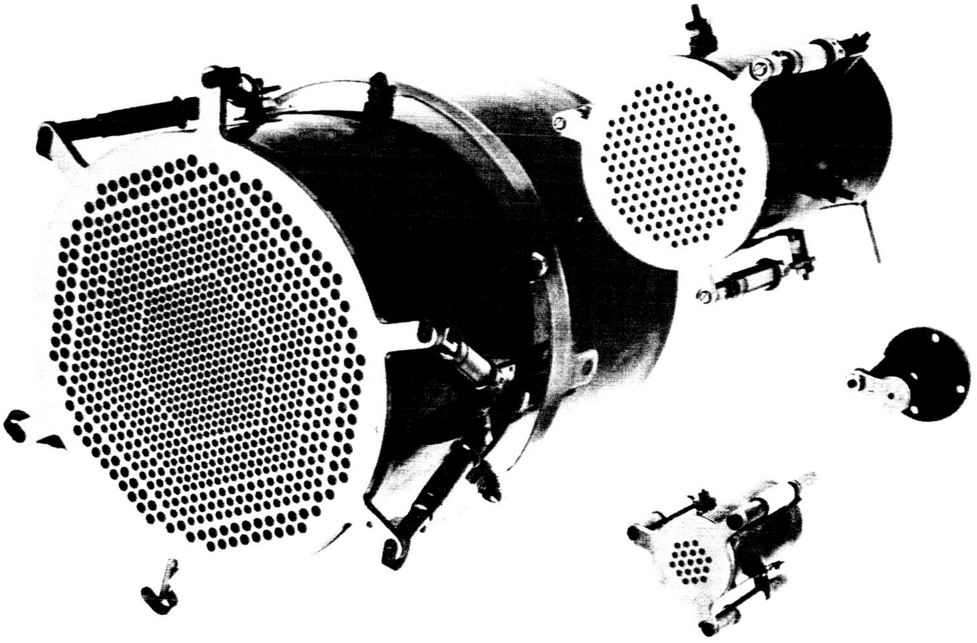

FIG. 11 - Flight-prototype electron-bombardment microthrusters. Courtesy of Electro-Optical Systems, Inc., Pasadena, California.

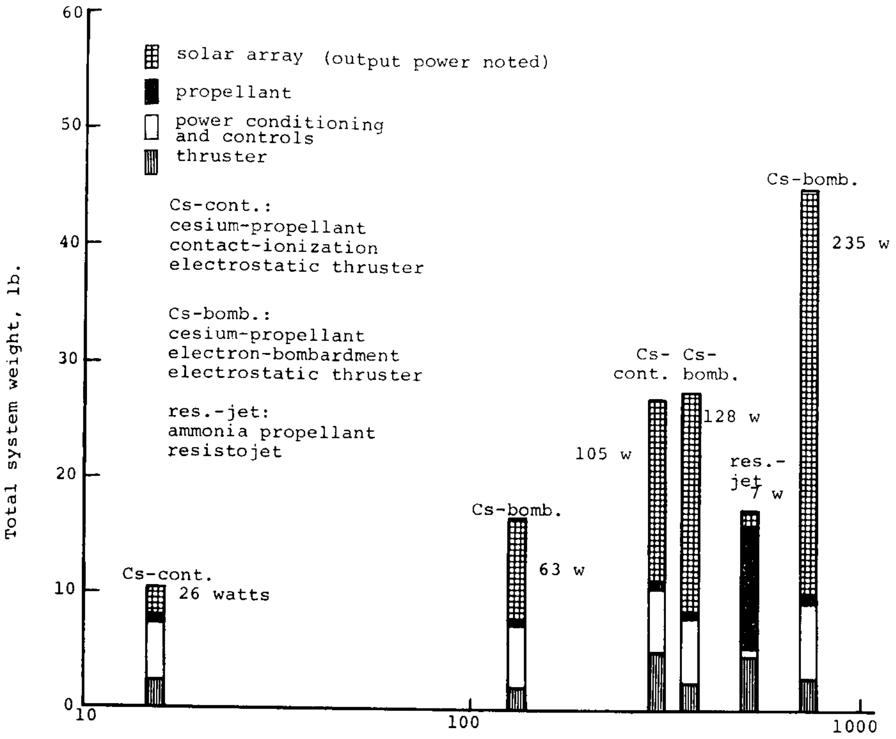

FIG. 12 - Flight-prototype ion thruster systems. Propulsion time: 1,000 hr.

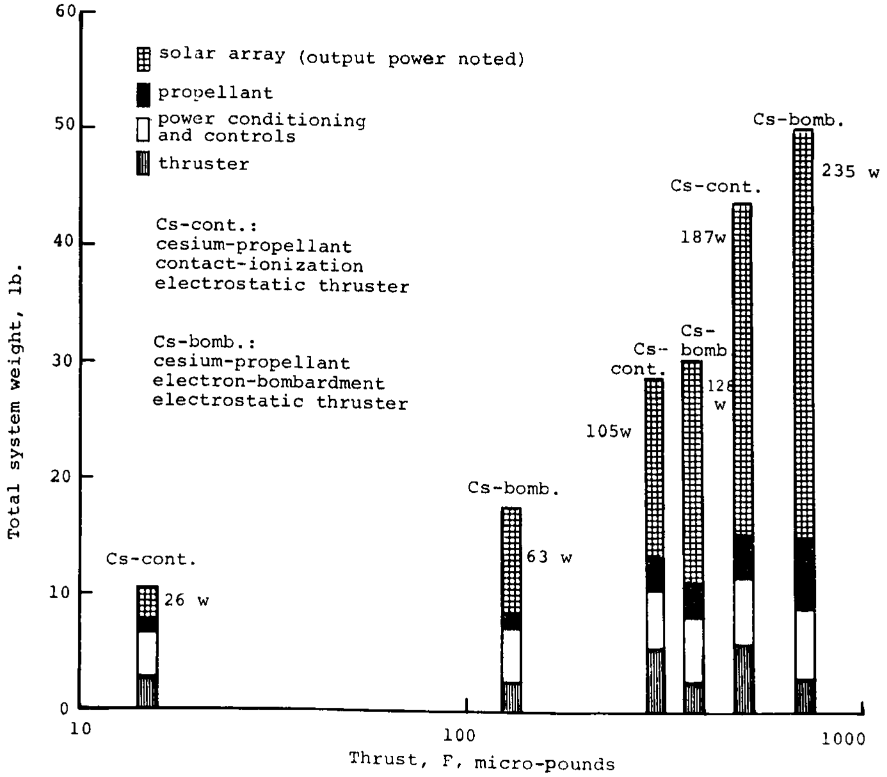

FIG. 13 - Flight-prototype ion thruster systems. Propulsion time: 10,000 hr.

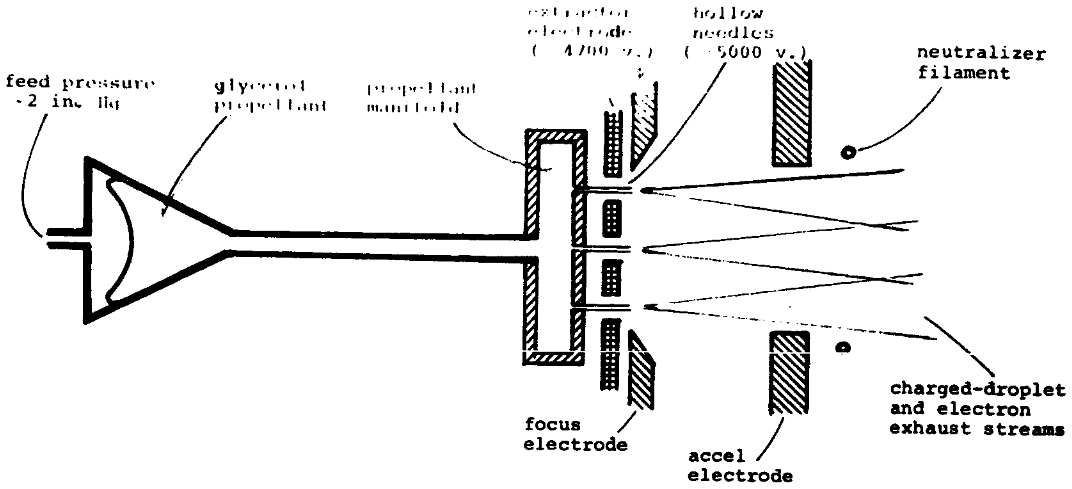
feed pressure
-2 in. Hg
glycerol
propellant
propellant
manifold
extractor
electrode
(4700 v.)
hollow
needles
(5000 v.)
neutralizer
filament
charged-droplet
and electron
exhaust streams
focus
electrode
accel
electrode

FIG. 14 - Conceptual diagram of liquid-spray charged-particle experimental microthruster.

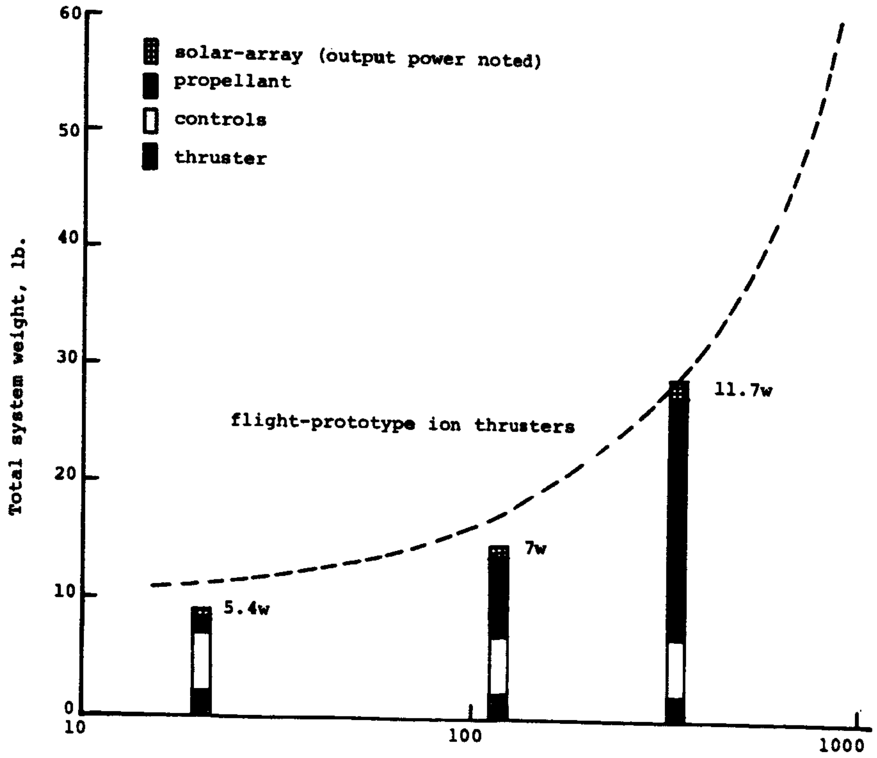

FIG. 15 - Estimated performance of experimental charged-particle electrostatic thruster in auxiliary propulsion systems. Propulsion time: 10,000 hrs.

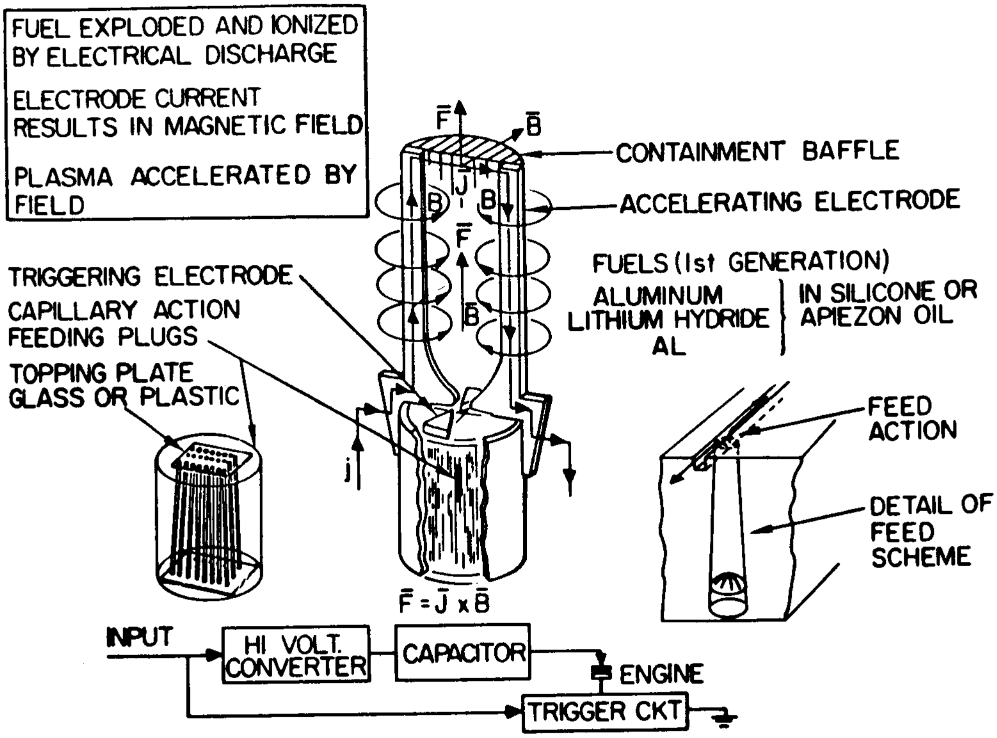
FUEL EXPLODED AND IONIZED BY ELECTRICAL DISCHARGE
ELECTRODE CURRENT RESULTS IN MAGNETIC FIELD
PLASMA ACCELERATED BY FIELD
F̄
B̄
J̄
CONTAINMENT BAFFLE
ACCELERATING ELECTRODE
FUELS (1st GENERATION)
ALUMINUM
LITHIUM HYDRIDE
AL
IN SILICONE OR APIEZON OIL
TRIGGERING ELECTRODE
CAPILLARY ACTION FEEDING PLUGS
TOPPING PLATE GLASS OR PLASTIC
j
FEED ACTION
DETAIL OF FEED SCHEME
F̄ = J̄ x B̄
INPUT
HI VOLT. CONVERTER
CAPACITOR
ENGINE
TRIGGER CKT

FIG. 16 - Diagram of the SPET experimental microthruster.

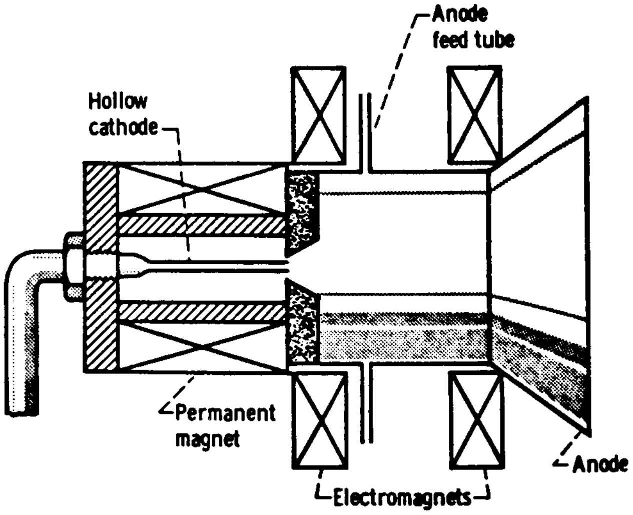
Anode feed tube
Hollow cathode
Permanent magnet
Electromagnets
Anode

FIG. 17 - Experimental EM-PM MPD microthruster.

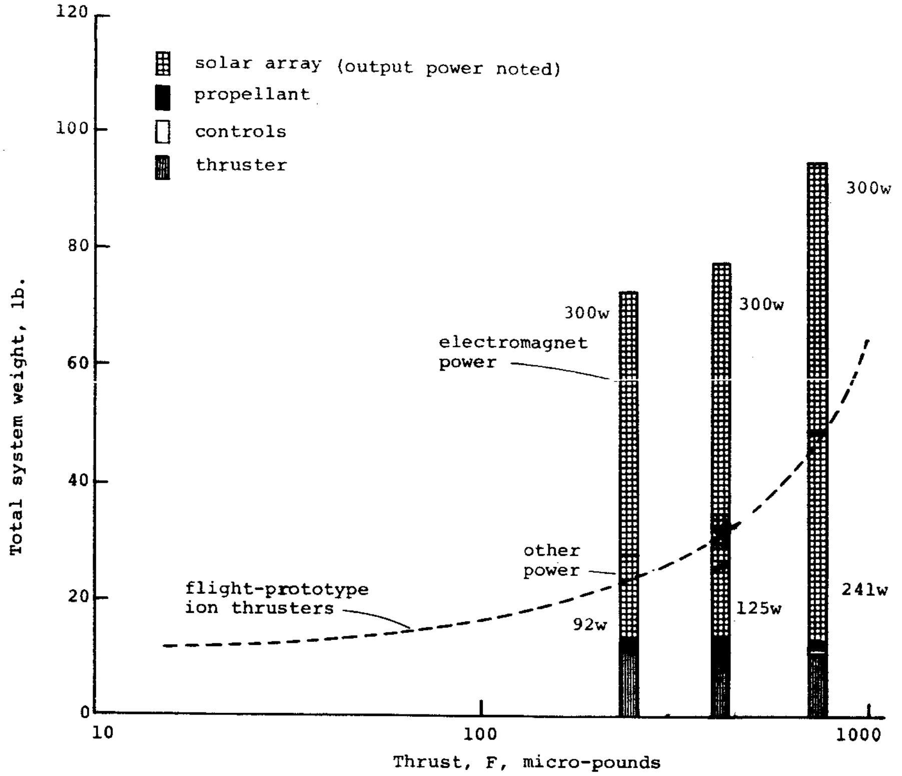

FIG. 18 - Experimental MPD microthruster. NASA-Lewis design, two-coil electromagnet and one permanent magnet. Argon propellant. Propulsion time: 1,000 hr.

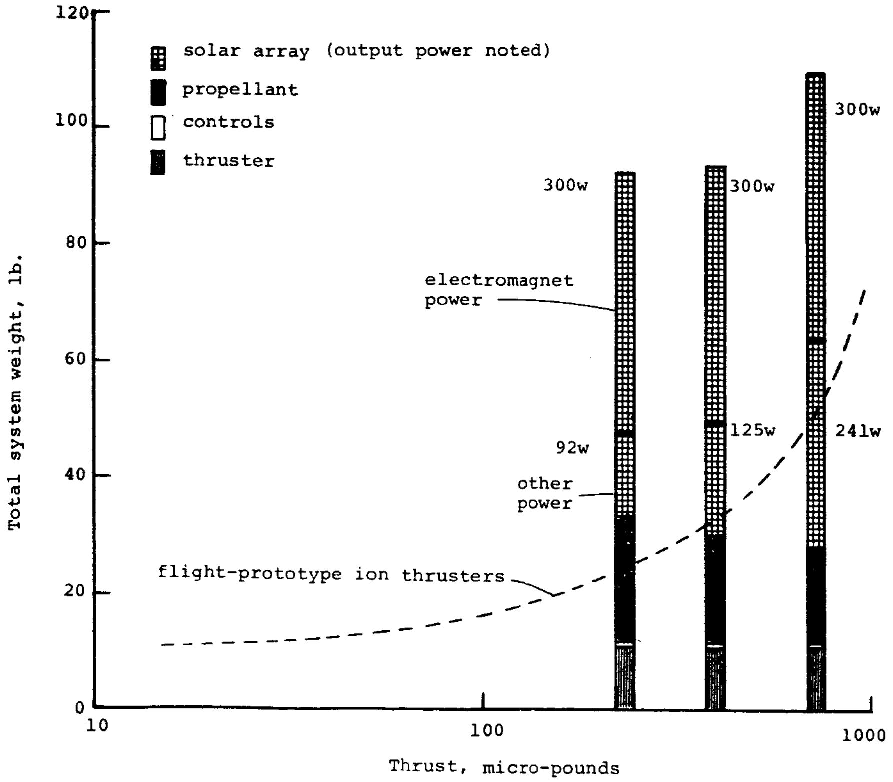

FIG. 19 - Experimental MPD microthruster. NASA-Lewis design, two-coil electromagnet and one permanent magnet. Argon propellant. Propulsion time: 10,000 hr.

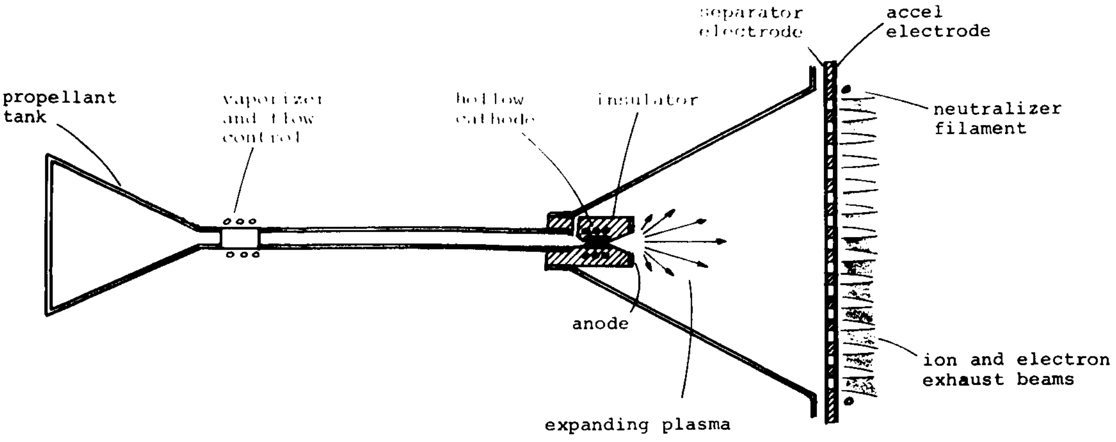
separator electrode
accel electrode
propellant tank
vaporizer and flow control
hollow cathode
insulator
neutralizer filament
anode
ion and electron exhaust beams
expanding plasma

FIG. 20 - Diagram of plasma-separator microthruster concept

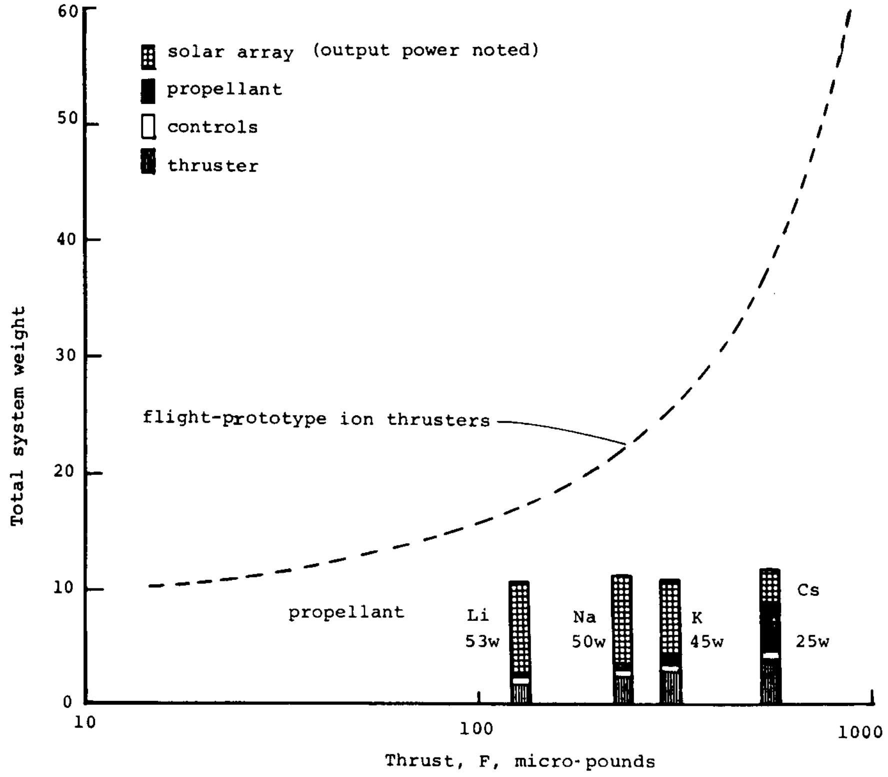

FIG. 21 - Hypothetical plasma-separator thruster systems. Accelerator voltage: 28 volts d.c Propulsion time: 1,000 hr.

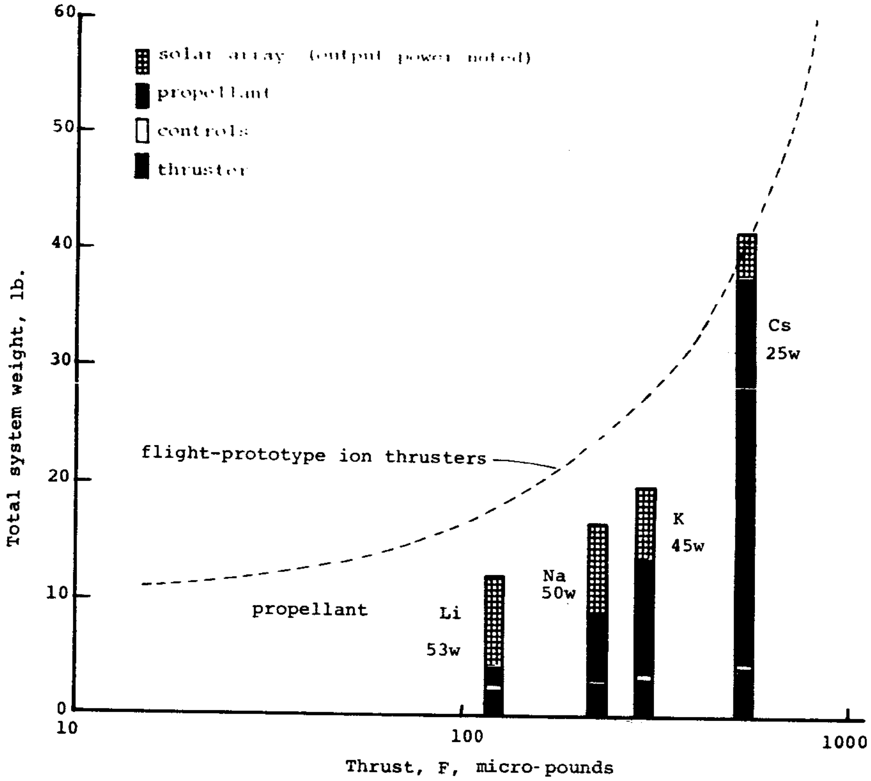

FIG. 22 - Hypothetical plasma-separator thruster systems. Accelerator voltage: 28 volts d.c. Propulsion time: 10,000 hr.

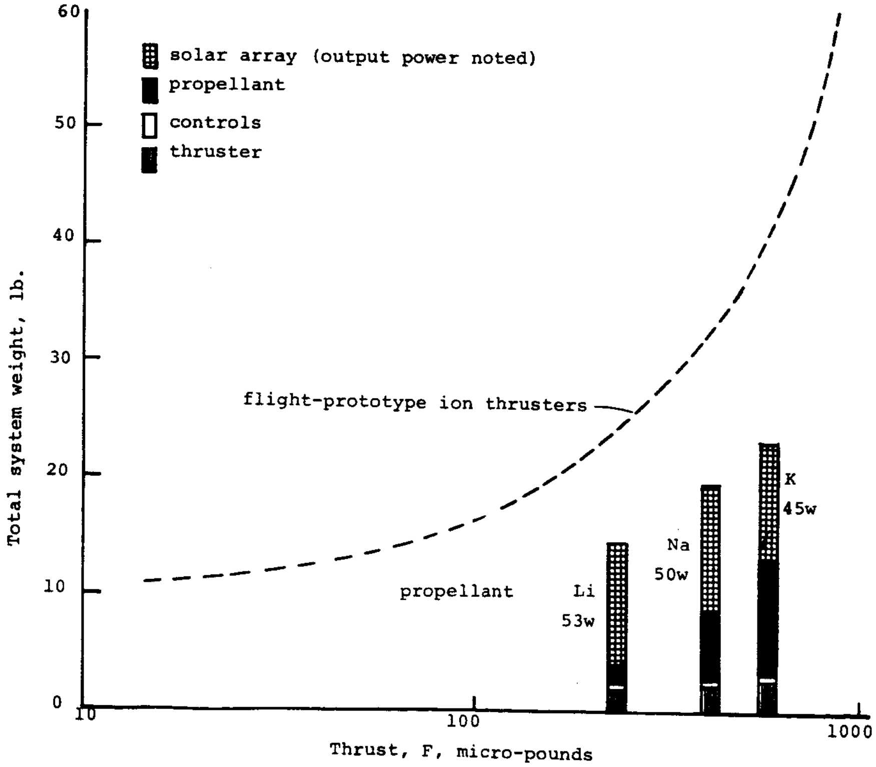

FIG. 23 - Hypothetical plasma-separator thruster systems. Accelerator voltage: 100 volts d.c. Propulsion time: 10,000 hr.

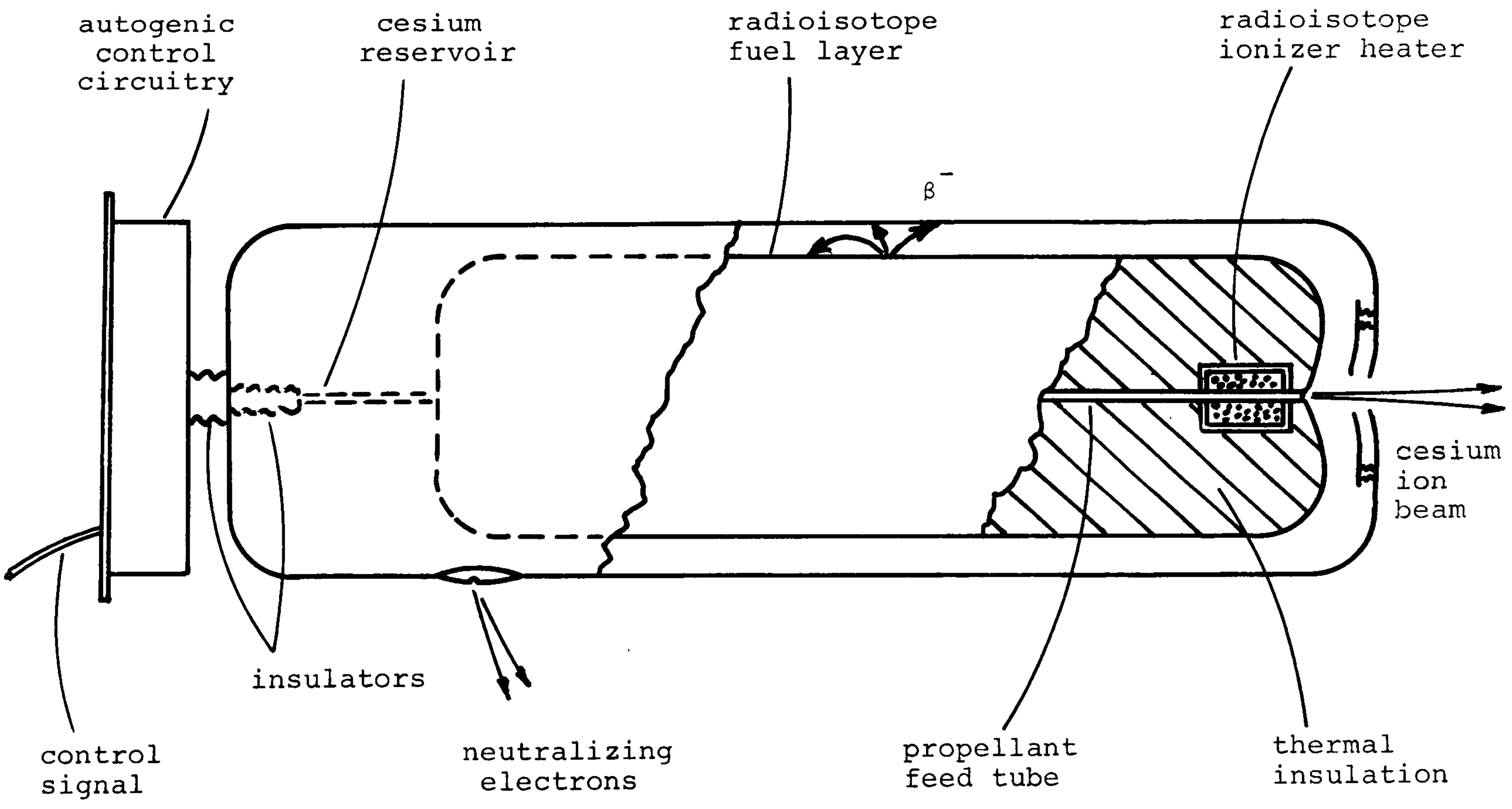

autogenic control circuitry
cesium reservoir
radioisotope fuel layer
β^-
radioisotope ionizer heater
cesium ion beam
control signal
insulators
neutralizing electrons
propellant feed tube
thermal insulation

FIG. 24 - ACCENT system principles.

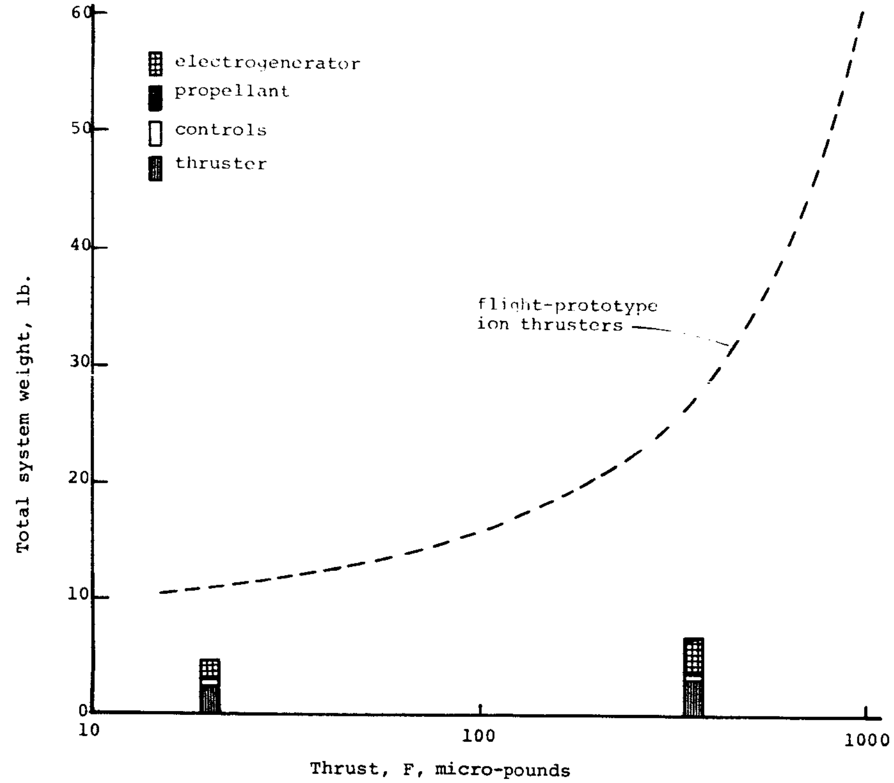

FIG. 25 - ACCENT concept. Propulsion time: 1,000 hr. Mission time: 10,000 hr.

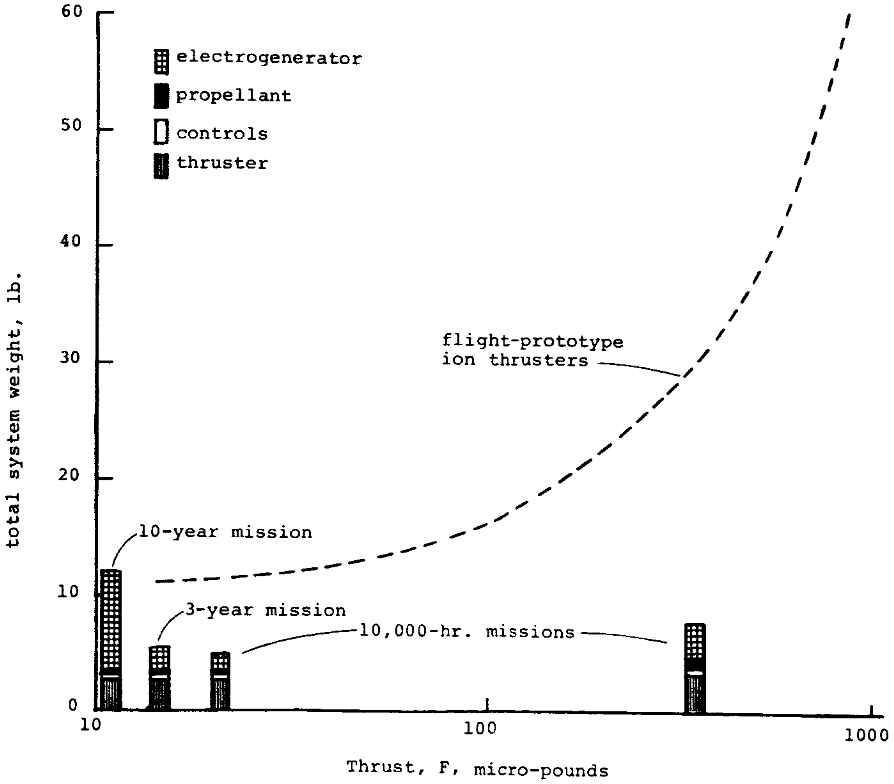

FIG. 26 - ACCENT concept. Propulsion time=mission time.

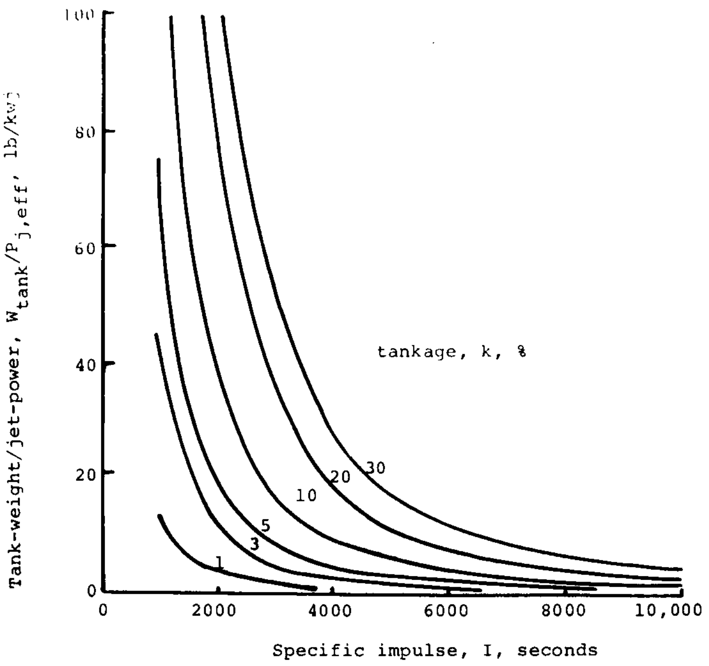

FIG. 27 - Specific weight of propellant tanks for electric propulsion systems. Propulsion time: 1 year.

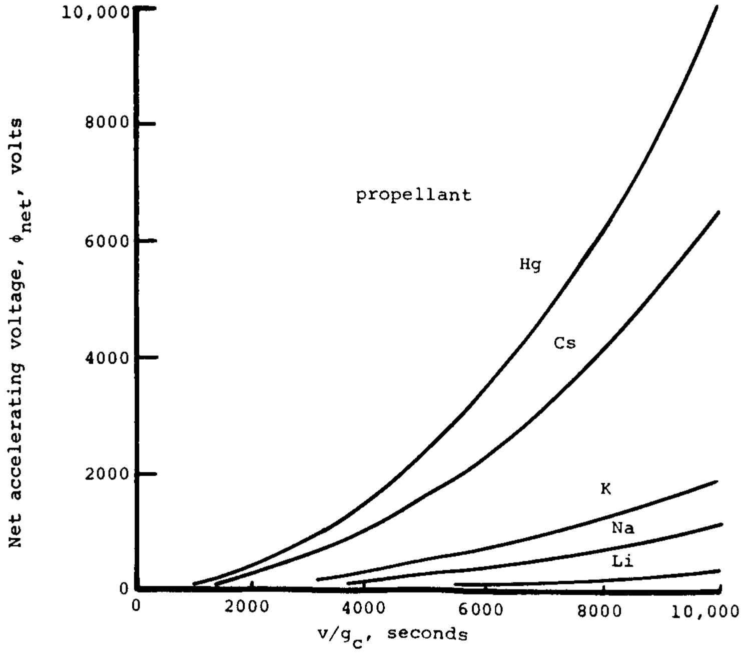

FIG. 28 - Net accelerating voltage for various singly-charged atomic-ion propellants. Specific impulse $I = \eta_U v/g_c$, where η_U is propellant utilization efficiency, and v is exhaust velocity.

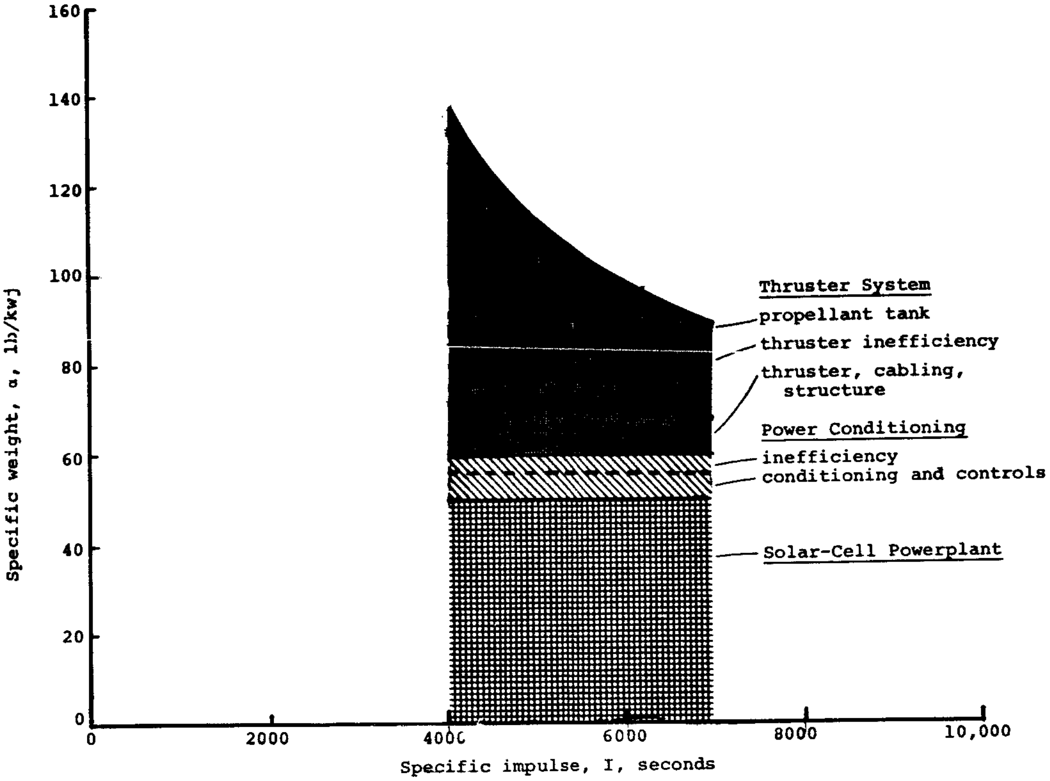

FIG. 29 - Total propulsion-system specific weight for Kaufman thruster. α_{pp} = 50 lb/kwe, α_c = 6 lb/kwe, k = 7%, propulsion time: 1 year.

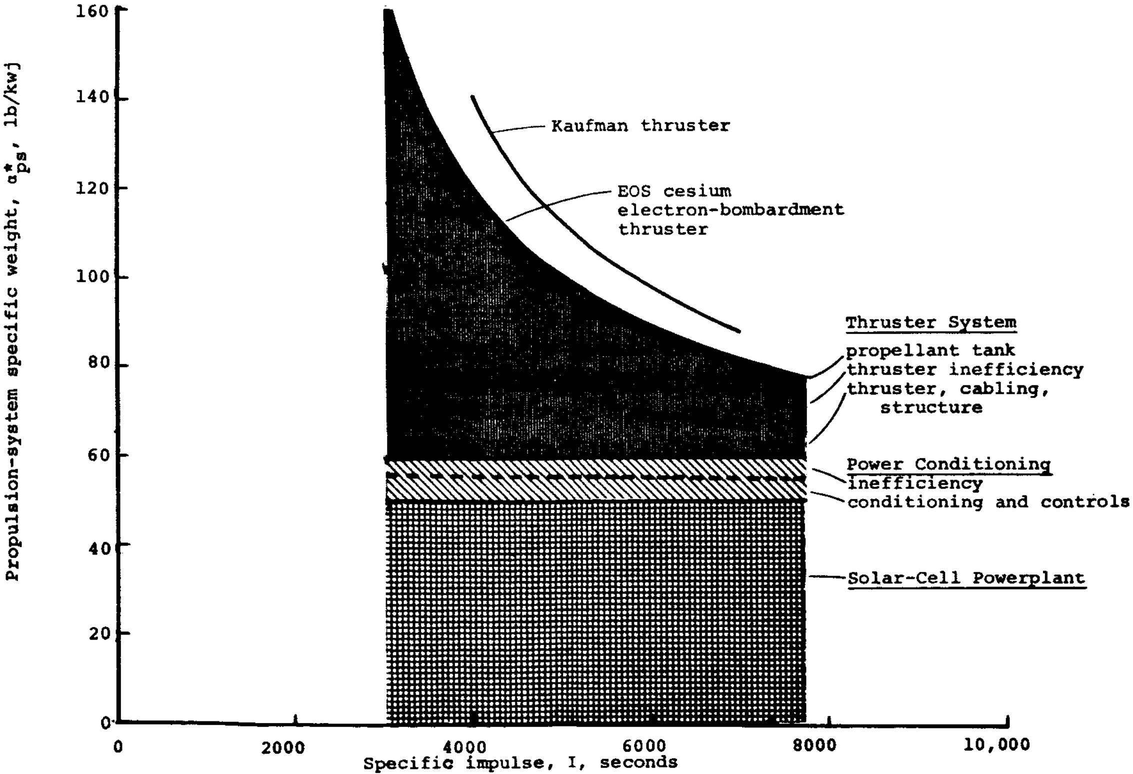

FIG. 30 - Total propulsion-system specific weights for flight-prototype thrusters. α_{pp} = 50 lb/kwe, α_c = 6 lb/kwe, k = 7%, propulsion time: one year.

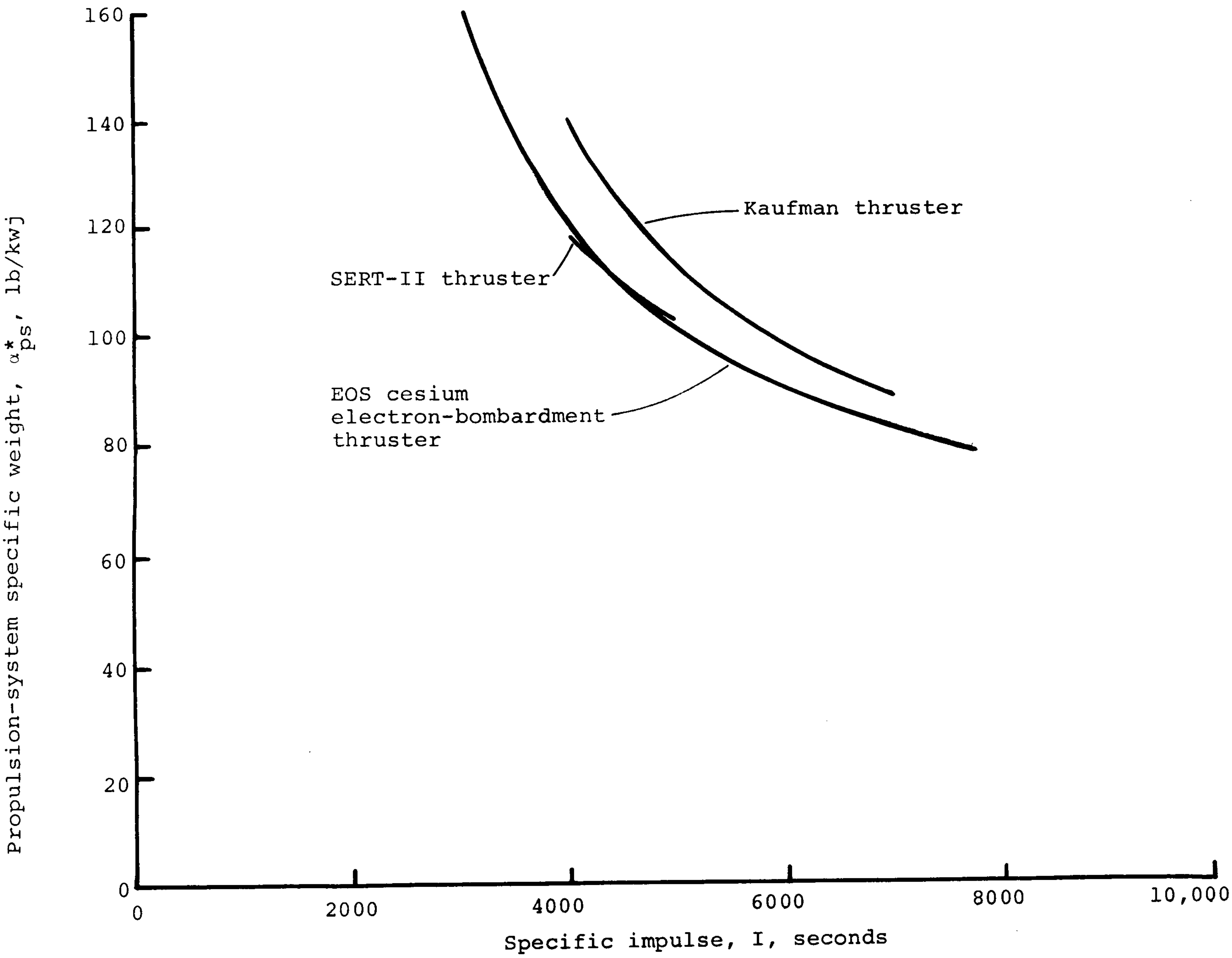

FIG. 31 - Total propulsion-system weight for SERT-II experimental thruster. α_{pp} = 50 lb/kwe, α_c = 6 lb/kwe, k = 7%, propulsion time: 1 year.

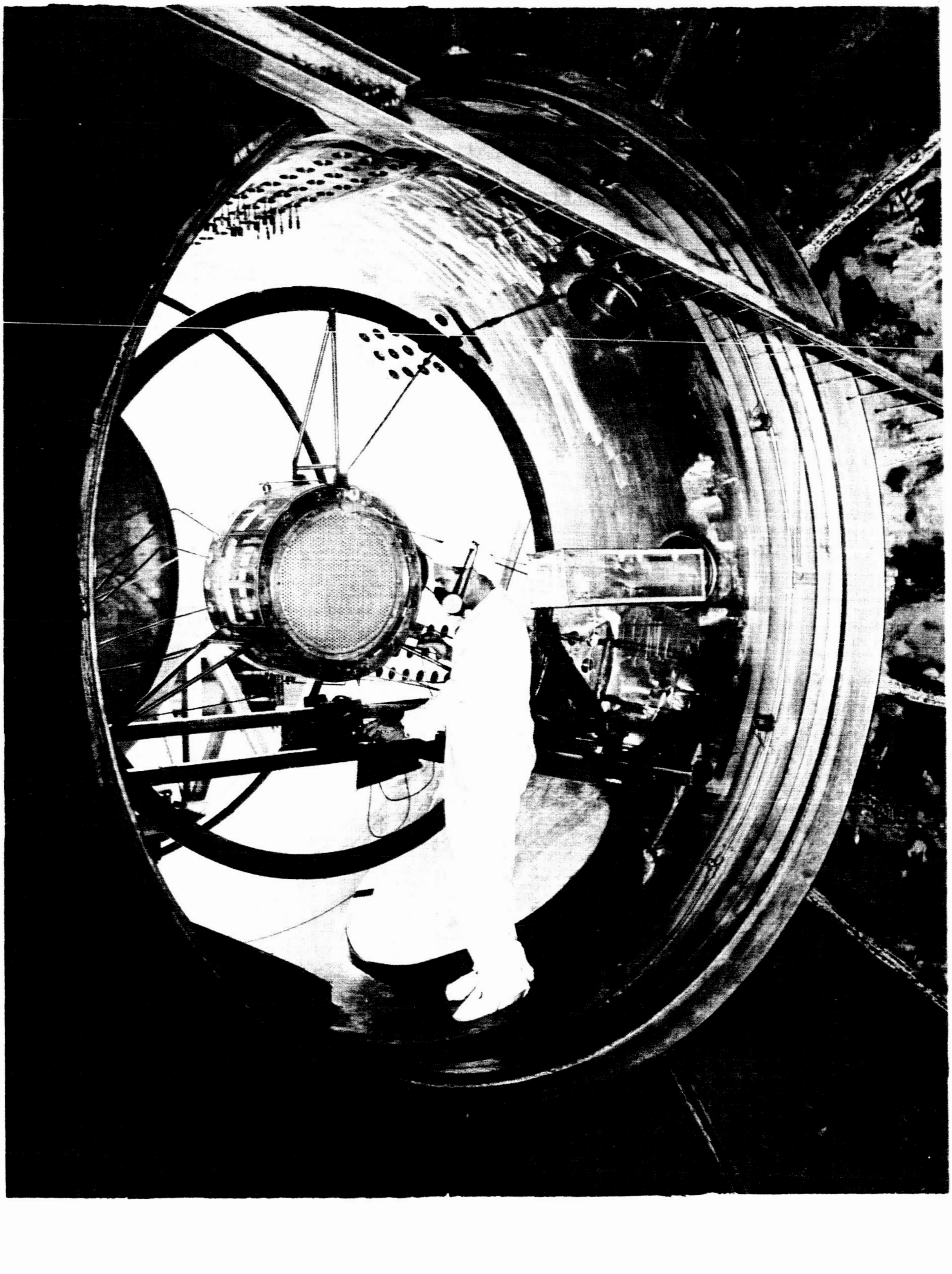

FIG. 32 - 30-kilowatt Kaufman electron-bombardment thruster.

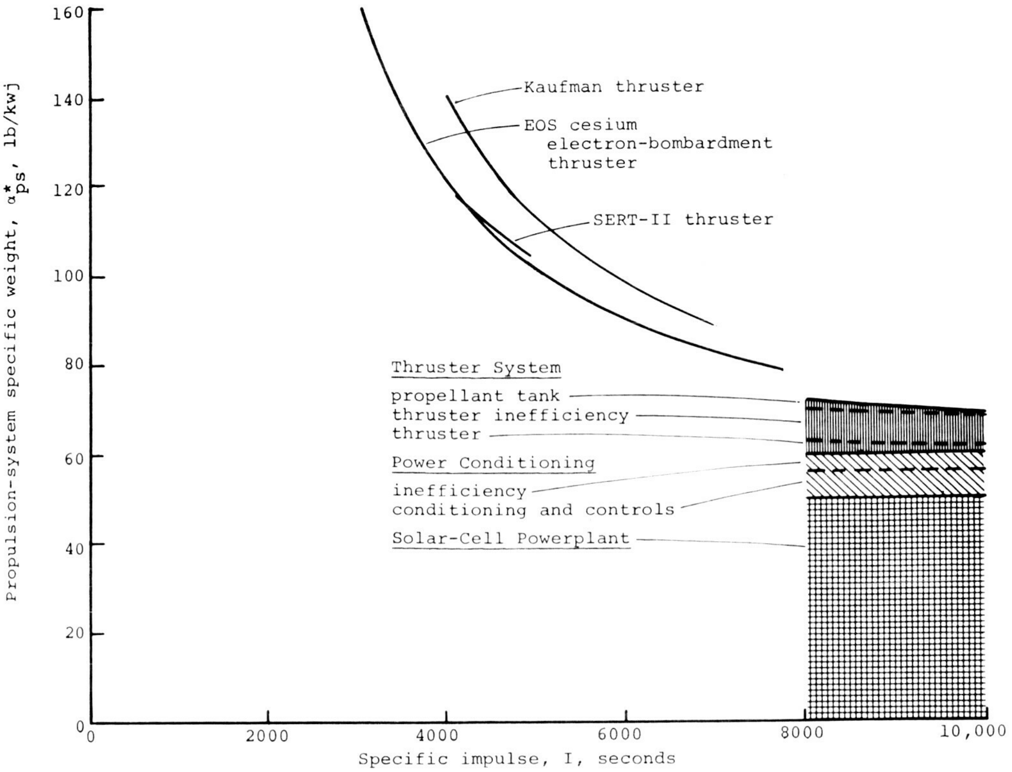

FIG. 33 - Total propulsion-system specific weight with Kaufman 30-kw thruster. α_{pp} = 50 lb/kwe; α_c = 6 lb/kwe; k = 7%, propulsion time: 1 year.

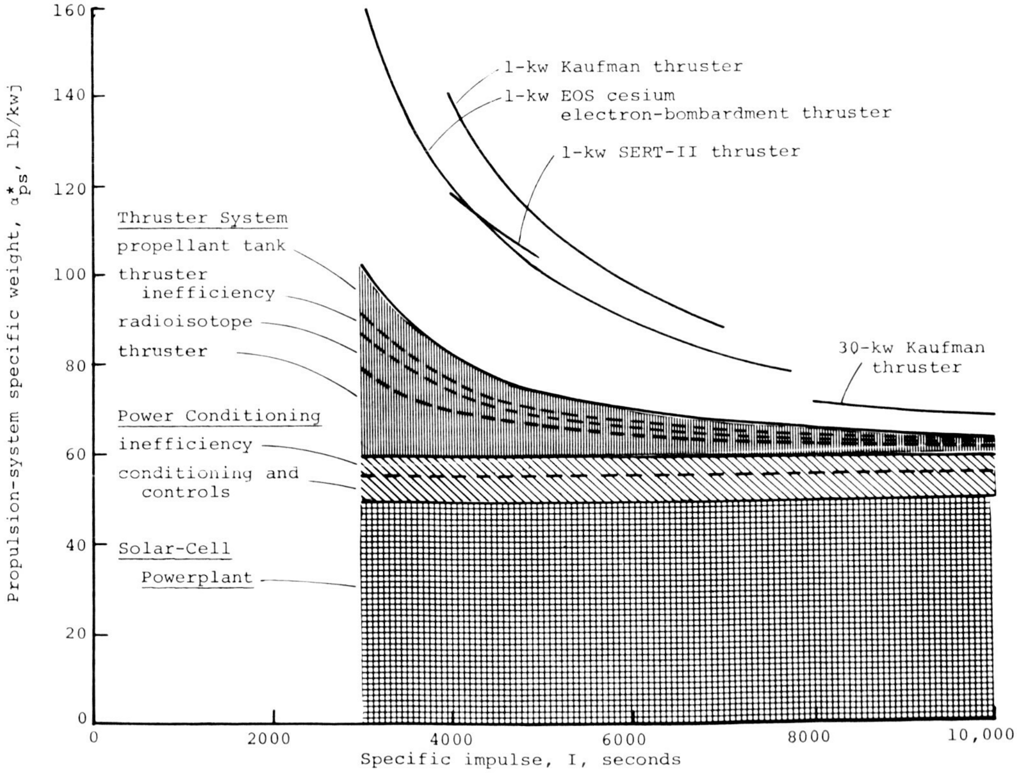

FIG. 34 - Estimated total propulsion-system specific weight of radioisotope-heated contact-ion advanced concept. α_{pp} = 50 lb/kwe; α_c = 6 lb/kwe; k = 7%, propulsion time: 1 year.

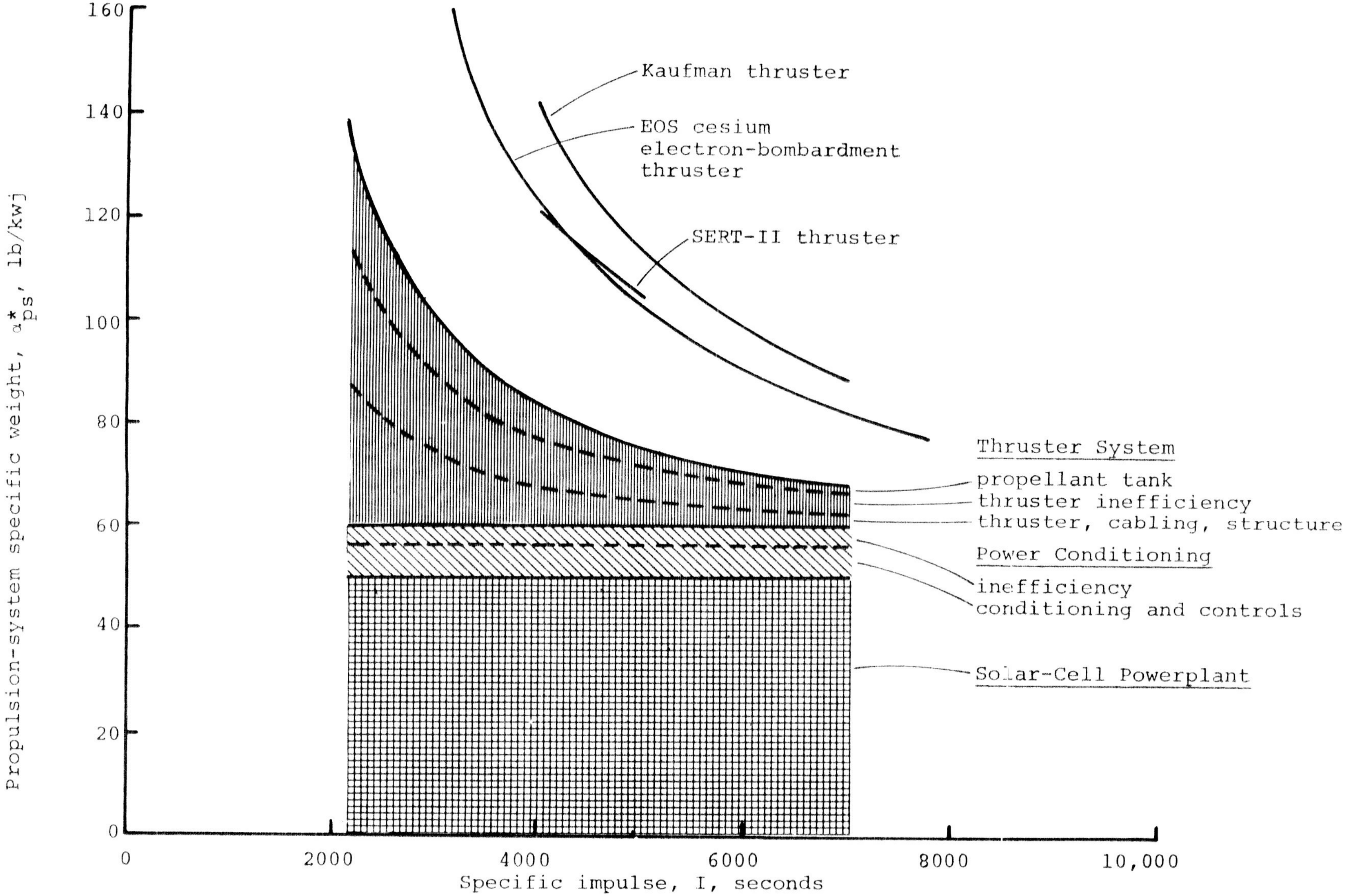

FIG. 35 - Estimated total propulsion-system specific weight for 15-cm cesium plasma-separator thruster advanced concept. α_{pp} = 50 lb/kwe, α_c = 6 lb/kwe, k = 7%, propulsion time: 1 year.

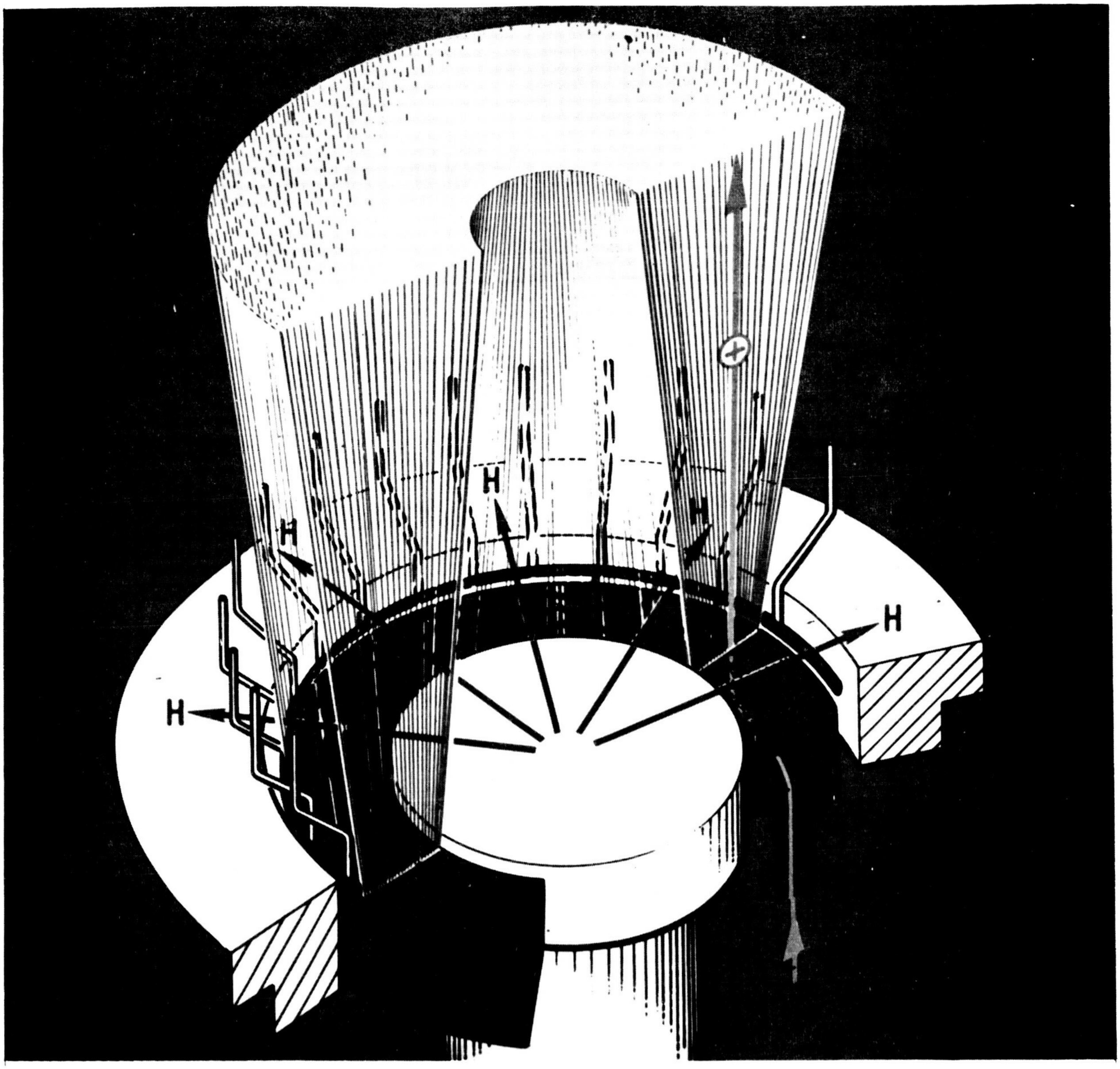

FIG. 36 - Diagram of space charge sheath electric thruster. Courtesy of the Aerospace Corporation.

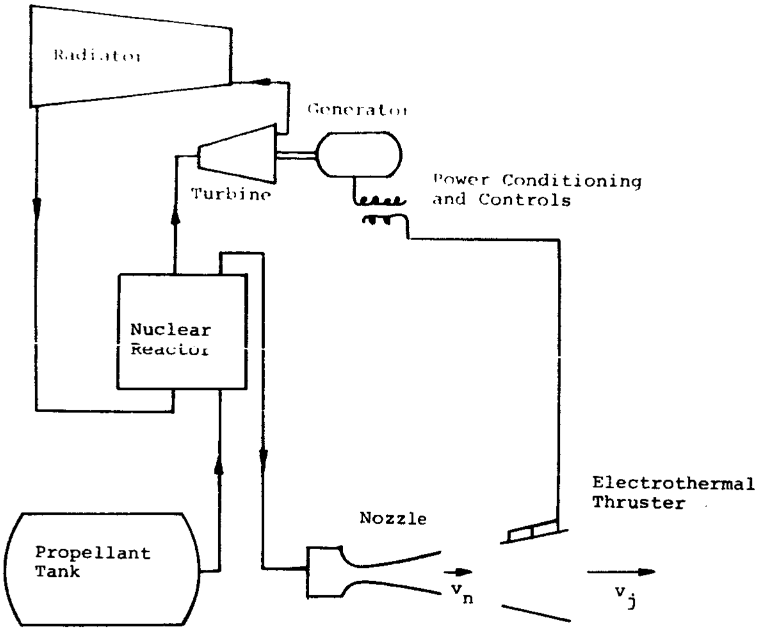
Radiator
Generator
Power Conditioning
and Controls
Turbine
Nuclear
Reactor
Electrothermal
Thruster
Nozzle
Propellant
Tank
v_n
v_j

FIG. 37 - Diagram of an electrothermal thruster in an ATEP system.

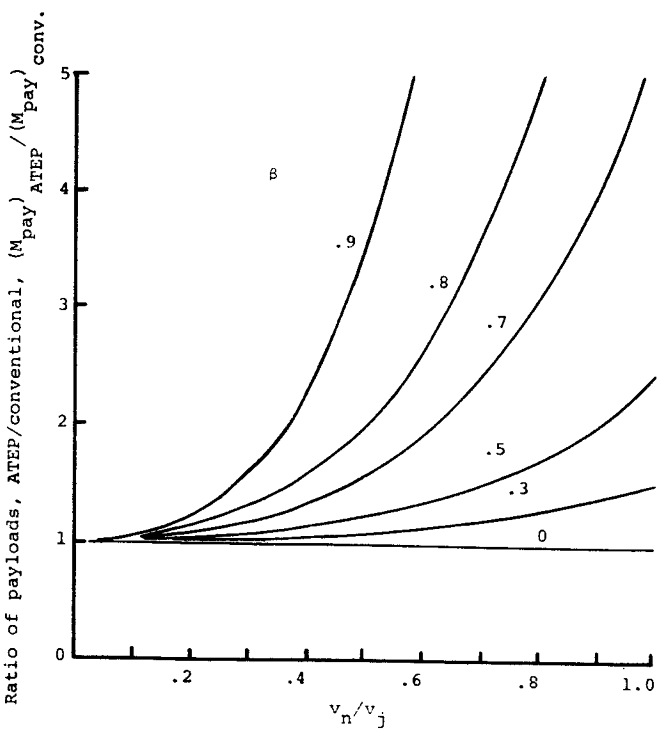

FIG. 38 - Payload capacity of ATEP system.

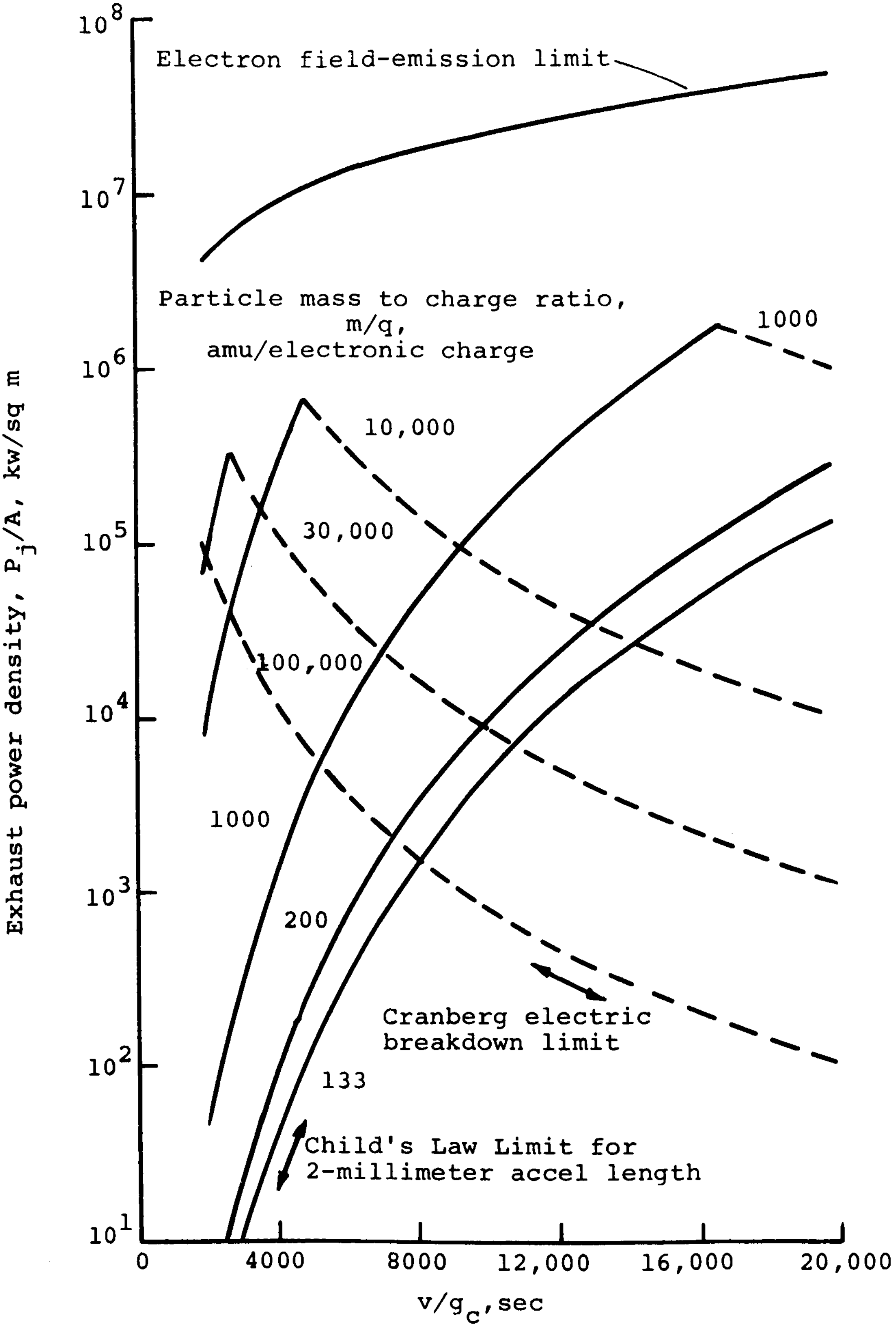

FIG. 39 - Theoretical exhaust jet power density for paraxial flow electrostatic thrusters.

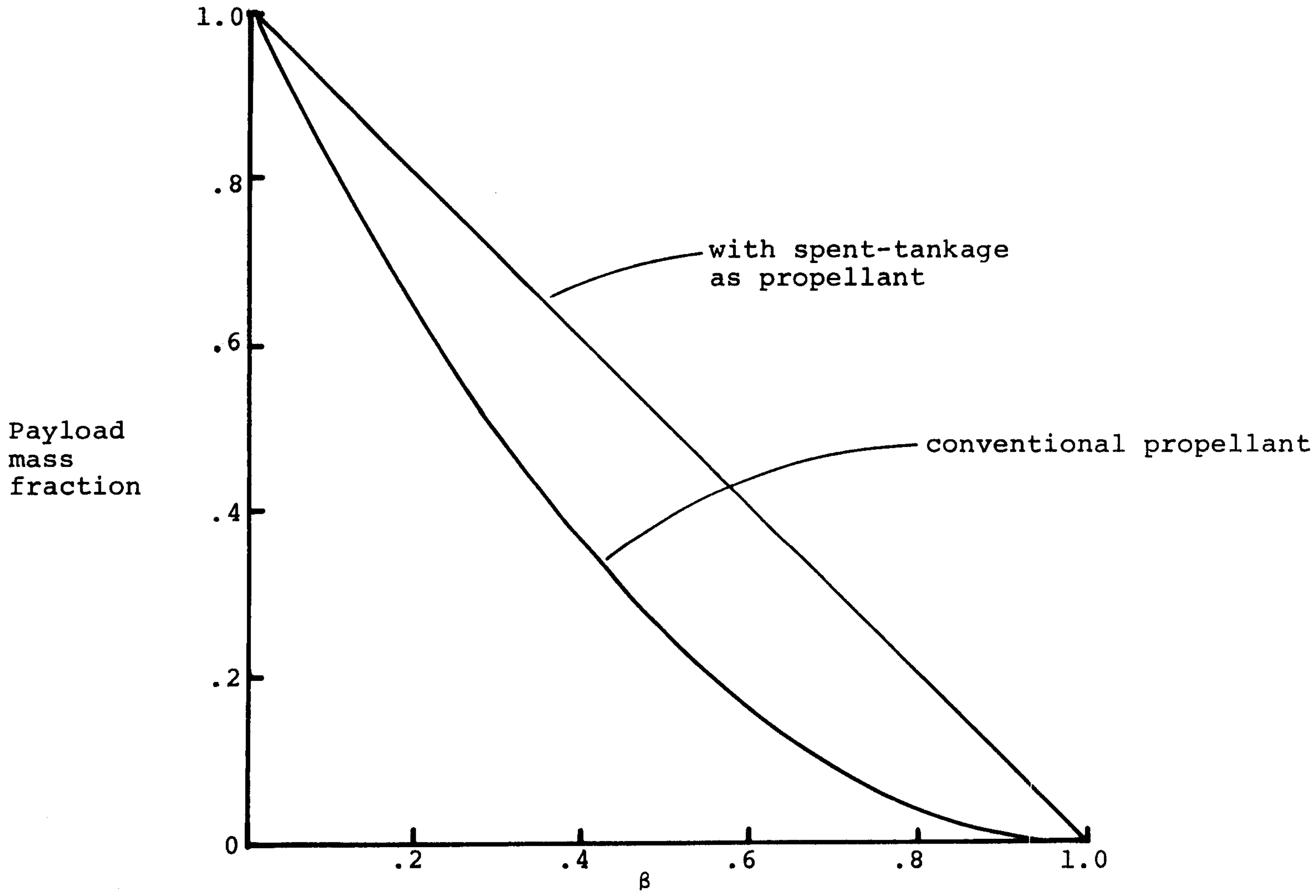

FIG. 40 - Payload capacity of electric spacecraft with and without spent-tankage propellant.

2.1

PARTICLE CHARGING BY ELECTRON BOMBARDMENT

N67-36943

by James P. Rybak and William R. Mickelsen

An understanding of the nature of the aluminum particles (10^4-10^5 amu) to be used as the propellant in electric thrusters is of importance if a comprehension of the charging mechanism is to be reached.

Since the particles are formed by a condensation process from the vapor state, it is apparent that the nascent particle has the characteristics of a dense vapor. Ordinarily, one would assume that as the particle cools it passes from the vapor phase to the liquid phase and ultimately on to the solid phase. However, there is much discussion concerning whether or not it is meaningful to attribute to particles of this small size the characteristics of the liquid or solid phase, regardless of their temperature. Even if it is meaningful to speak of a change of phase in particles of this size, it is not at all clear over what time scale such a change would take place.

Some researchers[2.1] have reported on the possibility of using ionized atoms as the condensation nuclei of the particles. Such an approach is very attractive because much more is known about the ionization of single atoms than is known about the charging of colloid particles. However, the actual nucleation process in the formation of the particles is not well enough understood to predict the likelihood of success of this method without considerable experimental investigation.

In the following discussion it is assumed that the charging process occurs after the particles have been formed and that the charging mechanism employed is that of positive ionization due to electron bombardment. Due to the uncertainty concerning the nature of the particles, three distinct cases will be investigated. They are that the particle at the time of charging can be considered to be (1) a dense vapor, (2) a liquid droplet, and (3) a solid particle. Case (1) may well be the most realistic, and it yields more readily to analysis than does case (2). Case (3) is probably the least realistic of all and may be thought of as an "extreme value case."

The Particle as a Region of Dense Vapor

If at the time of charging, the particle is considered to be a region of very dense vapor, the concepts developed in the theory of ionized gases can be applied. While very little experimental data exists for the ionization of aluminum vapor atoms by electron collision, good estimates of the cross section for this process can be made. Theoretical calculations for this cross section based on the Gryzinski[2.2] method yield values of 1 - 4 x 10^{-16} cm^2 for the primary electron energy range 6 ev $\leq$ E $\leq$ 100 ev. The maximum cross section occurs for a primary electron energy of 18 electron volts. When the Gryzinski method is applied to elements for which cross sections have been measured experimentally, results are obtained which agree with the measured cross sections to within a factor of two or better. The ionization cross section of aluminum atoms as a function of primary electron energy as determined by the Gryzinski method is shown in Figure 2.1.

It is of interest to calculate the probability that (1) an electron strikes a particle while traversing the diameter of the beam of particles and (2) an electron causes ionization if it does strike a particle.

The laboratory power supply available limits the particle beam current to 5 milliamperes. If it is assumed that all the particles are singly ionized, there would be 3.13 x 10^{16} particles produced per second. If the particle beam has a diameter in the ionization chamber of D = 2.0 cm, then the particle flux would be nv = 1.0 x 10^{16} cm^{-2} sec^{-1} where n is the number of particles per cm^3 and v is their velocity in cm/sec. It is expected that the particles will have a velocity of about 2.0 x 10^5 cm/sec. Thus n = 5.0 x 10^{10} cm^{-3}. The number of collisions, N_c, that an electron makes in traversing the particle beam diameter, D, is:

$$N_c = n\sigma_c D \tag{2.1}$$

where $\sigma_c = \pi r^2$ is the geometric cross-section of the particles. Taking r = 50 Å = 5.0 x 10^{-7}cm, equation (2) yields:

$$N_c = 7.9 \times 10^{-2} \tag{2.2}$$

The fraction of the electrons which collide with a particle is:

$$\eta_c = (1 - e^{-N_c}) = .076 = 7.6\% \tag{2.3}$$

In other words, 7.6% of the electrons traversing the diameter of the particle beam undergo a collision with a particle.

Since not all the electrons traverse the diameter of the particle beam, the overall average number of electrons which undergo a collision with a particle is somewhat smaller. The fraction of the electrons which undergo a collision with a particle depends upon the angle θ between the electron's path and the beam diameter, as shown in Figure 2.2.

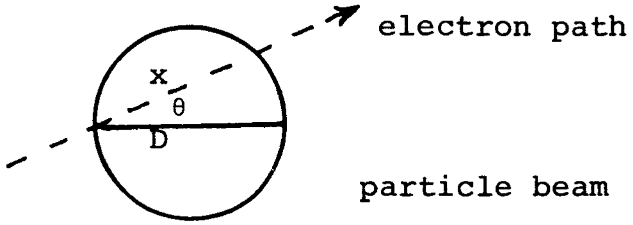

FIGURE 2.2

It is apparent that x = D cos θ with the assumption that the electron path is normal to the particle beam. If it is assumed that the number of electrons traversing the particle beam and making an angle θ with the diameter is independent of θ, the average distance traveled is:

$$\bar{x} = \frac{2D}{\pi} = 1.27 \text{ cm} \tag{2.4}$$

The average number of collisions made by an electron is:

$$\bar{N}_c = n\sigma_c\bar{x} = 5.0 \times 10^{-2} \qquad (2.5)$$

and the fraction of the electrons which undergo a collision is:

$$\bar{\eta}_c = (1 - e^{-\bar{N}_c}) = .049 = 4.9\% \qquad (2.6)$$

$\bar{\eta}_c$ is called the average electron collision efficiency. A plot of $\bar{\eta}_c$ versus the particle radius, r, for a particle mass of 5×10^4 amu is shown in Figure 2.3.

Once an electron has made a collision with a particle it is of interest to determine the probability that it ionizes one of the atoms in the particle. The number of ionizing collisions, N_i that such an electrom makes while traveling a distance x through the particle is:

$$N_i = n\sigma_i x \qquad (2.7)$$

where n is the density of atoms in the particle and σ_i is the ionization cross section. If it is again assumed that the average distance an electron must travel to pass through the particle is:

$$\bar{x} = \frac{2d}{\pi} \qquad (2.8)$$

where d is the diameter of the particle, equation (2.7) becomes:

$$\bar{N}_I = n\sigma_i\frac{2d}{\pi} \qquad (2.9)$$

The average probability that an electron produces an ion in passing through the particle is then:

$$\bar{\eta}_i = (1 - e^{-\bar{N}_i}) \qquad (2.10)$$

$\bar{\eta}_i$ is called the average electron ionization efficiency. For a particle that has a mass of 5×10^4 amu and a diameter, d, of 100 angstroms, the density of atoms in the particle is $n = 3.5 \times 10^{21}\text{cm}^{-3}$, and the mass density, ρ, is .147 gm/cc. The ionization cross section, σ_i is obtained from Figure 2.1. A plot of $\bar{\eta}_i$ versus primary electron energy, E, for particles with a mass of 5×10^4 amu but with different values of mass density is shown in Figure 2.4.

The product of $\bar{\eta}_c$ and $\bar{\eta}_i$ is the average probability that an electron collides with a particle and causes ionization. This is called the electron utilization efficiency and is denoted by $\bar{\eta}_{eu}$. A plot of $\bar{\eta}_{eu}$ versus the primary electron energy, E, is shown in Figure 2.5 for particles in the vapor phase. The curves for $\rho = 1.0$ and 2.7 gm/cc represent densities of liquid or solid aluminum. These curves are included for completeness and it should be kept in mind that the vapor phase theory probably does not yield very accurate results to particles of these densities.

After the primary electron has ionized an atom, both the primary and secondary electrons must escape the particle if the particle is to have a net positive charge.

Either of two phenomena may keep the electrons from escaping. An electron may form a negative ion by attachment to an atom or, in the process of being scattered by the other atoms of the particle, an electron may recombine with the positive ion.

Cobine[2.3] states that, in the absence of a wall, the recombination of an ion and electron is most likely to occur in the following way. The electron first attaches itself to a neutral atom and then this negative ion collides with a positive ion and the process of recombination is completed. Another mechanism for recombination is radiative recombination. Radiative recombination occurs when a electron and a positive ion come together with a photon carrying off the excess energy. The probability of this reaction occuring is very small. Generally only about one collision in 1×10^7 between an electron and a positive ion results in radiative recombination. It is also improbable that the two step recombination process will occur in the particle because the two step process depends upon an electron becoming attached to a neutral atom.

The coefficient of attachment, γ, which is the average number of collisions the electron must make before attaching itself to a neutral atom, seems to be related only to the relative speed between the electron and neutral atom and electronegative character of the neutral atom. Since the electronegativity of aluminum is a low 1.5, it is expected that γ is large, say 10^8. The presence of an electric field will speed up the electron and make attachment even less probable.

If it is again assumed that the particle has a mass of 5×10^4 amu and a diameter of 100 angstroms, the density of atoms in the particle is $n = 3.5 \times 10^{21}$ cm^{-3}. The classical cross section for a collision between an electron and an atom is $\sigma = 1.25 \times 10^{-15}$ cm^2 assuming that the atom has a radius of 2 angstroms and that the electron radius is negligible in comparison. The mean free path between collisions is $\lambda = \frac{1}{n\sigma} = 23$ Å. It is therefore very probable that the primary and secondary electrons will escape the particle after having made only a few collisions at most and that the probability of electron attachment taking place is negligible.

The Particle as a Liquid Droplet

It seems reasonable to assume that the particle, at the time of charging, might be described by saying that it has the properties of a liquid droplet, with a diameter of 10 to 100 angstroms, in equilibrium with its vapor. By "in equilibrium with its vapor" is meant that the colloid particle is neither increasing in size due to condensation nor decreasing in size due to evaporation, at least not at any appreciable rate.

This description, while not very difficult to visualize, has the drawback that very little, if anything, is known about the interactions of low energy electrons with liquids. It might be argued that one could extend the analysis used earlier with a dense vapor to include the liquid droplet case merely by using a greater particle density in the formulas. The results obtained, however, would probably bear little resemblence to actuality because of the basic differences between gases and liquids.

It is probably safe to say that the phenomena involved in the charging of liquid droplets lie on some middle ground between those of a dense vapor and those of solid particles. An appeal would have to be made to experimental results in order to come to any more definite conclusions.

The Particle as a Solid Particle

If the particle is in the solid phase when it is charged, the mechanism by which positive charging takes place is that of secondary electron emission. In order to understand the mechanisms involved, a simplified discussion of the secondary emission phenomenon is in order.

Elementary secondary emission theory[2.4] is based upon the assumption that the secondary yield, δ, as a function of the energy E_o, of the incident primaries may be written in the form:

$$\delta = \int_o^\infty n(x,E_o)\, f(x)\, dx \qquad (2.11)$$

where $n(x,E_o)$ is the average number of secondary electrons produced per indicent primary electron in a layer of thickness dx at a depth x below the surface and f(x) is the probability that a secondary electron migrates to and escapes from the surface.

It is generally taken that:

$$f(x) = B\, e^{-\alpha x} \qquad (2.12)$$

and that $n(x,E_o)$ is proportional to the average energy loss per unit path length, $-\frac{dE}{dx}$, per incident primary. Then equation (2.11) can be written:

$$\delta = -\frac{B}{\varepsilon} \int_o^\infty \frac{dE}{dx}\, e^{-\alpha x}\, dx \qquad (2.13)$$

where ε is the average energy required to produce a secondary electron inside the solid.

The above is an over-simplification of the secondary emission process due to the following assumptions which are tacitly made in the mathematics.

1. It is assumed that a clear cut distinction exists between the production mechanism and the escape mechanism. This is not particularly true in the

case of metals or semiconductors because of the cascade nature of the process. This distinction can be meaningful for insulators which have a large forbidden energy gap.

2. It is assumed that merely the number of secondary electrons need be taken into account and not their energy distribution.
3. The escape mechanism of the secondary electrons is assumed to follow an exponential absorption law. No consideration is given to the physical processes involved.

This simplified theory cannot predict the magnitude of the yield of a particular material. Likewise, it gives no information for determining the energy distribution of the emitted electrons but it does provide information concerning the reduced yield curves (δ/δ_m vs E_o/E_{om}), where δ_m is the maximum secondary emission yield and E_{om} is the energy of the primaries for which $\delta = \delta_m$.

Some of the electrons emitted by the solid are elastically reflected primaries, inelastically backscattered primaries and true secondaries. The number of the first two types of electrons is small compared with the number of true secondaries, even for E_o considerably smaller than E_{om}.

For aluminum, $\delta_m = .96$ with $E_{om} = 300$ electron volts. A plot of δ versus E_o is shown in Figure 2.6.

If the solid particle is to have a net positive charge, both the secondary electron and the primary electron must escape from the particle. In other words, the range of the primary electron must be greater than the diameter of the particle. J. R. Young[2.5] has established a range-energy relation for electrons of energy 500 ev $\leq E_o \leq$ 11 kev in aluminum. A plot of this relation is shown in Figure 2.7. It is apparent from the extrapolated portion of this curve that primary electrons with 100 ev $\leq E_o \leq$ 200 ev would be needed to completely penetrate the particles in the size of interest, if they were in the solid phase.

The product of the average electron collision efficiency, $\bar{\eta}_c$, for $\rho = 2.7$ gm/cc and the secondary electron emission coefficient, δ, gives the average electron utilization coefficient, $\bar{\eta}_{eu}$, for solid particles. This is shown in Figure 2.8.

Particle Charging Experiments

As yet no experiments have been conducted on the charging of aluminum particles. Several experimental concepts are in the planning stage and it is anticipated that they will become more fully developed in the near future. The devices under consideration for charging the particles are in a hollow cathode-ring anode arrangement such as is used in the Plasma Separator Ion Engine[2.6] and a modified Kaufman[2.7] type ionization chamber.

Since the exact nature of the particles is uncertain at this point, the experimental apparatus for charging the particles will have to be designed to operate over the range of electron energies and electron utilization efficiencies indicated in the preceeding analyses. The energy of the primary electrons may be anywhere between about 20ev and 200ev. The electron utilization efficiencies may lie between approximately .004 and .04. This results in the energy required to charge the particles ranging between 500 ev and 36 kev per particle if each electron produces a charged particle. This wide range of parameter values may mean that several experimental designs will have to be developed to cover the whole range of interest. Special consideration will be given to making the electron utilization efficiency as high as possible.

References

2.1. Cox, A. L. and Harrison, S.: The Controlled-Growth Colloidal Ion Source. AIAA Paper 63049, 1963.

2.2. Gryzinski, M.: Classical Theory of Electronic and Ionic Inelastic Collisions. Phys. Rev., Vol 115, No. 2, July 15, 1959, pp 374-383.

2.3. Cobine, J. D.: Gaseous Conductors. Dover Publications, Inc., 1958.

2.4. Dekker, A. J.: Secondary Electron Emission. Solid State Physics, Volume 6, edited by F. Seitz and D. Turnbull, Academic Press, Inc., 1958.

2.5. Young, J. R.: Penetration of Electrons and Ions in Aluminum. J. Appl. Phys., Vol. 27, No. 1, January, 1956, pp 1-4.

2.6. Free, B. A., and Mickelsen, W. R.: Plasma Separator Ion Thruster Development. AIAA Paper 66-598, 1966.

2.7. Kaufman, Harold R.: An Ion Rocket with an Electron-Bombardment Ion Source. NASA TN D-585, 1961.

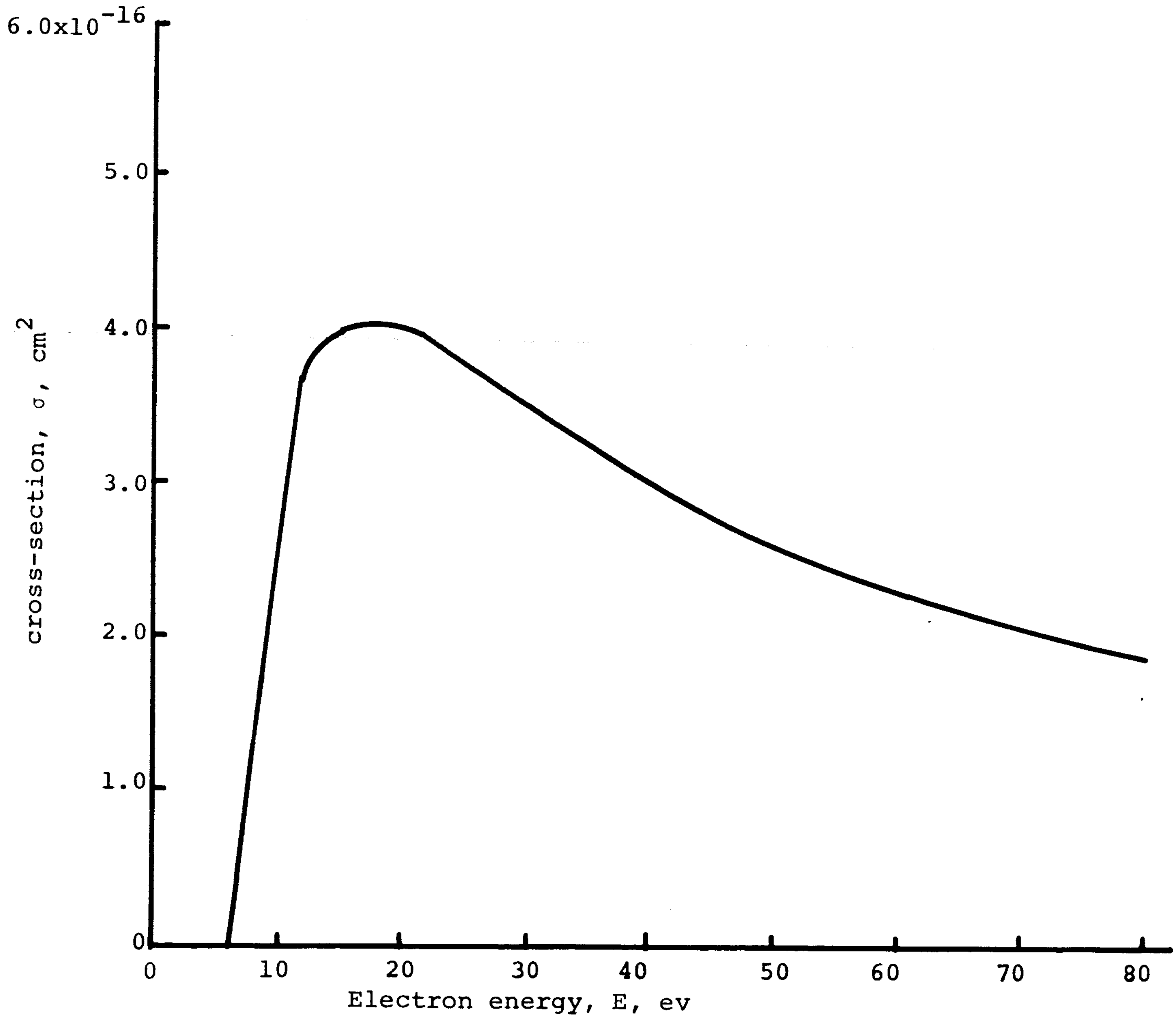

FIG. 2.1 - Cross Section, σ, vs. Electron Energy, E, for Ionization of Aluminum.

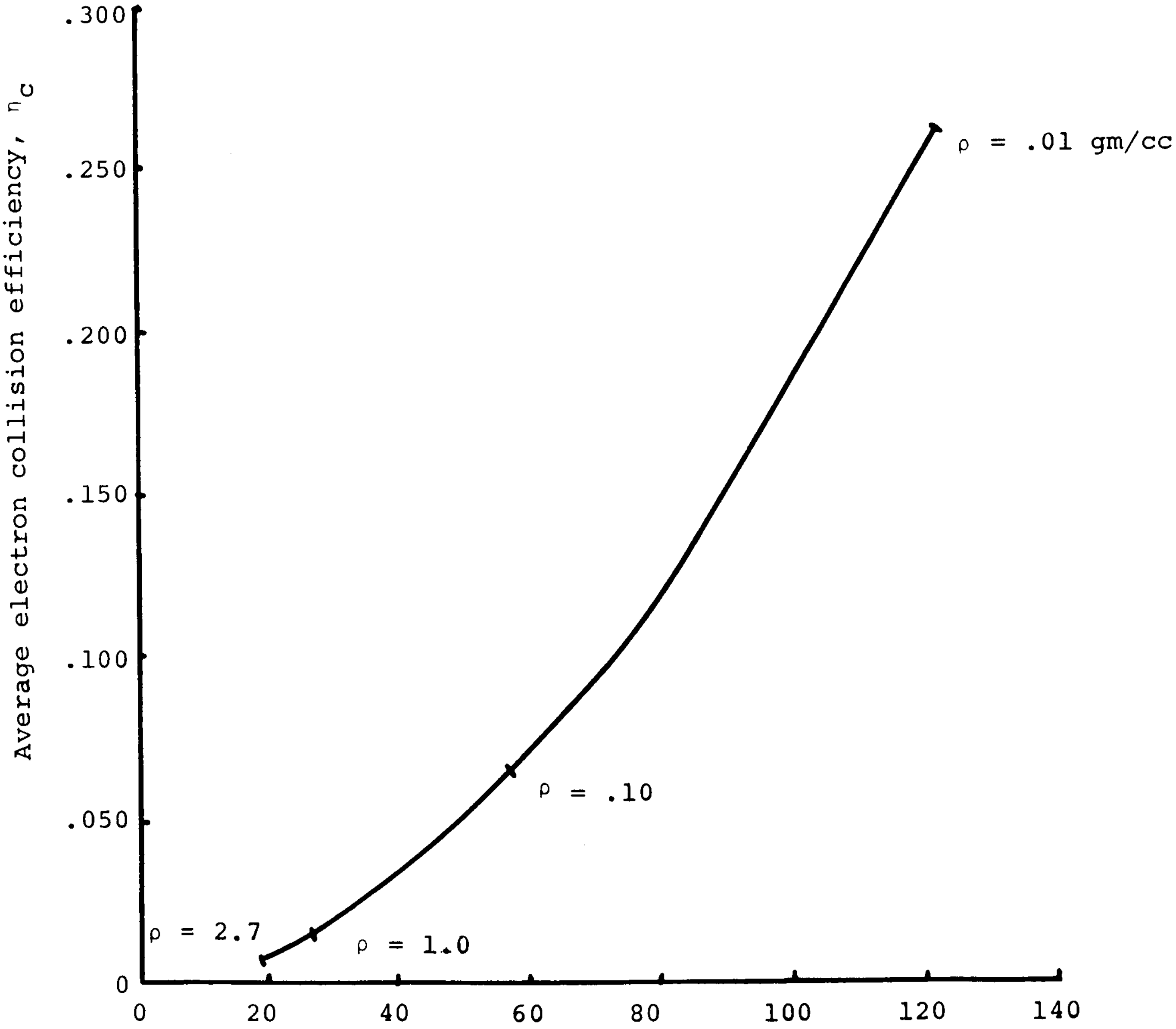

Figure 2.3. Average Electron Collision Efficiency, $\bar{\eta}_c$ versus Particle Radius, r, for a 5 ma, 2 cm Diameter Beam of 5 x 10^4 amu Particles.

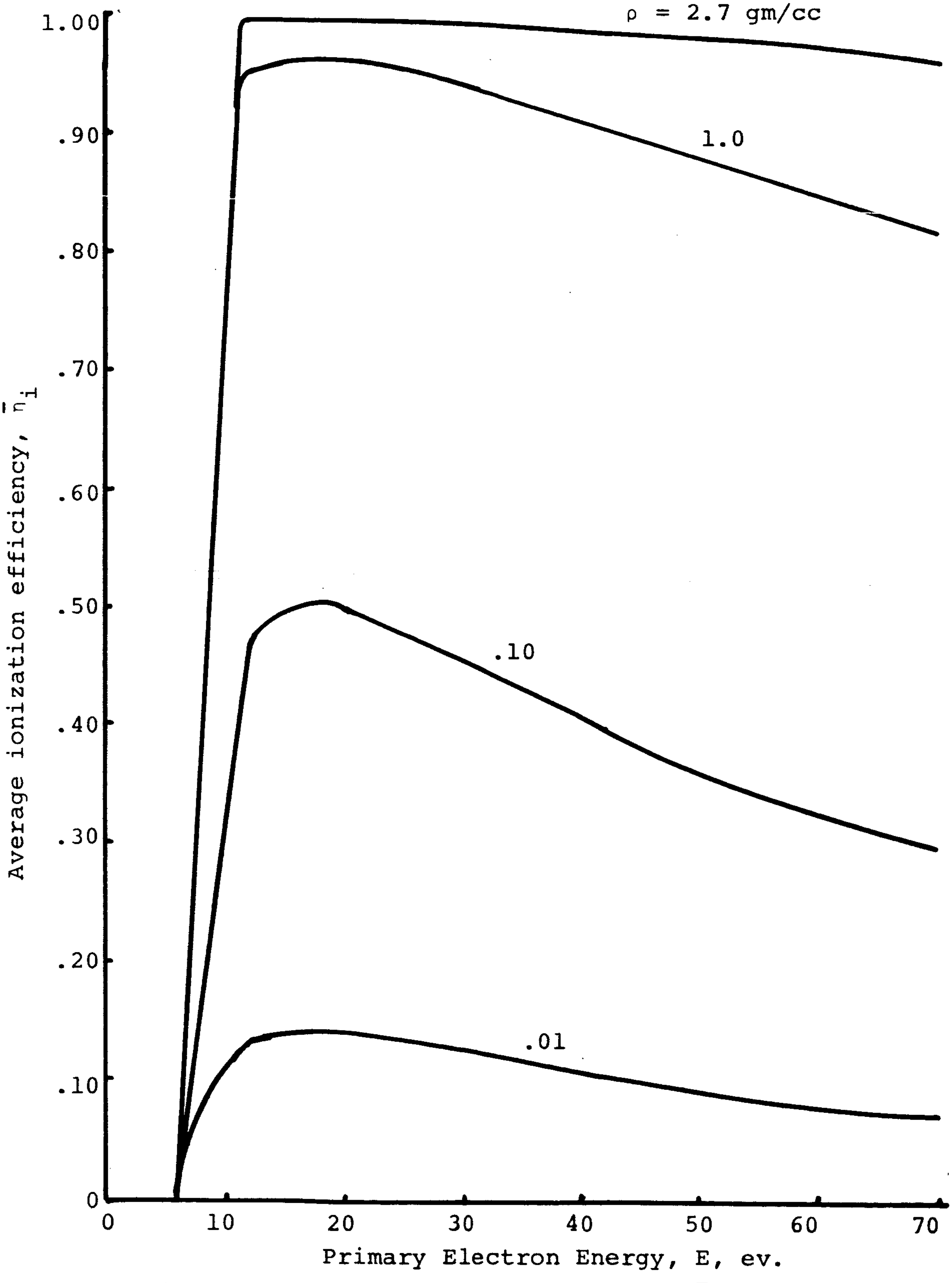

Figure 2.4. Average Ionization Efficiency, $\bar{\eta}_i$ versus Primary Electron Energy, E, for a 5×10^4 amu Aluminum Vapor Particle.

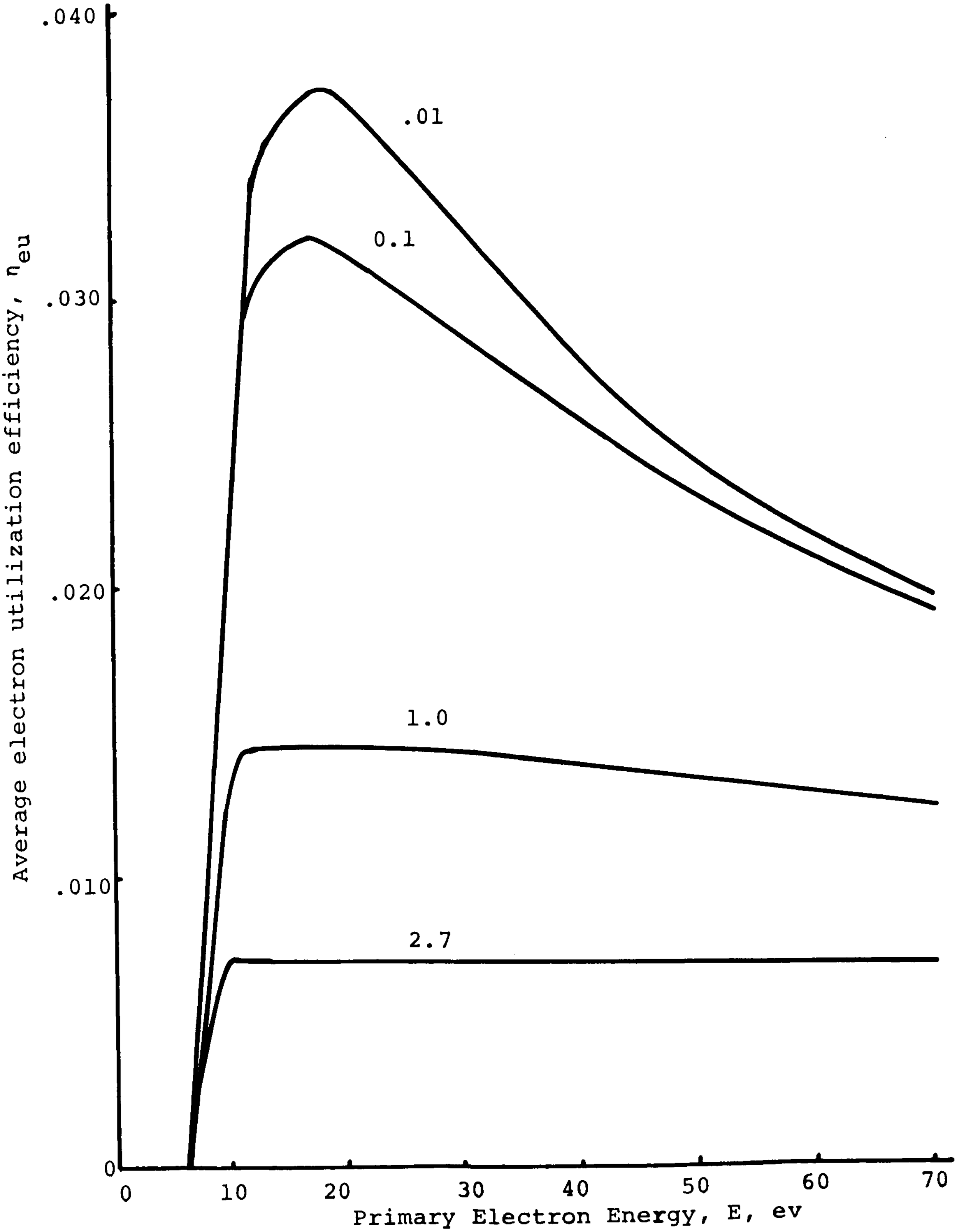

Figure 2.5. Average Electron Utilization Efficiency, $\bar{\eta}_{eu}$, versus Primary Electron Energy, E for a 5 x 10^4 amu Aluminum Vapor Particle.

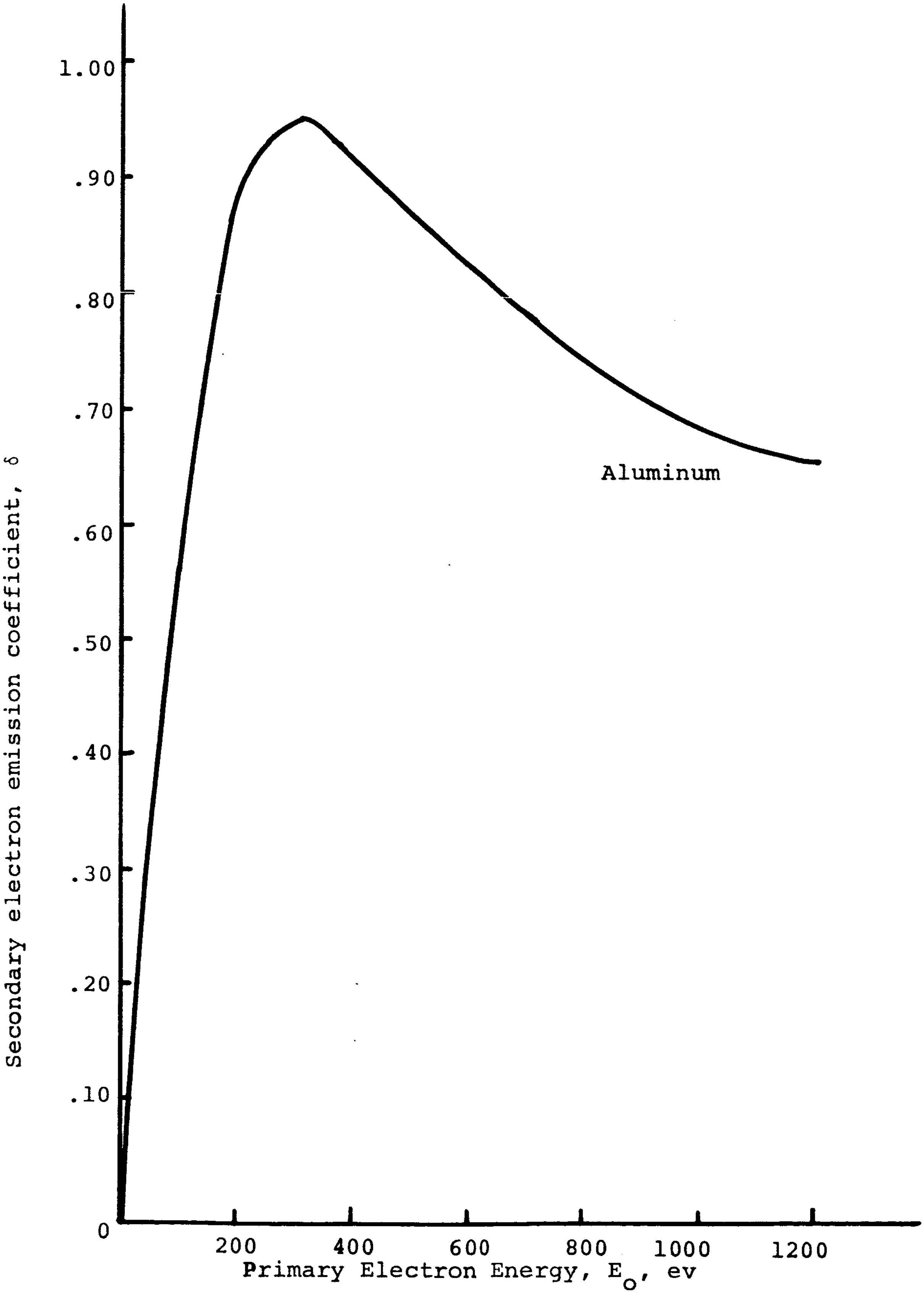

FIG. 2.6 - Secondary Emission Coefficient, δ, vs. Primary Electron Energy, E_o, for Aluminum.

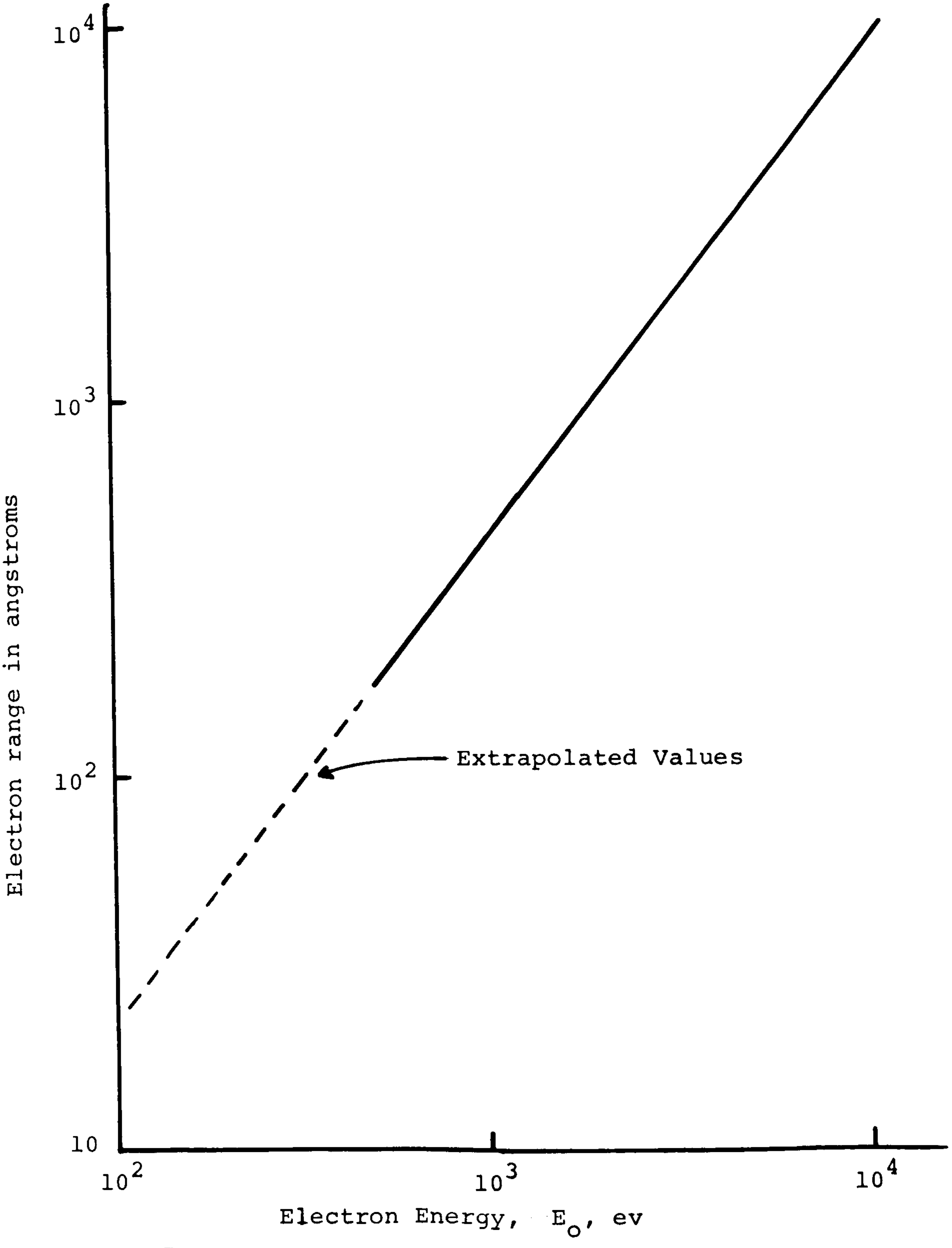

FIG. 2.7 - Range vs. Energy of Electrons in Aluminum

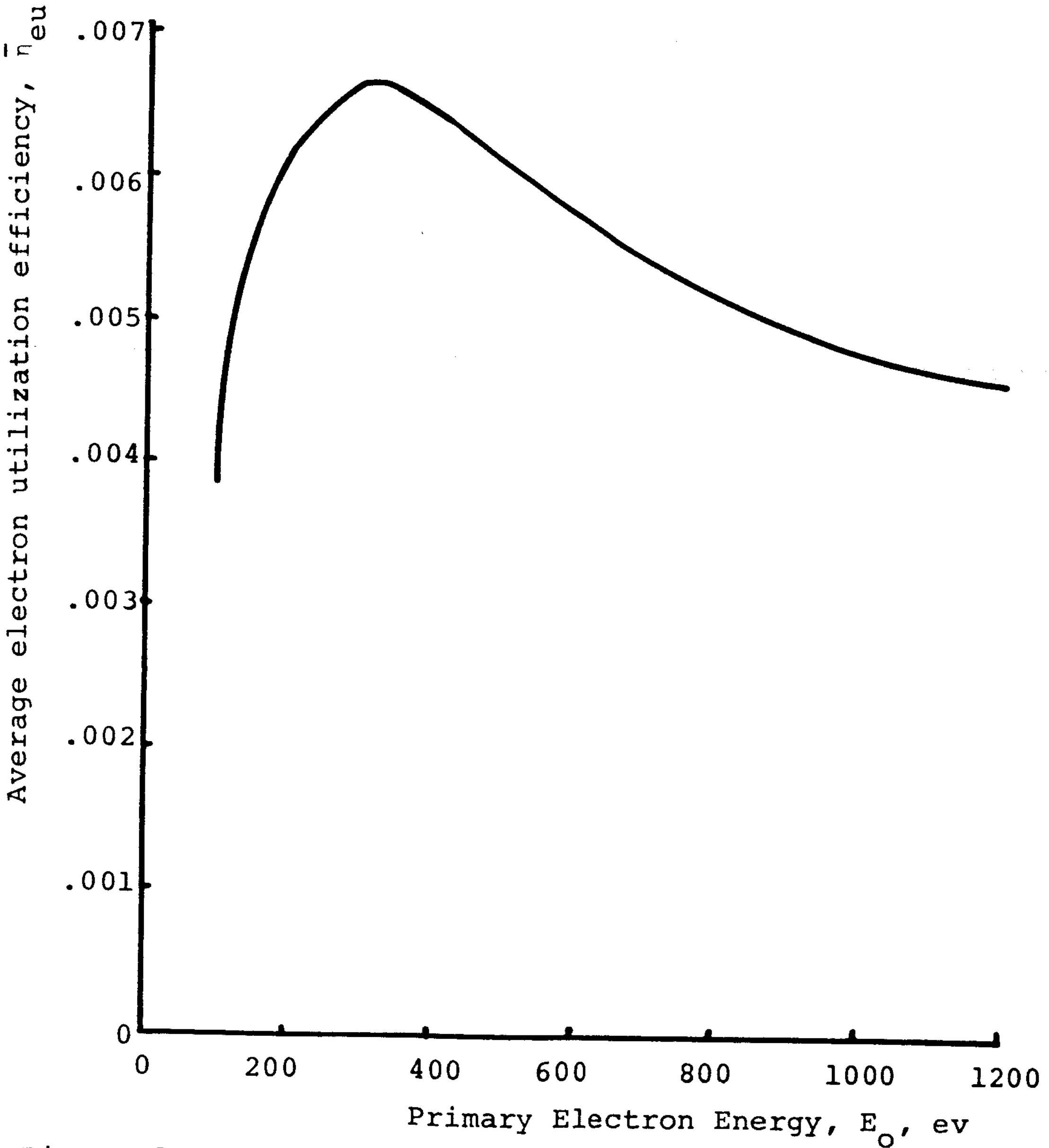

Figure 2.8. Average Electron Utilization Efficiency, $\bar{\eta}_{eu}$ Versus Primary Electron Energy for a 5×10^4 amu Solid Aluminum Particle.

N67-36944

ELECTROTHERMAL THRUSTERS IN THE ATEP SYSTEM

by Daniel C. Garvey and William R. Mickelsen

Analysis of the ATEP concept[3.1] has shown that significant improvement in mission performance would be possible if the ATEP concept could be applied to real electric propulsion systems. Because of this promise, it is of interest to examine the general feasibility of using electrostatic, electrothermal and electromagnetic thrusters in the ATEP concept. The results of a preliminary examination of the electrostatic thruster have been previously reported[3.1]. A preliminary examination of the ideal performance of the ATEP system with electrothermal thrusters is described in this section.

Electrothermal Thrusters

Application of electrothermal thrusters to the ATEP concept requires the addition of heat to a supersonic stream[3.1]. Hence, the theoretical performance of electrothermal thrusters with supersonic inlet velocities becomes of interest.

The operating mode of the propulsion system is depicted by Figure 3.1. A nuclear reactor is part of the thermodynamic cycle which provides power for the electrical heating of the propellant. Lithium was selected as the propellant for this analysis because of its advantages as a reactor coolant, low molecular weight and good tankage properties. After cooling the reactor, the propellant is accelerated by the nozzle to a supersonic Mach number M_1.

In this preliminary study the effects of propellant ionization and dissociation are avoided by considering temperatures and pressures for which the percentage of total enthalpy invested in ionization or dissociation is small. The propellant upon exiting the nozzle enters the heat addition region of the thruster, where heat is added to the supersonic stream. Employing the mathematical relations of Crocco[3.2], several cases of heat addition to a supersonic stream are considered. The performance of the electrothermal thruster is evaluated from the viewpoint of attaining maximum exit velocity from the heat addition region for a given area ratio and for total heat added to the stream.

Supersonic nozzle. In the model, the nozzle is depicted by Sketch A (symbols are defined on pp. 3.19 and 3.20):

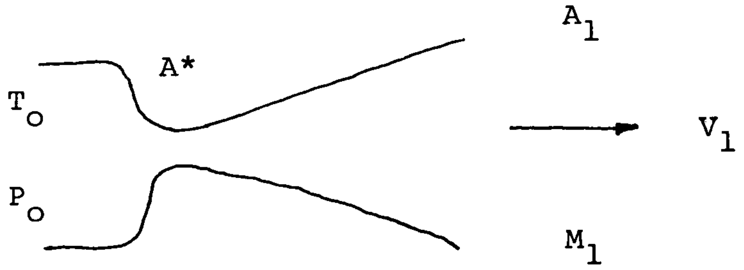

Sketch A

For the case of steady one dimensional flow through the nozzle, the exhaust velocity as obtained from the conservation of energy equation is described by:

$$v_1 = \sqrt{2\ (h_o - h_1)} \tag{3.1}$$

The degree of ionization in the monatomic lithium propellant is determined from the Saha Equation[3.3].

$$\log\left(\frac{\alpha^2}{1-\alpha^2}\right) P_o = \frac{-9072}{T_o\,(^oR)} + \frac{5}{2}\log\frac{T_o\,(^oR)}{1.8} + 2\log\frac{Q^+}{Q} - 6.491 \tag{3.2}$$

The partition functions Q, Q^+ and the ionization potential E_i of the lithium molecule were obtained from the literature[3.4]. In Figure 3.2 the degree of ionization α is plotted for different values of stagnation temperature T_o and pressure P_o. In Equation 3.1 the enthalpy is defined by:

$$h = e + \frac{P}{\rho} \tag{3.3}$$

Neglecting the excitation energy of the lithium atoms, ions, and electrons, the internal energy, e, of the lithium propellant is composed of:

a) the total heat required to vaporize the liquid propellant, h_v (BTU/lbm)

b) the translational energy of the propellant,

$$\frac{3}{2}(1+\alpha)\frac{R}{\overline{M}}(T - T_v) \quad \text{(BTU/lbm)}$$

c) the ionization energy of the propellant,

$$h_i = \frac{41526\alpha E_i}{\overline{M}} \quad \text{(BTU/lbm)} \tag{3.4}$$

or

$$e = h_v + \frac{3}{2}(1+\alpha)\frac{R}{\overline{M}}(T - T_v) + \frac{41526\alpha E_i}{\overline{M}} \tag{3.5}$$

Hence, with the equation of state:

$$p = (1+\alpha)\,\rho\frac{R}{\overline{M}}T \tag{3.6}$$

the stagnation enthalpy is characterized by:[3.5]

$$h_o = \frac{5}{2}(1+\alpha)\frac{R}{\overline{M}}(T_o - T_v) + h_v + h_i \tag{3.7}$$

Figure 3.3 depicts the lithium propellant vaporization curve employed in determining the stagnation enthalpy h_o[3.6].

The percentage of stagnation enthalpy invested in ionization is determined from Equations 3.4 and 3.7.

$$\eta_i = \frac{h_i}{h_o} \tag{3.8}$$

Equation 3.8 is depicted in Figure 3.4 for values of stagnation pressure and temperature. From Figure 3.4 it is observed that less than five percent of the stagnation enthalpy is invested in ionization for:

$T_o \leqslant 3000^{o}K$
$p_o \geqslant 0.001$ atmospheres

From these results it is concluded that for nozzle plenum chambers described by:

$T_o \leqslant 3000^{o}K$
$p_o \geqslant 0.001$ atmospheres

an analysis based on an ideal expansion in the nozzle is suitable.

Considering the nozzle flow to be reversible and adiabatic, the isentropic relations are employed for various area ratios A_1/A^* and stagnation temperatures T_o to determine the exit Mach number M_1 and the specific impulse I_1. The results are plotted in Figures 3.5 and 3.6.

Heat addition region. In solving flow problems with heat addition, the assumption of constant pressure or constant area is frequently made. The wall force integral in the momentum equation is then conveniently handled. To enlarge the scope of flow solutions, treatment of cases other than constant pressure or constant area is desirable. A simple relation expressing mathematically the variation of pressure and flow area developed by Crocco[3.2] is characterized by:

$$\frac{P}{P_1} = \left(\frac{A}{A_1}\right)^{\frac{\varepsilon}{1 - \varepsilon}} \tag{3.9}$$

with $\varepsilon \equiv$ power index.

It is noted that Equation 3.9 does not define the geometry of the duct. Hence, no restriction is placed on duct length. The relation between pressure and area is determined by the transformation which occurs in the duct as heat is added to the stream. Therefore, an arbitrarily assumed variation of pressure with area might be obtained by controlling duct length and area ratio such that the constant rate of heat addition yields the assumed pressure-area relation[3.7]. Despite this lack of a definition in duct geometry, the convenience of Equation 3.9 becomes apparent in the evaluation of the integral which occurs when the conservation of momentum equation is applied to the duct. When this integral is evaluated, a generalized expression is obtained which contains the cases of constant pressure heat addition ($\varepsilon = 0$) and constant area heat addition ($\varepsilon = 1$) as particular cases[3.2,3.7,3.8]. Thus, a broader approach in the addition of heat to a supersonic stream is provided by Equation 3.9.

One dimensional flow of the lithium propellant with heat addition is depicted by Sketch B.

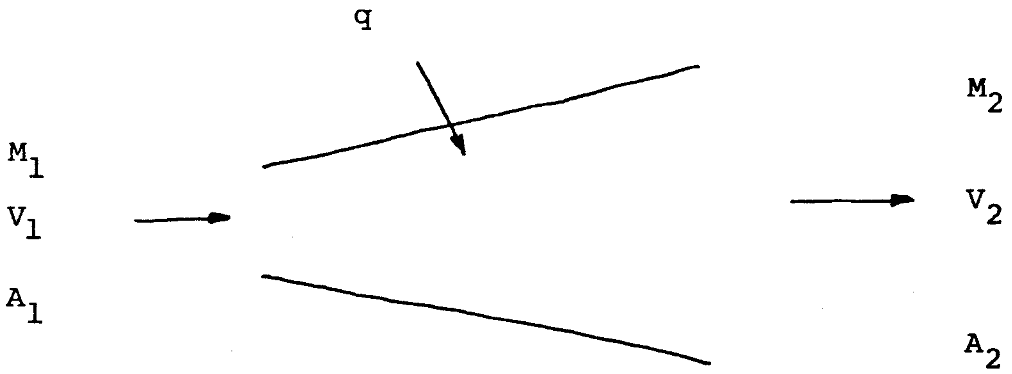

Sketch B

Application of the conservation equations in Sketch B yields:

Conservation of Mass

$$\rho_1 \, v_1 \, A_1 = \rho_2 \, v_2 \, A_2 = \dot{m} \qquad (3.10)$$

Conservation of Momentum

$$(\rho_2 \, v_2 \, A_2) \, v_2 - (\rho_1 \, v_1 \, A_1) v_1 = P_1 \, A_1 - P_2 \, A_2 + \int_1^2 P \, d \, A \qquad (3.11)$$

Conservation of Energy

$$\rho_1 \, v_1 \, A_1 \, (h_1 + \frac{v_1^2}{2}) + q \, A_w = \rho_2 \, v_2 \, A_2 \, (h_2 + \frac{v_2^2}{2}) \qquad (3.12)$$

The ideal gas equation of state and the Crocco pressure-area relation are also employed:

$$P = \rho RT \qquad (3.13)$$

$$PA^{\varepsilon/(\varepsilon-1)} = \text{constant} \qquad (3.14)$$

With the Crocco pressure-area relation, the wall force integral in Equation 3.11 may be evaluated.

$$\int_1^2 PdA = \int_1^2 P_1 \left(\frac{A}{A_1}\right)^{\frac{\varepsilon}{1 - \varepsilon}} dA = (1 - \varepsilon) \; (P_2 \, A_2 - P_1 \, A_1) \qquad (3.15)$$

The solutions of Equations 3.10 to 3.13 for an ideal gas may be written as dimensionless ratios which are functions of ε, γ and the Mach numbers M_1 and M_2. (see Appendix A)

$$\frac{P_2}{P_1} = \left[\frac{\varepsilon + \gamma\, M_1^{\,2}}{\varepsilon + \gamma\, M_2^{\,2}}\right]^{\varepsilon} \tag{3.16}$$

$$\frac{A_2}{A_1} = \left(\frac{P_2}{P_1}\right)^{\frac{1-\varepsilon}{\varepsilon}} = \left[\frac{\varepsilon + \gamma\, M_1^{\,2}}{\varepsilon + \gamma\, M_2^{\,2}}\right]^{1-\varepsilon} \tag{3.17}$$

$$\frac{T_2}{T_1} = \left[\frac{M_2}{M_1} \cdot \frac{\varepsilon + \gamma\, M_1^{\,2}}{\varepsilon + \gamma\, M_2^{\,2}}\right]^{2} \tag{3.18}$$

$$\frac{T_{02}}{T_{01}} = 1 + \frac{q\, A_w}{\dot{m}\, C_p\, T_{01}} = \left[\frac{2 + (\gamma - 1) M_2^{\,2}}{2 + (\gamma - 1) M_1^{\,2}}\right] \left[\frac{M_2}{M_1} \quad \frac{\varepsilon + \gamma\, M_1^{\,2}}{\varepsilon + \gamma\, M_2^{\,2}}\right]^{2} \tag{3.19}$$

The objective of this work is to maximize the specific impulse I_2 with respect to area ratio A_2/A_1 and the total energy added Q where:

$$Q = \frac{q\, A_w}{\dot{m}} \tag{3.20}$$

The velocity at the exit plane is described by:

$$v_2 = M_2 \sqrt{\gamma R}\, \sqrt{T_2} \tag{3.21}$$

Utilizing relation 3.18 the static temperature is expressed in the form:

$$T_2 = T_1 \left(\frac{M_2}{M_1}\right)^{2} \left[\frac{\varepsilon + \gamma\, M_1^{\,2}}{\varepsilon + \gamma\, M_2^{\,2}}\right]^{2} \tag{3.22}$$

Hence,

$$I_2 = \frac{M_2^2}{9.8} \cdot \frac{\sqrt{\gamma R T_1}}{M_1} \cdot \left[\frac{\varepsilon + \gamma M_1^2}{\varepsilon + \gamma M_2^2}\right] \tag{3.23}$$

describes the specific impulse at the exit plane. At the duct entrance for specified parameters (T_{01}, M_1, γ, C_p), the independent variables A_2/A_1 and Q are related to the dependent variables ε and M_2^2 by Equations 3.17 and 3.19. Equation 3.17 is written as:

$$M_2^2 = \left(\frac{A_2}{A_1}\right)^{\frac{-1}{1-\varepsilon}} \left[\frac{\varepsilon}{\gamma} + M_1^2\right] - \frac{\varepsilon}{\gamma} \tag{3.24}$$

and Equation 3.19 is described by:

$$1 + \frac{Q}{C_p T_{01}} = \left[\frac{2 + (\gamma - 1)M_2^2}{2 + (\gamma - 1)M_1^2}\right] \left(\frac{M_2}{M_1}\right)^2 \left(\frac{A_2}{A_1}\right)^{2/(1-\varepsilon)} \tag{3.25}$$

It is pointed out that for known parameters (C_p, T_{01}, γ, M_1) and specified values of the variables Q and A_2/A_1 Equations 3.24 and 3.25 may be solved for ε and M_2^2. The results obtained are employed in Equation 3.23 to obtain the exit specific impulse. The solutions to Equations 3.24 and 3.25 are subject to the conditions:

a) The exit Mach number $M_2 \geq 1.0$

b) The change in entropy from state 1 to state 2 is described by $S_2 - S_1 = \Delta S = C_p \ln \frac{T_2}{T_1} - R \ln \frac{P_2}{P_1} \geq 0$

This change in entropy may be written as:

$$\Delta S = C_p \ln \left\{ \left[\frac{\varepsilon + \gamma M_1^2}{\varepsilon + \gamma M_2^2}\right]^{\frac{2\gamma + \varepsilon(1-\gamma)}{\gamma}} \left(\frac{M_2}{M_1}\right)^2 \right\} \tag{3.26}$$

It is convenient to map the above constraints on all heat addition processes which follow the Crocco relation into the pressure-area ratio plane described by Equation 3.16. Equation 3.16 is depicted in Figure 3.7 for several values of ε. In Figure 3.7 the previously mentioned constraint (a) implies that all heat addition processes are bound on the right by the line $M_2 = 1.0$. The constraint (b) indicates that all heat addition processes are bound on the left by an isentropic line ($\Delta S = 0$) through the initial point[3.8] ($P_2/P_1 = 1.$, $A_2/A_1 = 1$). As an example, in Figure 3.7 it is assumed that for the lithium propellant conditions at the duct entrance are described by

P_{01} = 1 atmosphere

T_{01} = 1000°K

M_1 = 3.0

C_p = 0.716 (Btu/lb.m - $^{\circ}$R)

γ = 1.66

The constraints (a) and (b) are also depicted for this case in Figure 3.7.

Digressing for a moment, two specific examples of heat addition processes to a supersonic stream employing the Crocco relations are considered. In the first case the rise in entropy due to heat addition is investigated. This rise in entropy is described by Equation 3.26. Billig[3.8] points out that to increase performance in a heat addition process it is desirable to minimize the rise in entropy due to heat addition at an incorrect Mach number. As a result of minimizing the rise in entropy the exit Mach number is desbribed by (See Appendix B):

$$M_2 = \left(\frac{\varepsilon}{\gamma - \varepsilon(\gamma - 1)}\right)^{1/2} \qquad (3.27)$$

Equation 3.27 describes the exit Mach number at which thermal choking occurs and all real values of M_2 are obtained for:

$$0 \leq \varepsilon \leq \frac{\gamma}{\gamma - 1}$$

In Figure 3.7 Equation 3.27 is plotted. It is noted in Figure 3.7 that in a constant area process ($\varepsilon = 1.0$) for a minimum rise in entropy the Mach number at which thermal choking occurs is given by $M_2 = 1.0$, as would be expected.

As the second example a heat addition process which maintains a constant Mach number is considered. The constant Mach number heat addition process is characterized by (See Appendix C):

$$\varepsilon = -\gamma M_1^{\,2} \tag{3.28}$$

The case of constant Mach number heat addition is also depicted in Figure 3.7.

However, the objective of this study is to determine the heat addition process which achieves the maximum exit specific impulse I_2 with Q and A_2/A_1 as independent variables. Therefore, Equations 3.24 and 3.25 were solved subject to constraints (a) and (b) for values of ε and $M_2^{\,2}$ via digital computer program. The results obtained were inserted in Equation 3.23 to determine the specific impulse I_2. Figure 3.8 describes the results obtained for the previously mentioned example. In Figure 3.8 it is pointed out that to achieve a significant increase in specific impulse and also maintain a moderate temperature ($T_2 \leq 2000^{\circ}K$) extremely large area ratios ($\frac{A_2}{A_1} \geq 10^4$) are required. It is also noted that a maximum point in specific impulse occurs for area ratios $\frac{A_2}{A_1} < 60$ but for a given $\frac{A_2}{A_1} \geq 60$ the maximum specific impulse which satisfies constraints (a) and (b) occurs at $M_2 = 1.0$. It is observed that the intersection of the area ratio curve with the ordinate axis in Figure 3.8 denotes the specific impulse obtained for the case of isentropic expansion. Thus, solutions for a maximum exit specific impulse with heat addition lie to the right of the ordinate ($\Delta S > 0$) and on or above the $M_2 = 1$ curve in Figure 3.8.

Several cases of constant values of ε are depicted in Figure 3.8. The process of constant-area heat addition ($\varepsilon = 1.0$) is not shown as heat addition to a supersonic stream in a constant area duct yields a decrease in specific impulse[3.9]. It is observed in Figure 3.8 that constant pressure heat addition ($\varepsilon = 0$) yields no increase in specific impulse but maintains a constant specific impulse regardless of area ratio or total amount of heat added. However, a constant static temperature heat addition process ($T_1 = T_2$) yields a significant increase in the specific impulse for large area ratios while maintaining a desirable exit temperature T_2. A constant Mach number heating process ($\varepsilon = -\gamma M^2$) also displays a desirable increase in specific impulse for $T_2 \leqslant 2000^{\circ}K$ but again large area ratios are required. In Figure 3.8 assuming a fixed value of area ratio $\frac{A_2}{A_1} < 10.0$ there is only a small difference in magnitude of specific impulse obtained between a constant Mach number and a constant static temperature heat addition process. However, for area ratios larger than ten a constant initial Mach number process while requiring more heat with area ratio constant results in a larger specific impulse. But, from another viewpoint, if the total heat which may be added is limited and the area ratio is arbitrary, a constant static temperature process yields the larger specific impulse for $\frac{A_2}{A_1} < 10$ in Figure 3.8.

The results obtained for different examples are illustrated in Figures 3.9, 3.10, 3.11, and 3.12. From these Figures it is observed that a high stagnation temperature is desirable at the duct entrance. It is again noted in each of these Figures that for a constant area ratio $\frac{A_2}{A_1} < 10$ and a total amount of heat added $Q \leqslant 2.4 \times 10^4 \frac{kw}{kg/sec}$ a constant Mach number process while requiring more heat yields a larger specific impulse than a constant static temperature process. However, if the heat which may be added is limited and area ratio arbitrary the above processes are interchanged.

From the above results it is apparent that large area ratios, quantities of total heat added and stagnation temperatures are required to obtain a substantial increase in specific impulse.

Further analysis of the model ATEP thruster considers a variation of parameters study in which three distinct cases are assumed:

a) fixed duct entrance conditions, arbitrary area ratio and limited Q

b) fixed duct entrance conditions arbitrary Q and limited area ratio

c) specified Q and area ratio with variable duct entrance parameters.

Case (a) From previous results it would be expected that the constant static temperature heat addition process would be more favorable than constant Mach number heat addition. As an example consider

$M_1 = 3.0$

$T_{01} = 3000^{\circ}K$

$T_1 = 750^{\circ}K$

$Q = 8 \times 10^3 \frac{kw}{kg/sec}$

Referring to Figure 3.11 the two heat addition processes are compared:

a) Constant Mach number heat addition

$I_2 = 505$ seconds

$T_2 = 1300^{\circ}K$

$\frac{A_2}{A_1} = 10^2$

b) Constant static temperature heat addition

$I_2 = 560$ seconds

$T_2 = 750^{\circ}K$

$\frac{A_2}{A_1} \simeq 10^4$

If the initial Mach number is increased reference to Figure 3.12 indicates that while the specific impulse increases in both cases, the constant static temperature process again yields a larger specific impulse than a constant Mach number heat addition process.

Case (b) In Figure 3.13 are depicted the results obtained for a very optimistically area-ratio-limited thruster described by:

$$\frac{A_2}{A_1} = 10^6$$

With the assumption of an initial Mach number M_1 and that an arbitrary amount of Q is available it would be expected that a constant Mach number heat addition process would yield a larger specific impulse than a constant static temperature process. This point is illustrated in Figure 3.13 by considering an example where:

$M_1 = 3.0$

$T_{01} = 3000^{\circ}K$

$T_1 = 750^{\circ}K$

Hence, for

a) constant Mach number heat addition

$I_2 = 890$ seconds

$T_2 = 4200^{\circ}K$

$Q = 4.0 \times 10^4 \; \frac{kw}{kg/sec}$

b) constant static temperature heat addition

$I_2 = 652$ seconds

$T_2 = 750^{\circ}K$

$Q = 1.3 \times 10^4 \; \frac{kw}{kg/sec}$

It is pointed out that in a constant Mach number heat addition process small values of Mach number are desirable as illustrated in Figure 3.13.

Case (c) For a Q and area ratio limited thruster with arbitrary initial conditions consider an example where

$T_{01} = 3000^{\circ}K$

$\frac{A_2}{A_1} = 10^6$

$Q = 2.4 \times 10^4 \; \frac{kw}{kg/sec}$

Referring to Figure 3.13 the constant static temperature and constant Mach number processes are compared.

a) Constant Mach number heat addition

$I_2 = 740$ seconds

$3 < M_2 < 5$

$T_2 \approx 2000^{\circ}K$

b) Constant static temperature heat addition

$I_2 = 800$ seconds

$M_1 \approx 2.$

$T_2 \approx 850^\circ K$

With this example the following points are made in Figure 3.13:

a) In the ATEP thruster with limits on both area ratio and Q the constant static temperature process is more favorable than the constant Mach number heat addition process.

b) In the constant static temperature process a large stagnation temperature is desirable.

c) A low initial Mach number would be favorable.

d) It is apparent that points (b) and (c) conflict and that it would be necessary to trade off the initial static temperature with initial Mach number in the heat addition process.

To evaluate the performance of the ideal ATEP electrothermal thruster model, the effect of heat addition upon thruster efficiency is evaluated. In Sketch C the points at which power levels are defined in the ATEP model are depicted.

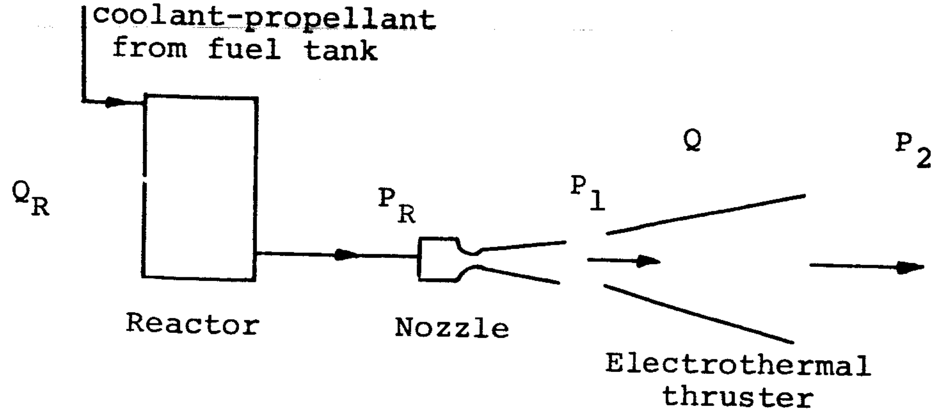

Sketch C

The parameters in Sketch C are defined as follows:

Q_R, power added to the coolant-propellant as it passes through the reactor.

$Q_R = H_v + P_R$ (kw/kg/sec)

H_v, heat of vaporization of the coolant-propellant. (kw/kg/sec)

P_R, total power per unit mass rate of flow available for use in a thermodynamic expansion process (equivalent to the stagnation enthalpy). (kw/kg/sec)

P_1, stream power per unit mass rate of flow at the nozzle exit plane. (kw/kg/sec)

Q, total power per unit mass ratio of flow added to the propellant as it passes through the electrothermal thruster. (kw/kg/sec)

P_2, stream power per unit mass rate of flow at the electrothermal thruster exit plane. (kw/kg/sec)

The efficiencies of the nozzle and electrothermal thruster in Sketch C are defined as:

$$\eta_n = \frac{P_1}{P_R} \tag{3.29}$$

$$\eta_{th} = \frac{P_2 - P_1}{Q + P_2 - P_1} \tag{3.30}$$

It is pointed out that with this definition of thruster efficiency when no heat is added to the propellant the efficiency approaches a value of unity. The process then becomes an adiabatic expansion with an approximately infinite area ratio.

Since previous analysis has shown that to achieve a significant increase in specific impulse large initial stagnation temperatures and thruster area ratios are required, the thruster efficiency is evaluated from this viewpoint. In Figures 3.14 and 3.15 the results obtained for the case of $T_{01} = 3000^{\circ}K$ and variations of initial Mach number and thruster area ratio are illustrated. From these Figures it is observed that thruster efficiency as defined by Equation 3.30 increases with increasing area ratio, but decreases as initial Mach number and the amount of heat added increase. The nozzle efficiency also increases with increasing Mach number M_1.

It is of interest to apply all of the results obtained for previous examples to a single case. Therefore assume an ATEP thruster configuration in which

$$\frac{A_2}{A_1} = 10^6$$

$$Q = 2 \times 10^4 \ \frac{\text{kw}}{\text{kg/sec}}$$

$$T_o = 3000^{\circ}K$$

with a significant increase in propellant specific impulse between entrance and exit of the electrothermal thruster desired. Reference to Figure 3.13 shows that a constant static temperature heat addition process with an initial Mach number $M_1 = 2.0$ would be very desirable yielding an exit specific impulse

$$I_2 = 750 \text{ seconds}$$

Equations 3.29 and 3.30 indicate that the nozzle and thruster efficiencies are characterized by

$$\eta_n = 0.36$$

$$\eta_{th} = 0.90$$

Summary

As a result of this preliminary analysis of the ATEP concept as applied to the electrothermal thruster for the purpose of increasing thruster specific impulse the following points are made:

- In the nozzle plenum chamber for stagnation conditions described by

  $$P_o \geqslant 0.001 \text{ Atmospheres}$$

  $$T_o \leqslant 3000^{o}K$$

  less than five percent to the total enthalpy is tied up in ionization. Therefore, with these stagnation conditions, ionization losses are small and the nozzle is assumed ideal.
- Constant area and constant static pressure heat addition processes are undesirable.
- Constant static temperature or constant Mach number heat addition processes are quite favorable.
- With the assumption that the ATEP electrothermal thruster is $Q\left(\frac{kw}{kg/sec}\right)$ limited while an arbitrary area ratio is available a heat addition process described by the Crocco pressure-area relation indicates that:
  a) Extremely large area ratios are required:

  $$\frac{A_2}{A_1} > 10^4$$

b) Large stagnation temperatures at the duct entrance are desirable.

c) A constant static temperature heating process is more favorable than a constant Mach number process.

d) At the entrance to the duct large values of Mach number are desired.

e) For the example considered in Figure 3.12 where:

$M_1 = 5.0$

$I_1 = 410$ seconds

$T_{01} = 3000^{\circ}K$

and a constant static temperature heat addition process is maintained with:

$$\frac{A_2}{A_1} = 10^6$$

$$Q = 2. \times 10^4 \ \frac{kw}{kg/sec}$$

the exit specific impulse is described by:

$I_2 \approx 690$ seconds

$T_2 = 327^{\circ}K$

$\eta_n = .90$

$\eta_{th} = .65$

- If the ATEP electrothermal thruster is area ratio limited while the heat energy available is described by:

$$Q \leqslant 4.8 \times 10^4 \ \frac{kw}{kg/sec}$$

the Crocco model of the heat addition process indicates that:

a) While being limited, extremely large area ratios are needed for an increase in specific impulse.

b) At the duct entrance large values of stagnation temperature are desirable.

c) A constant Mach number heat addition process is more favorable than a constant static temperature process.

d) At the entrance of the duct small values of Mach number are most favorable. A process in which the heating of the propellant begins at the throat would be preferred.

e) In the example of Figure 3.13 for the Conditions

$M_1 = 3.0$ $\qquad$ $I_1 = 375$ seconds

$T_{01} = 3000^{\circ}K$

with a constant Mach number heat addition process employed and

$\frac{A_2}{A_1} = 10^6$ $\qquad$ $Q = 4.1 \times 10^4 \ \frac{\text{kw}}{\text{kg/sec}}$

the exit specific impulse is characterized by

$I_2 = 890$ seconds $\qquad$ $\eta_n = .75$

$T_2 \approx 4300^{\circ}K$ $\qquad$ $\eta_{th} = .71$

- If the ATEP electrothermal thruster is area ratio and Q limited the Crocco model of the heat addition process indicates that
  a) Once again, while being limited large area ratios are required to increase the specific impulse.
  b) At the duct entrance large values of stagnation temperature are favorable.
  c) A constant static temperature process is more favorable than a constant Mach number process of heat addition.
  d) At the entrance to the duct small values of Mach number are most desirable. A process in which addition begins at the throat yields the largest exit specific impulse. However, because of the large stagnation temperature and low Mach number requirements, a trade off between initial Mach number and initial static temperature would be required.

e) In the example of Figure 3.13 for the conditions

$T_{01} = 3000^{\circ}K$ $\quad Q = 2.4 \times 10^{4} \ \frac{kw}{kg/sec}$

$\frac{A_2}{A_1} = 10^{6}$

and constant static temperature heat addition process, the exit specific impulse is described by

$I_2 = 750$ seconds $\quad \eta_n = .36$

$M_1 = 2.$ $\quad \eta_{th} = .90$

$T_2 = 850^{\circ}K$

- The nozzle efficiency as defined by Equation 3.29 increases with increasing Mach number M_1.
- The electrothermal thruster efficiency as given by Equation 3.30 decreases with increasing values of initial Mach number M_1 and total heat added per unit mass rate of flow in the duct. However, increasing duct area ratios cause an increase in thruster efficiency.
- The authors are not entirely satisfied with the definition of thruster and nozzle efficiencies as described by Equations 3.29 and 3.30. It is the intent of future analysis to evaluate the ATEP thruster by considering the effect upon propulsion system specific mass (lbm/kw) when heat is added to a supersonic stream.
- It is also realized that the assumption of the Crocco relation while facilitating this preliminary analysis is a restricted approach to the concept of heat addition to a supersonic stream. At the present time, it is intended that a future analysis based on increments in duct length and accounting for real gas effects be performed. The applicability of optimization techniques to this concept will them be investigated.

References

3.1. Mickelsen, W. R.: Annual Report on Advanced Electric Propulsion Research, January 1, 1966 to December 31, 1966, National Aeronautics and Space Administration Grant NGR06-002-032.

3.2. Crocco, L.: One Dimensional Treatment of Steady Gas Dynamics. Fundamentals of Gas Dynamics, vol. 3 of High Speed Aerodynamics and Jet Propulsion, H. W. Emmons, ed., Princeton University Press, 1958, pp. 100-110.

3.3. Zemansky, Mark: Heat and Thermodynamics. Fourth Edition, McGraw Hill Book Co., Inc., p. 439.

3.4. Allen, C. W.: Astrophysical Quantities. The Athlone Press, University of London.

3.5. Jack. John R.: Theoretical Performance of Propellants Suitable for Electrothermal Jet Engines. NASA TN D-682, 1961.

3.6. Stull, D. R. and Sinke, G. C.: Thermodynamic Properties of the Elements. Washington, American Chemical Society, 1956.

3.7. Dobrowolski, Andrzej: Analysis of Nonconstant Area Combustion and Mixing in Ramjet and Rocket-Ramjet Hybrid Engines. NASA TN D-3626, 1966.

3.8. Billig, F. S.: Design of Supersonic Combustors Based on Pressure-Area Fields. Eleventh International Symposium on Combustion, University of California, August 14-20, 1966.

3.9. Shapiro, A. H.: The Dynamics and Thermodynamics of Compressible Fluid Flow, Volume I, The Ronald Press Co., p. 199.

Symbols

A	area
C_p	specific heat constant 0.716 (Btu/lbm°R)
E_i	ionization potential electron volts
e	internal energy (Btu/lbm)
I	specific impulse sec.
h	enthalpy (Btu/lbm)
M	Mach number
$\dot{m}$	mass flow rate (lbm/sec)
$\bar{M}$	molecular weight of Lithium 6.94 (lbm/lbm-mole)
P	pressure (dyne/cm^2) or atmospheres

q	rate of heat addition $\frac{\text{Btu}}{\text{ft}^2\ \text{sec}}$
Q	total heat added $\frac{\text{Btu}}{\text{lbm}}$ or $\frac{\text{kw}}{\text{kg/sec}}$
R	universal gas constant 1.98 (Btu/lbm-mole $^{\circ}$R)
S	entropy (Btu/lbm)
T	temperature $^{\circ}$K or $^{\circ}$R
v	velocity (m/sec)
α	degree of ionization
ε	power index
ρ	density $\frac{\text{lbm}}{\text{ft}^3}$
γ	specific heat ratio
η	percent of total enthalpy in ionization

Subscripts

0	stagnation
1	duct entrance
2	duct exit
i	ionization
v	vaporization
w	wall
n	nozzle
th	thruster

Superscript

*	sonic point at which Mach number equals one.

Appendix A

The solutions to Equations 3.10 to 3.13 may be expressed in the form of dimensionless ratios which are a function of Mach number, power index and specific heat ratio. These ratios are obtained by a substitution of Equation 3.15 into 3.11 which yields:

$$\dot{m}\ (v_2 - v_1) = P_1A_1 - P_2A_2 + (1 - \varepsilon)\ (P_2A_2 - P_1A_1) \qquad (1)$$

or

$$(\rho_1 A_1 v_1)\ v_1 + \varepsilon P_1 A_1 = (\rho_2 A_2 v_2)\ v_2 + \varepsilon P_2 A_2 \qquad (2)$$

Employing Equations 3.10, 3.13 and the definition of the Mach number the mass flow rate may be expressed as:

$$\rho A v = \dot{m} = \frac{PAM\ \sqrt{\gamma}}{\sqrt{RT}} \qquad (3)$$

which combined with Equation (2) yields:

$$\frac{P_2A_2}{P_1A_1} = \frac{\varepsilon + \gamma\ M_1^{\ 2}}{\varepsilon + \gamma\ M_2^{\ 2}} \qquad (4)$$

The Crocco relation is defined by:

$$\frac{P_2}{P_1} = \left(\frac{A_2}{A_1}\right)^{\frac{\varepsilon}{1 - \varepsilon}} \qquad (5)$$

or:

$$\frac{A_2}{A_1} = \left(\frac{P_2}{P_1}\right)^{\frac{1 - \varepsilon}{\varepsilon}} \qquad (6)$$

Equations 4, 5 and 6 may be combined to describe the static pressure ratio and the area ratio:

$$\frac{P_2}{P_1} = \left[\frac{\varepsilon + \gamma\ M_1^{\ 2}}{\varepsilon + \gamma\ M_2^{\ 2}}\right]^{\varepsilon} \qquad (3.16)$$

$$\frac{A_2}{A_1} = \left[\frac{\varepsilon + \gamma M_1^2}{\varepsilon + \gamma M_2^2}\right]^{1 - \varepsilon} \qquad (3.17)$$

The ideal gas equation of state may be written as:

$$\frac{T_2}{T_1} = \frac{P_2}{P_1} \cdot \frac{\rho_1}{\rho_2} \qquad (7)$$

which with Equation (3) results in the static temperature ratio:

$$\frac{T_2}{T_1} = \frac{M_2^2}{M_1^2}\left[\frac{\varepsilon + \gamma M_1^2}{\varepsilon + \gamma M_1^2}\right]^2 \qquad (3.18)$$

The conservation of energy equation may be written as:

$$\dot{m}\, C_p T_{01} + q\, A_w = \dot{m}\, C_p\, T_{02} \qquad (8)$$

or:

$$\frac{T_{02}}{T_{01}} = 1 + \frac{q\, A_w}{\dot{m}\, C_p\, T_{01}} \qquad (9)$$

and employing the isentropic relations:

$$\frac{T_{02}}{T_{01}} = \left[\frac{2 + (\gamma - 1)M_2^2}{2 + (\gamma - 1)M_1^2}\right]\left[\frac{M_2}{M_1}\;\frac{\varepsilon + \gamma M_1^2}{\varepsilon + \gamma M_2^2}\right]^2 \qquad (3.19)$$

Appendix B

The rise in entropy is described by Equation 3.26. For a minimum rise in entropy with respect to exit Mach number:

$$\frac{d(\Delta s)}{dM_2^{\,2}} = 0 \qquad (1)$$

Therefore, differentiating Equation 3.26:

$$\frac{d(\Delta s)}{dM_2^{\,2}} = C_p \left[- \frac{2\gamma + \varepsilon\ (1 - \gamma)}{\varepsilon + \gamma\ M_2^{\,2}} + \frac{1}{M_2^{\,2}} \right] \qquad (2)$$

and

$$\frac{1}{M_2^{\,2}} = \frac{2\ \gamma + \varepsilon\ (1 - \gamma)}{\varepsilon + \gamma M_2^{\,2}}$$

or

$$M_2^{\,2} = \frac{\varepsilon}{\gamma - \varepsilon\ (\gamma - 1)} \qquad (3)$$

Hence, for a minimum rise in entropy the exit Mach number is described by:

$$M_2 = \left[\frac{\varepsilon}{\gamma - \varepsilon\ (\gamma - 1)} \right]^{1/2} \qquad (3.27)$$

Appendix C

Constant Mach number heat addition.

Employing Equation 3.24 described by :

$$M_2^{\,2} = \left(\frac{A_2}{A_1}\right)^{\frac{-1}{1-\varepsilon}} \left[\frac{\varepsilon}{\gamma} + M_1^{\,2}\right] - \frac{\varepsilon}{\gamma} \qquad (3.24)$$

for the case of constant Mach number

$$M_1^{\,2} = M_2^{\,2}$$

Hence,

$$M_1^{\,2} = \left(\frac{A_2}{A_1}\right)^{\frac{-1}{1-\varepsilon}} \frac{\varepsilon}{\gamma} + M_1^{\,2}\left(\frac{A_2}{A_1}\right)^{\frac{-1}{1-\varepsilon}} - \frac{\varepsilon}{\gamma}$$

and

$$M_1^{\,2}\left[1 - \left(\frac{A_2}{A_1}\right)^{\frac{-1}{1-\varepsilon}}\right] = -\frac{\varepsilon}{\gamma}\left[1 - \left(\frac{A_2}{A_1}\right)^{\frac{-1}{1-\varepsilon}}\right]$$

Therefore, the case of constant Mach number heat addition is characterized by

$$\varepsilon = -\gamma M_1^{\,2} \qquad (3.28)$$

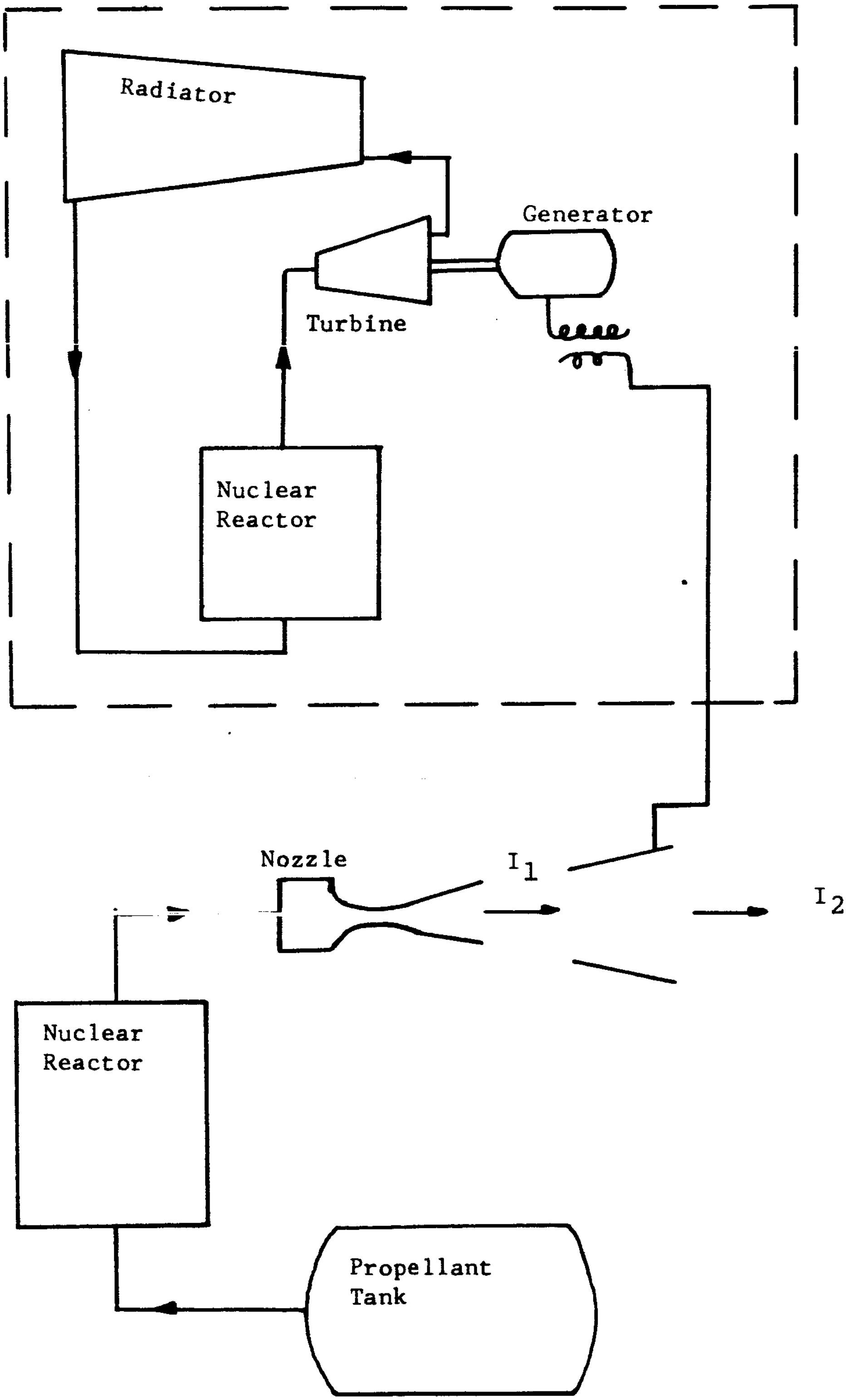
Radiator
Generator
Turbine
Nuclear Reactor
Nozzle
I_1
I_2
Nuclear Reactor
Propellant Tank

Figure 3.1 A schematic Diagram of an electrothermal thruster in an ATEP system.

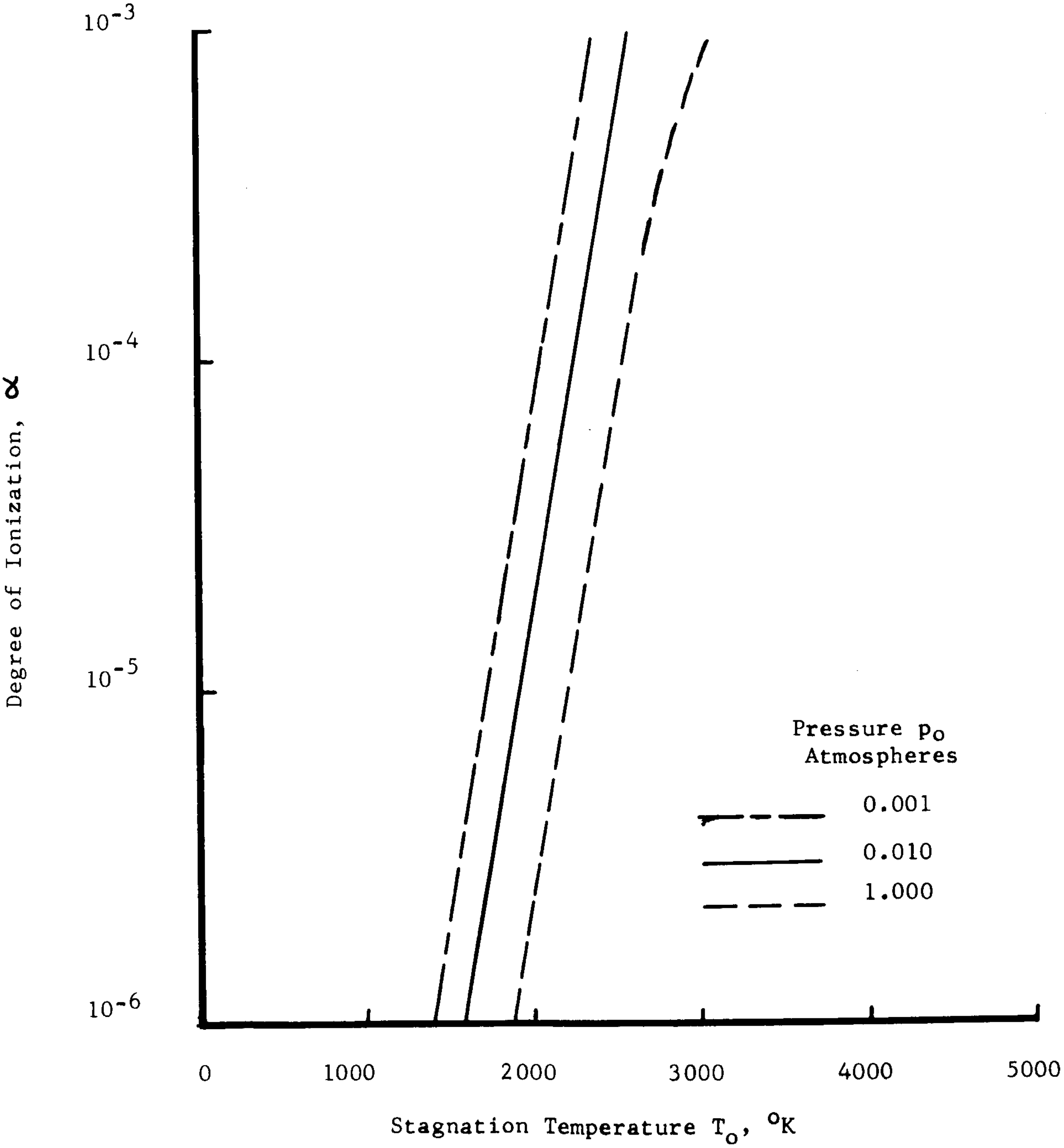

Figure 3.2 Degrees of ionization for lithium propellant at stagnation temperature T_o and pressure p_o.

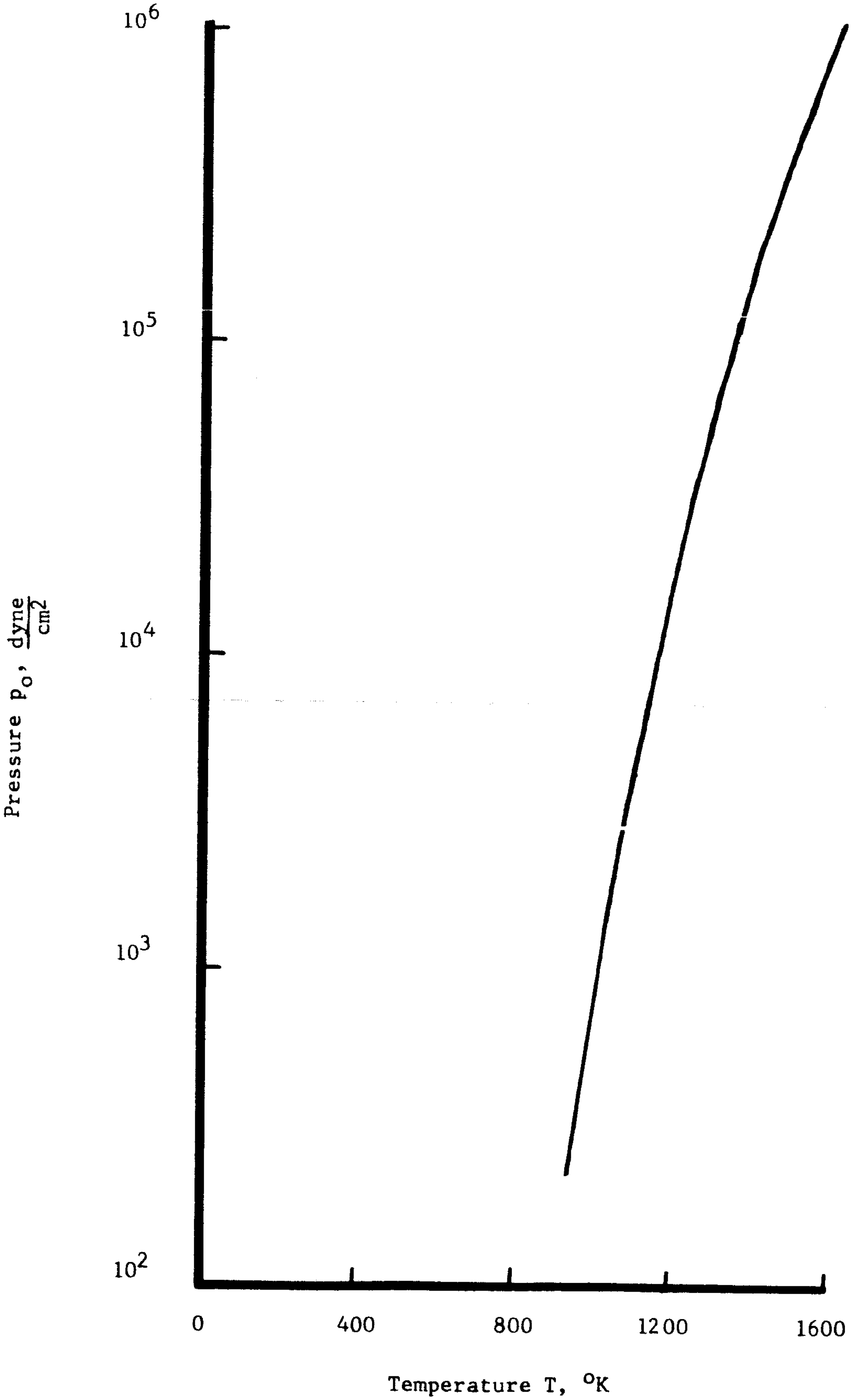

Figure 3.3 Vapor pressure curve for lithium propellant.

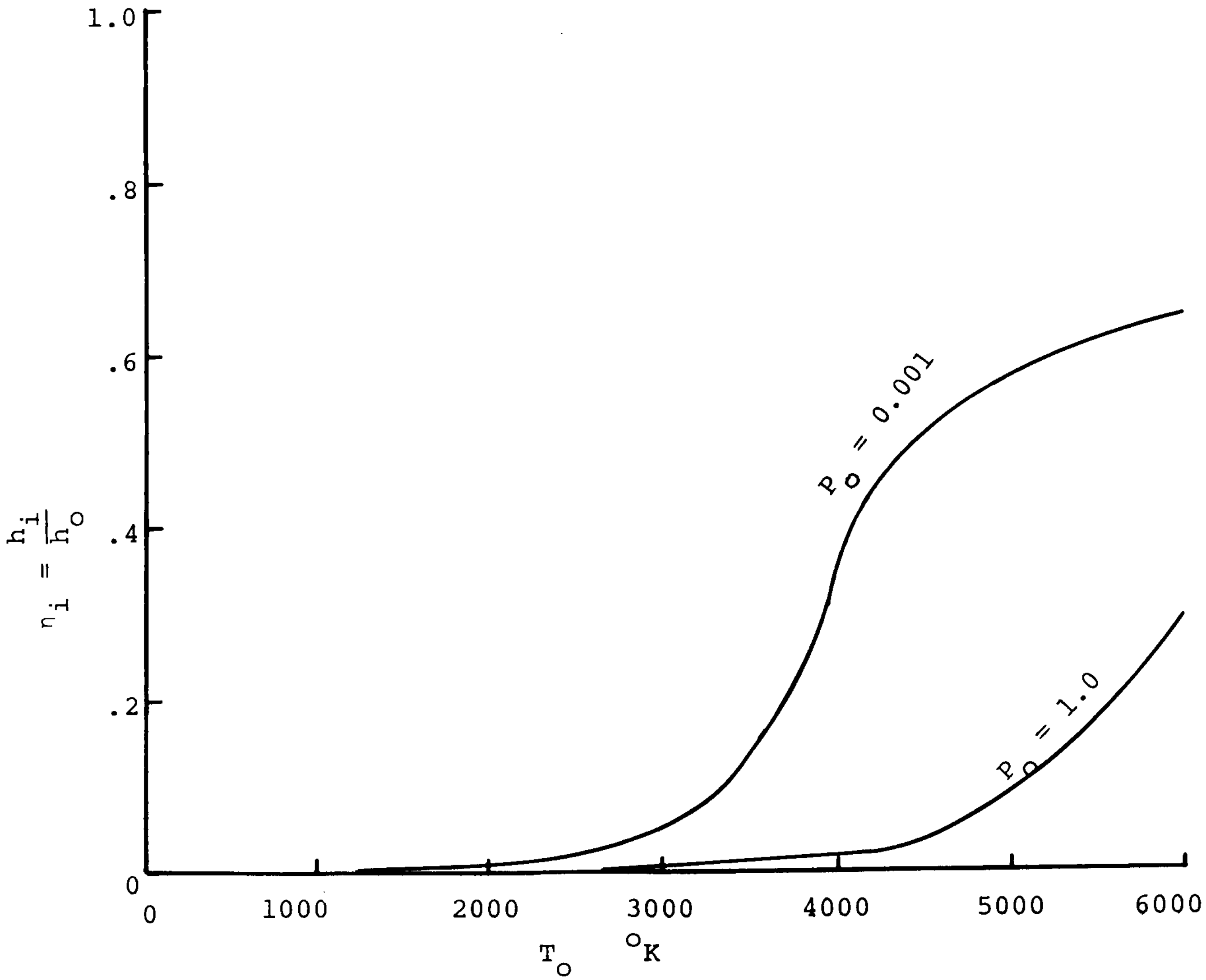

Figure 3.4 Percentage of stagnation enthalpy invested in ionization as a function of stagnation temperature and pressure.

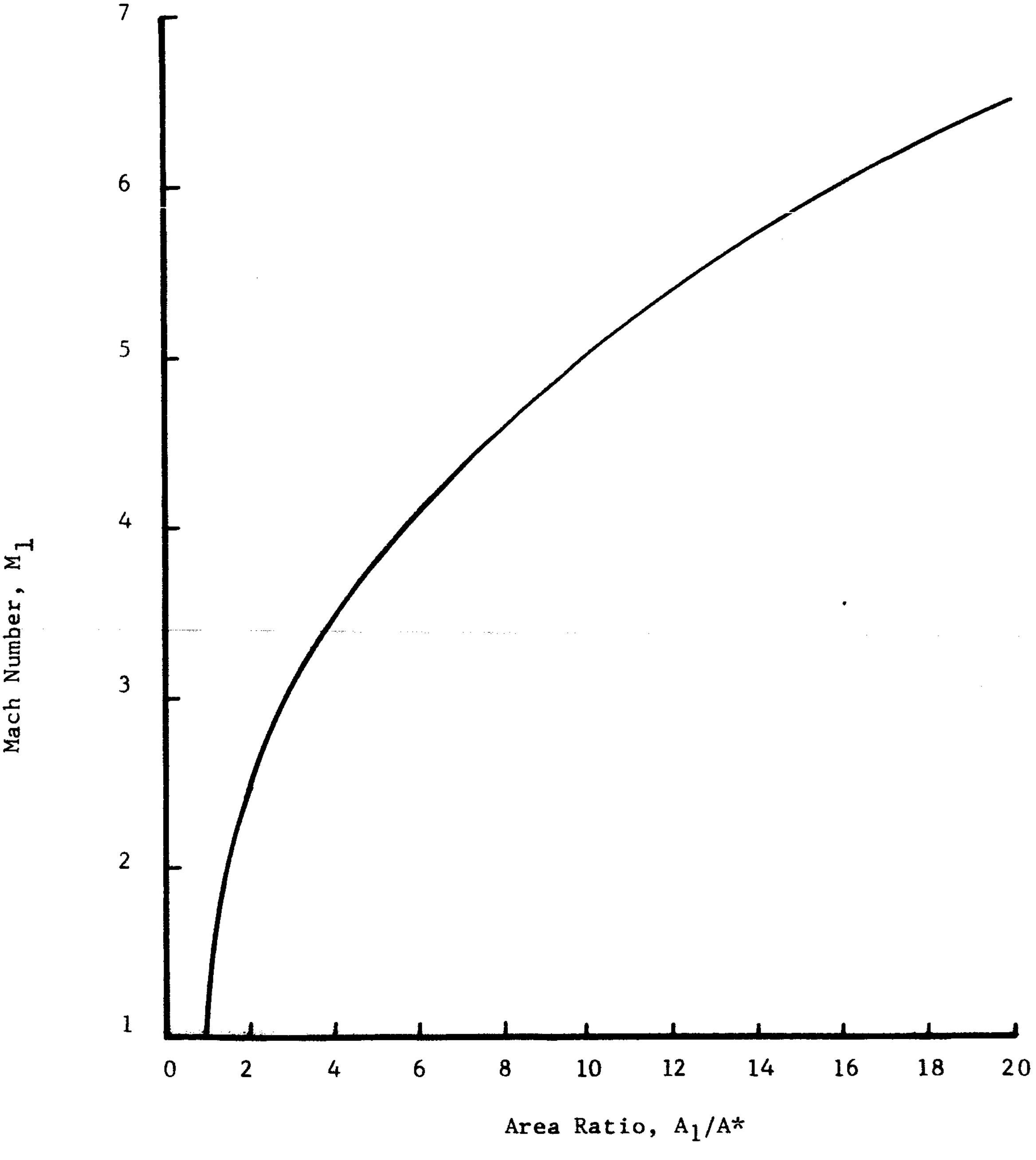

Figure 3.5 Plot of nozzle area ratio versus exit Mach number for an isentropic nozzle, for $\gamma = 1.66$.

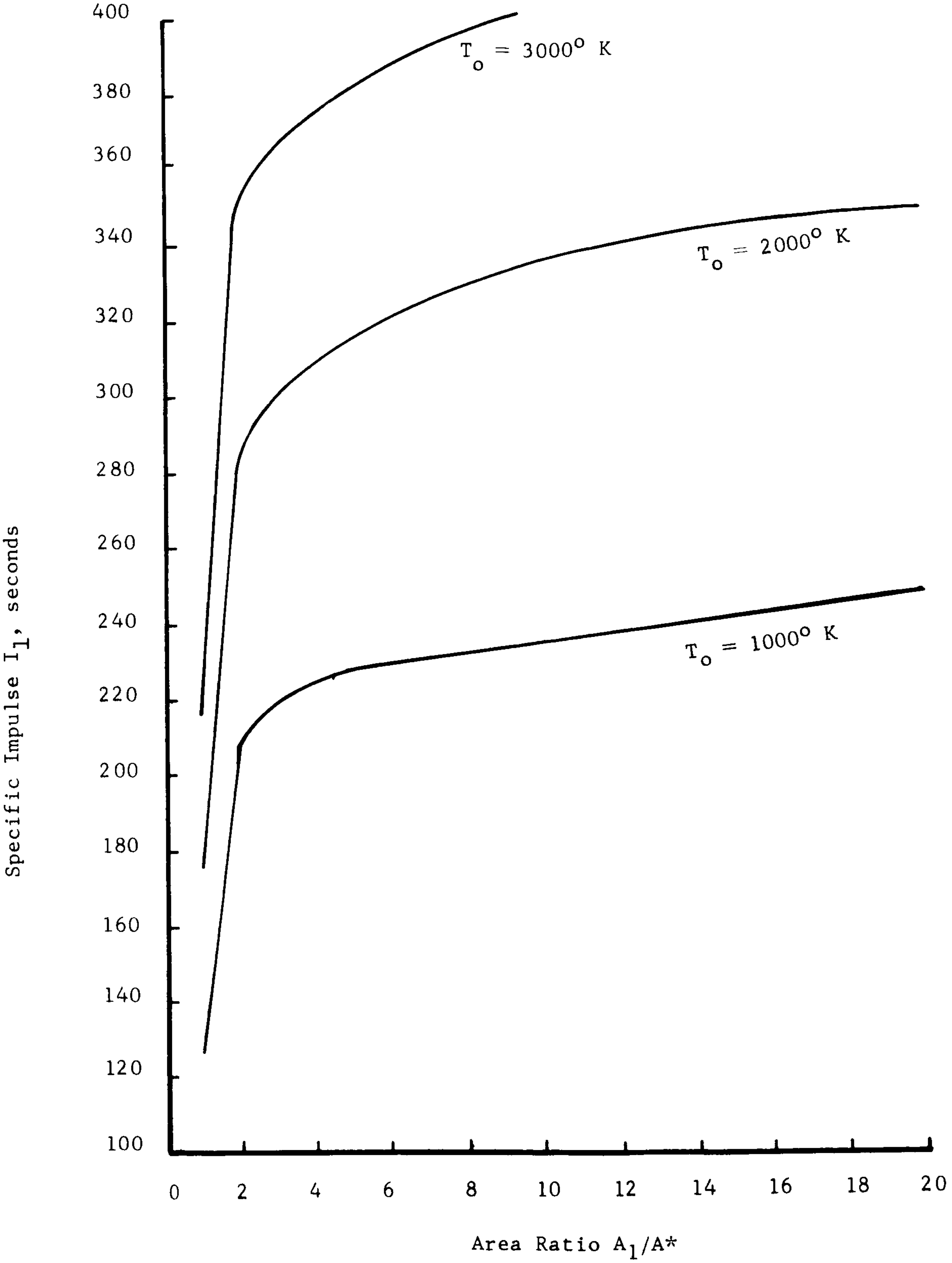

Figure 3.6 Nozzle specific impulse versus area ratio for the isentropic case, for $\gamma = 1.66$

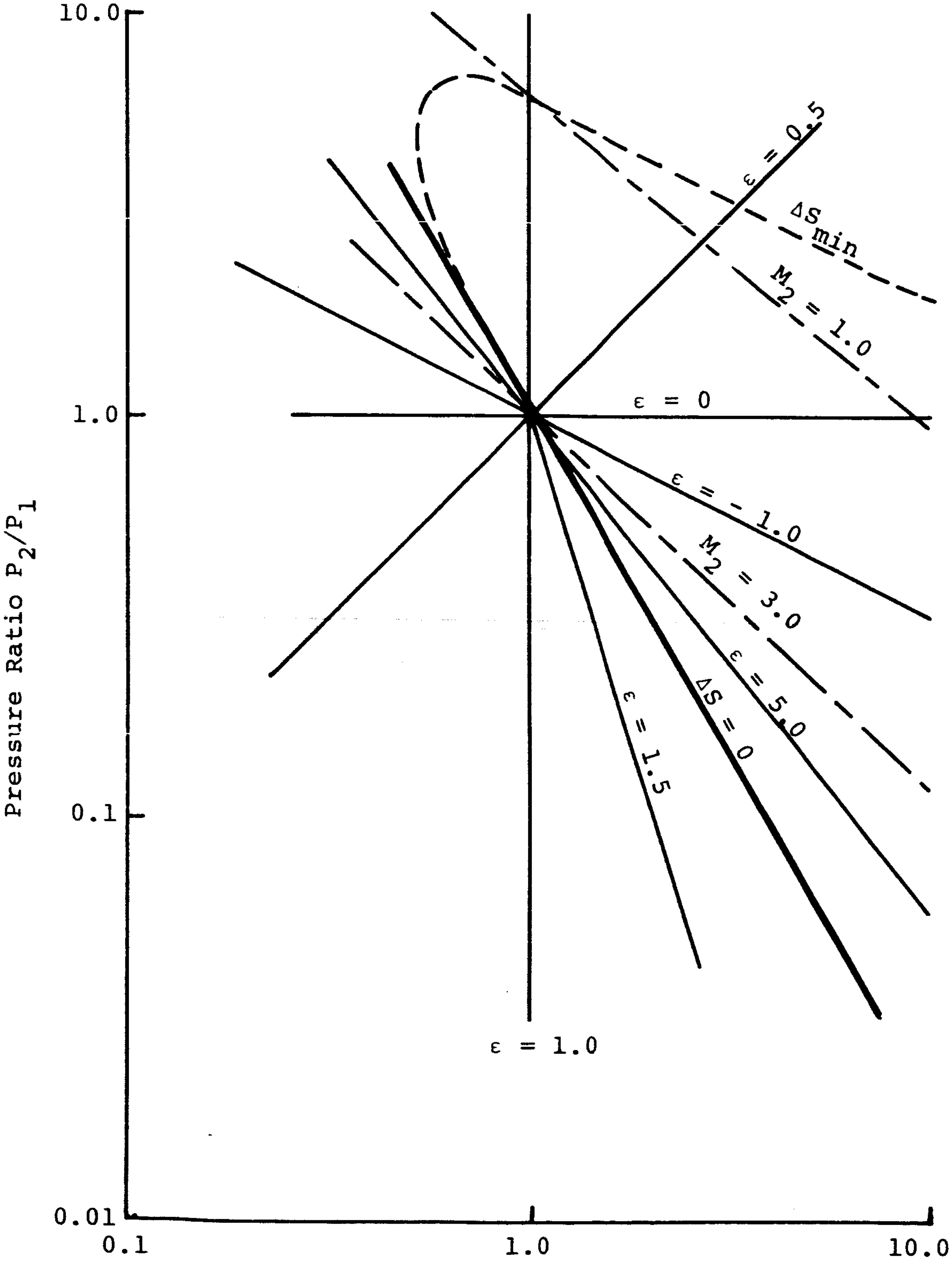

Figure 3.7 The Crocco pressure-area relation with constraints for the case $M_1 = 3.0$ and $T_{01} = 1000^{o}K$.

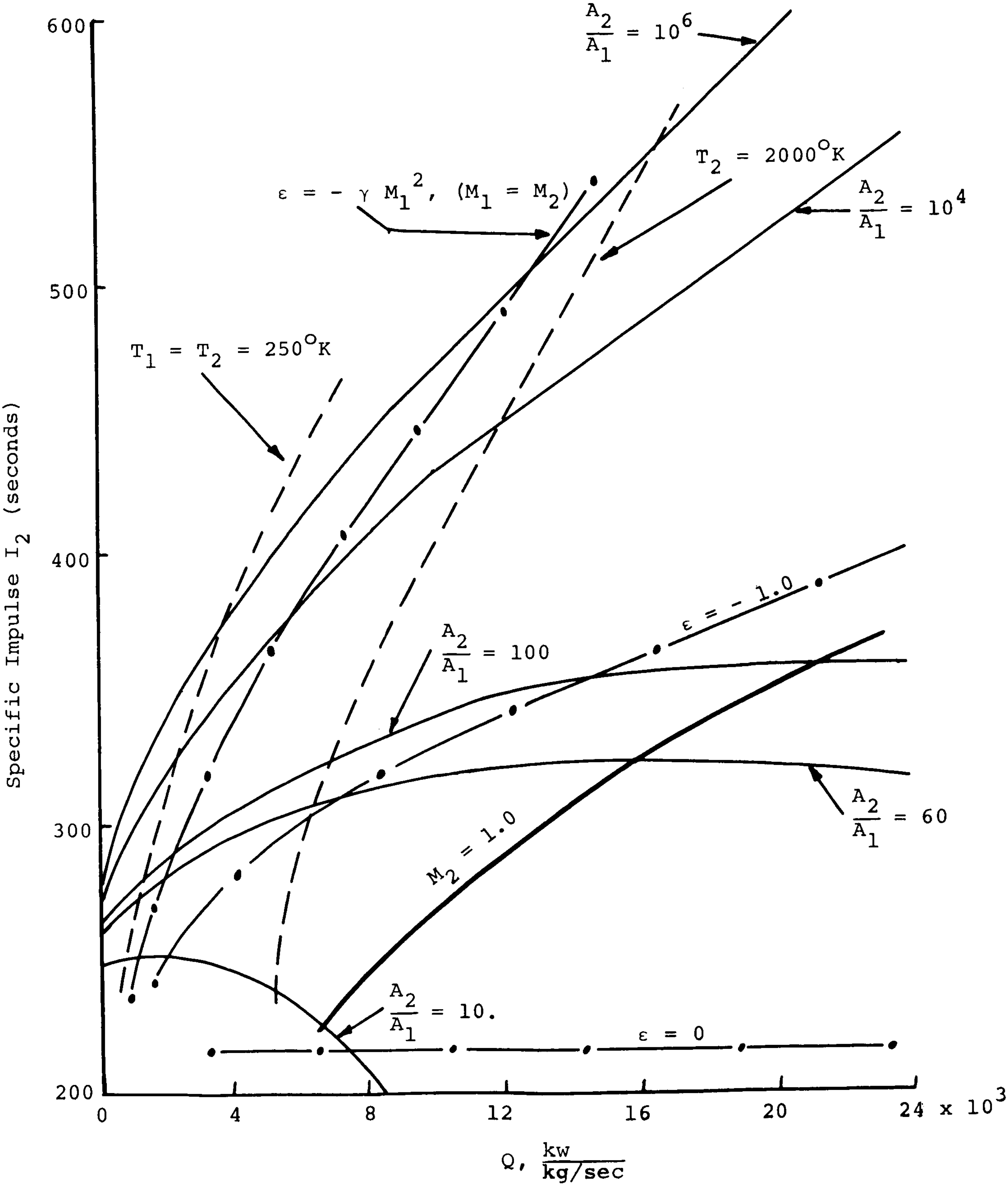

Figure 3.8 Solutions of Equations 3.23, 3.24, and 3.25 for the case $M_1 = 3.0$, $T_1 = 250^\circ K$ and $T_{01} = 1000^\circ K$. ($I_1 = 216$ sec.)

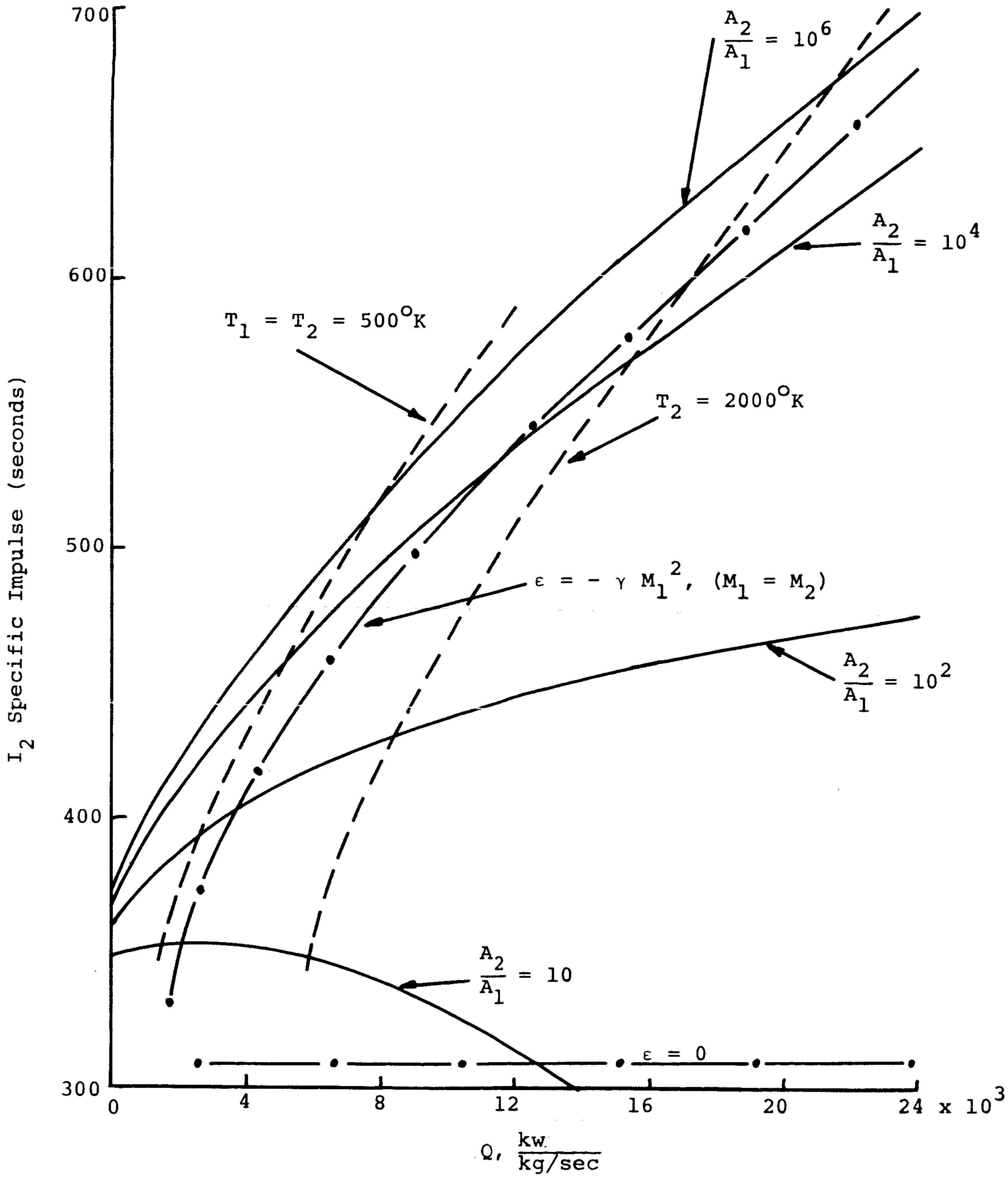

Figure 3.9. Solutions of Equations 3.23, 3.24, and 3.25 for the case $M_1 = 3.0$, $T_1 = 500^oK$, and $T_{01} = 2000^oK$. ($I_1 = 306$ sec.)

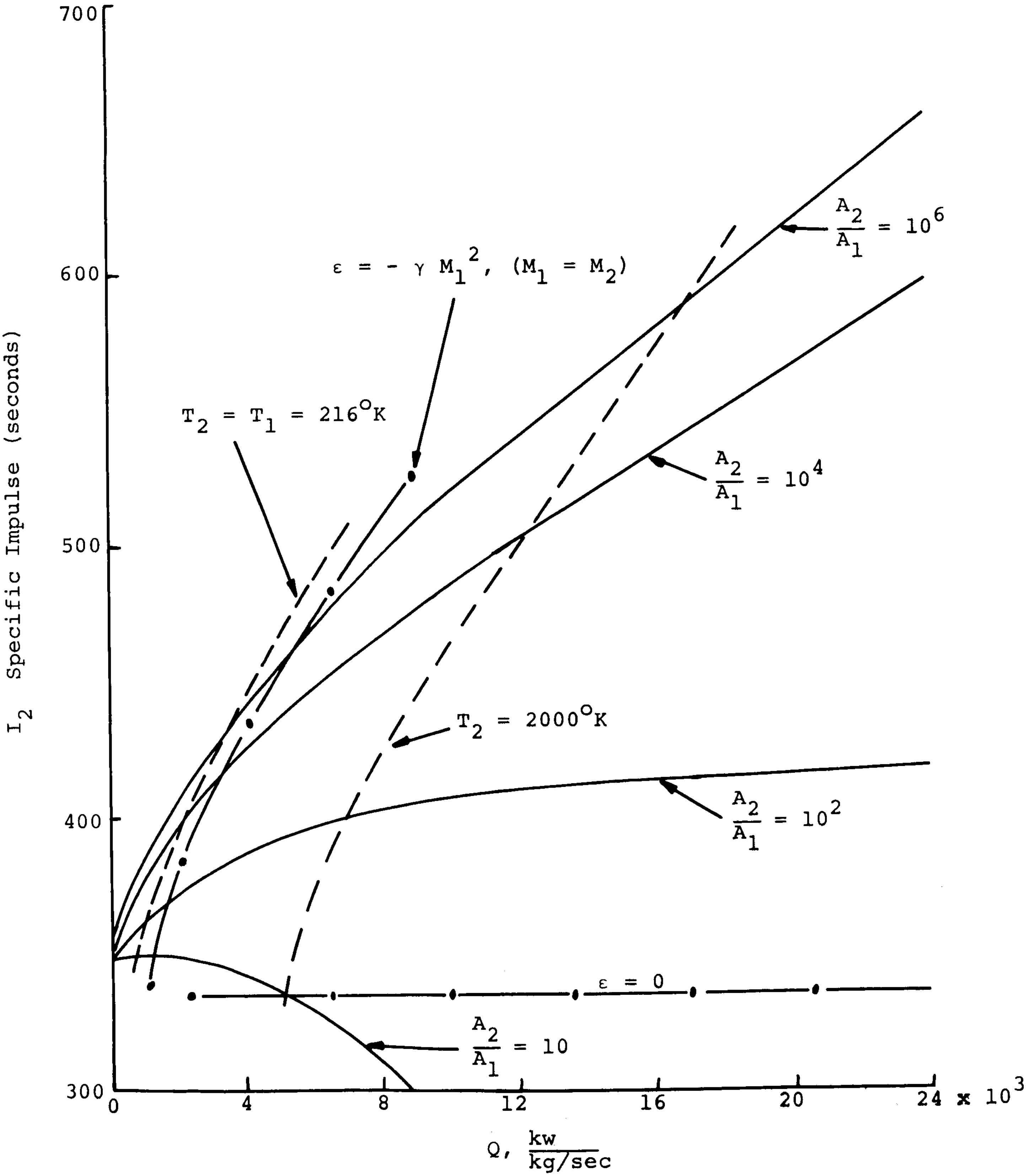

Figure 3.10. Solutions of Equations 3.23, 3.24, and 3.25 for the case $M_1 = 5.0$, $T_1 = 216^oK$, and $T_{01} = 2000^oK$. (I_1= 335 sec.)

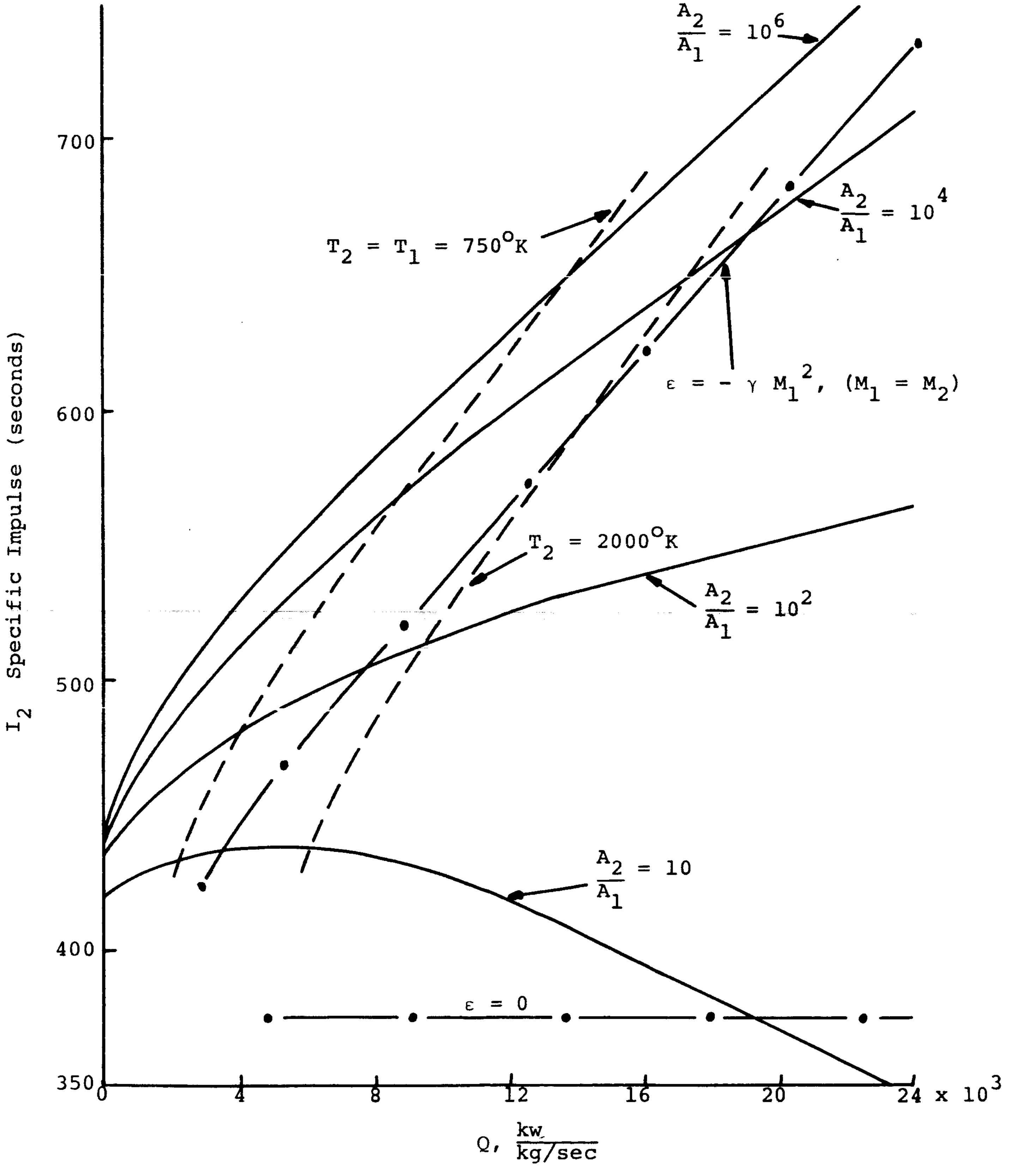

Figure 3.11. Solutions for Equations 3.23, 3.24, and 3.25 for the case $M_1 = 3$, $T_1 = 750^oK$, and $T_{01} = 3000^oK$. ($I_1 = 375$ sec.)

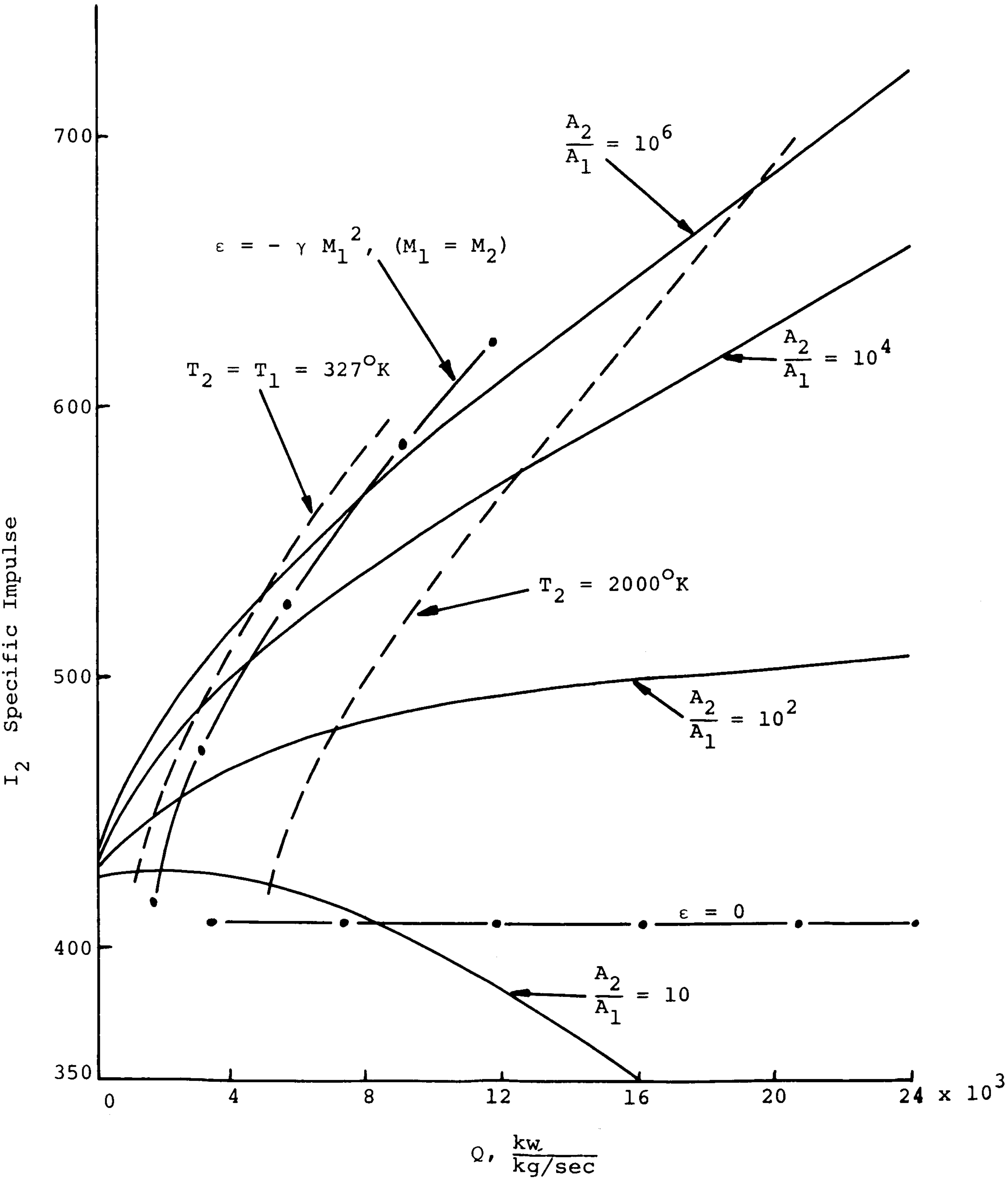

Figure 3.12. Solutions for Equations 3.23, 3.24, and 3.25 for the case $M_1 = 5.$, $T_1 = 327^\circ K$, and $T_{01} = 3000^\circ K$. ($I_1 = 410$ sec.)

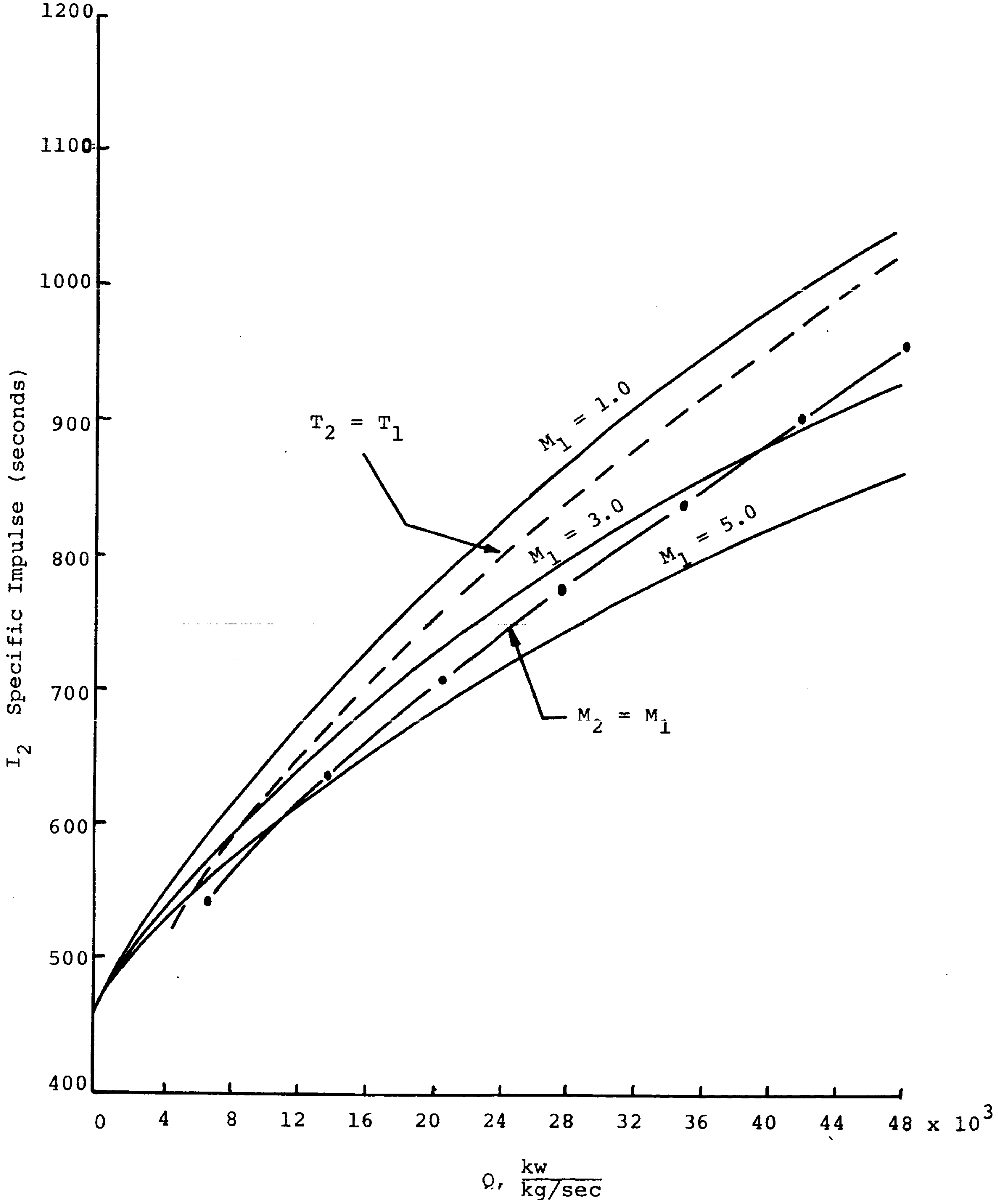

Figure 3.13. Solutions to Equations 3.23, 3.24, and 3.25 for the case $\frac{A_2}{A_1} = 10^6$ and $T_{01} = 3000^\circ K$.

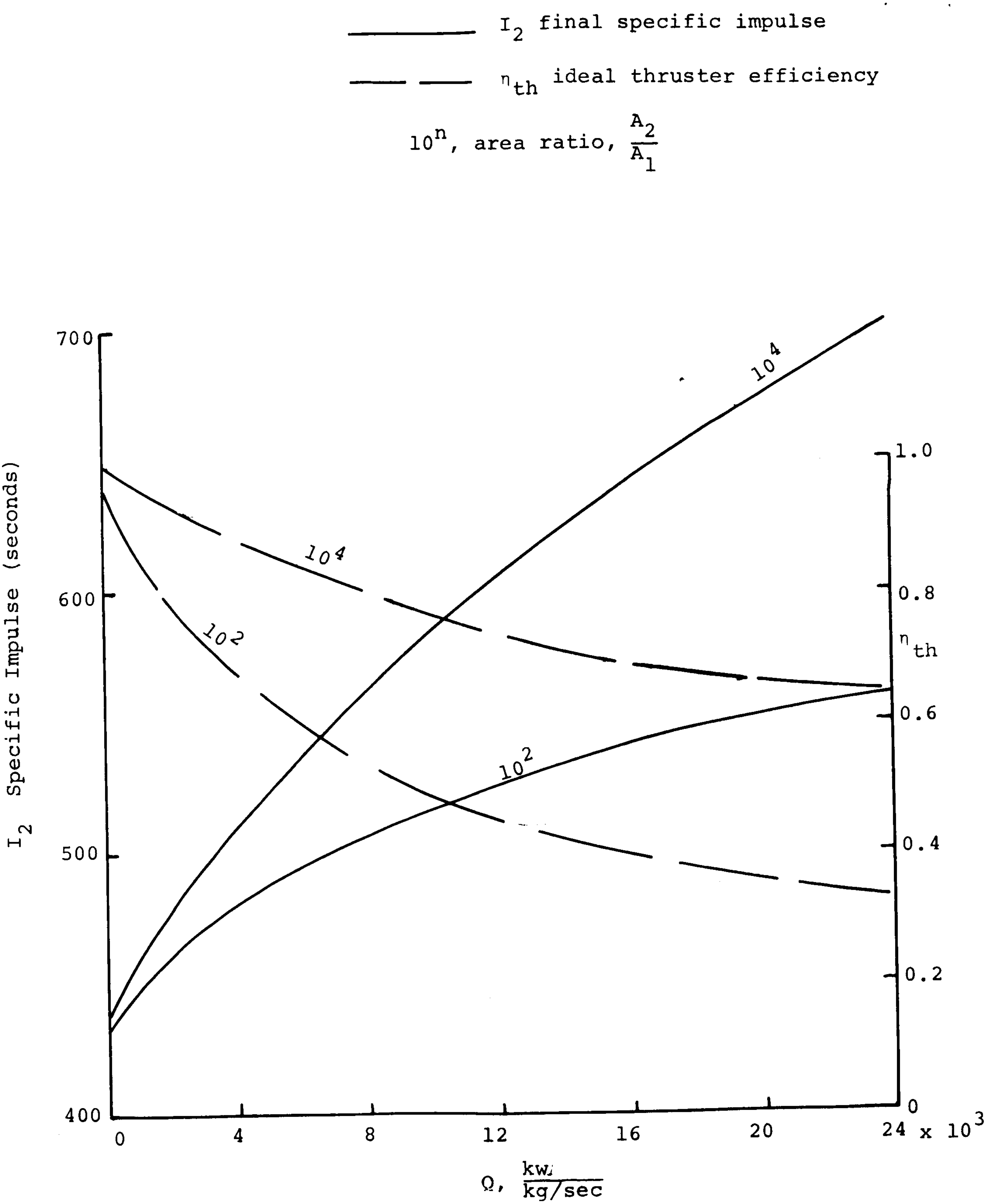

Figure 3.14. Solution to Equations 3.23, 3.24, 3.25, and 3.30 for the case $T_{01} = 3000^{\circ}K$, $M_1 = 3.0$.

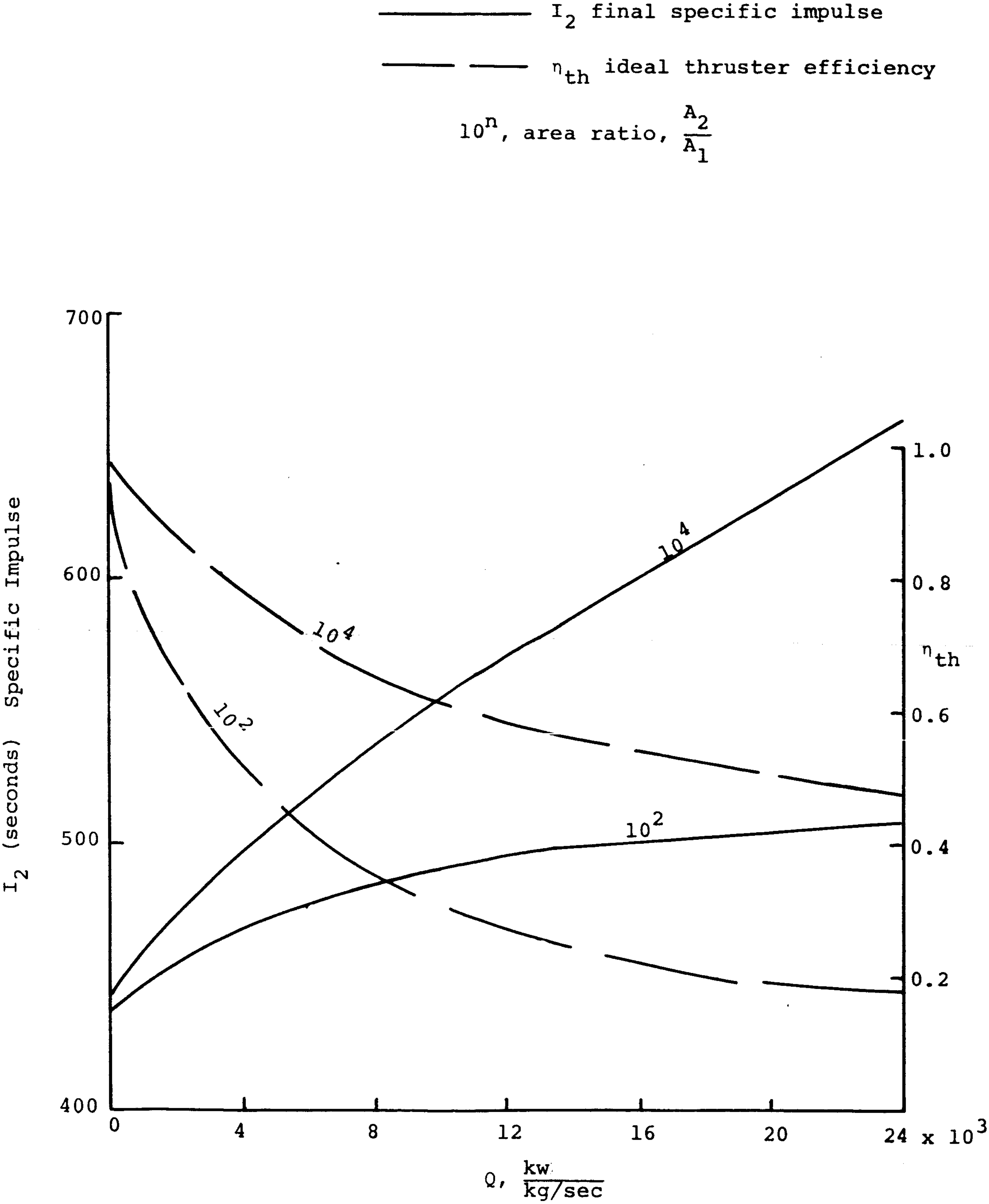

Figure 3.15. Solution to Equations 3.23, 3.24, 3.25, and 3.30 for the case $T_{01} = 3000^{\circ}K$ and $M_1 = 5.0$

N67-36945

FUNDAMENTAL PLASMA PROCESSES IN ELECTRON-BOMBARDMENT-THRUSTER IONIZATION CHAMBERS

by Rodney T. Hodgson, Dennis C. Fitzgerald,
and William R. Mickelsen

An experimental and theoretical program of investigation of the plasma characteristics of electron bombardment thrusters has been started. It is hoped that this program will lead to more detailed understanding of the processes taking place in these thrusters, and finally to development of a model which may be used to predict and optimize thruster performance.

"Ionization Probability" Distribution in an Electron Bombardment Thruster

In order to develop a feeling for the numbers and relations between the parameters in an electron bombardment thruster, some of the published data were cross-plotted and analyzed to give a representation of important properties such as electron temperature (T_e) spatial distribution and electron and ion density distributions (n_e and n_i). With these distributions, the probability distribution for ionization of a single neutral particle per unit time could be mapped out. With these data, various consistancy arguments may be followed through to see if the neutral efflux rate, ion production rate, etc. calculated from the microscopic data agree with the measured values.

The data used in the following analysis were taken from a paper by T. D. Masek[4.1]. A conventional Mercury electron bombardment thruster, and a "reversed current" cesium thruster were compared. The essential operating characteristics of these machines are reproduced in Table 4.1. The data for the density of the "Maxwellian" electrons in the mercury thruster are represented in Figure 4.1 in the form of a topographical map. Lines of equal normalized electron density are plotted as a function of the normalized axial and the normalized radial position in the thruster. Figure 4.2 depicts the energy of these "Maxwellian" electrons expressed in electron volts. Figures 4.3 and 4.4 show the density and energy of the "primary" electron group.

The rate of production of ions in a unit volume is given by an expression of the form:

$$\frac{dn_i}{dt} = n_o\, n_e \int_o^{\infty} \left[f(v_e)\right]\, v_e \left[Q_{e+}(v_e)\right] dv_e \qquad (4.1)$$

where n_o and n_e are the neutral particle and electron densities, $f(v_e)$ is the fraction of the electrons that have speeds in the range between v_e and $v_e + dv_e$, and $Q_{e+}(v_e)$ is the cross section for ionization by electron collision with a neutral particle. The probability of ionization per second for one neutral particle in the unit volume can be defined:

$$P(r,z) = \frac{1}{n_o}\frac{dn_i}{dt} = n_e \int_o^{\infty} \left[f(v_e)\right]\, v_e \left[Q_{e+}(v_e)\right] dv_e \qquad (4.2)$$

For the primary electrons, $f(v_e)$ is a δ function, and their contribution to $P(r,z)$ can be found easily if n_{e_p}, v_{e_p}, and $Q_{e+}(v_e)$ are known. To calculate the contribution of the "Maxwellian" electron group, the integral

$$\int_o^{\infty} \left[f(v_e)\right]\, v_e \left[Q_{e+}(v_e)\right] dv_e \equiv \Sigma_m$$

was taken from Figure 12 of reference 1. A topographical map of the contribution of the primary electrons to $P(r,z)$ is given in Figure 4.5, while the total probability is shown in Figure 4.6. The primary electrons have a much higher probability of ionizing the neutral particles near the anode than the maxwellian electrons. The results of analysis for the reversed current Cs thruster are shown in the plot of probability of ionization in Figure 4.7.

The number of neutral particles that leave the discharge chamber wall and travel to the screen grid without being ionized is of interest. Figure 4.8 shows the probability of ionization along a line straight across the chamber from one wall to the other through the center of the Hg discharge plotted as a function of the normalized radius position. The same graph also shows the probability of ionization for a path at 45° to the normal towards the screen grid. Using an analytic fit to the curve

$$P(r) = 7500 \cos^2 \left(\frac{\pi r}{2R}\right) \qquad , \sec^{-1}$$

we can calculate how many neutral atoms that leave the wall and follow a given path will be ionized.

The change in the flux $\dot{N}_o$ of a beam of neutral atoms over a distance dx is given by Equation (4.3)

$$d\dot{N}_o = - \dot{N}_o \, P \, \frac{dx}{v} \qquad , \sec^{-1} \text{cm}^{-2} \tag{4.3}$$

where P is the ionization probability per second for one neutral atom in a unit volume and v is the speed of the neutral atoms in the beam. The neutral atoms leaving the wall in a thruster can be considered in free molecular flow. Hence Equation (4.3) may be integrated considering v a constant

$$\int \frac{d\dot{N}_o}{\dot{N}_o} = - \frac{1}{v} \int P \, dx \tag{4.4}$$

The two paths chosen in Figure 4.8 have analytical expressions for P in terms of the dimensionless ratio r/R. Replacing dx by $\frac{R}{\cos\theta} \, d \left(\frac{r}{R}\right)$, (where θ is the angle the path makes from the normal as indicated in the inserted diagram of Figure 4.8), Equation (4.4) may be evaluated between the limits r/R = - 1 and r/R

$$\int_{r/R = -1}^{r/R} \frac{d\dot{N}_o}{\dot{N}_o} = - \frac{R}{v \cos\theta} \int_{r/R = -1}^{r/R} P \left(\frac{r}{R}\right) \, d \left(\frac{r}{R}\right) \tag{4.5}$$

$$\ln \frac{N_o(\frac{r}{R})}{N_o(\frac{r}{R} = -1)} = - \frac{7500\ R}{v \cos\theta} \frac{2}{\pi} \left[\frac{1}{2} \left(\frac{\pi}{2} \frac{r}{R}\right) + \frac{1}{2} \sin \left(\frac{\pi}{2} \frac{r}{R}\right) \cos \left(\frac{\pi r}{2R}\right) \right]_{\frac{r}{R} = -1}^{\frac{r}{R}} \qquad (4.6)$$

After applying the limits to the right side, the equation for N_o may be written:

$$N_o \left(\frac{r}{R}\right) = N_o \left(\frac{r}{R} = -1\right) e^{- \frac{7500}{v \pi \cos\theta} \left(\frac{\pi}{2} \left(1 + \frac{r}{R}\right) + \sin \left(\frac{\pi r}{2R}\right) \cos \left(\frac{\pi r}{2R}\right) \right)} \qquad (4.7)$$

The percent η that have been ionized at (r/R) is:

$$\eta = \left\{ \frac{N(\frac{r}{R} = -1) - N(\frac{r}{R})}{N(\frac{r}{R} = -1)} \right\} 100\% \qquad (4.8)$$

In the case of a straight path across the chamber $\cos\theta = 1$. If, for example, the percent ionized by the middle of the chamber $(\frac{r}{R} = 0)$ is wanted, the velocity is assumed to be $2.5 \times (10^4)$ cm/sec, (to correspond to a wall temperature of 500°K) and the radius of the chamber is 7.5 cm, the equation above yields a value of η of 67.5%.

The percent ionized as a function of the radial position for the two given paths is plotted in Figure 4.9. Note that only about 30% of the neutrals leaving at a 45° angle are ionized before they reach the screen grid. The remaining 70% of the neutrals would either pass through the screen grid or strike its surface.

Figure 4.10 is a plot of the probability of ionization per neutral per second for a given path in the Reversed Current Cesium Engine. Figure 4.11 is the calculated percent ionization over this path. The dashed line in Figure 4.10 shows a curve of the approximate analytical expression used. Note that the Reversed Current Cesium Engine has a much smaller fraction of the neutrals ionized than the Mercury Engine for the same path and neutral speed.

The ionization probability distribution may be used in consistency arguments. For example, if the neutral particle density (n_o) throughout the discharge volume is assumed constant, the neutral efflux from the screen grid could be used to find it.

ie $$\dot{n}_{0_{out}} = b \; \frac{1}{4} \; n_o \; \bar{v}_o \quad \pi R^2 \tag{4.9}$$

where $\dot{n}_{0_{out}}$ = the neutral particle efflux rate, b is a blockage factor at the screen grid, and R is the thruster radius. For the Hg thruster with 85% mass utilization efficiency, $\dot{n}_{0_{out}}$ = 31 ma.

Assume $\dot{v}_o \doteq 2 \times 10^4$ cm/sec, R = 7.5 cm and b = $\frac{1}{2}$, then

$$n_o = 4.5 \times 10^{11} \text{ cm}^{-3}$$

The ion production rate per unit volume per unit time is as given by Equation (4.2)

$$\frac{dn_i}{dt} = n_o \; n_e \int_o^\infty \{f(v_e)\} v_e \{Q_{e+}(v_e)\} \; dv_e$$

$$= n_o \; P(r,z)$$

The ion production rate over the whole volume is then

$$\frac{dN_i}{dt} = \int \frac{dn_i}{dt} \, dv = \int_{\text{volume}} n_o \; P(r,z) \; dv$$

$$= n_o \int_o^L dz \int_o^R P(r,z) \; 2\pi r \; dr$$

P(r,z) can be approximated by

$$P(r,z) \doteq 7500 \cos^2 \left(\frac{\pi r}{2R}\right) \qquad , \text{sec}^{-1}$$

hence the total ion production rate is

$$\frac{dN_i}{dt} = 2\pi L \; n_o \times 7500 \int_o^R r \cos^2 \left(\frac{\pi r}{2R}\right) dr$$

$$= 2\pi L \, n_o \times 7500 \times 0.15 \, R^2$$

$$= 1.8 \times 10^{18} \text{ sec}^{-1}$$

This is equivalent to 0.29 amperes which may be compared to the 3 amp arc current and the 0.21 amp beam current. This would mean that only $\frac{1}{40}$ of the available electron energy goes into ionization.

A more accurate analysis to calculate the total rate of production of ions taking the variation in neutral particle density into account is in progress. It is not inconceivable that nearly all of the ions formed could be extracted to the screen grid by the fields and pressure gradients in the plasma.

Current Density Distribution in an Electron Bombardment Thruster

Several detailed studies of the discharge mechanism and plasma conditions in an electron bombardment ion engine have been carried out[4.2-4.5]. Masek[4.1] has made a first attempt to develop an analytical model describing the factors affecting plasma properties. If a satisfactory model were found, factors such as propellant distribution, cathode position, and thruster geometry could be studied more generally by analytic methods than they are now studied analytically.

The investigations[4.1,4.6] have shown that further detailed experimental data are required to formulate and use such a model. Preliminary studies have been made of the feasibility of measuring the current density distribution in the bombardment chamber by measuring the changes in the magnetic field produced by these currents. The studies have shown that the data from such an experiment would be difficult to reduce to the interesting axial and radial current densities. However, they have shown that a large azimuthal current density (which has a large effect on the axial magnetic field) is produced.

Consider an idealized thruster ionization chamber in the form of an infinitely long cylinder with an impressed uniform axial magnetic field $\vec{B}_o$. The electric field $\vec{E}$ has a radial component, but the axial and aximuthal components are zero. Usually, when electric and magnetic fields in a plasma are crossed, if the electrons carry the current, the current density vector $\vec{j}$ forms an angle θ with the electric field vector $\vec{E}$, where

$$\tan\theta = \omega\tau$$

Here, ω is the gyrofrequency of the electron (eB/m), and τ is the mean time between collisions. If $\vec{E}$ has a component only in the radial direction, then

$$\tan\theta = j_\theta / j_r = \omega\tau,$$

and since $\omega\tau \doteq$ 100-1000 (in the Kaufman thruster using mercury described in Reference 4.1), the azimuthal component of the current density can be much greater than the radial component. As an example, we may estimate the components of the current density in the mercury thruster described in Reference 4.1.

$$j_r \doteq \frac{I}{2\pi RL} \qquad (4.10)$$

where j_r is the radial component of the current density, I is the arc current, R is the anode radius, and L is the anode length. Hence

$$j_\theta \doteq \frac{\omega\tau\ I}{2\pi RL} \qquad (4.11)$$

But then this j_θ produces a magnetic field B_z' which perturbs the impressed magnetic field B_z^o. This disturbance field may be estimated using Ampere's Law.

$$\int_{\text{closed loop}} \vec{B}\cdot d\vec{l} = \mu_o \text{ (current enclosed by loop)}$$

$$L\,B_z'(r) \doteq \mu_o\,L \int_o^r j_\theta\,dr$$

$$\doteq \mu_o\,L\,\frac{\omega\tau\ I}{2\pi RL}\,r$$

and

$$B_z' \ (R) \cong \mu_o \frac{\omega\tau \ I}{2\pi \ L}$$

$$= 6 \text{ gauss}$$

For the conditions that $\omega\tau = 100$, $I = 3$ amp, and $L = 10$ cm.

A more detailed iterative solution using the complete magnetic field distribution and taking the change of ω into account is not required. The importance of induced magnetic fields should, however, be recognized.

The estimation above does not take the ion currents nor the density gradients in the plasma into account. An estimation of the effects of these properties can be made from the equations of motion of the ions and electrons. After Spitzer[4.7], these equations may be written.

$$n_e \, m_e \left(\frac{\partial \vec{v}_e}{\partial t} + (\vec{v}_e \cdot \text{grad}) \right) \vec{v}_e = - n_e \, e \left(\vec{E} + \vec{v}_e \times \vec{B} \right) - \text{grad } P_e + P_{ei} \tag{4.12}$$

m_e and e are the electron mass and charge; n_e, P_e and $\vec{v}_e$ are the electron density, pressure, and drift velocity; and $\vec{P}_{ei}$ is a "friction" term to account for the momentum transfer between the electrons and the ions when they have different drift velocities. The same equation with the subscripts e and i interchanged and a positive $(\vec{E} + \vec{v} \times \vec{B})$ term may be used for the ions.

If we consider the same idealized thruster geometry, we may estimate the order of magnitude of each term in these equations from the measured densities and currents. Usually, $v_e >> v_i$ and the current is carried mostly by electrons. We may safely assume that $|\vec{j}_e| >> |\vec{j}_i|$ and

$$\vec{j} \equiv \vec{j}_e + \vec{j}_i \cong - n_e \, e \, \vec{v}_e$$

since we have shown that the total ion current must be less than 0.29 amperes compared with 3 amperes total current. Consider each term in the equation of motion for the electrons:

a) $n_e \, m_e \dfrac{\partial \vec{v}_e}{\partial t} \equiv 0$ in steady state operation

b) $n_e \, m_e \, (\vec{v}_e \cdot \mathrm{grad}) \, \vec{v}_e$

Assume $\vec{v}_e \doteq \vec{j}/n_e e$ and this term becomes

$$\doteq \frac{m_e}{n_e \, e^2} \; j_r \, \frac{\partial}{\partial r} \left(j_r \, \vec{e}_r + j_\theta \, \vec{e}_\theta \right)$$

since

$$\frac{\partial}{\partial z} = \frac{\partial}{\partial \theta} \equiv 0$$

If $j_r \doteq \frac{I}{2\pi RL}$, $j_\theta = \omega\tau \; j_r$, $n_e \doteq 3 \times 10^{17} \; m^{-3}$, then the two components of this term are

$$\doteq 7 \times 10^{-6} \left(\vec{e}_r + 100 \; \vec{e}_\theta \right)$$

joules/m^4

c) $n_e \, e \, \vec{E} = 3.4 \times 10^{-1} \; \vec{e}_r$, joules/m^4

for $E_r \doteq 7$ volt/m and $E_\theta = 0$

d) $n_e \, e \, (\vec{v}_e \times \vec{B})$

$$\doteq j_r \, B_z \left(\omega\tau \; \vec{e}_r + \vec{e}_\theta \right)$$

$$\sim 6.4 \left(\vec{e}_r + 10^{-2} \; \vec{e}_\theta \right) \; , \quad \text{joules/m}^4$$

if $B = 10^{-3}$ webers/m^2 and $\omega\tau = 10^2$

e) $\mathrm{grad} \; P_e = \frac{\partial P_e}{\partial r} \; \vec{e}_r$

This term may be approximated by

$$\frac{n_e k T_e}{R} \; \vec{e}_r$$

$= 6.4$ joules/m^4

for $n_e = 3 \times 10^{17} \; m^{-3}$: $\frac{kT}{e} \doteq 10$ e volt

f) $\vec{P}_{ei} \cong \eta \; n_e \; e \; \vec{j}$

where η is the resistivity of the plasma. From Spitzer[4.7]

$$\eta = 6.53 \times 10^{3} \; \frac{\ln\Lambda}{T^{\frac{3}{2}}} \; \text{ohm-cm}$$

$$\ln \Lambda = 12, \; T_e = 10^{5} \; (^{o}K)$$

$$\eta = 2.5 \times 10^{-5} \; \text{ohm-m}$$

and $P_{ei} = 7.6 \times 10^{-5} \left(\vec{e}_r + 100 \; \vec{e}_\theta\right)$

The results of these estimations are repeated in Table 4.2.

It is clear that a large azimuthal current density is the only means by which the electron density pressure gradient can be supported.

Fast-Neutral-Atom Model for an Electron-Bombardment Thruster

An averaging technique may be used to produce analytical results with little experimental data. In this way, the gross effect of one parameter on another may be more easily calculated with a relatively crude model. The following section uses a model of the electron bombardment thruster to calculate the mass utilization ratio as a function of the average neutral-atom speed, several geometry factors, and the averaged electron velocity.

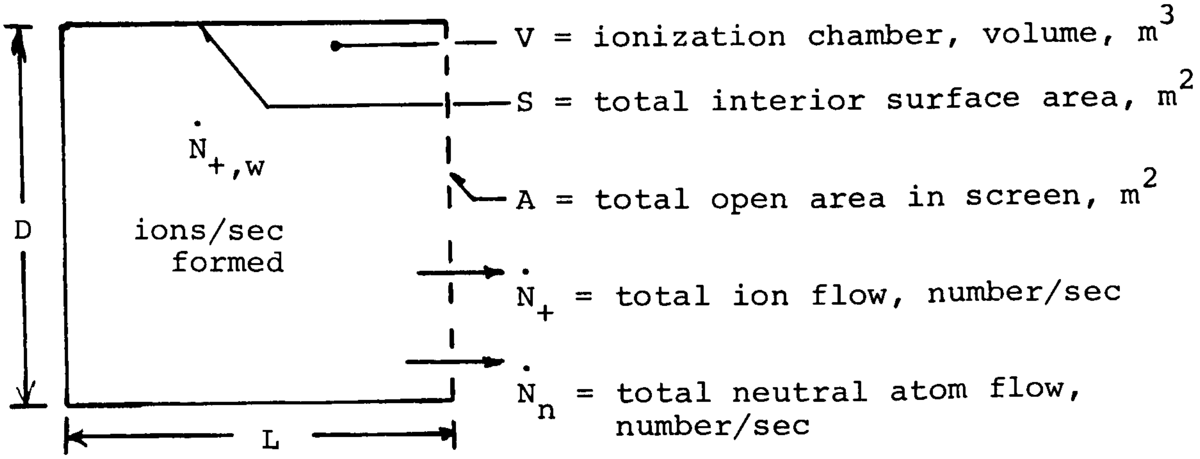

V = ionization chamber, volume, m^3

S = total interior surface area, m^2

A = total open area in screen, m^2

$\dot{N}_+$ = total ion flow, number/sec

$\dot{N}_n$ = total neutral atom flow, number/sec

In this model, it is assumed that fresh propellant atoms entering with thermal speeds constitute only a small portion of the total neutral atom flow in the chamber. This assumption is supported by the calculations reported in Reference 4.8 which show that less than about 8% of the neutral atoms entering through a ring-shaped injector in the rear wall can reach screen grid holes in a direct line-of-flight. The remaining 92% will either be ionized or will hit an interior surface.

It is further assumed that neutral atoms have greater than thermal energies, except for the very small portion (of neutral atom total population) which has just entered the chamber from the injector. Another assumption is that the neutral atoms leave the interior surfaces with much greater than thermal energy. A mechanism for high neutral atom energy has been proposed in Reference 4.9 in which ions falling from the plasma to the interior surfaces impart some of their energy to neutral atoms adsorbed on the surface. Neutral atoms leave the surface by this mechanism with energies much higher than thermal energy. With such high energy, it is possible that atoms continue in essentially molecular flow even after being ionized by electron bombardment.

With the foregoing assumptions, the analysis can proceed.

The number of ions/second $\dot{N}_{+,w}$ falling onto the interior surface S is:

$$\dot{N}_{+,w} = \dot{N}_{+,V} - \dot{N}_{+} \tag{4.13}$$

By the assumption of molecular flow:

$$\dot{N}_{+,w} = \frac{1}{4} n_+ v_+ S \tag{4.14}$$

and:

$$\dot{N}_{+} = f_+ \frac{1}{4} n_+ v_+ A \tag{4.15}$$

where f_+ is a factor to account for directed flow of ions toward the screen grid holes. The factor f_+ must be greater than unity. Directed flow is achieved by controlling the plasma potential field with magnetic and electrostatic means. From Equations (4.14) and (4.15):

$$\frac{\dot{N}_{+,w}}{\dot{N}_{+}} = \frac{1}{f_+}\frac{S}{A} \tag{4.16}$$

The number if ions/second $\dot{N}_{+,V}$ being formed in the ionization chamber is:

$$\dot{N}_{+,V} = n_- \; v_- \; \sigma \; n_n \; V \tag{4.17}$$

where n_- and v_- are electron number density and speed respectively, σ is the ionization cross-section, and n_n is the neutral-atom number density. Neutral atoms/second $\dot{N}_{n,w}$ leaving the interior surface S is:

$$\dot{N}_{n,w} = \frac{1}{4} \, n_n \; v_n \; S \tag{4.18}$$

Combining Equations (4.17) and (4.18):

$$\dot{N}_{+,V} = n_- \; v_- \; \sigma \; V \; \frac{4 \, \dot{N}_{n,w}}{v_n S} \tag{4.19}$$

and using Equation (4.13) in Equation (4.19)

$$\frac{4 \, n_- \; v_- \; \sigma \; V}{v_n \; S} \, \dot{N}_{n,w} = \dot{N}_{+,w} + \dot{N}_{+} \tag{4.20}$$

Of the neutral atoms/second $\dot{N}_{n,w}$ leaving the surface S, a number/second $\dot{N}_{+,V}$ will be ionized. This leaves $\dot{N}_{n,w} - \dot{N}_{+,V}$ neutral atoms/second in molecular flow in the chamber. Neutral atoms leaving the chamber each second are denoted by $\dot{N}_n$, and can be related to $\dot{N}_{n,w} - \dot{N}_{+,V}$ by a form factor f_n (i.e., a view factor for molecular flow):

$$f_n \; (\dot{N}_{n,w} - \dot{N}_{+,V}) = \dot{N}_n \tag{4.21}$$

An estimate of the form factor f_n can be obtained from Reference 4.10. For L/D = 1 and a 50% screen-grid blockage, $f_n < 0.2$. Equations (4.20) and (4.21) can be combined:

$$\frac{4 \, n_- \; v_- \; \sigma \; V}{v_n \; S} \left(\frac{\dot{N}_n}{f_n} + \dot{N}_{+,V} \right) = \dot{N}_{+,w} + \dot{N}_{+} \tag{4.22}$$

Equation (4.13) can be used again to replace $\dot{N}_{+,V}$ in Equation (4.22):

$$\frac{4\, n_-\, v_-\, \sigma\, V}{v_n\, S}\left(\frac{\dot{N}_n}{f_n} + \dot{N}_{+,w} + \dot{N}_+\right) = \dot{N}_{+,w} + \dot{N}_+ \qquad (4.23)$$

rearranging equation (4.23):

$$\frac{4\, n_-\, v_-\, \sigma\, V}{v_n\, S}\;\frac{N_n}{f_n} = (\dot{N}_{+,w} + \dot{N}_+)\left(1 - \frac{4\, n_-\, v_-\, \sigma\, V}{v_n\, S}\right) \qquad (4.24)$$

from which:

$$\frac{\dot{N}_n}{\dot{N}_+} = \frac{f_n\, v_n\, S}{4\, n_-\, v_-\, \sigma\, V}\left(\frac{\dot{N}_{+,w}}{\dot{N}_+} + 1\right)\left(1 - \frac{4\, n_-\, v_-\, \sigma\, V}{v_n\, S}\right) \qquad (4.25)$$

Using Equation (4.16):

$$\frac{\dot{N}_n}{\dot{N}_+} = \frac{f_n\, v_n\, S}{4\, n_-\, v_-\, \sigma\, V}\left(\frac{1}{f_+}\,\frac{S}{A} + 1\right)\left(1 - \frac{4\, n_-\, v_-\, \sigma\, V}{v_n\, S}\right) \qquad (4.26)$$

or:

$$\frac{\dot{N}_n}{\dot{N}_+} = f_n\left(\frac{1}{f_+}\,\frac{S}{A} + 1\right)\left(\frac{v_n\, S}{4\, n_-\, v_-\, \sigma\, V} - 1\right) \qquad (4.27)$$

Assuming that $n_- = n_+$, and using Equation (4.15) for n_+ in Equation (4.27):

$$\frac{\dot{N}_n}{\dot{N}_+} = f_n\left\{\frac{1}{f_+}\,\frac{S}{A} + 1\right\}\left\{\frac{f_+\quad S/V}{16\, v_-\, \sigma}\;\frac{1}{\dot{N}_+/A}\; v_n^{\,2} - 1\right\} \qquad (4.28)$$

References

4.1. Masek, T. D.: Plasma Characteristics of the Electron Bombardment Ion Engine. Proceedings of 2nd International Conference on Electron and Ion Beam Science and Technology, April 19, 1966, in New York.

4.2. Strickfaden, W. B. and Geiler, K. L.: Probe Measurements of the Discharge in an Operating Electron Bombardment Ion Engine. AIAA Journal, Vol. 1, p. 1815-23. 1963.

4.3. Masek, T. D., and Kerrisk, D. J.: Plasma Characteristics for Mercury and Cesium Bombardment Ion Engines. SPS No. 37-32. Vol. IV pp. 141-150. Jet Propulsion Laboratory, Pasadena, California. (Feb. 1965)

4.4. Masek, T. D.: Plasma Studies in the Electron Bombardment Engine. SPS 37-42. Vol. IV, pp 131-138. Jet Propulsion Laboratory, Pasadena, California.

4.5. Masek, T. D.: Plasma Investigation in a Reversed Current Electron Bombardment Ion Engine. AIAA Journal **4**, 692-698, 1967.

4.6. Masek, T. D.: Plasma Studies in the Electron Bombardment Engine - Magnetic Field Effects. SPS 37-44 Vol. IV.

4.7. Spitzer, L.: Physics of Fully Ionized Gases. Interscience Publishers, New York, (1956).

4.8. Richley, E. A., and Mickelsen, W. R.: Effects of Molecular Flow in Plasma Generation and Some Analyses of Space Charge Flow in Ion Acceleration. AIAA Preprint No. 64-7. January, 1964.

4.9. Knauer, W., Hagen, G., Gallagher, H., and Stack, E.: Investigation of the Discharge in Electron Bombardment Thrusters. AIAA Paper No. 66-244. March, 1966.

4.10. Richley, E. A., and Bogart, C. D.: Numerical Solutions of Knudsen Flow Entering a Circular Tube Through a Small Axial Orifice. NASA TN D-2115. February, 1964.

Table 4.1

	Conventional Mercury Thruster	Reversed Current Cesium Thruster
Anode Radius	7.5 cm	5 cm
Anode Length	10.5 cm	6.3 cm
Magnetic Field Strength	~10 gauss	5 gauss
Arc Current	3.0 amp.	11.75 amps
Arc Voltage	45 volts	9.45 volts
Ion Beam Current	210 ma.	183 ma.
Accel Voltage	3.5 kv	3.2 kv
Decel Voltage	-2.0 kv	-2.0 kv
Propellant Flow rate	1.9 gm/hr	1.08 gm/hr
Mass Utilization Efficiency	85%	82%

Table 4.2

Term	r component	θ component
	$\frac{\text{joules}}{m^4}$	$\frac{\text{joules}}{m^4}$
a) $n_e m_e \frac{\partial \vec{v}_e}{\partial t}$	0	0
b) $n_e m_e (\vec{v}_e \cdot \text{grad}) \vec{v}_e$	7×10^{-6}	7×10^{-4}
c) $n_e e \vec{E}$	3.4×10^{-1}	0
d) $n_e e (\vec{v}_e \times \vec{B})$	6.4	6.4×10^{-2}
e) grad P_e	6.4	0
f) $\vec{P}_{ei}$	7.6×10^{-5}	7.6×10^{-3}

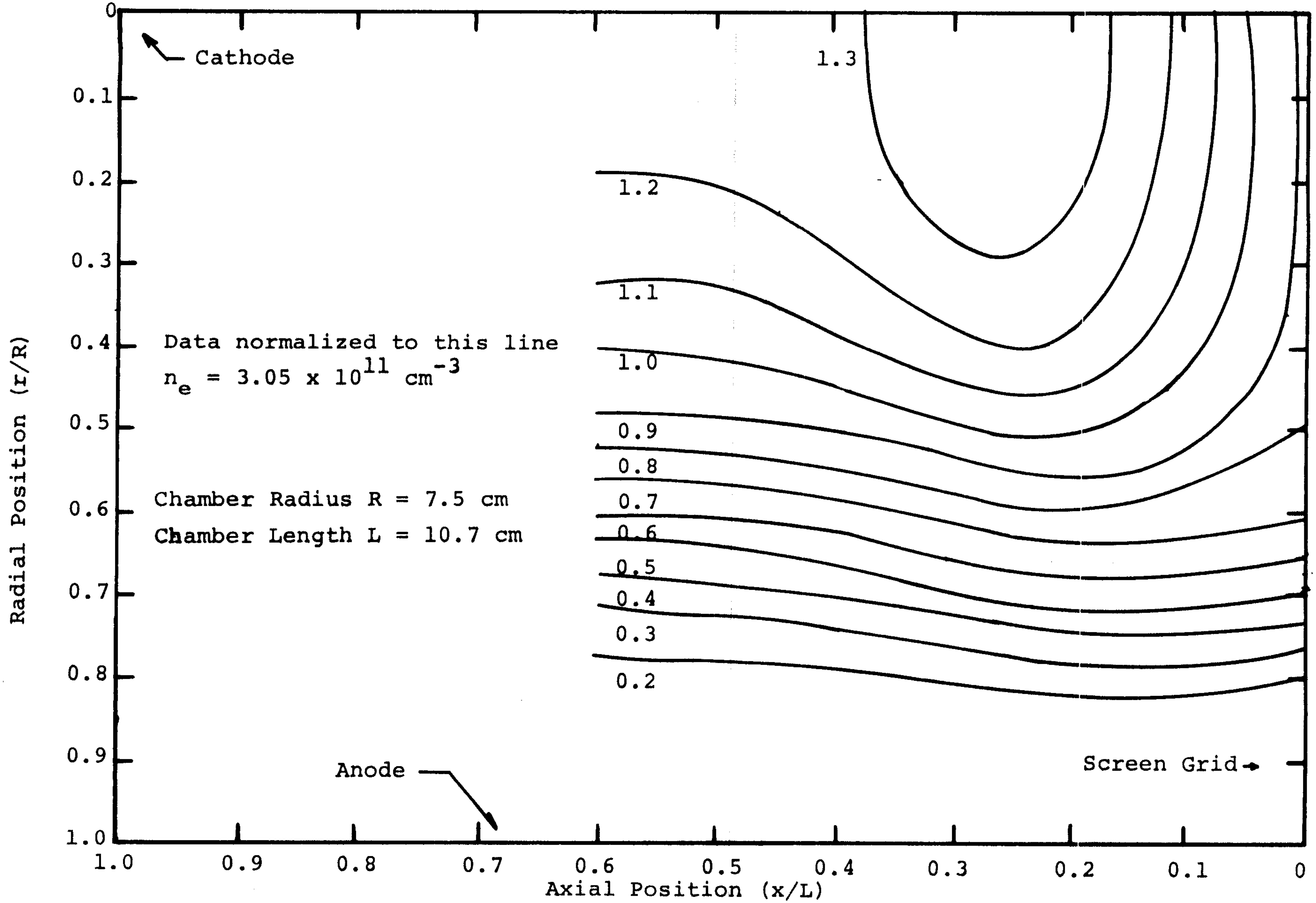

Figure 4.1. Normalized "Maxwellian" Electron Density Distribution in Hg Thruster.

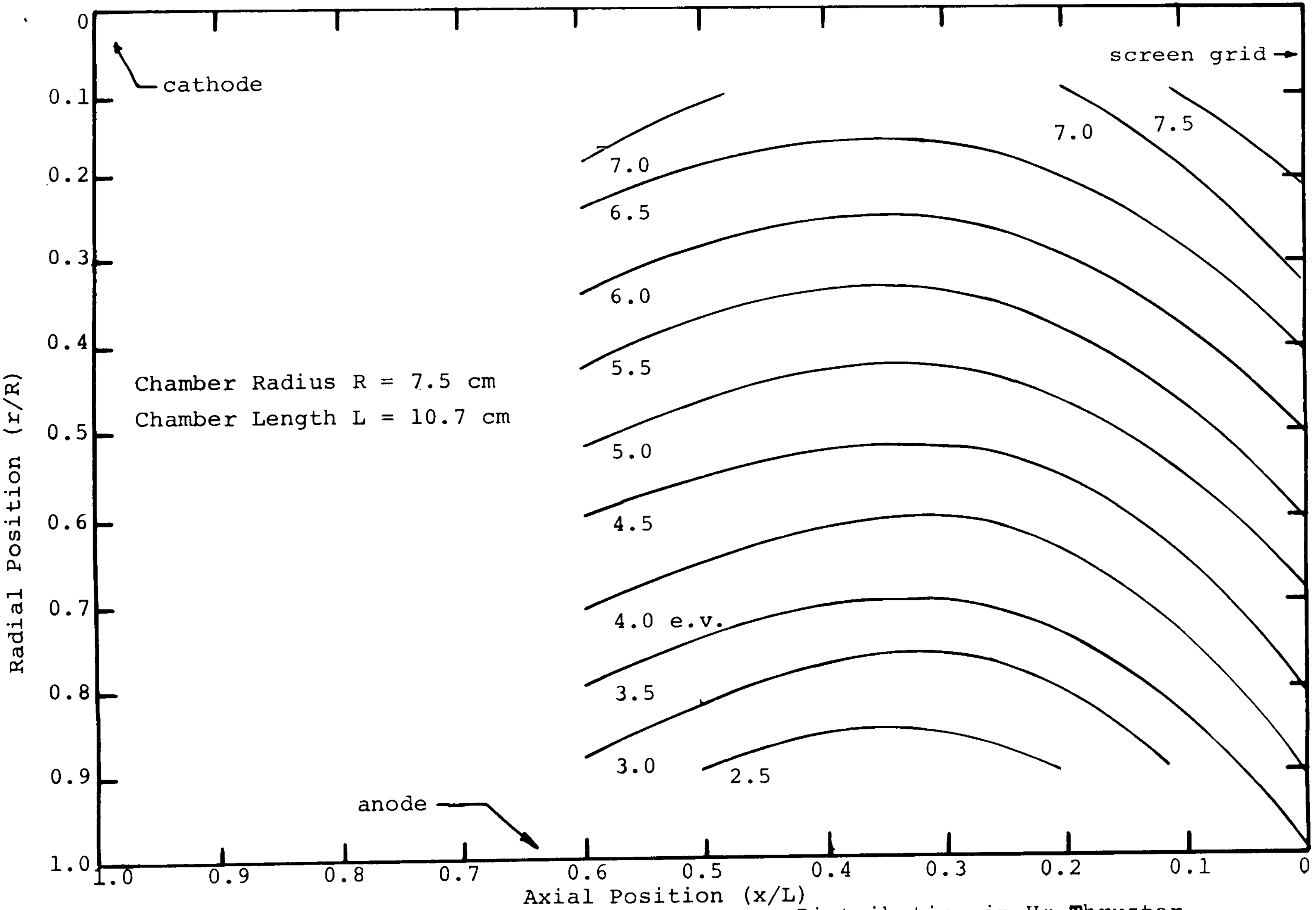

Figure 4.2. "Maxwellian" Electron Energy Distribution in Hg Thruster.

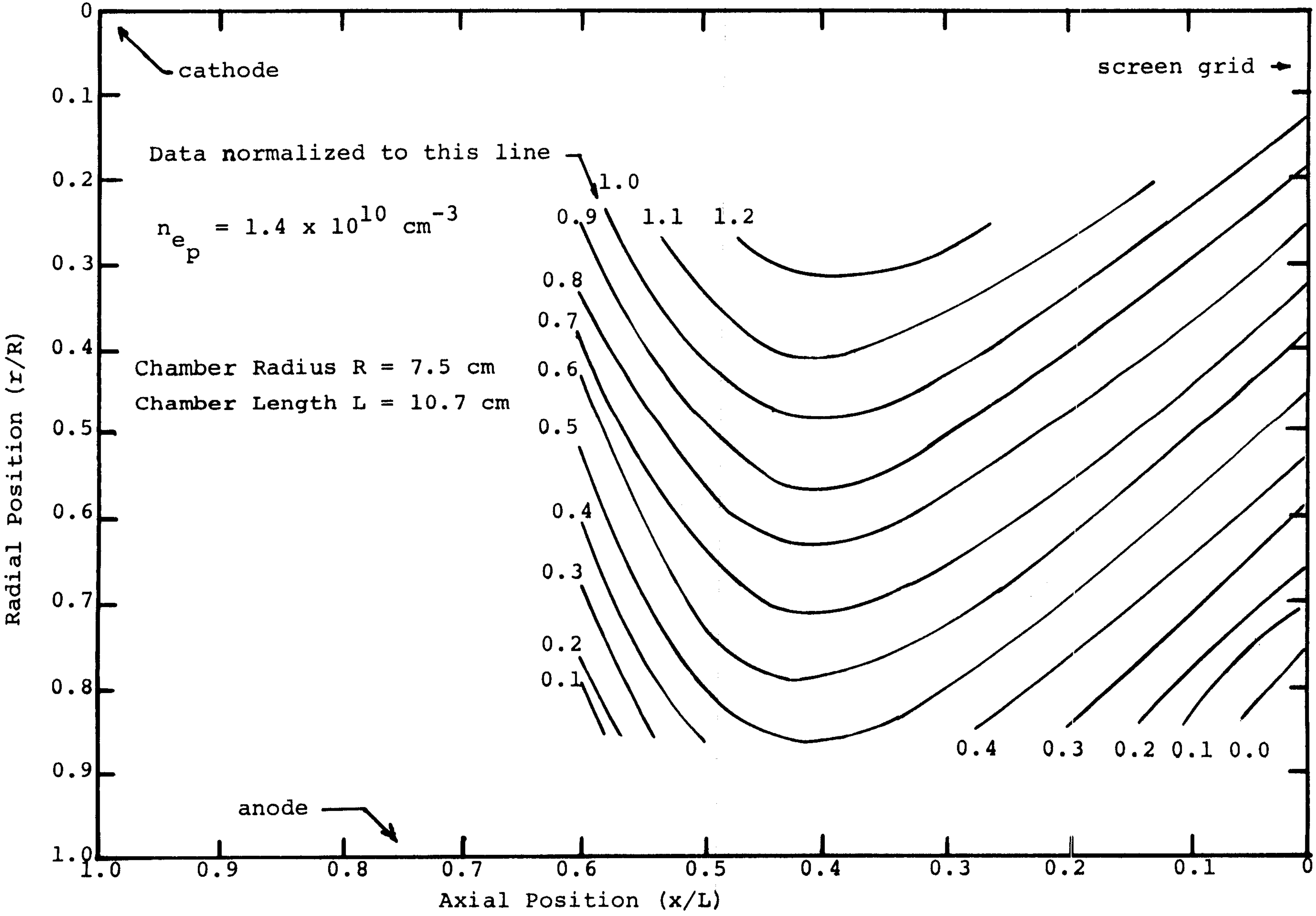

Figure 4.3. Normalized "Primary" Electron Density Distribution in Hg Thruster.

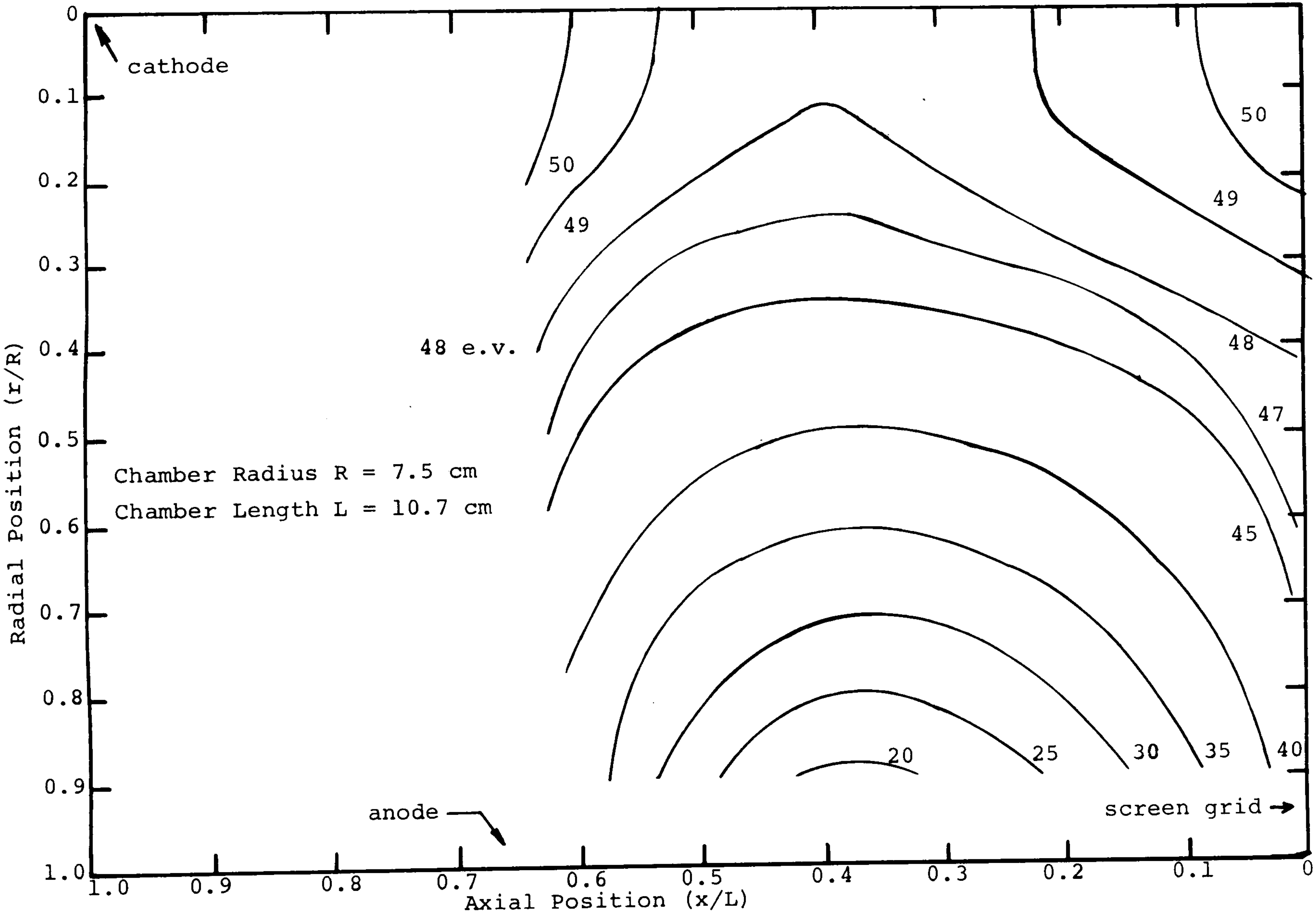

Figure 4.4. "Primary" Electron Energy Distribution in Hg Thruster.

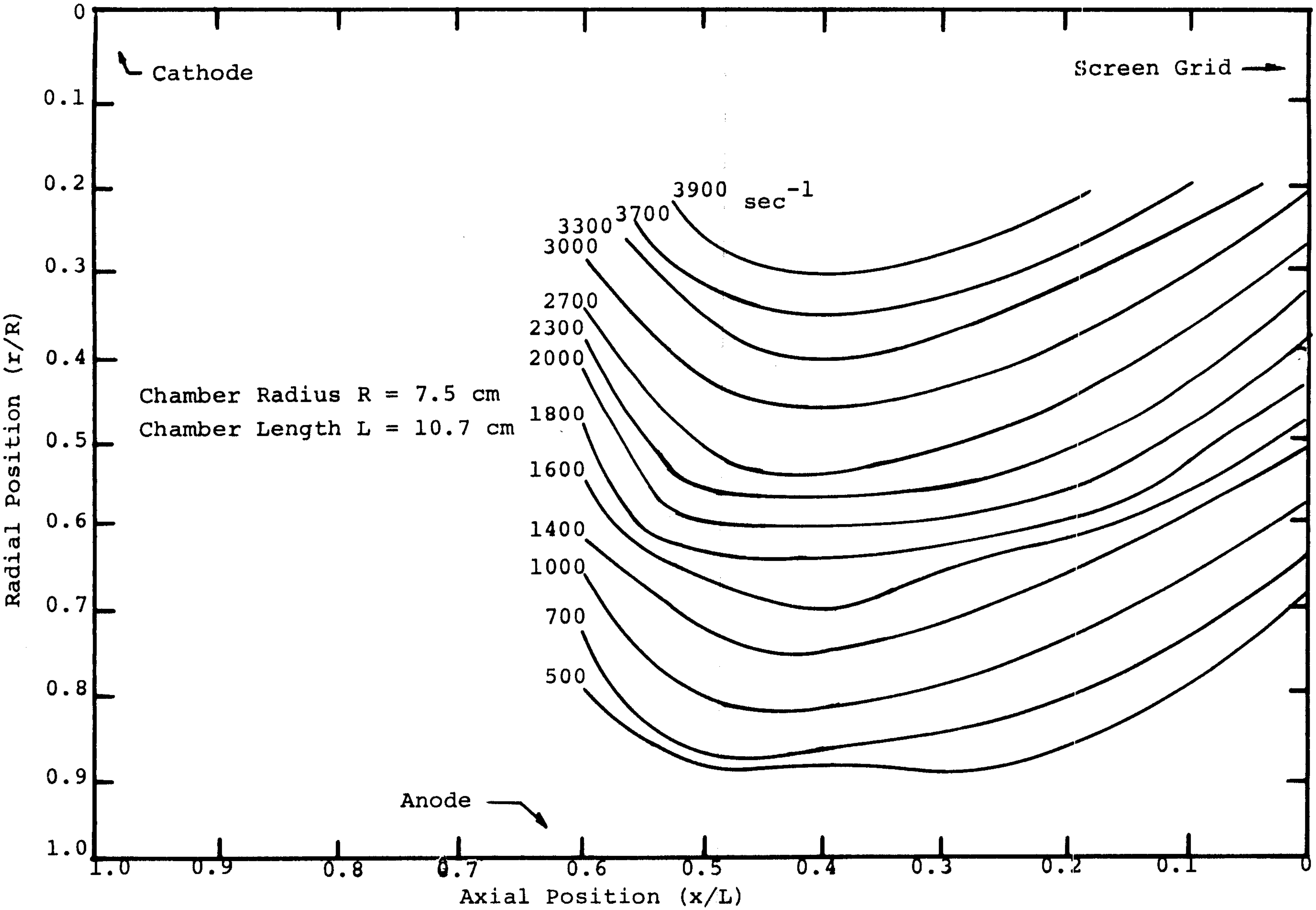

Figure 4.5. Probability of Ionization from "Primary" Electrons in Hg Thruster.

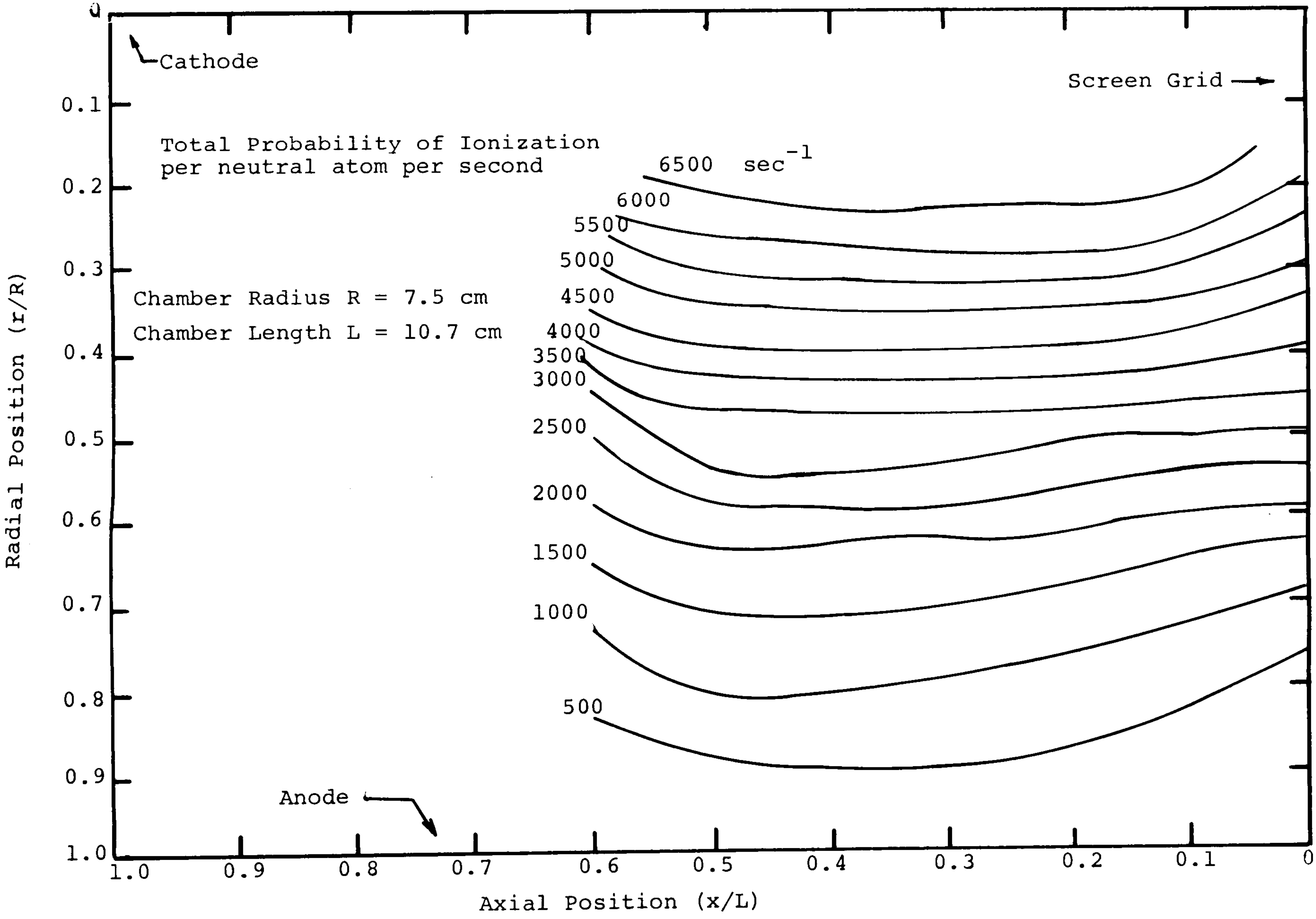

Figure 4.6. Total Probability of Ionization in Hg Thruster.

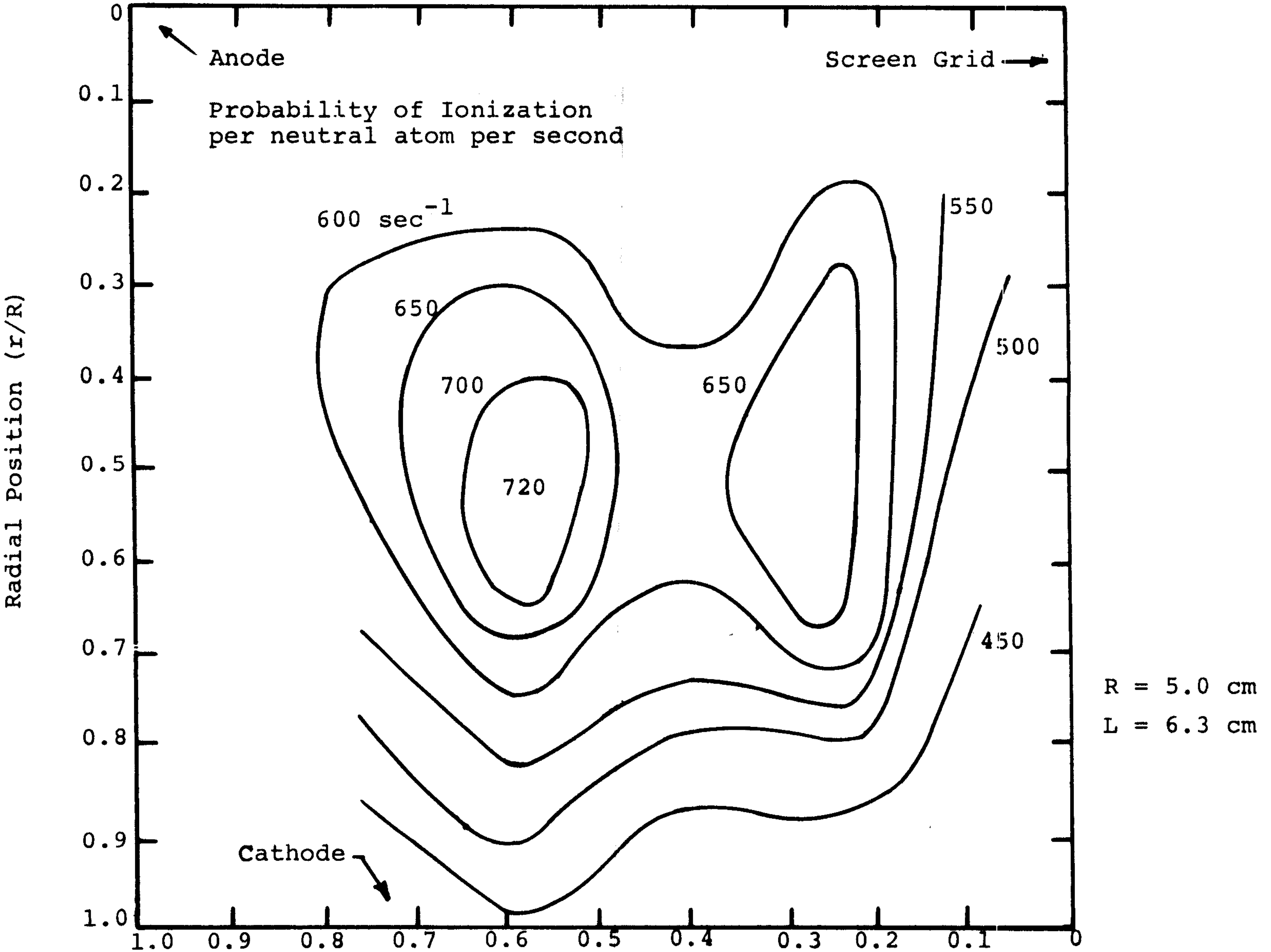

Figure 4.7. Total Probability of Ionization in "Reversed Current" Cesium Thruster.

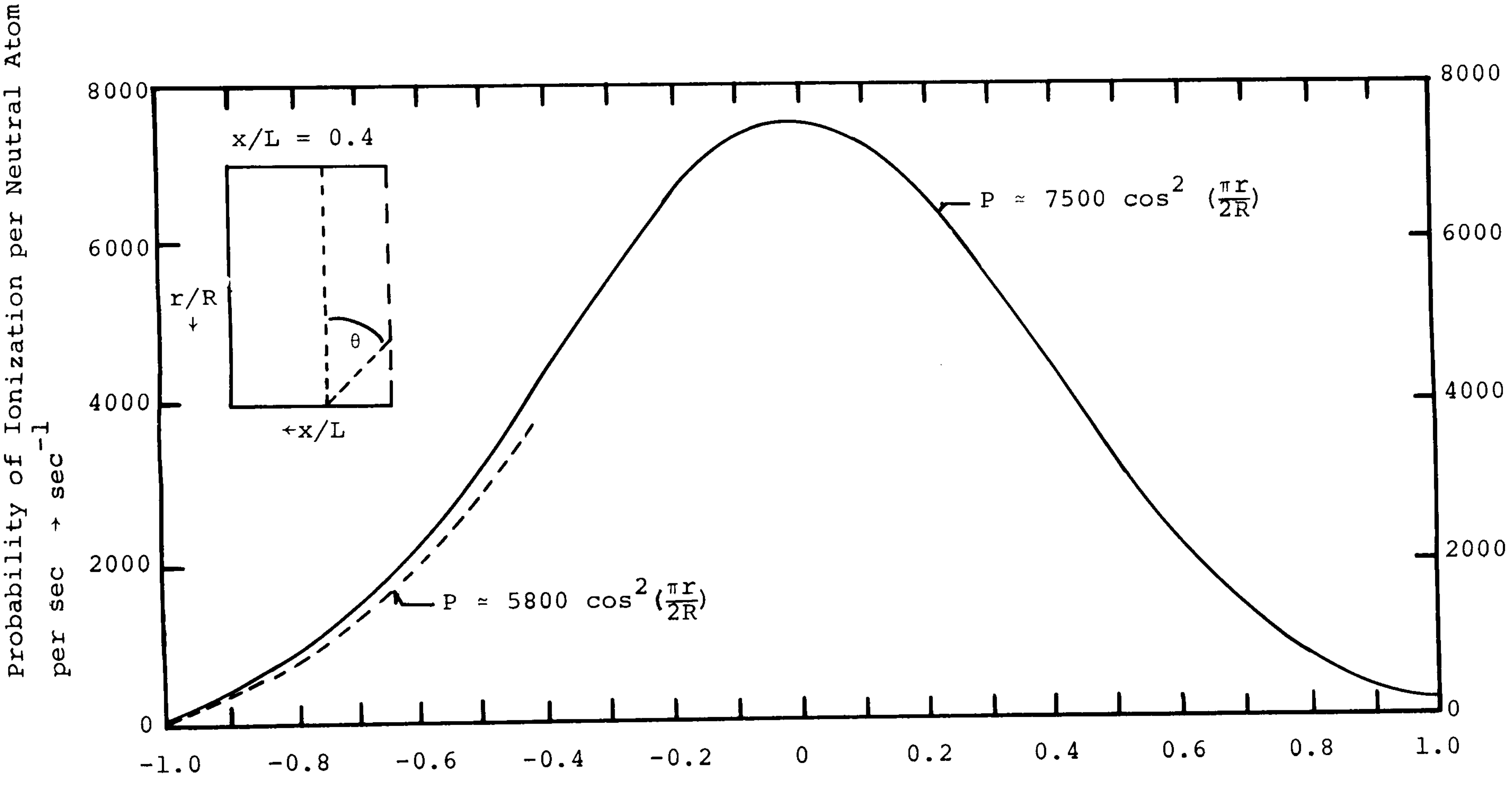

Figure 4.8. Probability of Ionization for Two Different Paths Followed by a Neutral Atom in Hg Thruster.

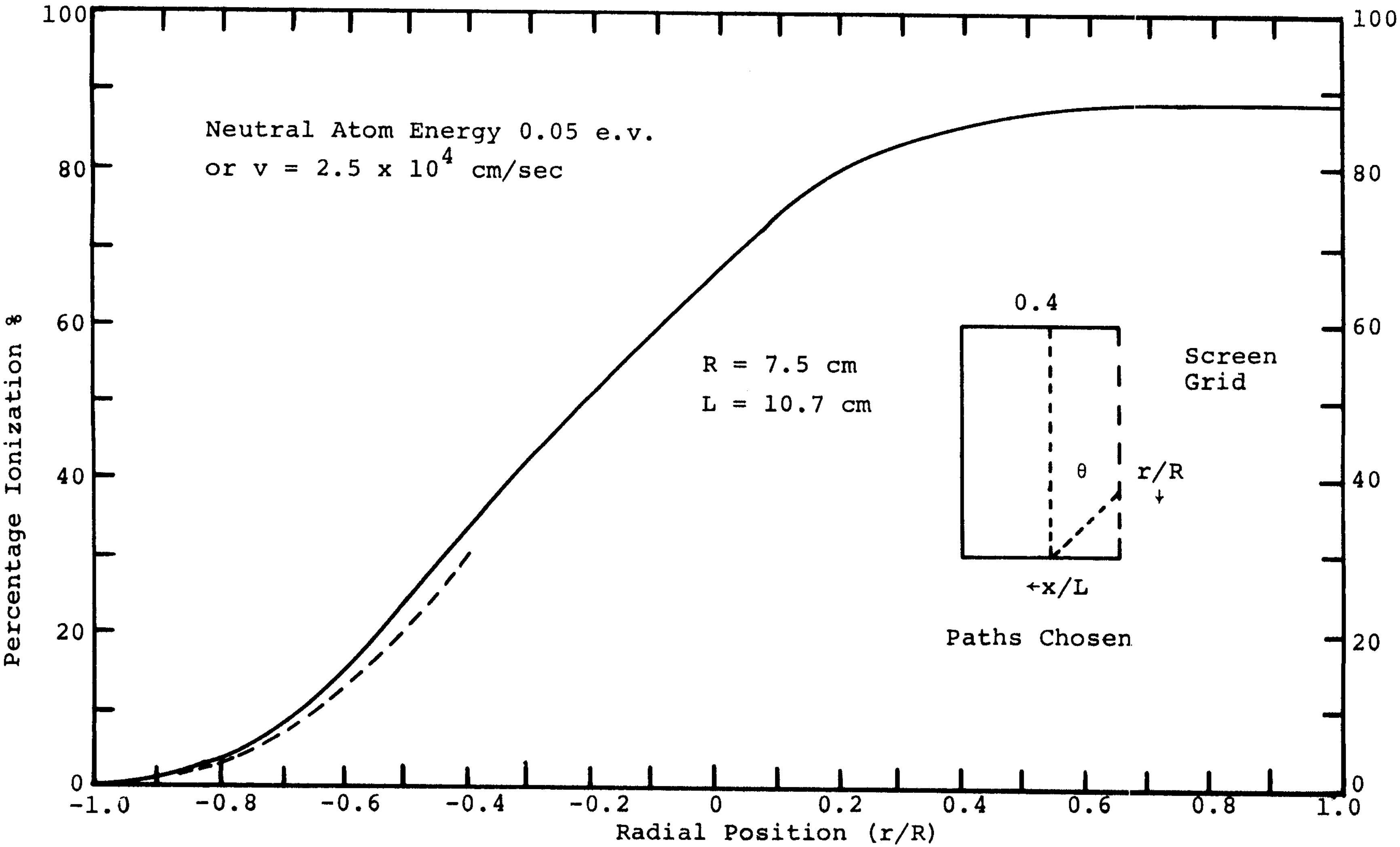

Figure 4.9. Percentage Ionization for Neutral Atoms Following Two Different Paths in Hg Thruster.

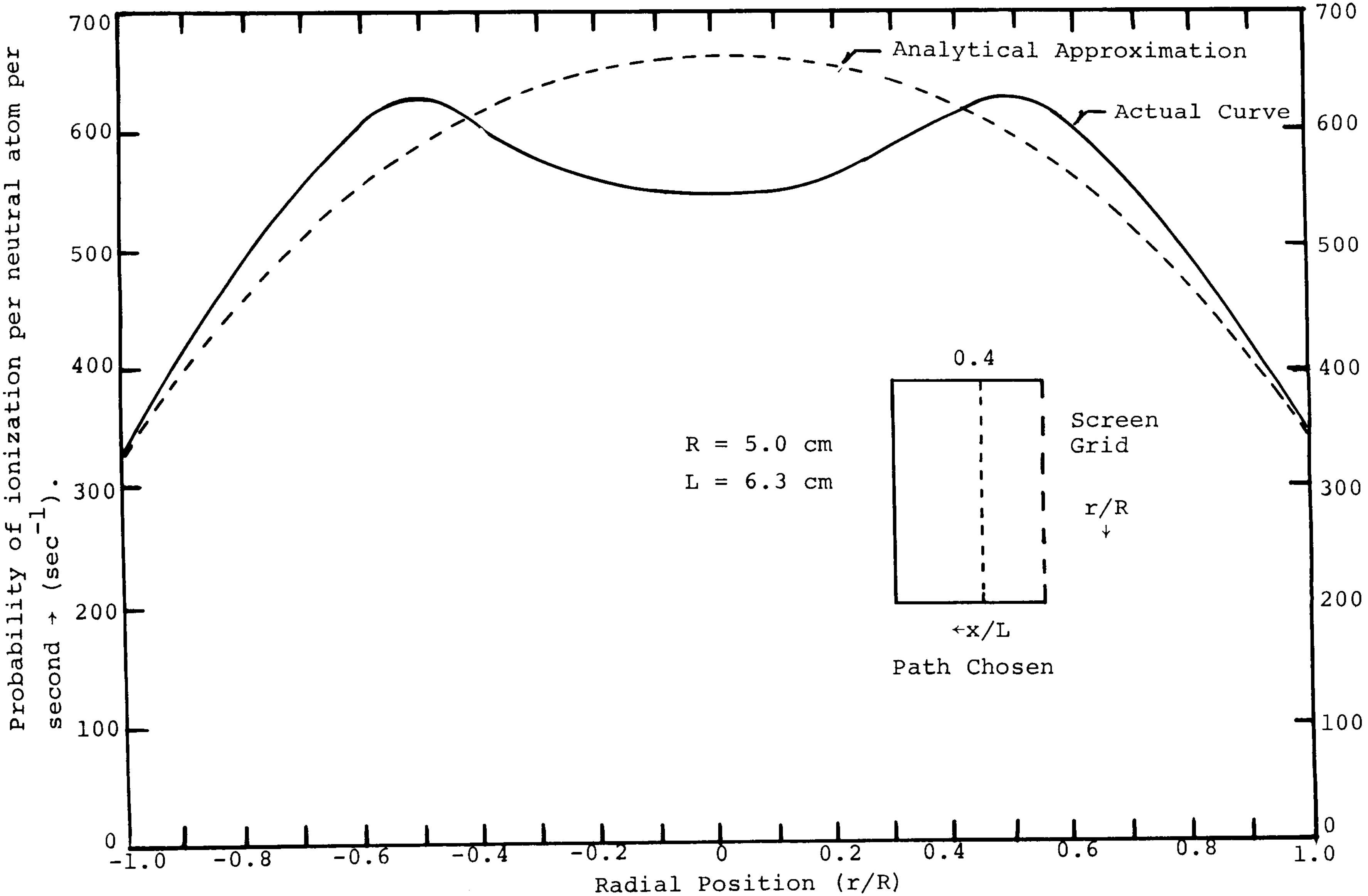

Figure 4.10. Probability of Ionization for One Path Followed by a Neutral Atom in Cs "Reversed Current" Thruster.

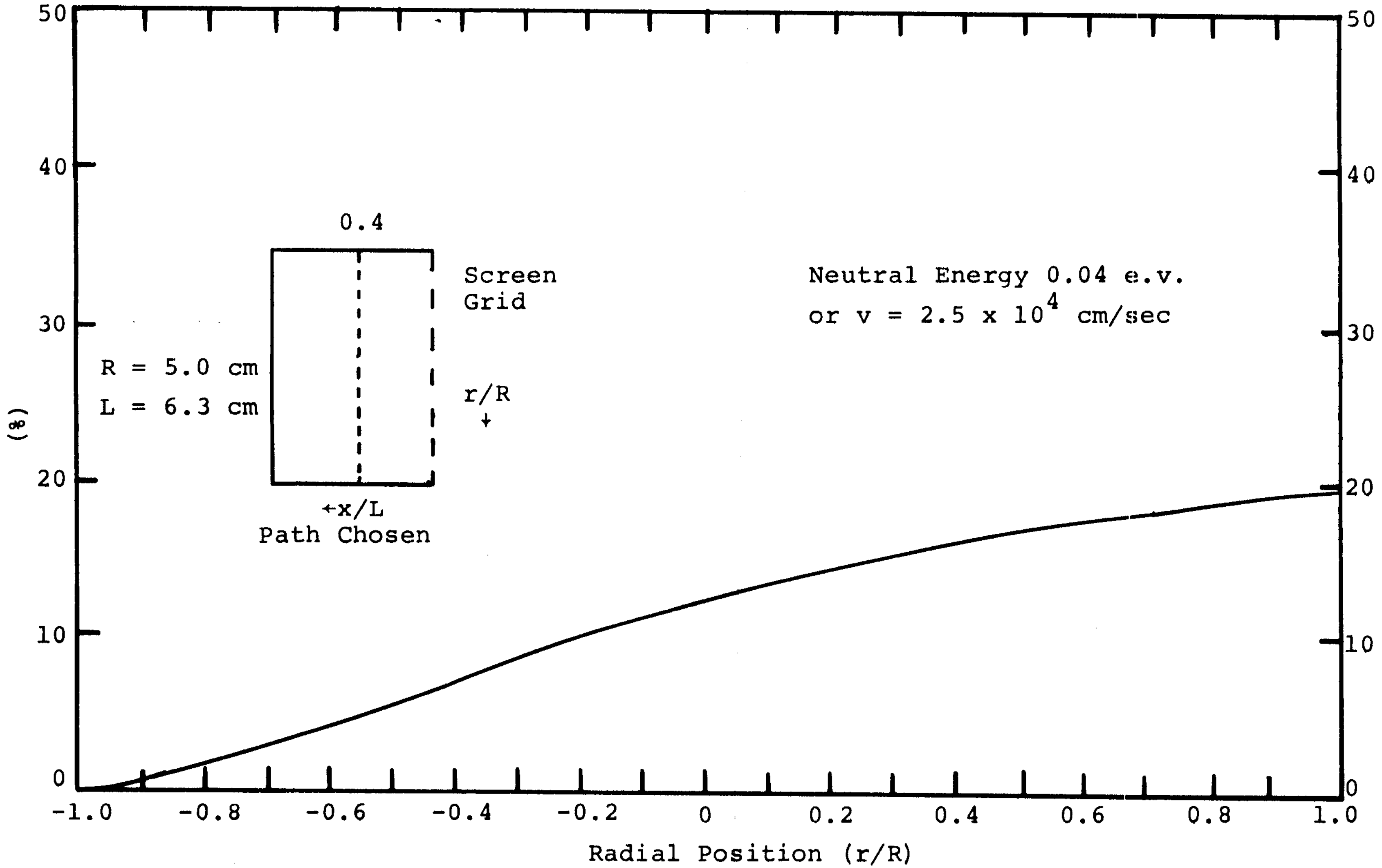

Figure 4.11. Percentage Ionization for Neutral Atoms Following a Path in Cs "Reversed Current" Thruster.

DETECTION OF HIGH VELOCITY NEUTRAL ATOMS IN AN ELECTRON BOMBARDMENT IONIZATION CHAMBER

by Rodney T. Hodgson and Richard Moore

Energy many times the ionization energy is required to produce each ion in the beam of an electron bombardment thruster. Analysis such as those presented in the last section of Chapter 4 of this report and in Reference 5.1 show that high speed neutral atoms in the discharge chamber could contribute to the high power requirements.

High speed neutral atoms would have a much higher probability of reaching the screen grid without being ionized than the lower speed neutral atoms. In order to keep the propellant utilization efficiency at a reasonable level, then the arc current and voltage would have to be raised to increase the electron density and energy, and thus the probability of ionization. In addition, if high speed neutral atoms are ionized, they would follow their original paths (if their energy in electron volts is greater than the potential difference in the plasma) and have a high probability of hitting the walls and losing their energy.

A mechanism for producing high speed neutral atoms has been proposed by Knauer[5.1]. Ions would fall through the potential sheath separating the plasma and the container. They would acquire, for example, energy of 10 ev at the anode, and 55 ev at the back wall or screen grid of the Hg thruster mentioned in Reference 5.1. It is possible that they impart some of this energy to an absorbed neutral atom in a sputtering like process. Such low energy impact phenomena on gas covered surfaces have not been studied extensively[5.2].

If high speed neutral atoms exist in the discharge chamber, it is possible that they would be reflected several times from the walls and could finally escape from the screen grid. Kaminsky[5.2] gives data on ion reflection from metal surfaces, but it is questionable whether a neutral atom with 1-5 ev energy will behave like an ion when it impinges on a surface. Kaminsky[5.2] quotes data on the accomodation coefficient of low energy Hg atoms impinging on a platinum surface. The atoms collide inelastically with the walls, and come off again with the surface temperature.

In April, an experimental program to detect high speed neutral particles was started. A refined velocity selector method has been devised to sort out high speed from low speed neutral atoms. In principle, the device works like two rotating disks with holes out of alignment by a certain amount. Only those particles with a certain range of velocities parallel to the axis of rotation can pass through both the holes.

In practice, several techniques have been used to increase signal, and decrease background and noise. The two discs have been replaced by a solid aluminum cylinder with grooves cut in the outside surface. In this way, a practically continuous stream of selected particles come through instead of one pulse each revolution.

A photograph of the velocity selector without driving motor is shown in Figure 5.1. A schematic diagram of the device in place is given in Figure 5.2.

A Kaufman thruster has been received from the Jet Propulsion Laboratory in Pasadena, California, and will be mounted in one of the 15 inch diameter bell jars of the C.S.U. cryogenic vacuum tank. A 1/4" hole will be drilled in the side of the device to let the neutral particles escape. The electrons and ions will be sorted out with charged screens. After the neutral particles pass the velocity selector, they will be detected with an ionization gauge. Preliminary calculations of the expected signal and the background signal indicate that an input chopper and phase sensitive detector may have to be used to increase signal to background and signal to noise ratio. The number of neutral atoms entering the detector from the vacuum tank has been decreased by making their inlet path with essentially a large length to diameter ratio. The blades of the velocity selector will act as a pump as they spin at right angles to the inlet mouth of the ion gauge, and so few of the background gas molecules may enter the detector through the holes.

The rotating cylinder was machined from solid aluminum by the Colorado Gear Co., Denver. The grooved section is 3" diameter, 4" long, with 23 slots equally spaced around the circumference.

Each slot is 1/2" deep with 1/16" material between one slot and the next. A 1/8" thick, 3.5"diameter circular disk with 23 1/4" holes is screwed onto the back end of the rotating cylinder. Spacers keep this disk 3/1000" from the stationary support post. A 1/4" I.D. line will run from the hole in the support post to the ion gauge outside the vacuum tank.

The cylinder may be rotated with a Globe MM-16 D.C. motor modified for high vacuum operation. With a great drive, the cylinder may be run up to 22,000 r.p.m. to discriminate against neutral atoms with energies less than about 2 e.-volts. A cylinder with spiral grooves may be used to measure an accurate velocity distribution at lower energies.

At this time, the motor, gears, and cylinder have been mounted. Preliminary testing and speed calibration will be done soon, and the preliminary experiments with manual interruption of the beam may be run as soon as the thruster is operating.

References

5.1. Knauer, W., Hagen, G., Gallagher, H., and Stack, E.: Investigation of the Discharge in Electron Bombardment Thrusters. AIAA Paper No. 66-244, March, 1966.

5.2. Kaminsky, M.: Atomic and Ionic Impact Phenomena on Metal Surfaces. Academic Press, New York. (1965).

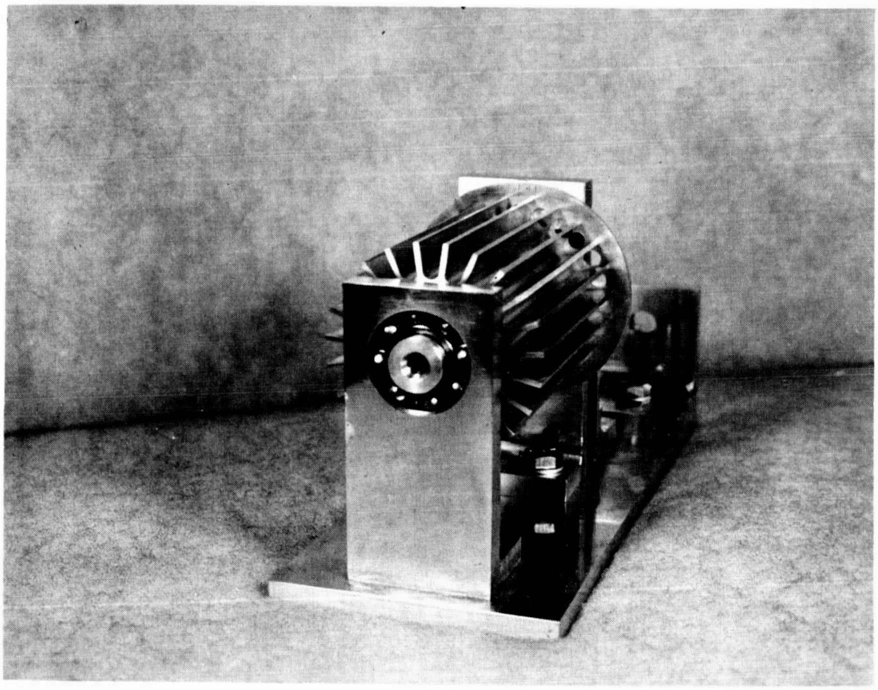

Figure 5.1. Photograph of Velocity Selector.

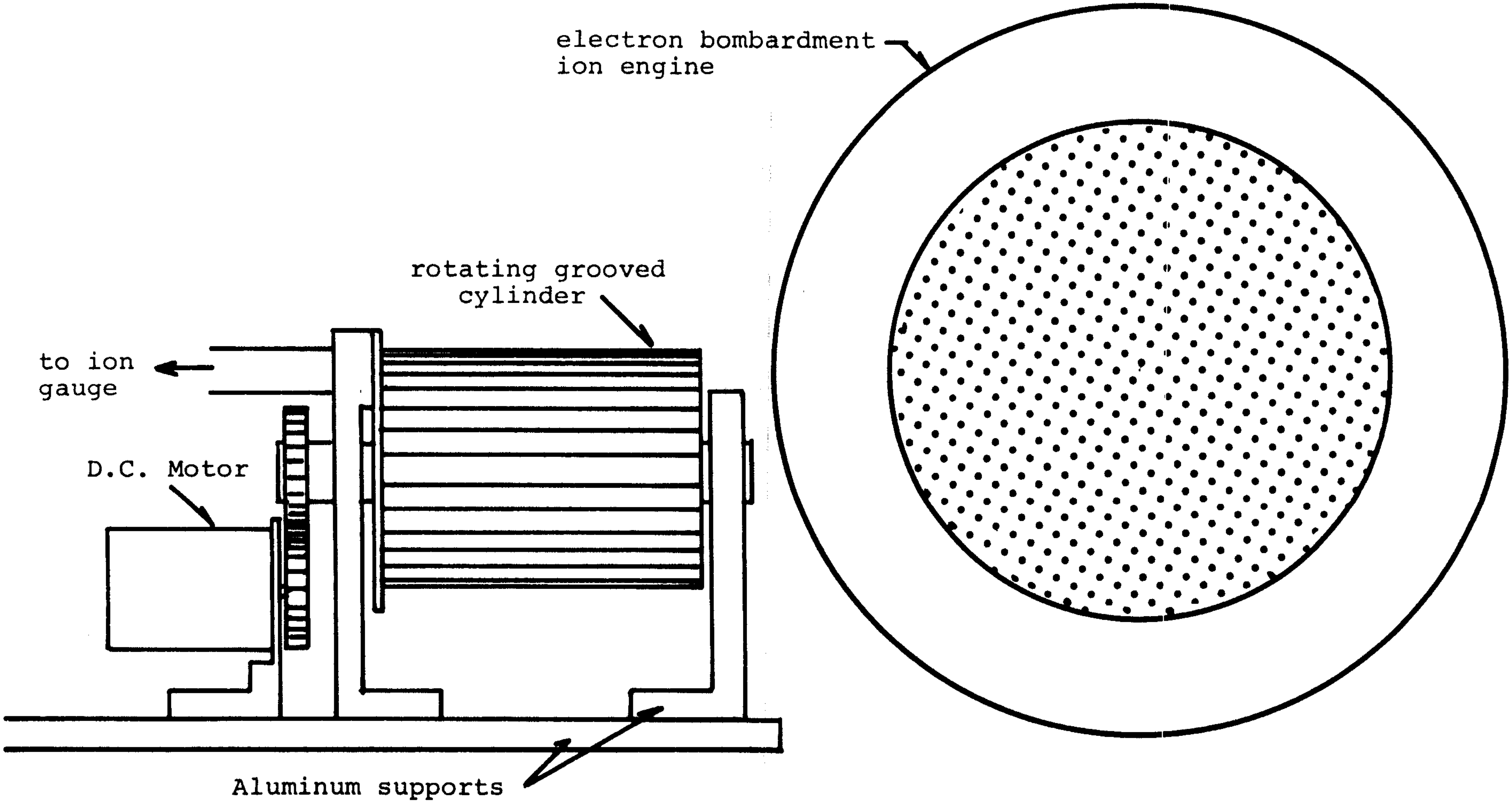
electron bombardment ion engine
rotating grooved cylinder
to ion gauge
D.C. Motor
Aluminum supports

Figure 5.2. Schematic Diagram of Velocity Selector

N67-36946

APPROXIMATE METHODS IN ELECTRIC PROPULSION MISSION ANALYSIS

by W. R. Mickelsen and C. B. Winn

A considerable amount of work has been done in low-thrust trajectory analysis. Essentially all of this work has been with the patched-conic approximation, but has provided digital computer programs and trajectory data with about 1-2% accuracy. Digital programs of this kind require considerable time between definition of input and receipt of legible output. In addition, the mission analyst is not provided conveniently with an intimate knowledge of the variation of all parameters throughout the mission profile. More complex trajectory analysis such as optimized three-dimensional n-body programs with 0.1% accuracy, or double-precision three-dimensional n-body full-parameter-optimization programs, will provide even less insight, flexibility, and speed for the mission analyst. A simple, fast, and flexible analysis method is needed for preliminary mission analysis.

An ideal program, or method, for those working in electric propulsion should have certain characteristics. In the interest of providing these characteristics, accuracy could be sacrificed; for example an accuracy of 10% in payload would be adequate. The method should be analytic if possible, although some graphical interpolation would be acceptable. If the method were entirely analytic, then the ease in understanding would result in ease of modification of the method. The feature of easy modification would be of great importance in analyzing missions with unusual profiles.

An essential characteristic is that the method be independent from the accurate methods. Some simple and fast methods have been developed, but these depend on results obtained from the accurate trajectory analyses. To provide true flexibility, only the fundamental properties of the solar system should be necessary for evaluation of any mission profile.

Approximate optimization of the mission profile should be straightforward, and should provide a direct insight into the relative merits of various trade-offs. This feature would make it possible to compare various electric propulsion systems for each particular mission profile, or to compare various combinations of propulsion systems. A straightforward optimization procedure would also provide means for evaluating the performances of each component in the electric propulsion system.

Methods conceived in this research will be tested by comparison with existing trajectory analyses. Those methods which pass the test of the comparison will be joined together to form a complete manual of preliminary mission analysis. Correlating equations or graphs will be prepared, example mission profiles will be analyzed, and possible modifications will be listed.

Characteristic Length

The characteristic length is assumed to be the distance travelled by the vehicle from rest to rest in field-free space, and this length is assumed to be invariant for all thrust programs[6.1]. An example speed profile of rest-to-rest flight in field-free space is shown in Figure 6.1. Impulsive and low thrust brings the vehicle speed to $V^* + V_H$, then thrust is reversed and the vehicle is decelerated to a speed V_{HM}. Impulsive thrust brings the vehicle to rest at the mission time T. The total area under the speed profile is

$$\Sigma L_i = \Delta L_i + \Delta L_2 + \Delta L_3 + \Delta L_4 \tag{6.1}$$

this area, ΣL_i, must equal the characteristic length, L, of the mission; e.g., initial and final conditions and mission time will be satisfied when $\Sigma L_i = L$.

The individual components of $\Sigma\Delta L_i$ may be determined as follows. First a power profile, such as that shown on Figure 6.2, must be selected. Then velocity may be determined from

$$V(t) = \int_0^t a(t)dt = \int_0^t \frac{F}{M}\, dt \tag{6.2}$$

But $M = M_o - \dot{m}t$ (6.3)

and for constant exhaust jet velocity v_j:

$$F = \dot{m}v_j = F_o\left(\frac{F}{F_o}\right) = F_o\left(\frac{P}{P_o}\right)$$

so

$$V(t) = \int_0^t \frac{F}{M_o - \dot{m}t}\,dt = \int_0^t \frac{dt}{\frac{1}{F/M_o} - \frac{t}{F/\dot{m}}}$$

or

$$V(t) = \int_0^t \frac{dt}{\frac{1}{\left(\frac{F_o}{M_o}\right)x\left(\frac{P}{P_o}\right)} - \frac{t}{v_j}} = \int_0^t \frac{dt}{\frac{1}{a_o(P/P_o)} - \frac{t}{v_j}} \qquad (6.4)$$

Using this relation it is a simple matter to construct curves of V(t) for a given power profile and with a_o and v_j as parameters. A second integral may also be evaluated from which the lengths may be determined. From Figure 6.1 it is clear that

$$\Delta V_{TOT} = V_H + \Delta V_E + V_{HM} \qquad (6.5)$$

also

$$V^* + V_H = V_{HM} + \frac{1}{2}(\Delta V_E + V_H - V_{HM}) = \frac{1}{2}(V_H + \Delta V_E + V_{HM})$$

or

$$V^* + V_H = \frac{1}{2}\Delta V_{TOT}$$

Then

$$V^* = \frac{1}{2}\cdot\Delta V_{TOT} - V_H = \frac{1}{2}(\Delta V_E - V_H + V_{HM}) \qquad (6.6)$$

Then t* may be determined from the curves of V(t). Then the lengths are given by

$$\left.\begin{aligned}
\Delta L_1 &= V_H t^* \\
\Delta L_4 &= V_{HM}(T - t^*) \\
\Delta L_2 &= \int_0^{t^*}\left\{\int_0^t a\,dt\right\}dt \\
\Delta L_3 &= \Delta V_E\,(T - t^*) - \int_0^T\left\{\int_0^t a\,dt\right\}dt + \Delta L_2
\end{aligned}\right\} \qquad (6.7)$$

The values of the double integrals are easily determined from the second family of curves showing the integral of V(t).

The above results may be used to determine a graph of characteristic length as a function of a_o for given T, v_j, P/P_o. Then the mass fraction may be found from

$$\frac{M_{ps}}{M_o} = \alpha \frac{P}{M_o}$$

where

$$\frac{P}{M_o} = \frac{1}{2} a_o v_j$$

It should be emphasized that this analysis is based on the concept of rest-to-rest motion in field-free space. There is not a complete theoretical basis for this development and no conditions have been obtained that may be applied to determine the errors involved or the missions for which the method is not valid. For those missions that have been checked, the method has given results within 15 percent of the more accurate results. An improvement in accuracy might be obtained by expanding about this solution in such a way as to include the gravitational effects that exist.

The nonlinear power profile shown on Figure 6.2 was determined from Reference 6.2. This profile was used in a numerical evaluation of the integrals for velocity and length. Then the linear version of the power profile was employed in the numerical program and the results were nearly identical with those obtained from the nonlinear profile. Consequently it was assumed that a linear power profile may be used and then analytic expressions for V(t) and L(t) may be obtained. The power profile may be written as

$$\frac{P}{P_o}(t) = 1 - bt \qquad (6.8)$$

where $|bt| < 1$ for $t \in [o, T]$. Then

$$V(t) = \int_0^t \frac{dt}{\frac{1}{a_o(1 - bt)} - \frac{t}{v_j}} = \int_0^t \frac{a_o v_j (1 - bt)dt}{v_j - a_o(1 - bt)t}$$

Identify $A = a_o b$, $B = -a_o$, $C = v_j$, $D = a_o v_j$, $E = -a_o v_j b$;

then

$$V(t) = \frac{2}{\sqrt{q}}\left(D - \frac{BE}{2A}\right)\left[\tan^{-1}\left(\frac{2At + B}{\sqrt{q}}\right) - \tan^{-1}\left(\frac{B}{\sqrt{q}}\right)\right.$$

$$\left. + \frac{E}{2A}\left\{\log\,(AT^2 + Bt + C) - \log C\right\}\right.$$

where $q \equiv 4AC - B^2$. This expression may be expanded to give

$$V(t) = a_o t + a_1 t^2 + a_2 t^3 + a_3 t^4 \qquad (6.9)$$

where

$$a_1 = \frac{4a_o^{\,4} b^2 v_j}{q^2} + \frac{1}{4}\,\frac{a_o^{\,2}}{v_j} - \frac{1}{2}\,a_o b$$

$$a_2 = \frac{-8a_o^{\,4} b^3 v_j}{3q^2} - \frac{1}{2}\,\frac{a_o^{\,2} b}{v_j}$$

$$a_3 = \frac{a_o^{\,2} b^2}{4v_j}$$

Then the length is given by

$$L(t) = \frac{1}{2}\,a_o t^2 + \frac{1}{3}\,a_1 t^3 + \frac{1}{4}\,a_2 t^4 + \frac{1}{5}\,a_3 t^5 \qquad (6.10)$$

These two equations express the results for the first and second integrals of acceleration. They may be used in place of the graphs for velocity and length.

Approximate Analysis of Mars Orbiter Lander

This example illustrates the use of the approximate method as applied to a Mars mission reported in Reference 6.2. In that example the launch date was taken to be 9 May 1971, the injected weight was 2510 kg. the escape velocity was 2.06 km/sec, the flight time was 231 days, and the initial solar power was 9.6 kw at 1 AU.

There was no thrust reversal used in calculating the trajectory; consequently the velocity history to be used in the approximate technique is that shown on the following diagram.

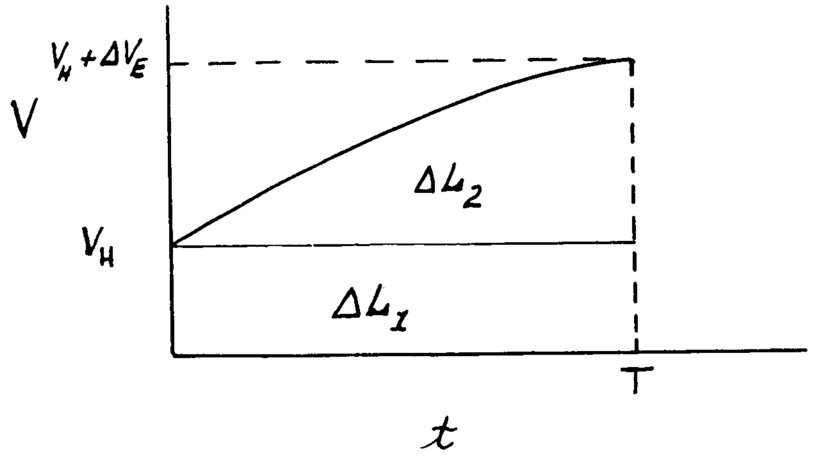

The variation of characteristic length with initial acceleration is shown in the following graph, and was determined by calculating ΔL_1, and ΔL_2 from the equations stated previously.

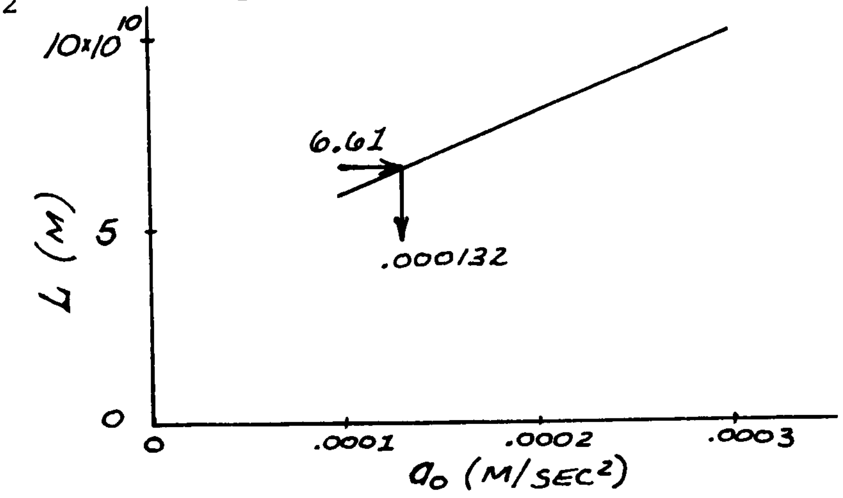

The characteristic length for the mission may be determined from impulsive transfer considerations and then the above graph may be used to determine the initial acceleration. The mission characteristic length was calculated by using impulsive transfer and the results in the Space Flight Handbooks, Vol. III, Part 2. Using the julian date 244 1081 as the launch date and a 231 day transfer time the total impulsive velocity addition is found to be 3.32 km/sec. Hence the length ($L = \frac{1}{2} \Delta V \times T$) is calculated as 6.61×10^{10} meters. The initial acceleration is then read to be

0.000132 m/sec^2. Then the initial power to mass ratio is, for I = 4000 sec

$$\frac{P}{M_o} = \frac{Fv}{2M_o} = \frac{a_o v_j}{2} = 2.59 \text{ watts/kg}$$

But M_o = 2510 kg so P = 6.5 kwj. Then, using efficiencies of 0.64 and 0.92 (Reference 6.2), the initial solar power is computed to be

$$P_{solar} = \frac{6.5}{(0.92)(0.64)} = 11.01 \text{ kw}$$

This result is within 14 percent of the figure of 9.6 kw as determined by a more precise analysis.

Approximate Analysis of Jupiter Flyby

This mission was also taken from Reference 6.2 but is more complex due to an initial period of reverse thrust. The trajectory data from Reference 6.2 are:

Launch 1 Dec 1973
Mission time = 900 days
Reverse low thrust for 20 days
Forward low thrust for 120 days
Leave Earth orbit at 140 days
Thrust termination time = 540 days
Retro hyperbolic speed = $\sqrt{C_3}$ = 1100 m/sec
Specific impulse = 3500 sec
Solar power = 17.0 kw
Injected weight = 1185 kg

The approximate analysis gave the result that the initial solar power was 18.0 kw. To obtain this it is first necessary to construct the velocity profile shown on Figure 6.3. Since the power ratio, P/P_o , is essentially constant during the initial phase the expression for velocity may be written as

$$\Delta V_1 = \int_0^{t_1} a dt = v_j \log \frac{1}{1 - \frac{a_o t_1}{v_j}} \qquad (6.11)$$

also

$$\Delta V_1 + \Delta V_2 = v_j \log \frac{1}{1 - \frac{a_o t_2}{v_j}} \tag{6.12}$$

so

$$a_o = \frac{a_2}{1 + \frac{a_2 t_2}{v_j}} \tag{6.13}$$

The speed with respect to Earth may then be plotted against time with a_o as a parameter. This is shown on Figure 6.4, where the values of a_o correspond to values for a_2 of 2×10^{-4} through 5×10^{-4} m/sec^2. The point at which the vehicle leaves Earth outbound is considered to be that time at which the speed with respect to Earth is zero. The values of ΔL_i may then be calculated for the values of a_o. The resulting graph of $\Sigma\Delta L_i$ is shown on Figure 6.5. Also shown is a curve of length vs. a_o for the impulsive transfer. This was obtained by using the Space Flight Handbooks, Vol III, Part 5. The initial acceleration is read to be 4.78×10^{-4} m/sec^2. Consequently

$$P_{j,eff,o} = \frac{1}{2} F v_{j,eff} = \frac{a_o}{2} g_c I M_o$$

$$= 9.76 \text{ kwj}$$

Then

$$P_{solar} = \frac{9.76}{\eta_e \eta_c} = \frac{9.76}{(.59)(.92)} = 18 \text{ kw}$$

This agrees to within 6 percent of the Hughes result. It should be emphasized that this is not an efficient thrust program. This example was considered merely to illustrate the approximate procedure as applied to a more complex thrust program.

Analysis of Payload Transport from Moon to Earth

Potential performance of electric spacecraft for transporting payloads from the Lunar surface to Earth can be studied by assuming various mission profiles. As an initial step in this examination, the following profile was assumed[6.3]:

1. The Saturn V boosts M_o = 220,000 lb. into a 300 n.m. Earth parking orbit. The mass M_o consists of:
   - (a) electric propulsion system of mass M_{ps} which includes powerplant, thruster, tank, and structures. This propulsion system performs the transfers from Earth-parking to Lunar-parking orbit, and return.
   - (b) propellant mass $M_{pr,o}$ for the outbound transfer from 300 n.m. Earth-parking to 50 n.m. Lunar-parking orbit with the constant-thrust electric propulsion system.
   - (c) a Lunar-lander chemical rocket of mass M_c = 7,500 lb. which includes a chemical-rocket engine, structure, and tank; the lander has a specific impulse of 300 sec.
   - (d) propellant mass $M_{c,d}$ for the chemical-rocket lander descent from 50 n.m. Lunar-parking orbit to the Lunar surface; for descent, ΔV = 1.72 km/sec.
   - (e) propellant mass $M_{c,a}$ for the chemical-rocket lander ascent from the lunar surface to the 50 n.m. Lunar-parking orbit; for ascent, ΔV = 1.72 km/sec.
   - (f) propellant mass $M_{pr,R}$ for the return transfer from 50 n.m. Lunar-parking to 300 n.m. Earth-parking orbit with the constant-thrust electric propulsion system.
2. Upon arrival in the 50 n.m. Lunar-parking orbit, the electric propulsion system of mass M_{ps} and return-transfer propellant of mass $M_{pr,R}$ remain in the Lunar-parking orbit awaiting the payload.
3. Upon arrival in the 50 n.m. Lunar-parking orbit, the chemical-rocket lander descends to the Lunar surface, acquires the payload mass M_{pay}, and ascends to rendezvous with the waiting electric spacecraft.

4. After rendezvous, the chemical-rocket lander remains in Lunar-parking orbit.
5. After acquiring the payload mass M_{pay}, the electric spacecraft of total mass M_R transfers from 50 n.m. Lunar-parking to 300 n.m. Earth-parking orbit.
6. Final mass delivered to Earth-parking orbit is the electric propulsion system mass M_{ps} and the payload mass M_{pay}.
7. Delivery of payload mass to Earth surface is done by atmospheric entry methods, which are assumed to involve negligible mass.
8. If multiple round-trips are to be made, and if the electric propulsion system has adequate durability, then subsequent boosters would not have to carry the masses M_{ps} and M_c, thereby allowing greater payloads delivered to Earth.

Analysis of this mission can be based on two mass summations:

$$M_o = M_{ps} + M_{pr,o} + M_c + M_{c,d} + M_{c,a} + M_{pr,R} \qquad (6.14)$$

$$M_R = M_{pay} + M_{ps} + M_{pr,R} \qquad (6.15)$$

Propellant masses $M_{c,d}$ and $M_{c,a}$ for the lander can be determined with the standard rocket equation for propellant mass fraction b:

$$b = 1 - \exp(- \Delta V_M/v_L) \qquad (6.16)$$

For $\Delta V_M = 1.723$ km/sec (either descent or ascent), and a chemical rocket specific impulse of 300 sec, b = .444. Propellant masses $M_{c,d}$ and $M_{c,a}$ are:

$$M_{c,d} = b(M_c + M_{c,a} + M_{c,d}) \qquad (6.17)$$

$$M_{c,a} = b(M_c + M_{pay} + M_{c,a}) \qquad (6.18)$$

The other masses in equations (6.14) and (6.15) can be determined from:

$$M_{ps} = \frac{\alpha v}{2} F \tag{6.19}$$

$$M_{pr,o} = \frac{T_o}{v} F \tag{6.20}$$

$$M_{pr,R} = \frac{T_R}{v} F \tag{6.21}$$

where α is the specific mass of the electric propulsion system (kg/watt), v is the effective exhaust velocity of the electric thruster ($v = g_c I$, m/sec), F is thrust (newtons), T_o is outbound transfer time, and T_R is return transfer time. Equations (6.17) to (6.21) can be used in equations (6.14) and (6.15) to obtain:

$$\frac{M_{pay}}{M_o} = \frac{1}{b}\left[(1 - b)^2 - \frac{M_c}{M_o}\right] - \frac{(1 - b)^2}{b}\left(\frac{\alpha v}{2} + \frac{T_o}{v} + \frac{T_R}{v}\right)\frac{F}{M_o} \tag{6.22}$$

$$\frac{M_{pay}}{M_o} = \left(\frac{1}{F/M_R} - \frac{\alpha v}{2} - \frac{T_R}{v}\right)\frac{F}{M_o} \tag{6.23}$$

Thrust-to-mass ratios F/M_R and F/M_o can be determined from a modified Sauer-Melbourne correlation[6.4] as described in the following paragraphs.

Stephenson[6.5] has used a correction factor of 0.92 to trip times, and found that calculations of Earth escape trajectories by London[6.6] could be used in determine payloads for Earth-parking to Lunar-parking orbit transfers. This same correction factor of 0.92 has been used in the present analysis to convert the Sauer-Melbourne escape-trajectory correlation to an Earth-Moon transfer.

The modified Sauer-Melbourne correlation which relates J to escape time T_e is[6.4]:

$$J = K' T_e^{-0.913} \tag{6.24}$$

The coefficient K′ is a function of radius r_p of the central body, radius r_o of the starting orbit, gravitation acceleration g_p at the central body surface, and the force constant μ_p of the central body:

$$K = .394\ g_p{}^2 \left(\frac{r_p}{r_o}\right)^4 \left(\frac{r_o}{\sqrt{\mu_p/r_o}}\right)^{1.913} \qquad (6.25)$$

When the Stephenson correction is used, then $T_p = 0.92\ T_e$ and a new constant K can be defined which absorbs the factor 0.92 (ie, $K = K'/.92^{.913}$):

$$J = K\ T_p{}^{-0.913} \qquad (6.26)$$

where T_p is the time spent in the field of the central body. In this way, the total J and total T for the Earth-Moon transfer are:

$$T = T_E + T_M \qquad (6.27)$$

$$J = J_E + J_M \qquad (6.28)$$

where the subscripts E and M refer to Earth and Moon respectively. Noting that for a maximum final mass fraction:

$$dJ = dJ_E + dJ_M = 0 \qquad (6.29)$$

and that for a fixed transit time:

$$dT = dT_E + dT_M = 0 \qquad (6.30)$$

By combining equations (6.29) and (6.30):

$$\frac{dJ_E}{dT_E} = \frac{dJ_M}{dT_M} \qquad (6.31)$$

Equations (6.26) and (6.31) can be used to obtain the ratio of T_M/T_E:

$$T_M/T_E = (K_M/K_E)^{0.523} \qquad (6.32)$$

Total J can be defined by combining equations (6.26) and (6.28):

$$J = K_E T_E{}^{-0.913} + K_M T_M{}^{-0.913} \qquad (6.33)$$

This expression can be combined with equation (6.31) to obtain:

$$J = \left[1 + (K_M/K_E)^{0.523}\right]^{1.913} K_E T^{-0.913} \qquad (6.34)$$

For a 300 n.m. Earth parking orbit and a 50 n.m. Lunar parking orbit equation (6.34) becomes:

$$J = KT^{-0.913} \qquad (6.35)$$

where J has the units watts/kg, T is in seconds, and $K = 1.81 \times 10^7$. Characteristic length L can be calculated[6.1] by using values of J found from equation (6.35) for various values of T.

Analysis of an Earth-Moon transfer can begin by specifying a starting mass M_o in Earth parking orbit, by specifying a transfer time T, and by specifying a specific impulse I. The expression for initial thrust-to-mass ratio F/M_o is[6.1]:

$$\frac{F}{M_o} = \frac{4L}{T^2} \frac{v^2}{(v + L/T)^2} \qquad (6.36)$$

where v is effective exhaust velocity defined by:

$$v = g_c I$$

where g_c is the gravitational conversion factor (9.806 m/sec^2).

By combining equations (6.26) and (6.37) with $L = \sqrt{\frac{JT^3}{3}}$ there results

$$\frac{F}{M_o} = \frac{K^{\frac{1}{2}} v^2}{T_o^{.952} (v + K^{\frac{1}{2}} T_o^{.048}/4)^2} \qquad (6.37)$$

$$\frac{F}{M_R} = \frac{K^{\frac{1}{2}} v^2}{T_R^{.952} (v + K^{\frac{1}{2}} T_R^{.048}/4)^2} \qquad (6.38)$$

With equations (6.37) and (6.38), the two payload equations (6.22) and (6.23) can be equated to form a relation between the two transfer times T_o and T_R:

$$T_R\left[\frac{(v + K^{\frac{1}{2}}T_R^{.048}/4)^2}{K^{\frac{1}{2}}vT_R^{.048}} - .305\right] = T_o\left[\frac{1.54(v + K^{\frac{1}{2}}T_o^{.048})^2}{K^{\frac{1}{2}}vT_o^{.048}} - .695\right]$$

$$+ .1525\alpha v^2 \qquad (6.39)$$

Functions $f(T_R)$ and $f(T_o)$ can be defined to replace the respective terms containing T_R and T_o in equation (6.39) so that:

$$f(T_R) = f(T_o) + .1525\alpha v^2 \qquad (6.40)$$

The functions $f(T_R)$ and $f(T_o)$ can be plotted for a range of specific impulse, I.

With the preceding relations and graphs, the payload mass M_{pay} can be found for specified values of M_o, v, α, and T_o. Calculation procedure is as follows:

1. For specified time T_o, find $f(T_o)$ from graph of $f(T_o)$ vs. T_o.
2. For specified v and α, and with $f(T_o)$, calculate $f(T_R)$ from equation (6.40).
3. With calculated $f(T_R)$, find T_R from graph of $f(T_R)$ vs. T_R.
4. Calculate F/M_o and F/M_R from equations (6.37) and (6.38) respectively.
5. Calculate M_{pay}/M_o from equation (6.36).
6. Total mission time is $T = T_o + T_R$

Graphs are being prepared to facilitate this method of analysis of Lunar return payloads.

REFERENCES

6.1. Zola, Charles L.: A Method of Approximating Propellant Requirements of Low-Thrust Trajectories. NASA TN D-3400. April, 1966.

6.2. "Solar Powered Electric Propulsion Program", Hughes Aircraft Co., Space Systems Division, Dec. 1966.

6.3. Fehr, T. D.: Electric Propulsion for Lunar Missions. Master of Science Thesis, Colorado State University, December, 1966. (Printed in entirety in Report No. 2, Space Propulsion Program, Colorado State University, as a part of NASA Grant NGR06-002-032. November 22, 1966.)

6.4. Sauer, C. G. and Melbourne, W. G.: Optimum Earth-to-Mars Roundtrip Trajectories Utilizing a Low-Thrust Power-Limited Propulsion System. TR 32-376, Jet Propulsion Laboratory, California Institute of Technology. March, 1963.

6.5. Stephenson, R. R.: The Electrically Propelled Lunar Logistic Vehicle. AIAA Paper No. 64-497. July, 1964.

6.6. London, H. S.: A Study of Earth-Satellite to Moon-Satellite Transfers Using Nonchemical Propulsion Systems. United Aircraft Corporation Report R-1383-1. May, 1964.

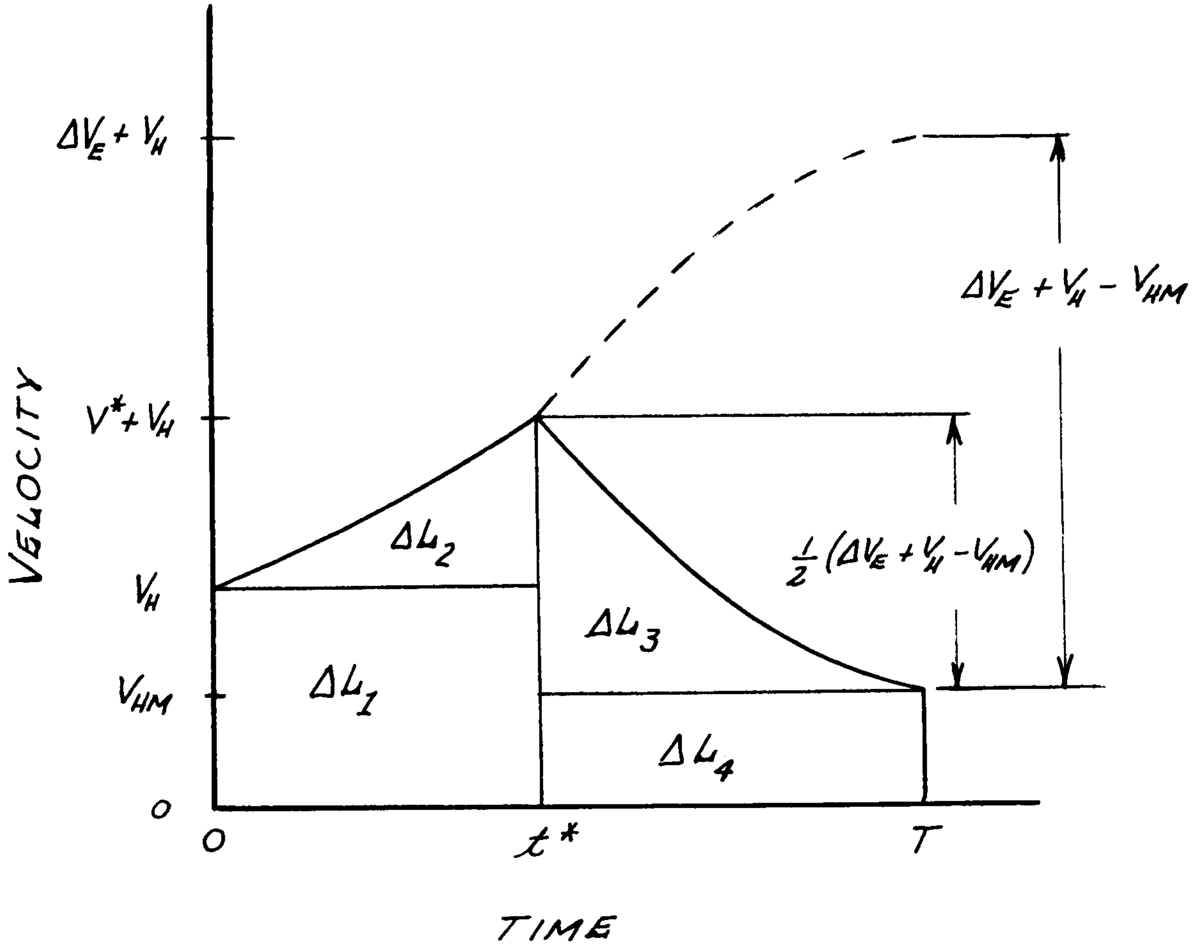
VELOCITY
$\Delta V_E + V_H$
$V^* + V_H$
V_H
V_{HM}
0
$\Delta V_E + V_H - V_{HM}$
$\frac{1}{2}(\Delta V_E + V_H - V_{HM})$
ΔL_2
ΔL_1
ΔL_3
ΔL_4
0
t^*
T
TIME

Figure 6.1. Velocity Profile for Rest to Rest Flight in Field Free Space.

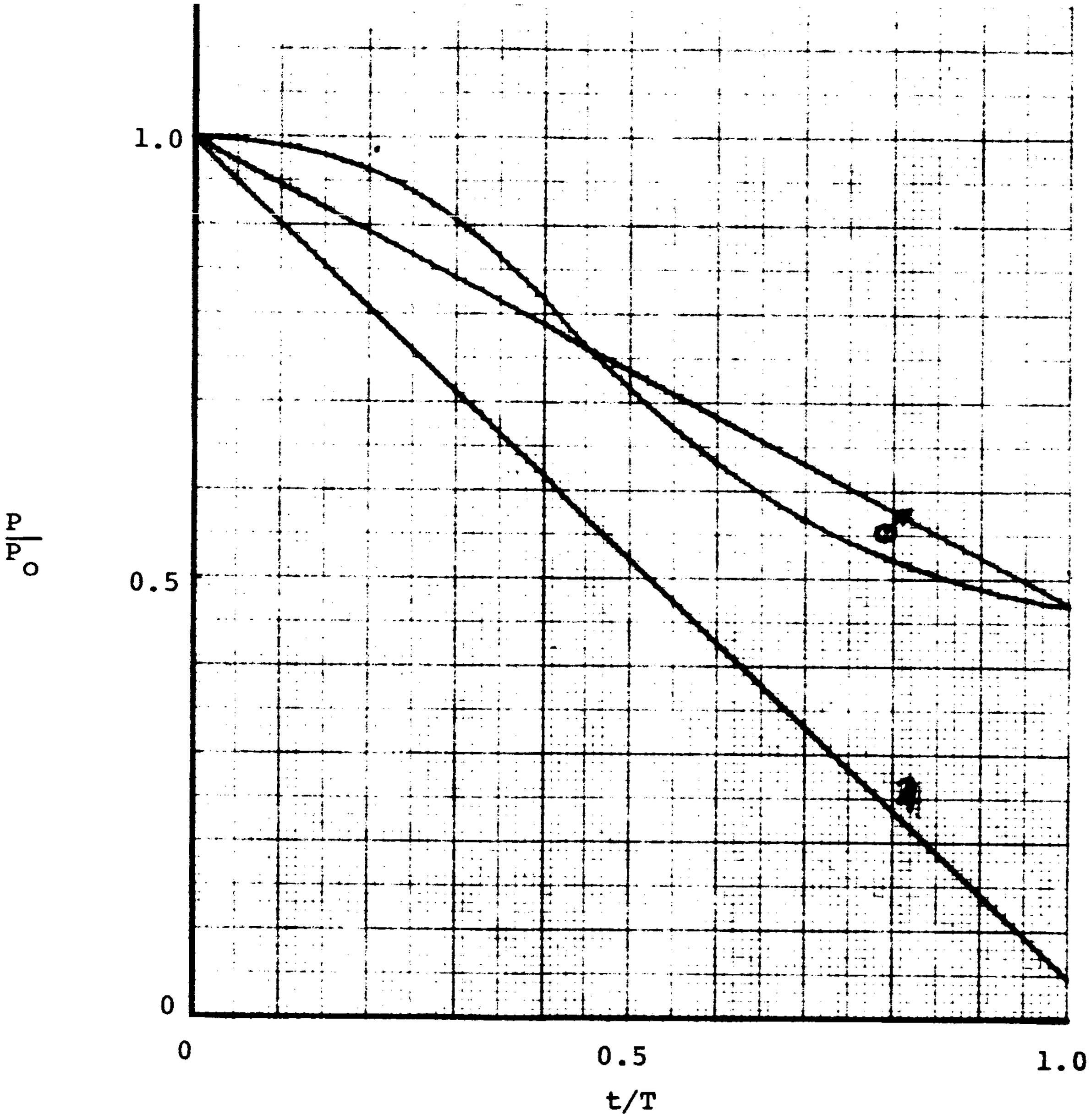

Figure 6.2. Power Profiles.

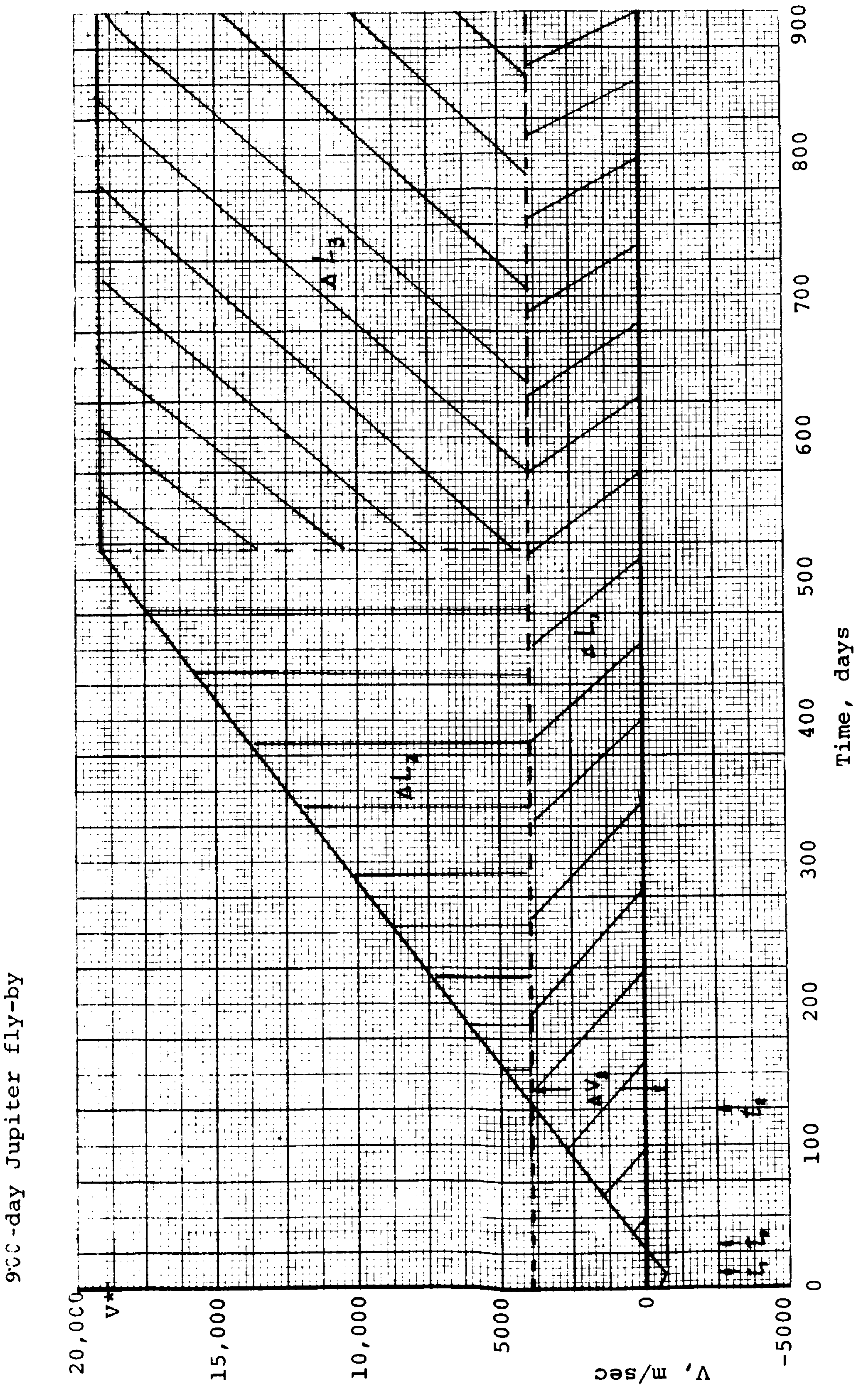

Figure 6.3. Velocity Profile for Jupiter Flyby

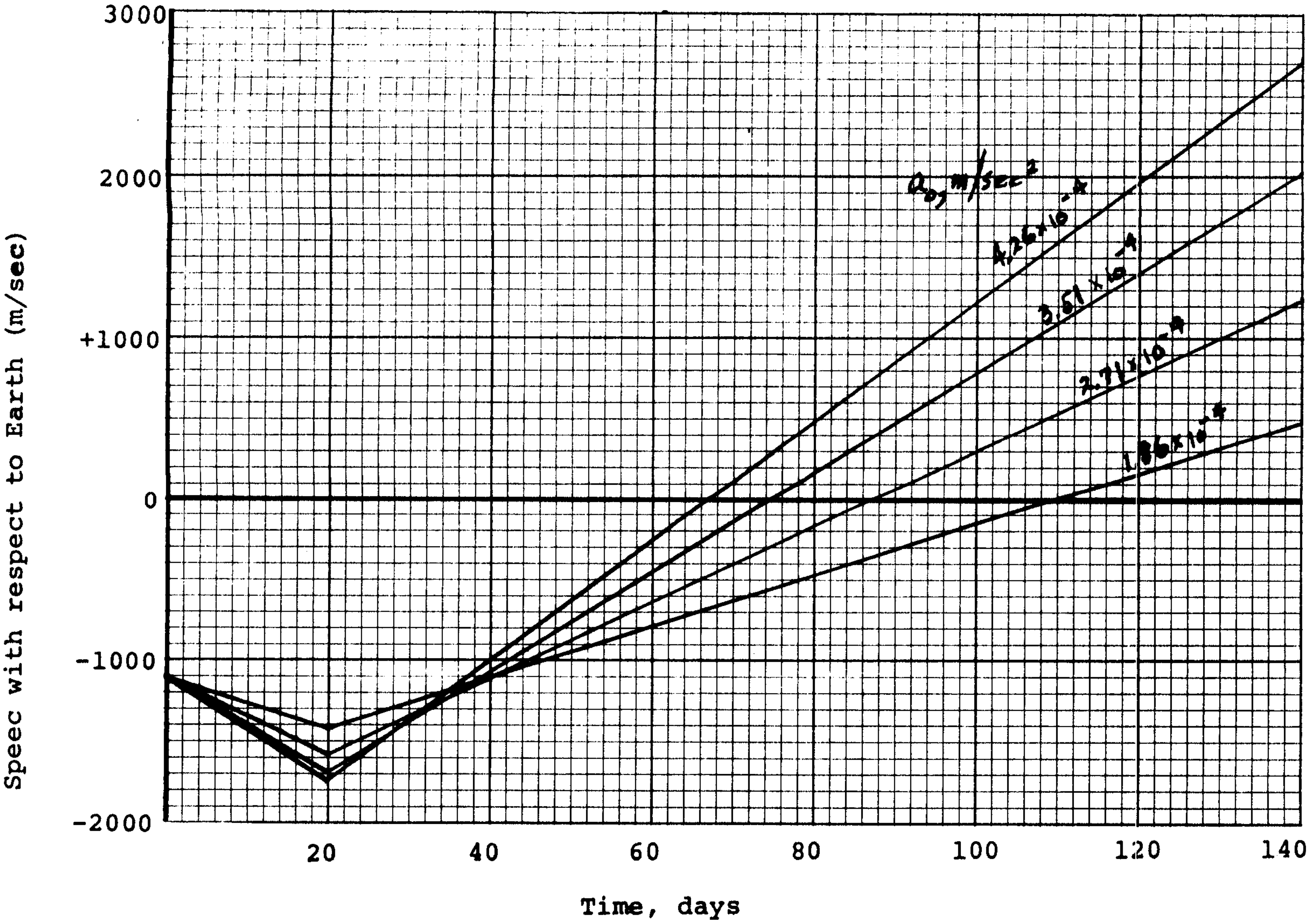

Figure 6.4. Speec Relative to Earth for Initial Phase of Jupiter Flyby.

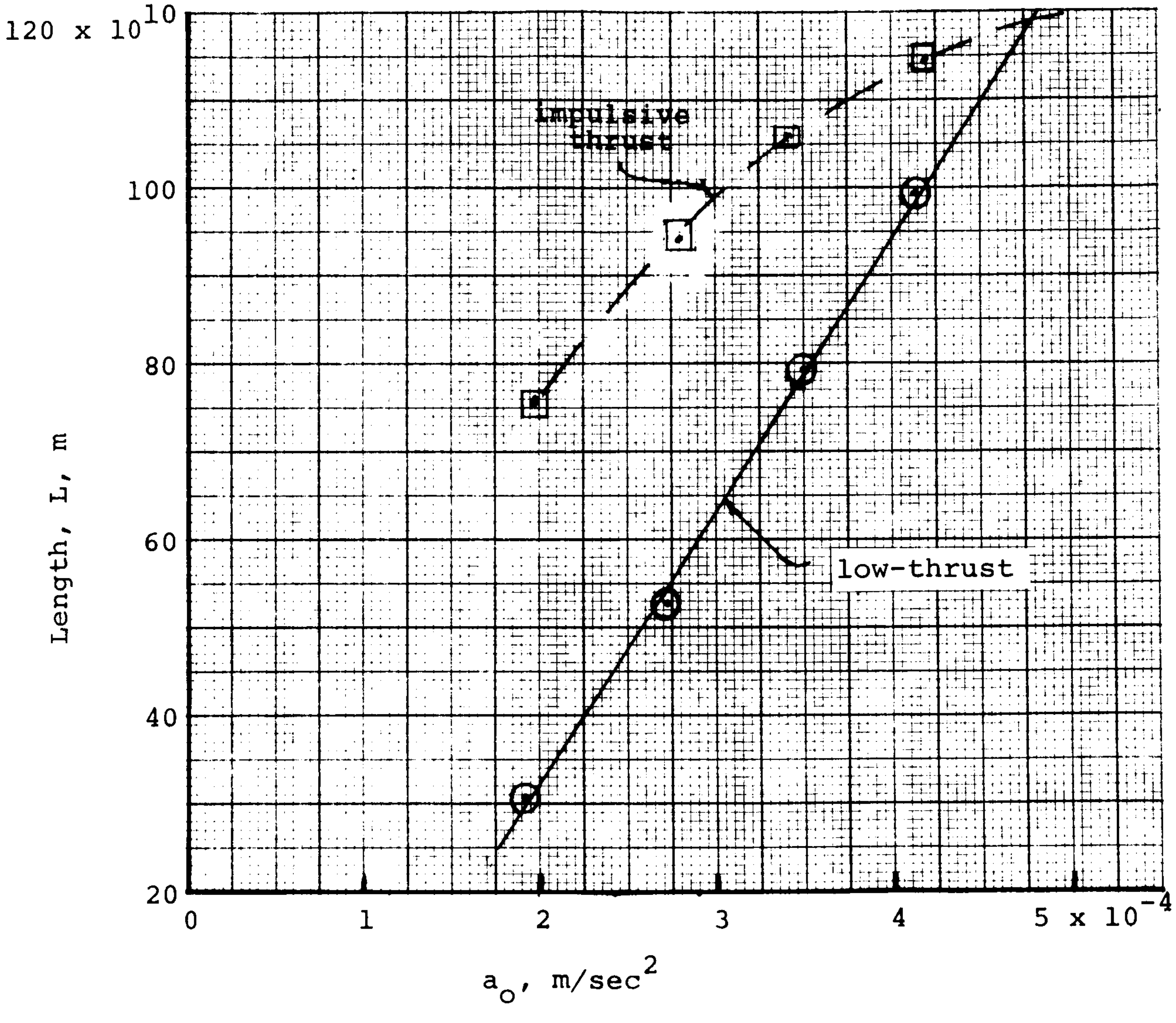

Figure 6.5. Characteristic Lengths for Jupiter Flyby.

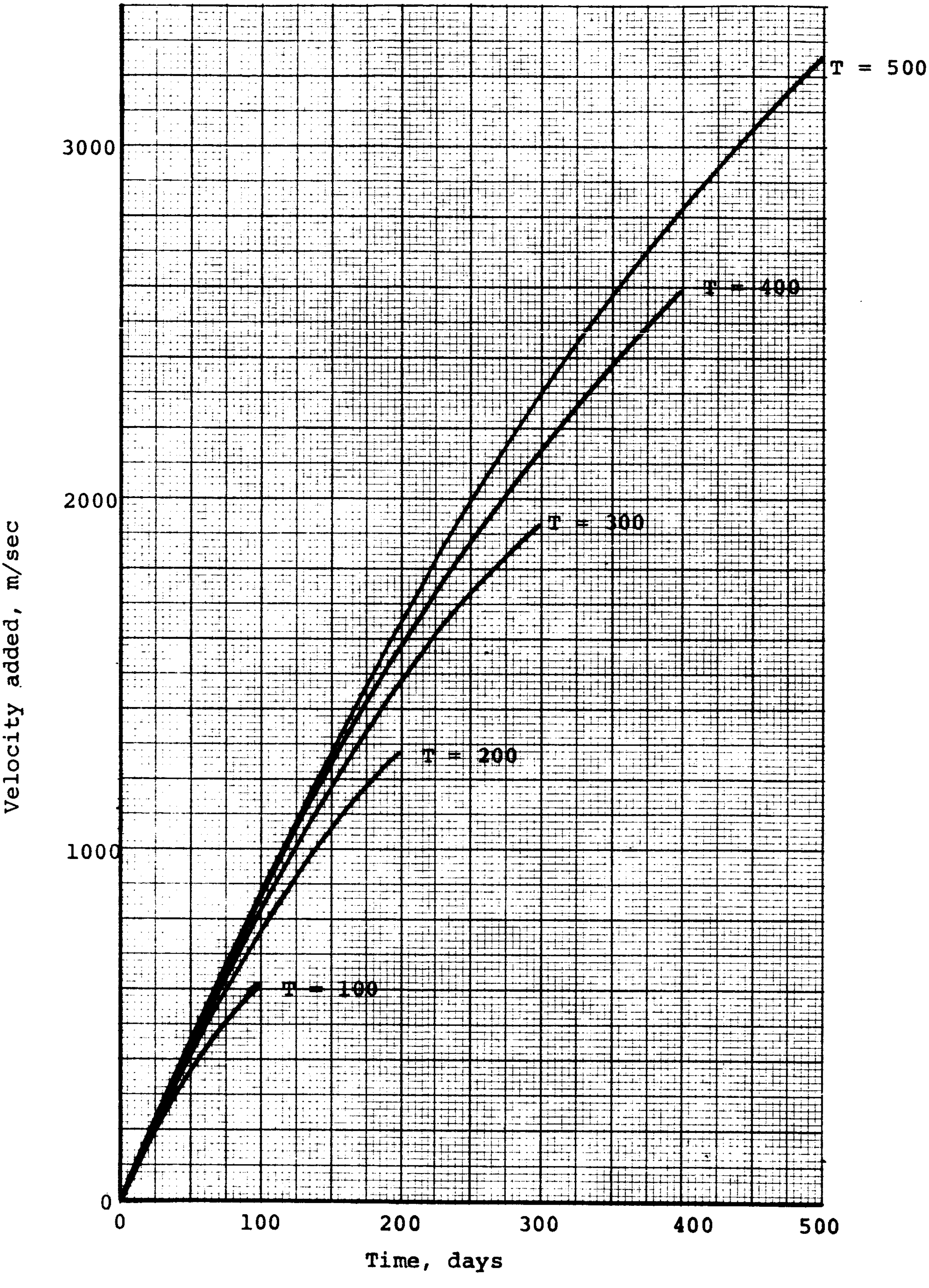

Figure 6.6. Integral of Acceleration Using a Linear Power Profile for Earth to Mars with $a_o = 0.0001$ m/sec^2, I = 4000 sec.

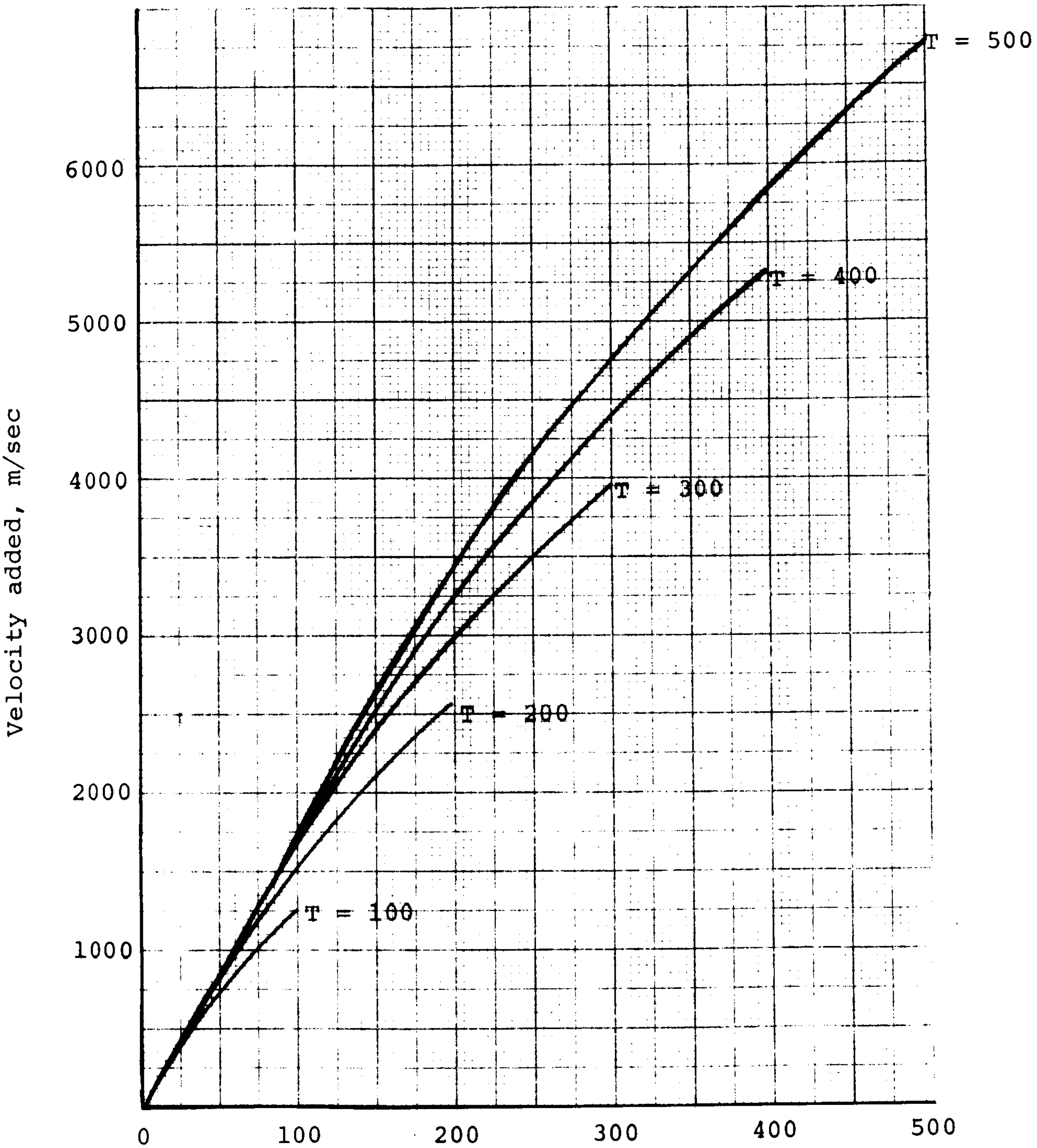

Figure 6.7. Integral of Acceleration Using a Linear Power Profile for Earth to Mars with $a_o = 0.0002$ m/sec^2, I = 4000 sec.

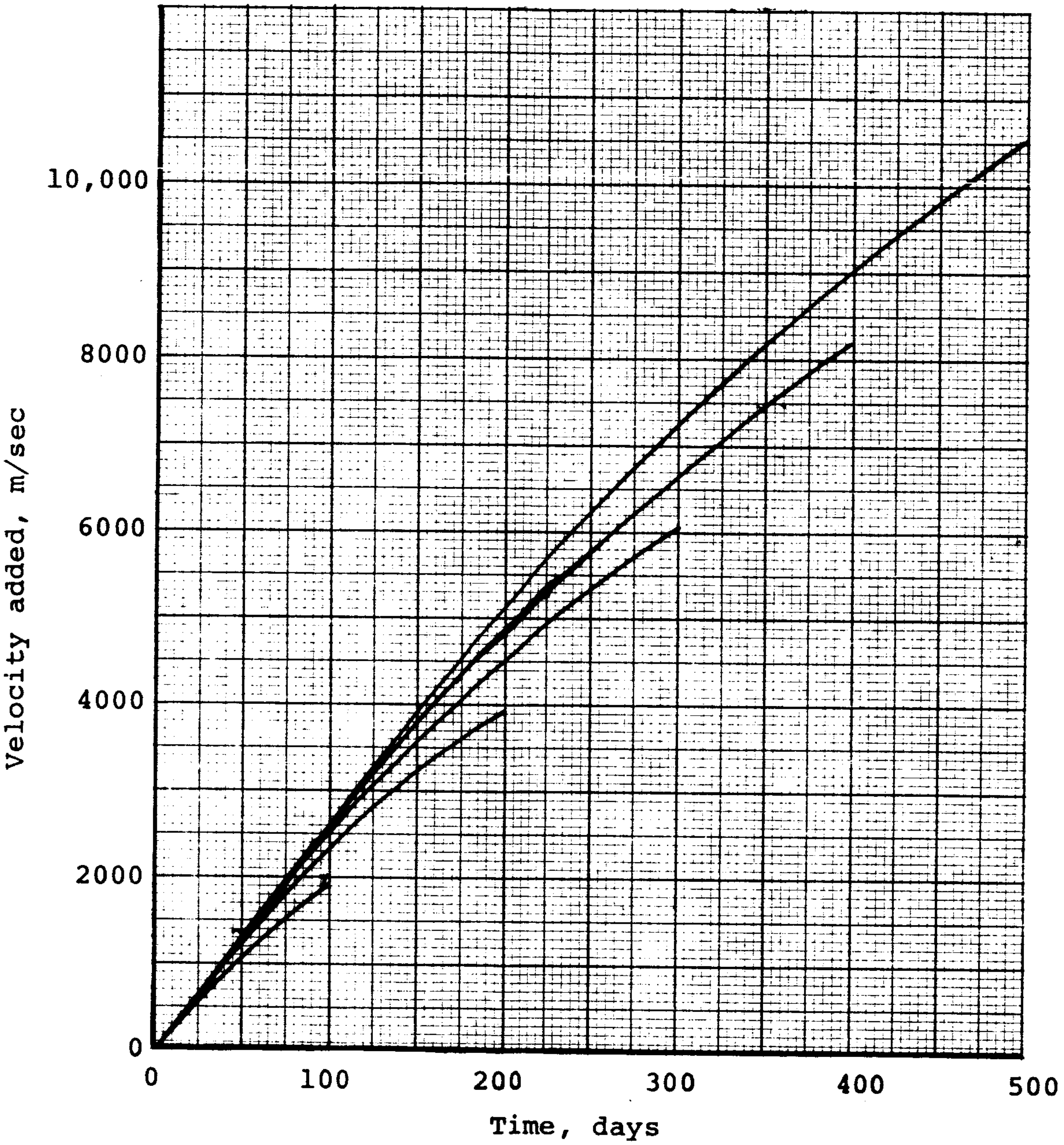

Figure 6.8. Integral of Acceleration Using a Linear Power Profile for Earth to Mars with $a_o = 0.0003$ m/sec^2 I = 4000 sec.

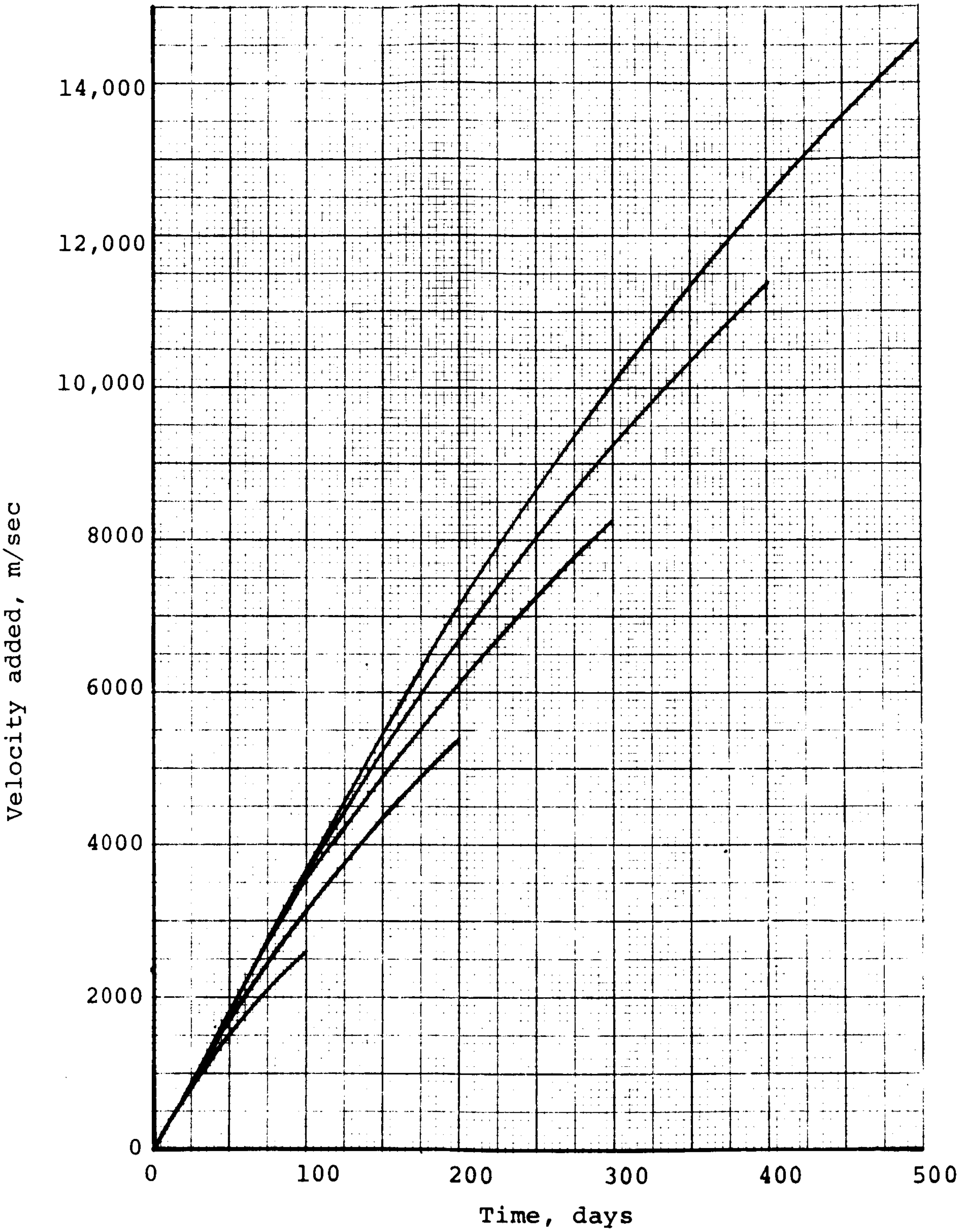

Figure 6.9. Integral of Acceleration Using a Linear Power Profile for Earth to Mars with $a_o = 0.0004$ m/sec^2 I = 4000 sec.

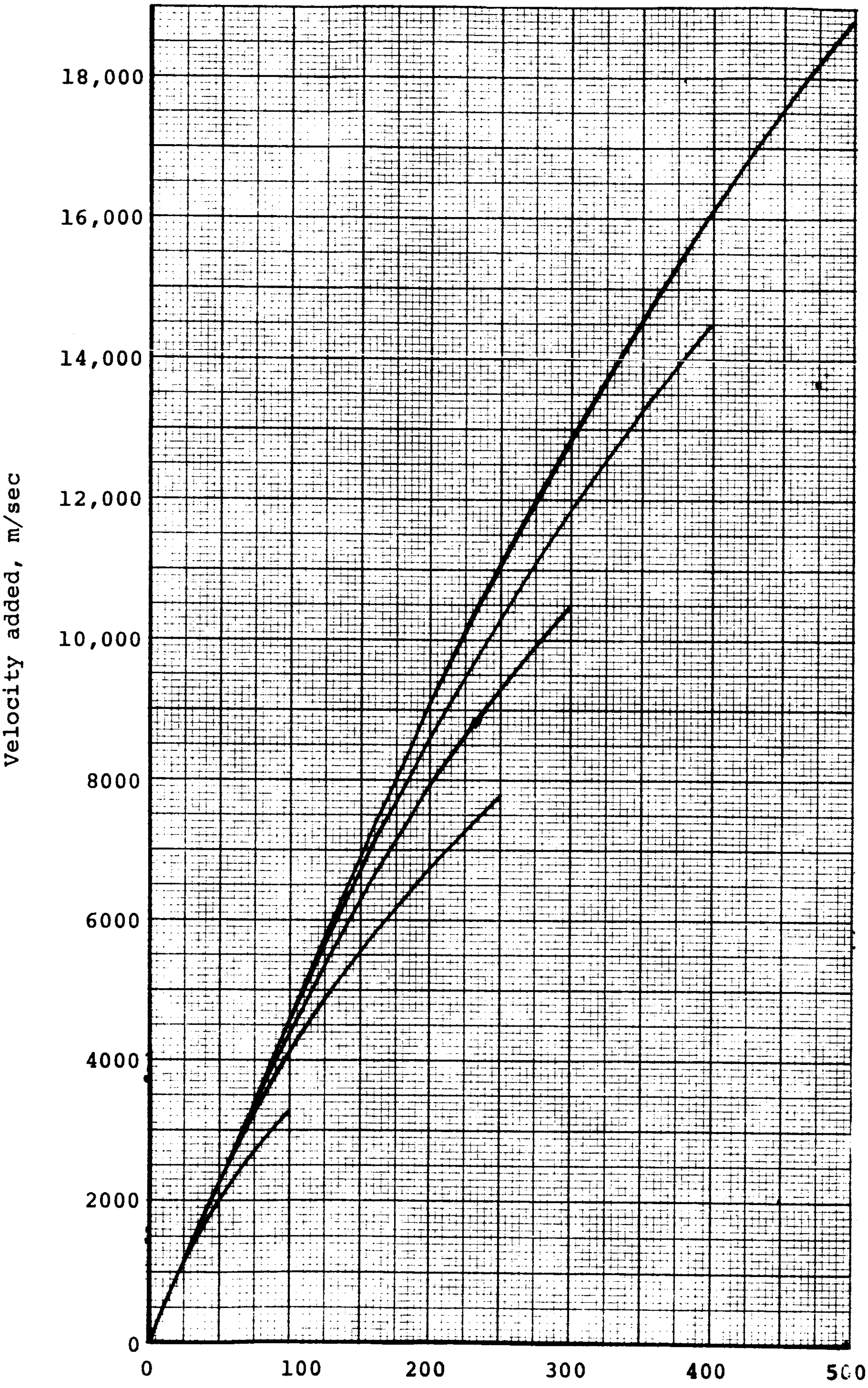

Figure 6.10. Integral of Acceleration Using a Linear Power Profile for Earth to Mars with $a_o = 0.0005$ m/sec^2 I = 4000 sec.

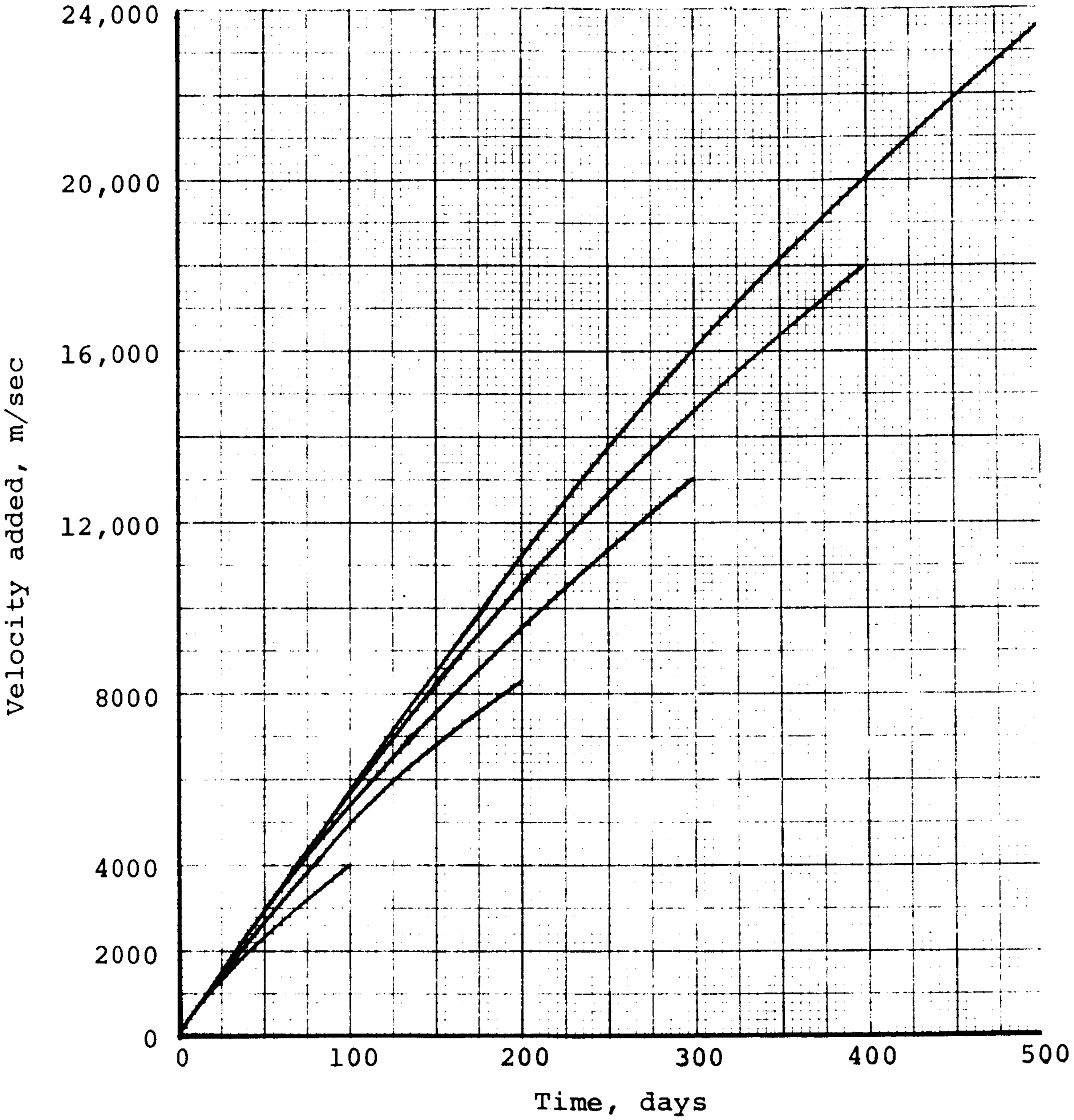

Figure 6.11. Integral of Acceleration Using a Linear Power Profile for Earth to Mars with $a_o = 0.0006$ m/sec^2 I = 4000 sec.

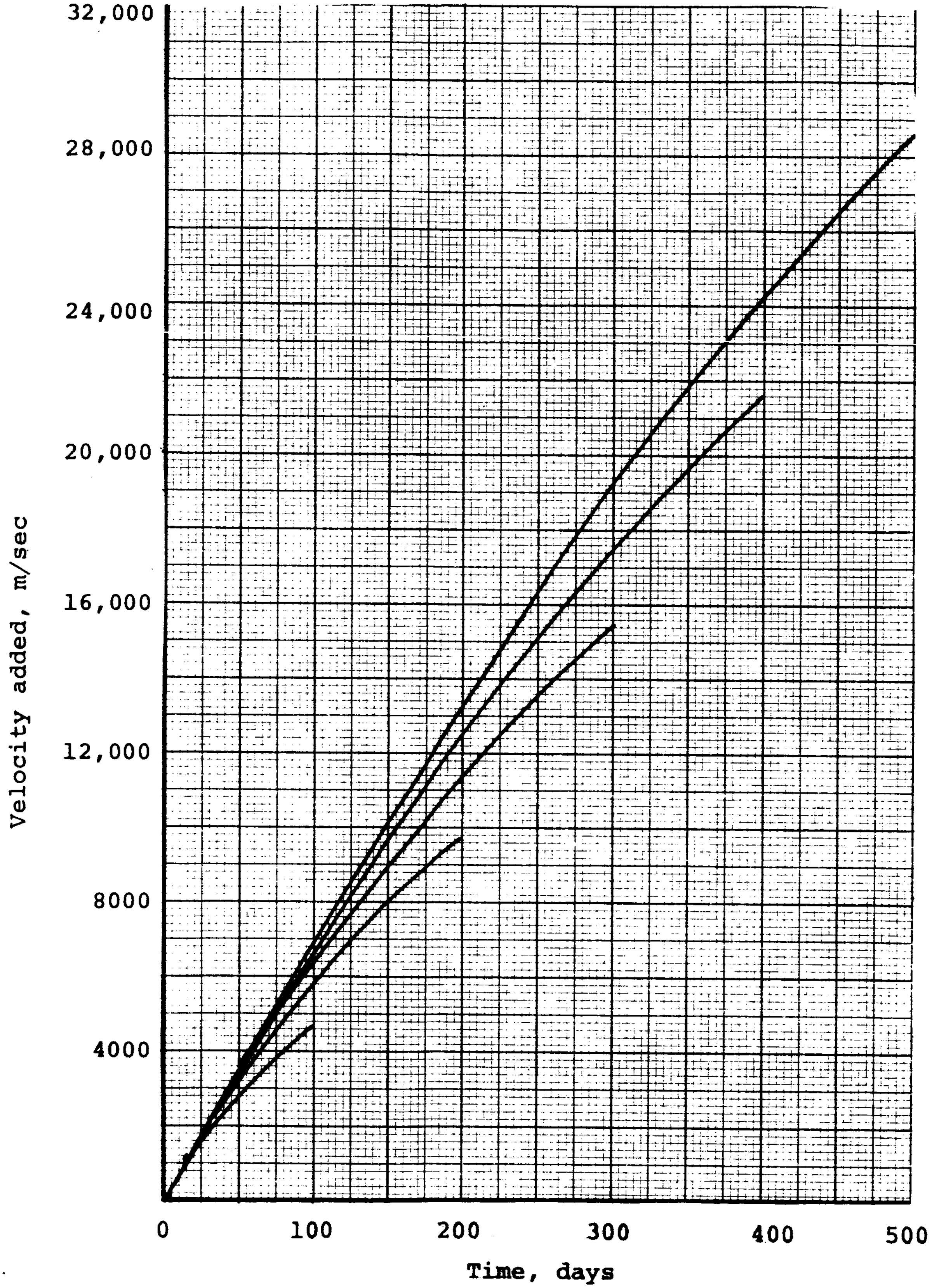

Figure 6.12. Integral of Acceleration Using a Linear Power Profile for Earth to Mars with $a_o = 0.0007$ m/sec^2, I = 4000 sec.

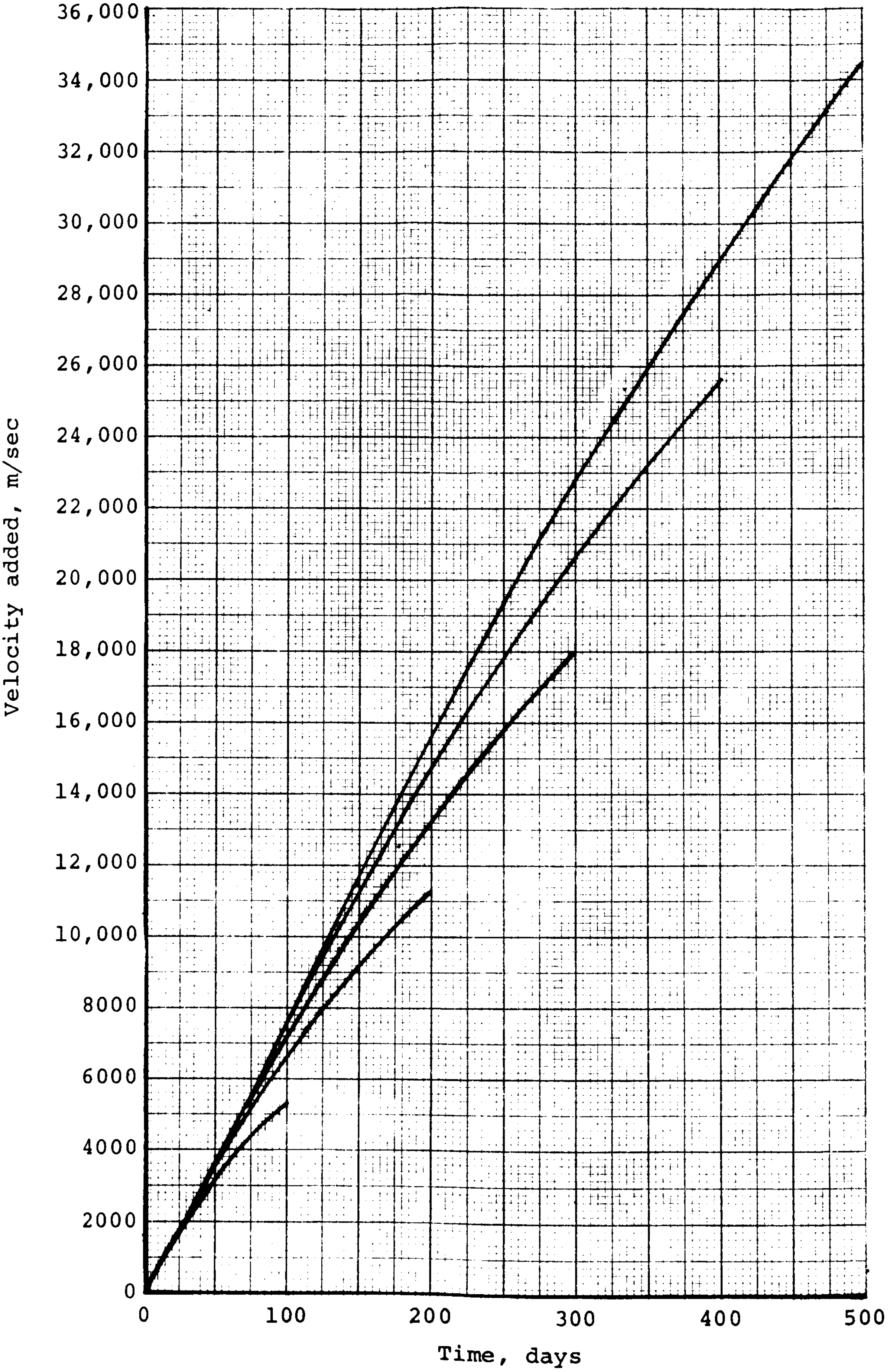

Figure 6.13. Integral of Acceleration Using a Linear Power Profile for Earth to Mars with $a_o = 0.0008$ m/sec^2 I = 4000 sec.

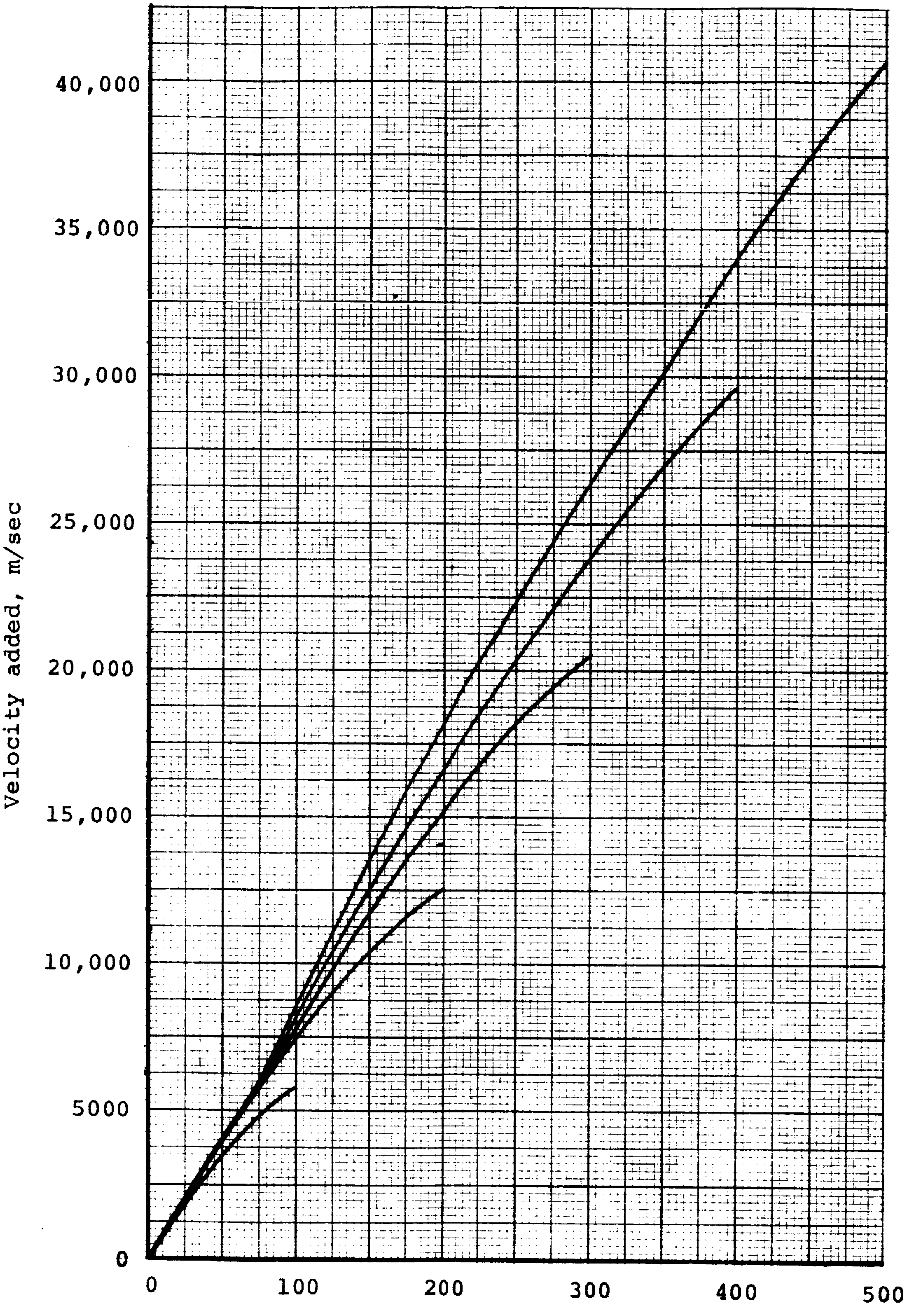

Figure 6.14. Integral of Acceleration Using a Linear Power Profile for Earth to Mars with $a_o = 0.0009$ m/sec^2 I = 4000 sec.

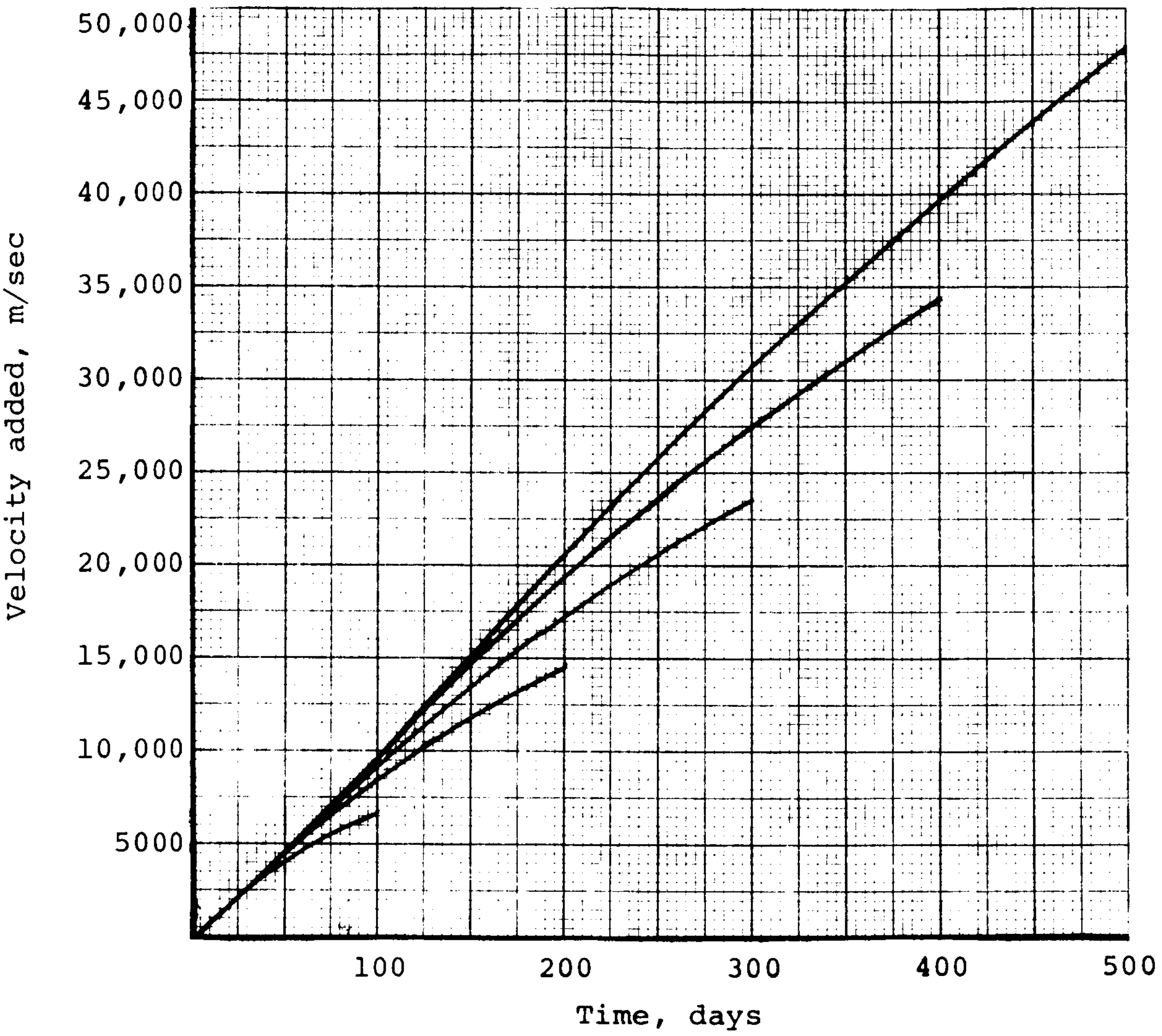

Figure 6.15. Integral of Acceleration Using a Linear Power Profile for Earth to Mars with $a_o = .001$ m/sec^2, I = 4000 sec.

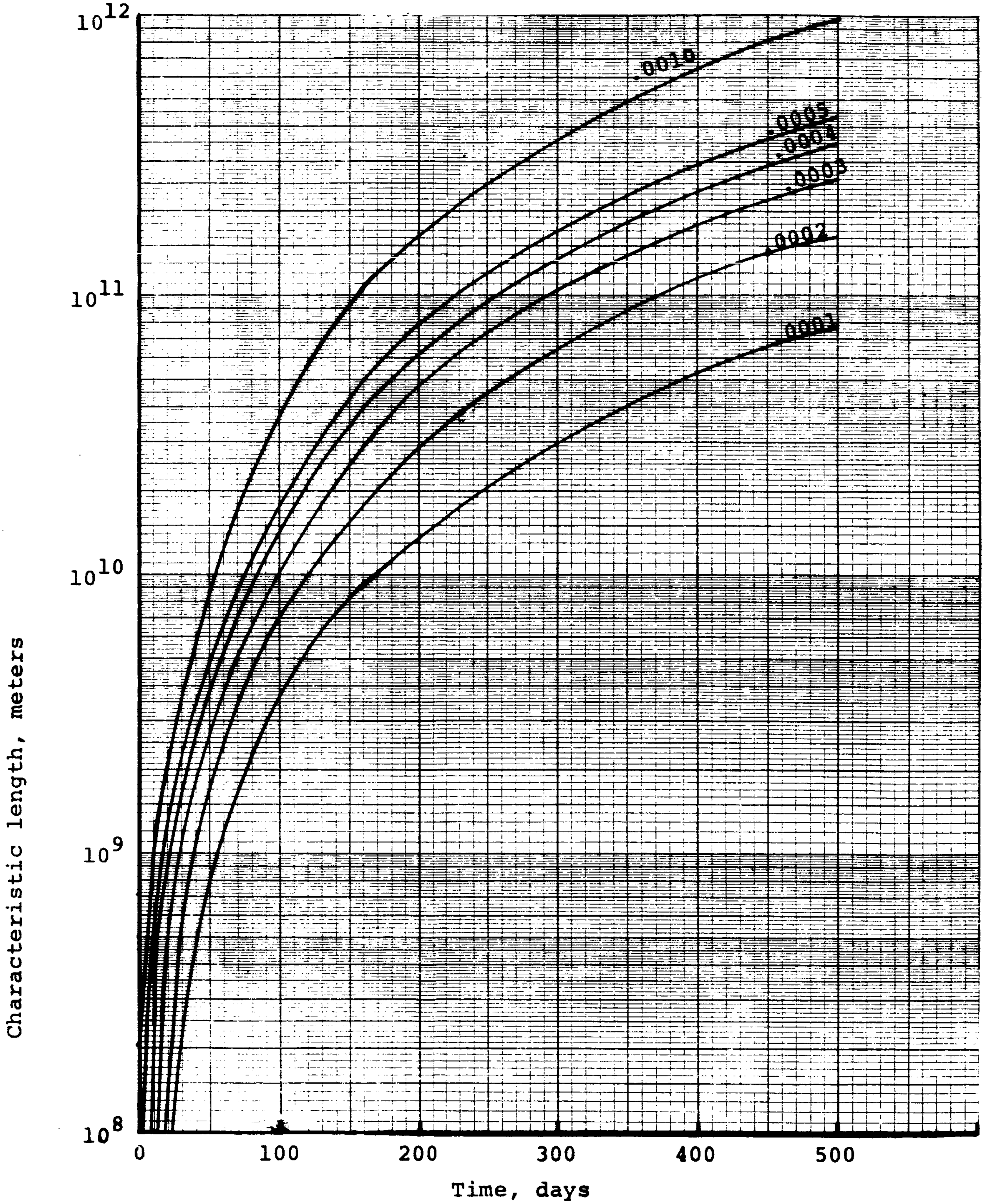

Figure 6.16 Length for Earth to Mars Transfer Using a Linear Power Profile, and I = 4000 sec.

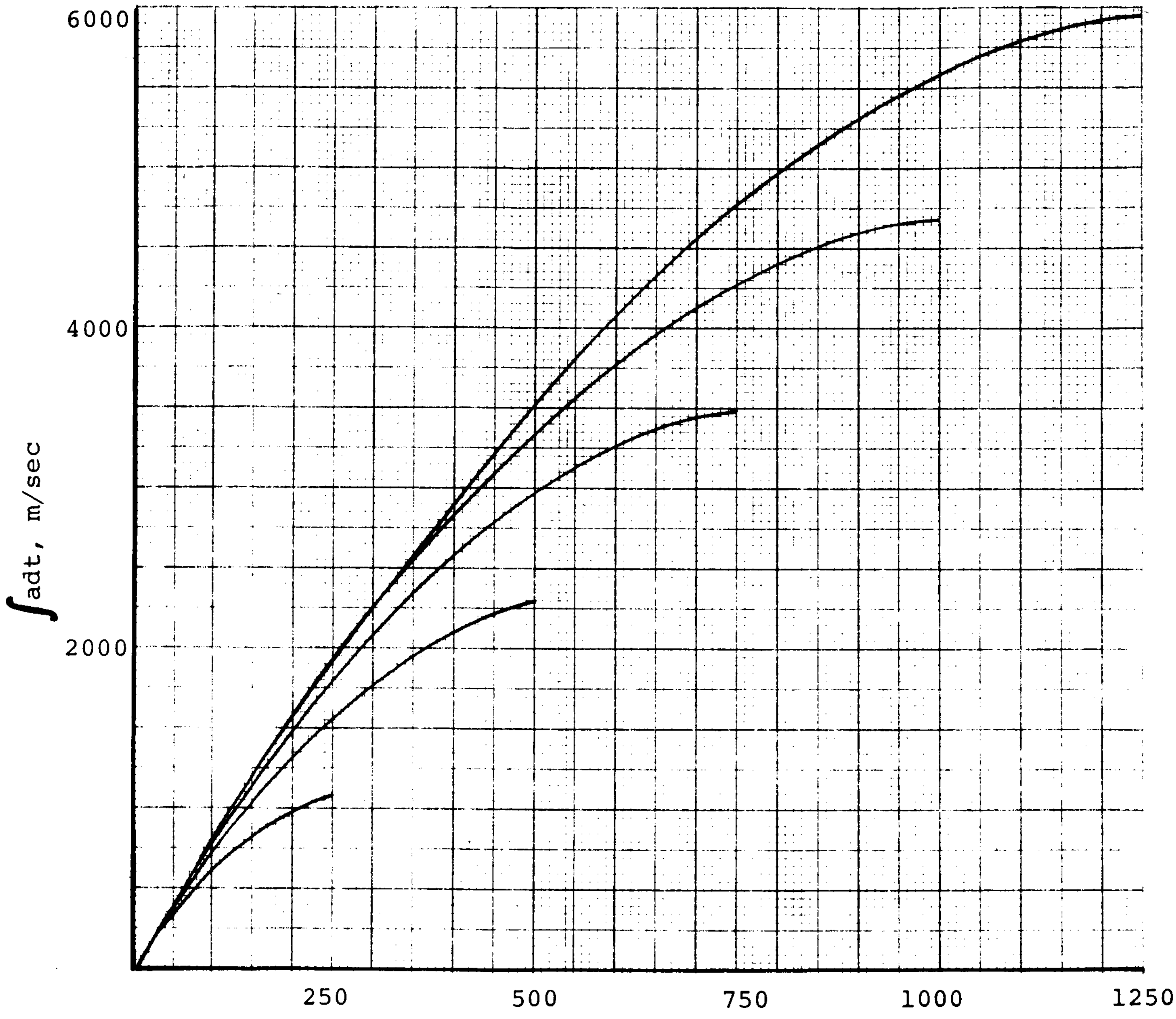

Figure 6.17. Velocity Added for Earth to Jupiter Transfer Using A Linear Power Profile, I = 3500 sec, a_o = 0.0001 m/sec^2.

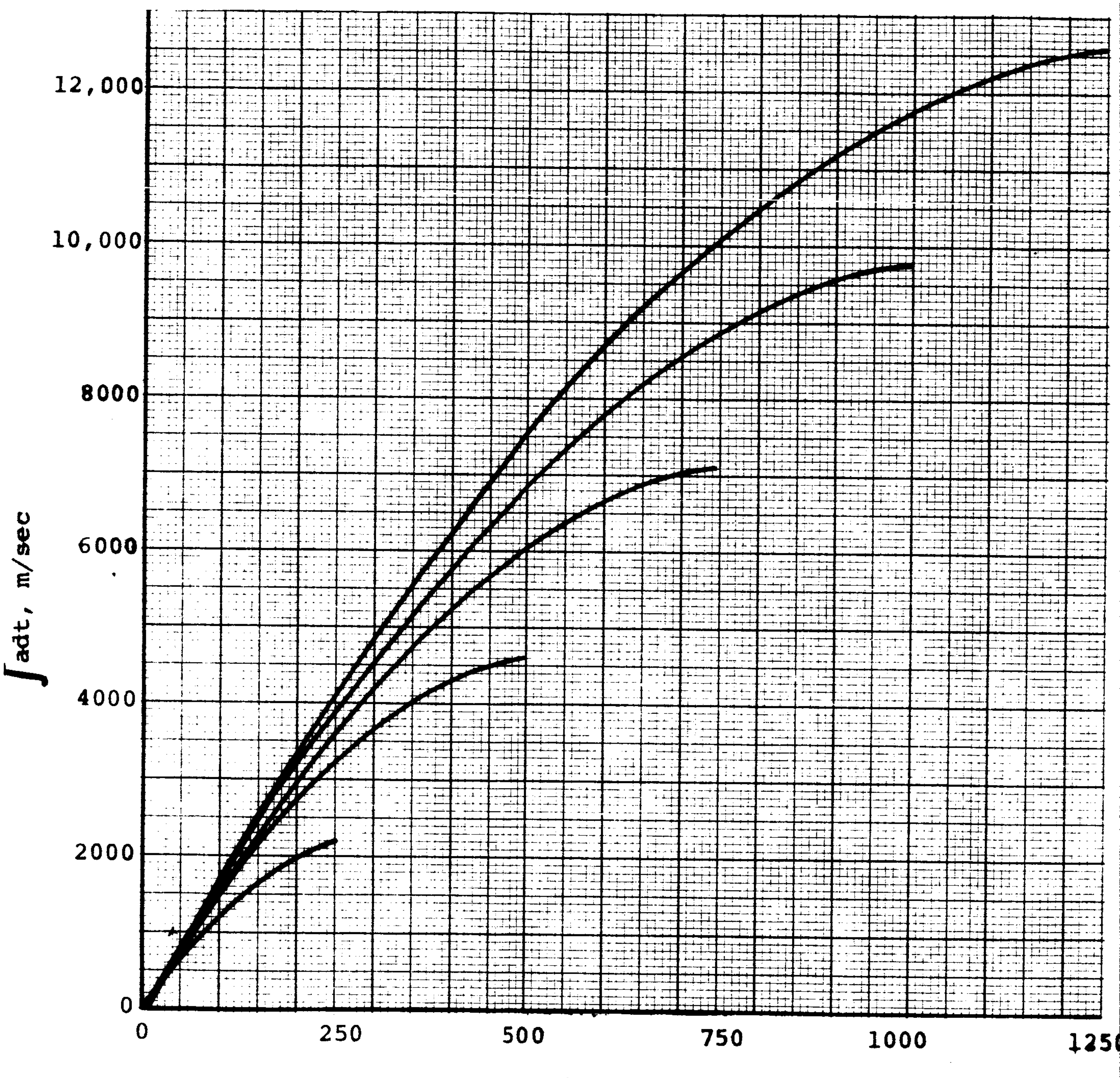

Figure 6.18. Velocity Added for Earth to Jupiter Transfer Using A Linear Power Profile, I = 3500 sec, $a_o = 0.0002\ m/sec^2$.

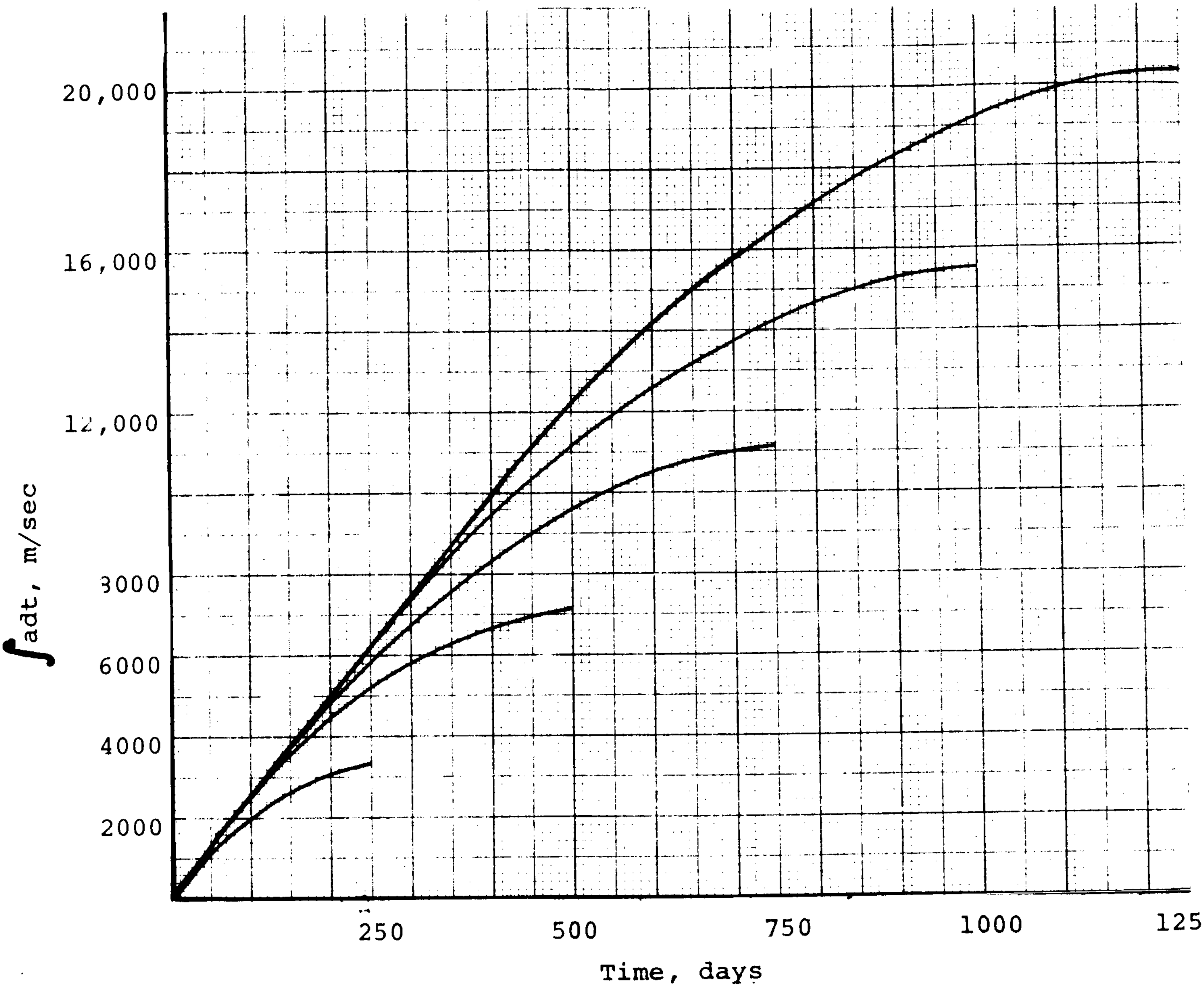

Figure 6.19. Velocity Added for Earth to Jupiter Transfer Using A Linear Power Profile, I = 3500 sec, $a_o = 0.0003$ m/sec^2.

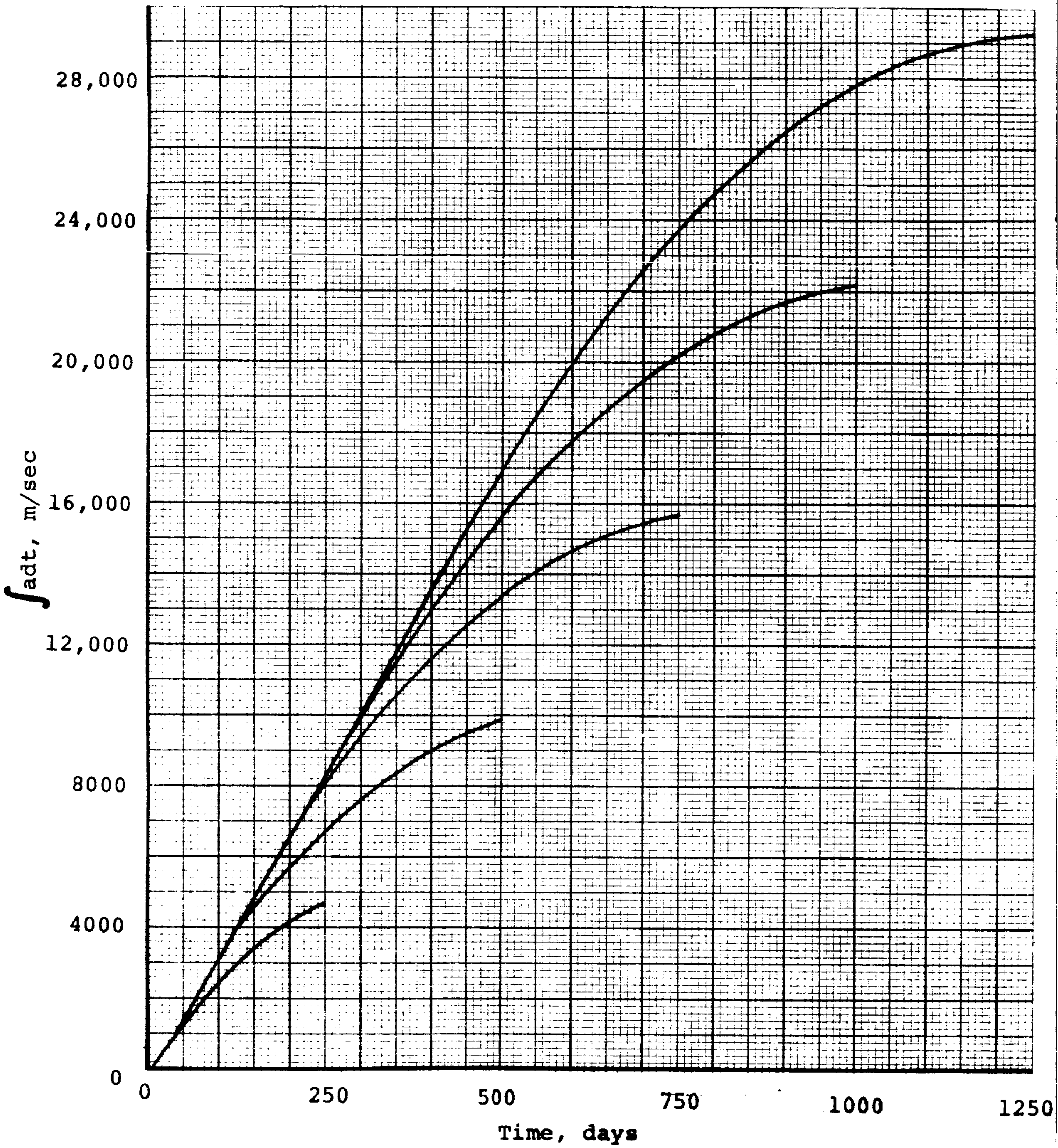

Figure 6.20. Velocity Added for Earth to Jupiter Transfer Using A Linear Power Profile, I = 3500 sec, a_o = 0.0004 m/sec^2

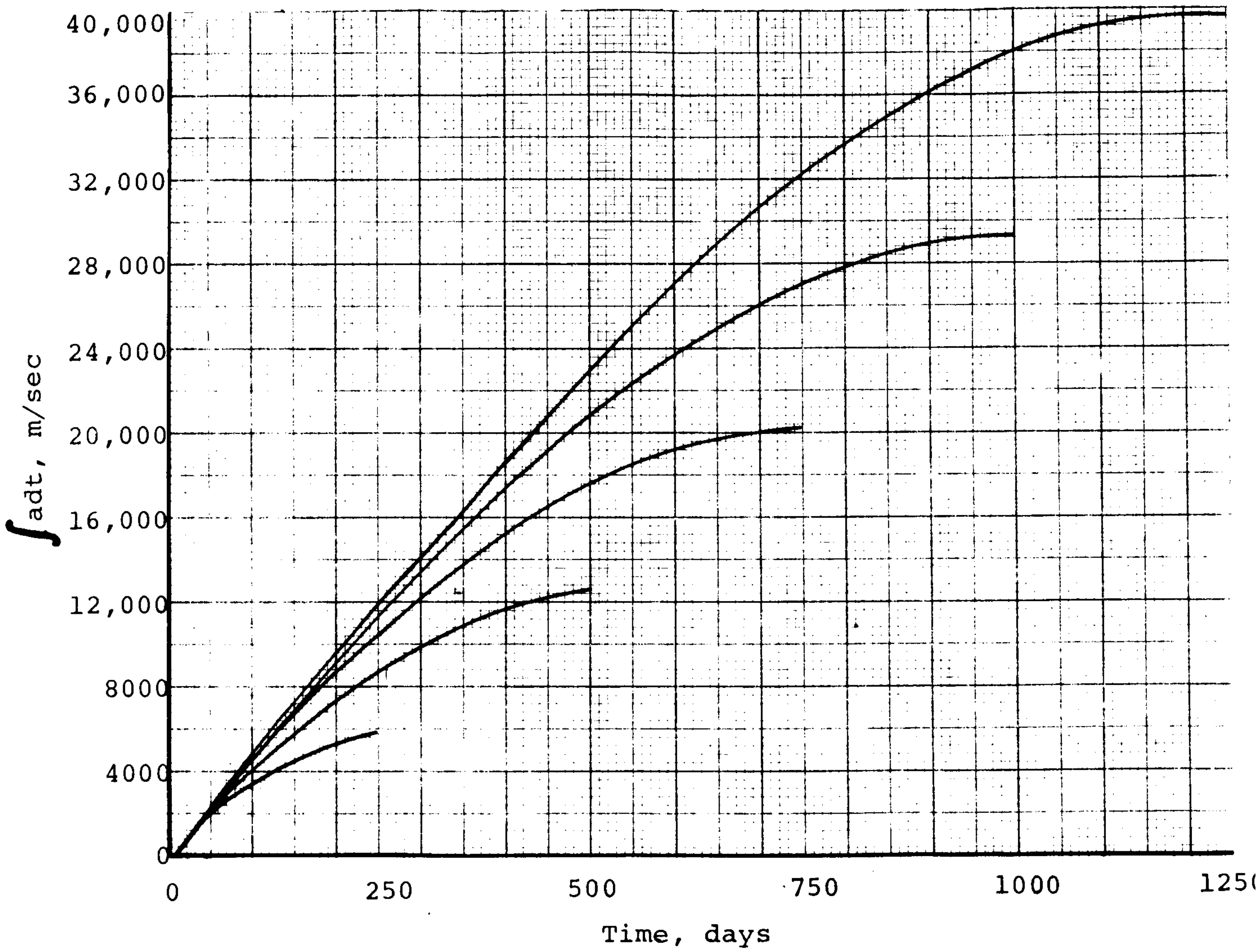

Figure 6.21. Velocity Added for Earth to Jupiter Transfer Using A Linear Power Profile, I = 3500 sec, $a_o = 0.0005$ m/sec^2.

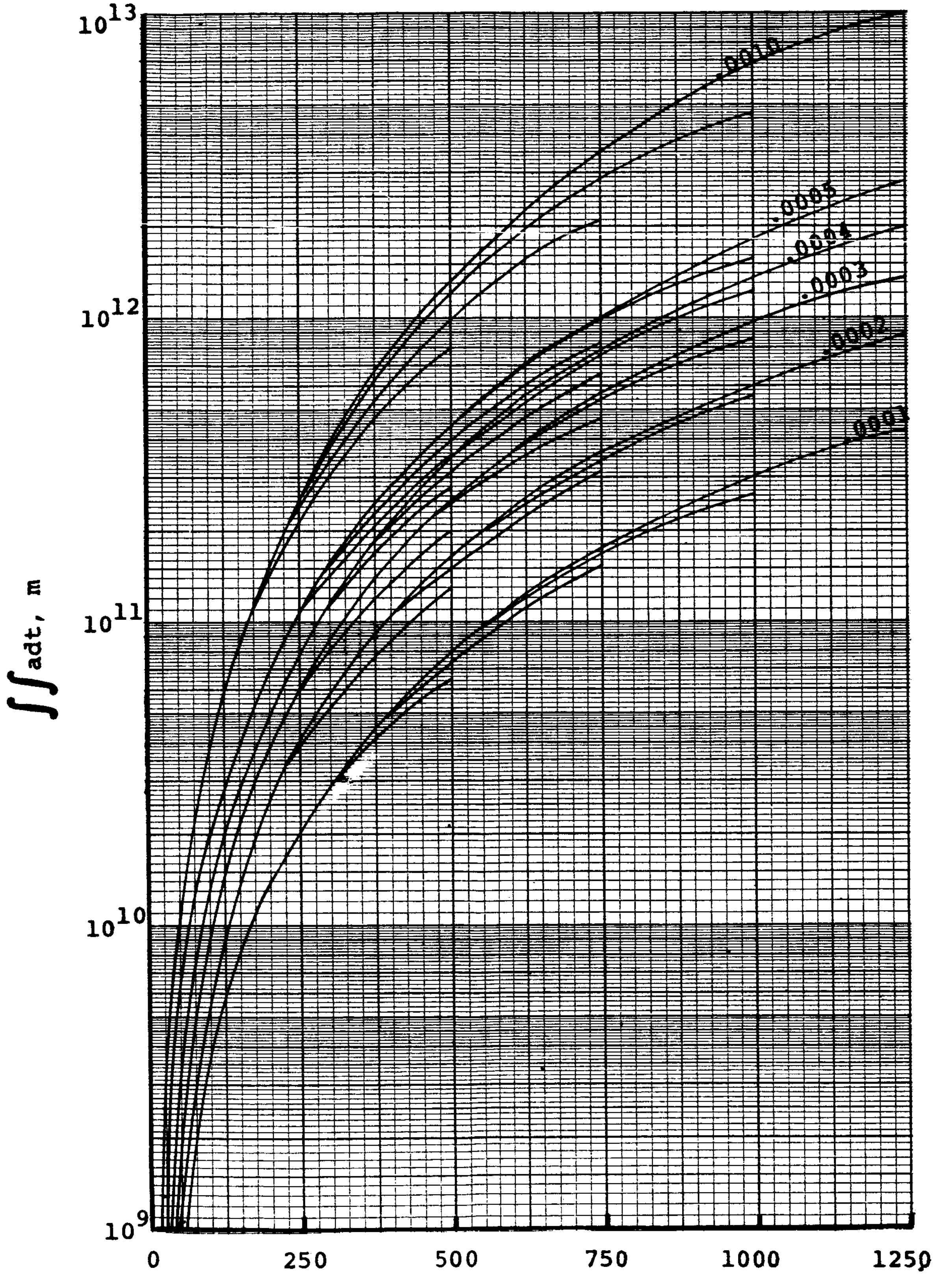

Figure 6.22. Length for Earth of Jupiter Transfer Using A Linear Power Profile and I = 3500 sec.

N67-36947

ALUMINUM COLLOID FORMATION BY HOMOGENEOUS NUCLEATION IN A SUPERSONIC NOZZLE

by Harry I. Leon, Fariborz P. Saheli, and
William R. Mickelsen

INTRODUCTION

The use of the spent booster rocket tankage as a propellant for electric spacecraft has been shown to be very desirable[7.1]. For many missions, the payload could be more than doubled if this spent tankage could be used. Research has been directed toward development of a charged-particle electrostatic thruster that can operate with aluminum propellant. This section contains the principles involved in aluminum colloid formation in a supersonic nozzle. The section also includes parameter studies made on the important variables to help determine the optimum nozzle design.

THEORY AND METHOD OF ANALYSIS

Condition for Condensation to Form During Supersonic Expansion

The rate of change of pressure with respect to temperature during an isentropic expansion is given by:

$$\frac{dp}{dT} = \frac{C_p}{R}\frac{P}{T} \tag{7.1}$$

where R is the gas constant of the vapor, and C_p is the specific heat of the vapor.

The rate of change of the saturation pressure with temperature is given by the Clausius - Chapeyron equation:

$$\frac{dP_\infty}{dt} = \frac{h_{fg}}{(V_v - V_L)T} \tag{7.2}$$

where V_L and V_v is the specific volume of the liquid and the vapor phases and h_{fg} is the latent heat of vaporization since $V_v - V_L \doteq V_v$ and $V_v = 1/\rho_v$ where ρ_v is the density of the vapor. Using the perfect gas law, $\frac{P}{RT} = \frac{1}{V_v}$, the Clausius - Clapeyron equation can be rewritten as:

$$\frac{dP_\infty}{dT} = \frac{P}{T^2}\frac{h_{fg}}{R} \qquad (7.3)$$

Comparing this to the rate of change of pressure with temperature with isentropic expansion:

$$\frac{dP_\infty/dt}{dP/dt} = \frac{Ph_{fg}/T^2R}{C_pP/RT} = \frac{h_{fg}/T}{C_p} \qquad (7.4)$$

The ratio for aluminum (at boiling point) is:

$$\frac{dP_\infty/dt}{dp/dt} = \frac{70{,}200 \text{ g-cal/g-atom}}{(2450 + 273)^\circ\text{K}/(5.1 \text{ g-cal/g-atom}^\circ\text{K})} = 5.04$$

Thus, when $h_{fg}/T > C_p$, the saturation vapor pressure decreases with decreasing temperature more rapidly than does the static pressure in an isentropic expansion.

Since

$$\frac{h_{fg}}{T} = 5.04\ C_p$$

aluminum should condense during a supersonic expansion.

The supersaturation ratio, P/P_∞, continually increases until saturation, and eventually supersaturation is obtained. This is shown on Figure 7.1 below.

If $h_{fg}/T < C_p$, an isentropic compression would be necessary for approach to saturation condition.

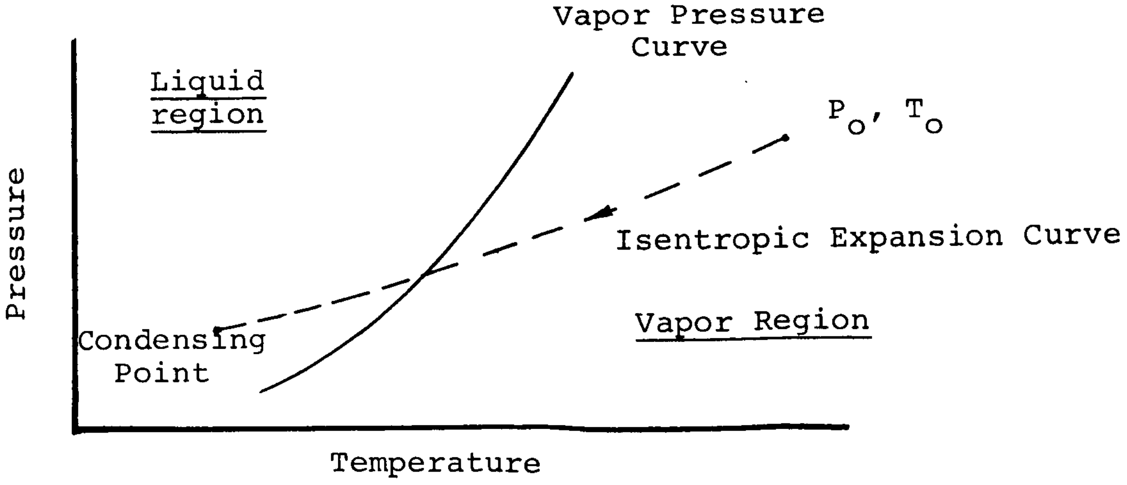
Vapor Pressure Curve
Liquid region
P_o, T_o
Pressure
Isentropic Expansion Curve
Vapor Region
Condensing Point
Temperature

Figure 7.1. The Comparison of Vapor Pressure Curve with an Isentropic Expansion for a Condensing Vapor

Formation of the Critical Size Droplet (or Colloid)

The energy required for droplet formation is given by the Gibbs free energy:

$$\Delta G = Vdp - s\ dT$$

V = specific volume, s = entropy

The minumum change of free energy for vapor molecules in reducing their pressure P to the saturation value P_∞ is:

$$\Delta G_1{}^* = 4/3\pi r^3\ \rho_L\ RT\ \ln P/P_\infty$$

The surface free energy for creation of small drops is:

$$\Delta G_2{}^* = 4\pi (r)^2 \sigma$$

Net change in free energy is:

$$\Delta G = \Delta G_2 - \Delta G_1$$

or

$$\Delta G = 4\pi (r^2)\sigma - 4/3\pi\ r^2\ \rho_L\ RT\ \ln\ (P/P_\infty)$$

The minimum size (critical radius, r*) droplets that can exist is given when $\frac{\Delta G}{dr} = 0$ which can be thought of as the maximum activation energy required for the formation of a droplet. This is shown on the figure below:

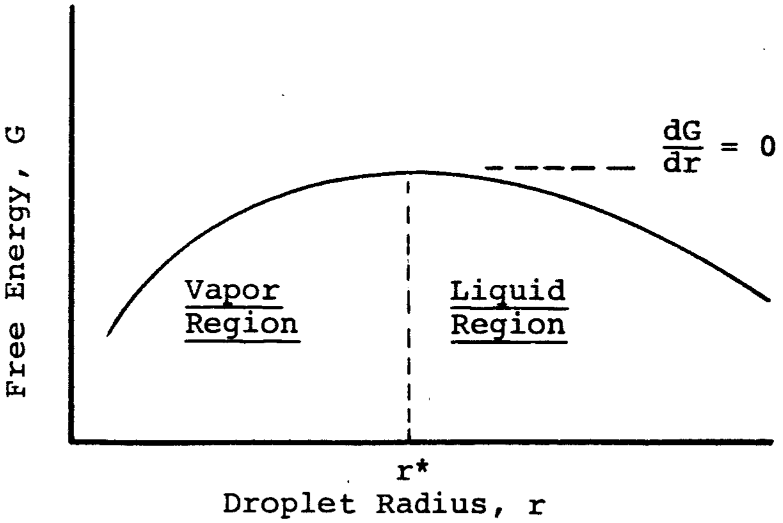

Figure 7.2. Free Energy Versus Droplet Radius

Taking the derivative of the equation above:

$$8\pi r^* \sigma = 4\pi r^2 \rho_L RT \ln (P/P_\infty)$$

or

$$r^* = \frac{2\sigma}{\rho_L RT \ln (P/P_\infty)} \qquad (7.5)$$

Note that the unknown in the equation is the ratio of P/P_∞ where the critical size is found. This ratio can be determined by test.

Example: The critical droplet size for aluminum condensation versus stagnation pressure, P, and temperature T, was computed using the following data:

surface tension = 520 dyne/cm
density of liquid = 2.26 g/cm^3
gas constant, R, = 8.317×10^7 ergs/^{o}K/mole
atomic weight = 26.97 g/mole

$$r^* = \frac{2(520)}{(2.26)\ \frac{(8.317 \times 10^7)}{26.97}\ T \ln (P/P_\infty)}$$

$$r^* = \frac{1.49 \times 10^{-4}}{T \ln (P/P_\infty)}$$

The value of r* is shown for various static temperatures and P/P_∞ ratios on Figure 7.3.

Rate of Droplet Formation

A distribution of embryos exists which satisfies a Boltzman type of distribution relation:

$$n_g = N_a e^{-\Delta G/KT} \qquad (7.6)$$

where n_g is the number of cluster of g molecules, and K is Boltzman constant.

Similarly, the rate of droplet formation, J, can be written:

$$J = \left(\frac{P}{KT}\right)^2 \frac{1}{\rho_L} \sqrt{\frac{2\sigma M}{\pi N_a}}\, e^{-4\pi r^{*2}\sigma/3KT} \qquad (7.7)$$

where M = Molecular weight, N_a = Avagadro's number, $P/KT\rho_L$ is proportional to number of molecules, $(2\sigma M/\pi N_a)^{1/2}$ is proportional to the diffusion rate. Note the strong dependence of nucleation rate on surface tension σ, especially since r^* is also proportional to σ.

PARAMETER STUDY FOR DESIGN OF A PROTOTYPE OF THE SUPERSONIC ALUMINUM COLLOID NOZZLE

Study of Plenum Conditions Required

This study was conducted to determine how the choice of stagnation conditions affects the size and initial ratio of particle nucleation. For this initial study, it was assumed that the expansion through the nozzle was isentropic and that the vapor behaved as a perfect gas. This assumption is good until a substantial fraction of the aluminum condenses.

The ratios of the stagnation pressure to the static pressure, the stagnation temperature T_o to the static temperature are a function of the Mach number, M, by the following relationships:

$$\frac{P}{P_o} = (1 + \frac{\gamma-1}{2} M^2)^{\gamma/(\gamma-1)} \qquad (7.8)$$

$$\frac{T_o}{T} = 1 + \frac{\gamma-1}{2} M^2 \qquad (7.9)$$

where γ = specific heat ratio, where the relationship between P and T can be written as:

$$P = P_o\left(\frac{T}{T_o}\right)^{\gamma/(\gamma-1)} \qquad (7.10)$$

Thus, as the vapor is expanded through the nozzle, the pressure P, and temperature, T, decrease. The vapor pressure, P_∞, for aluminum was found to decrease faster than the static pressure during an isentropic expansion. When the ratio of P/P_∞ at a given temperature is large enough to overcome the energy barrier between vapor and liquid phase (see Figure 7.2), droplets of critical radius should form. The critical ratio of P/P_∞ is believed to be about 6 for aluminum. Since the static temperature, T, and pressure, P, are only a function of the stagnation conditions, T_o, P_o, and the Mach number, M, (as shown by Equations (7.8) and (7.9), the choice of stagnation conditions will also determine the velocity at which condensation will occur. The effect of the choice of the plenum stagnation pressure and temperature on the condensate was studied using a design considered in previous work[7.1]. The design consisted of 2.6 mm throat diameter and plenum temperature of 1800°K and pressure of 0.005 atmosphere (3.8 mmHg). The flow-rate, $\dot{m}$, through the nozzle can be written as:

$$\dot{m} = \frac{A^* P_o}{\sqrt{T_o}} \sqrt{\frac{\gamma}{R}} \left(\frac{2}{\gamma + 1}\right)^{\frac{\gamma + 1}{2(\gamma - 1)}} \qquad (7.11)$$

From Equation (7.11), it is noted that, for a fixed nozzle throat area A^*, as long as the ratio $P_o/\sqrt{T_o}$ is held constant, the flow rate, $\dot{m}$, will be unchanged. To study the velocity of which condensation would form, various values of T_o were chosen and P_o was computed to hold the ratio of $P_o/\sqrt{T_o}$ constant. The Mach number, M, where condensation would begin was then computed as a function of the saturation ratio P/P_∞. The results of this analysis are shown on Figure 7.4. The importance of the stagnation temperature on the velocity is clearly shown on Figure 7.4. A stagnation pressure of 4 mmHg (.0053 atmospheres) pressure, a stagnation temperature of at least 2000°K is shown to be required to get the condensate to sonic velocity.

The rate of droplet formation, J, corresponding to the above nozzle design, was computed using Equation (7.7) and it shows J as a function of stagnation pressure, stagnation temperature, and saturation pressure ratio on Figure 7.5. The rate of droplet formation is shown on Figure 7.5 and was found to be too low for a nozzle design suitable for test in the CSU vacuum chamber. This rate of formation would require too large a nozzle to get a practical condensation fraction.

Study of Effects of Pressure and Temperature on Condensation Rates and Droplet Size

A general parameter study was made to determine the effects of the temperature and pressure on the condensation formation rates and the critical droplet sizes. A wide range of pressure and temperatures was chosen and an analysis was made using Equations (7.6) and (7.7). To have a high rate of droplet formation (see Figure 7.6), it was found that the static pressure where the condensate forms must be sufficiently large. It also should be noted from Figure 7.6 that the droplet sizes increase very rapidly (for a given static temperature) while the condensation rate falls rapidly because of inadequate static pressure.

Study of Nozzle Length Required

One of the basic requirements for the colloid nozzle for use in space is keeping the size as small as possible. The nozzle however, must be large enough for the heat of condensation to be removed or else the static temperature will increase quickly and the rate of condensate will decrease as shown on Figure 7.6. (More will be said on removal of the condensation heat later.) The length of the nozzle required for the aluminum vapor to condense, L, can be estimated as follows:

$$L = v_c \, t_c \qquad (7.12)$$

where v_c is the velocity of the condensate and t_c is the time for the aluminum to condense. This time for condensation to form can be approximated (assuming the rate of formation, J, and the critical droplet size, r* remains constant through the nozzle. Thus t_c can be written as:

$$t_c = \frac{\rho_v}{J \; 4/3 \pi r^{*3} \rho_L} \qquad (7.13)$$

where ρ_V = the density of the aluminum vapor and ρ_L = the density of the aluminum liquid. The velocity of the aluminum vapor, v, can be written as:

$$v = M\sqrt{\gamma RT} \tag{7.14}$$

Where M is the Mach number where the condensate forms, and $\sqrt{\gamma RT}$ is the velocity of sound in the aluminum vapor. If the temperature at which condensate forms is 1000°C, the velocity of sound in the aluminum vapor would be 805 m/sec. Assuming that the condensate forms at M = 1.25, the velocity of the condensate would be approximately 1000 m/sec. An analysis was made to roughly determine the length of the nozzle required for complete condensation of the aluminum vapor. This analysis assumed that:

1. The condensation rate J (shown on Figure 7.6) remained constant.
2. The velocity of the condensation was constant and equal to 1000 m/sec.

The distances required for condensation as a function of the static temperature and static pressure are shown on Figure 7.7. For testing in the CSU vacuum tank, the length would probably be between 10 to 100 cm. Using Figure 7.7, the pressure and the temperature required for an aluminum colloid nozzle test can be determined.

CONDENSATION HEAT REMOVAL

When the vapor in the nozzle forms the condensate, the latent heat of vaporization is released. The latent heat for liquid metals is very great compared to the specific heat. For example, the specific heat of liquid aluminum is 6.7 $\frac{\text{g cal}}{\text{g atom}^\circ\text{C}}$ while the latent heat of vaporization is 70,200 $\frac{\text{g cal}}{\text{g atom}}$. Thus, if the heat were not removed, the temperature of the aluminum droplet would greatly increase and the droplet would quickly re-evaporate. Furthermore, if the temperature of the aluminum vapor increases, the rate of condensation decreases rapidly (see Figure 7.6). It would be highly desirable, not only to remove the latent heat of the condensate, but also to lower the static temperature of the uncondensed aluminum vapor to help increase the rate of droplet formation. Two methods of removing the latent heat from the particles are being studied at present. These methods are cooling by the vapor expansion and cooling by gas injection.

Cooling by Vapor Expansion

It is possible to cool the vapor by expansion in the nozzle and to use this cooled vapor to remove the heat of the condensate droplets. The basic equation for this expansion cooling process is:

$$T_o = T + \frac{v^2}{2C_p} \tag{7.15}$$

Thus from Equation (7.15) it is seen that, in order to lower the static temperature, T, an increase of velocity, v, is required.

When the condensate starts to form in the nozzle the stagnation temperature of the stream is increased, as given by the equation below:

$$\dot{m}C_p \quad (T_{02} - T_{01}) = \dot{m}_L \, h_{fg} \tag{7.16}$$

where T_{01} and T_{02} are the respective stagnation temperatures upstream and downstream of the condensate, $\dot{m}$ is the total mass flow, $\dot{m}_L$ is the mass flow rate of the condensing liquid, and h_{fg} is the latent heat per unit mass of the condensing liquid. Equation (7.16) may be rearranged to give:

$$\frac{T_{02}}{T_{01}} = 1 + \frac{\dot{m}_L}{\dot{m}} \frac{h_{fg}}{C_p T_{01}} \tag{7.17}$$

The nozzle area charge required for the vapor expansion cooling of the condensate was studied for expansion having three basic criteria which are:

1. Constant Mach number of the vapor.
2. Constant velocity of the vapor.
3. Constant static temperature.

Using the criteria above, analyses were made to determine the area changes required to remove the condensation heat from various stagnation temperature ratios. The equations used in the analyses were derived from differential equations given in Chapter 8 of Reference 7.2. The equations are stated below.

The area charge required for condensation heat removal with a constant vapor Mach number is given by:

$$A_2/A_1 = \left(\frac{T_{02}}{T_{01}}\right)^{\frac{1 + \gamma M^2}{2}} \qquad (7.18)$$

The area charge required for condensation heat removal with a constant vapor velocity is given by:

$$\frac{A_2}{A_1} = \left(\frac{T_{02}}{T_{01}}\right)^{1 + \frac{\gamma - 1}{2} \overline{M}^2} \qquad (7.19)$$

where $\overline{M}$ is the average Mach number between point 1 and 2.

The area charge required for condensation heat removal with a constant vapor static temperature is given by:

$$\frac{A_2}{A_1} = \left(\frac{T_{02}}{T_{01}}\right)^{\frac{(\gamma \overline{M}^2 - 1)(1 + \frac{\gamma - 1}{2} \overline{M}^2)}{(\gamma - 1)\overline{M}^2}} \qquad (7.20)$$

A parameter study was made using Equations (7.18), (7.19), and (7.20) and the results of these analyses are shown on Figures 7.8, 7.9 and 7.10 respectively.

It should be noted that Equations (7.18), (7.19) and (7.20) assume that the vapor acts as a perfect gas and that the fraction of the condensing gas is small. When the condensation is a large fraction of the vapor, an additional term must be added to the above equation. More detailed analyses of the condensate vapor expansion cooling would require a computer program which is under study at present. The answer given by the above method, however, is satisfactory for this preliminary study.

To show the order of magnitude of the area charge required to cool the nozzle during a condensation process, a typical numerical example is given below.

Example Calculation of Cooling Condensation by Vapor Expansion.

This calculation is to determine the area charge of the velocity and temperature of the condensate cooled by vapor expansion. Given aluminum vapor condensation has started at a static pressure of .03 atmospheres and static temperature of $1200^{o}C$, ($1473\ ^{o}K$) and a Mach number of 1.25.

To find:

a. The stagnation pressure and temperature conditions.
b. The rate of droplet formation and droplet size.
c. The velocity of colloidal particle at condensation start.
d. The length required for 20% of the vapor to condense.
e. With 20% of the vapor condensing, find the area change, static temperature, and velocity of vapor for the following conditions:
  1. Constant Mach number during condensation.
  2. Constant velocity during condensation.
  3. Constant static temperature during condensation.

Solution:

a. The stagnation pressure and temperature can be found using Equations (7.8) and (7.9):

$$T_{01}/T_1 = 1 + \frac{\gamma - 1}{2} M^2 = 1 + \frac{1.67 - 1}{2} (1.25)^2 = 1.523$$

$$T_{01} = (1473)(1.523) = 2250^{o}K$$

$$P_{01}/P_1 = 1 + \frac{\gamma - 1}{2} M^2\ \gamma/(\gamma - 1) = (1.523)^{1.67/(1.67 - 1)} = 2.85$$

$$P_{01} = (.03)(2.85) = .0855 \text{ atmospheres}$$

b. The rate of droplet formation and droplet can be found using Figure 7.6 which gives:

$J = 1.6 \times 10^{21}$ particles/cm^{3}sec

$r^* = 3.5\ A^{o}$

c. The velocity at the start of condensation can be computed using Equation (7.14):

$$v_1 = M\sqrt{\gamma RT} = 1.25\left[1.67\,\frac{(8320)}{26.97}\,(1473)\right]^{1/2}$$

$$v_1 = 1.25\,(870) = 1090\ \text{m/sec}$$

d. The fraction of aluminum vapor condensing per cm length can be estimated as follows:

The density of the aluminum vapor, ρ_v at start of condensation is equal to:

$$\rho_v = \frac{P}{RT} = \frac{(.03)(26.97)}{(82.05)(1473)} = .67 \times 10^{-5}\ \text{g/cm}^3$$

The mass flow rate of the condensate, $\dot{m}_L$ is equal to:

$$\dot{m}_L = J(4/3\pi r^{*3})\,\rho_L = (1.6 \times 10^{21})\left[(4/3)\pi(3.5 \times 10^{-8})^3\right]2.26$$

$$\dot{m}_L = .65\ \text{g/cm}^3\text{sec}$$

The distance required for 20% of the aluminum vapor to condense $L_{.20}$ (assuming constant velocity and constant condensation rate) is given by Equation (7.12) as follows:

$$L_{.20} = \frac{(.20)(\rho_v)v_1}{\dot{m}_L} = \frac{.20(.67 \times 10^{-5})(1.09 \times 10^5)}{.65} = .225\ \text{cm}$$

e. The stagnation temperature rise, ΔT, due to condensation fraction, $\dot{m}_L/\dot{m}$ is equal to:

$$\Delta T = \frac{\frac{\dot{m}_L}{\dot{m}}\,h_{fg}}{C_{p_v}} \qquad (7.16)$$

The ΔT for the aluminum vapor with the 20% condensing is:

$$\Delta T = \frac{(.20)(70{,}200)}{5.1} = 2760^\circ K$$

Thus: $T_{02} = T_{01} + \Delta T$

$$T_{02} = 2250 + 2760 = 5010^{\circ}K$$

Case 1. Constant Mach number

For constant Mach number, the static temperature at the end of 20% condensation, T_2, can be solved for as follows:

$$\frac{T_{02}}{T_{01}} = \frac{T_2}{T_1} \qquad (7.21)^*$$

$$\frac{5010}{2250} = \frac{T_2}{1473}$$

$$T_2 = (2.223)(1473) = 3280^{\circ}K$$

The velocity at the end of 20% condensation, v_2, is found using Equation (7.14):

$$v_2 = 1.25 \left[1.67 \frac{(8320)}{26.97} (3280)\right]^{\frac{1}{2}} = 1{,}625 \text{ m/sec}$$

The area change required to maintain a constant Mach number during heating is given by Figure 7.8. Reading this figure at $T_{02}/T_{01} = 2.223$ and Mach number of 1.25, the area ratio required is:

$$A_2/A_1 = 4.2$$

Case 2. Constant velocity

The static temperature after 20% condensation is solved for using Equation (7.15) in the following form:

$$\frac{T_{02}}{T_{01}} = \frac{T_2 + \dfrac{V_2^2}{2C_p}}{T_1 + \dfrac{V_1^2}{2C_p}} \qquad (7.22)$$

---

* See Equation (7.11) of Reference 7.2.

Since $T_{02}/T_{01} = 2.223$, and $V_1 = V_2 = 1090$ m/sec, T_2 can be solved for as follows:

$$\frac{V_1^{\,2}}{2C_p} = \frac{(1090\ \text{m/sec})^2}{2\left(\dfrac{5.1\ \dfrac{\text{g. cal}}{\text{g atom}^{\circ}\text{K}}}{26.97\ \dfrac{\text{g}}{\text{g atom}}}\right)\left(4.184\ \dfrac{\text{joules}}{\text{cal}}\right)(1000\ \text{g/kg}} = 753^{\circ}\text{K}$$

substituting into Equation (7.22) gives:

$$2.223 = \frac{T_2 + 753}{1473 + 753}$$

and

$$T_2 = 4117^{\circ}\text{K}$$

The area change for this constant velocity expansion is given on Figure 7.9. However, before the curve can be used, the average Mach number $\overline{M}$ between points 1 and 2 must be solved. At point 2, the Mach number can be solved for, using Equation (7.14):

$$1090 = M_2 \left[1.67 \left(\frac{8320}{26.97}\right)(4117)\right]^{\frac{1}{2}}$$

$$M_2 = 1.335$$

The average Mach number $\overline{M}$ is approximately equal to:

$$\overline{M} = \frac{M_1 + M_2}{2} = \frac{1.25 + 1.335}{2} = 1.292$$

Thus, using Figure 7.19, the area charge ratio is obtained:

$$A_2/A_1 = 3.48$$

Case 3. Constant static temperature

For constant static temperature during condensation, the velocity V_2 and the area ratio A_2/A_1 are computed below. To solve for V_2, Equation (7.22) can be written as follows:

$$2.223 = \frac{1473 + \dfrac{V_2^{\,2}}{(2)\dfrac{(5.1)}{26.97}(4.184)(1000)}}{1473 + 753}.$$

Therefore:

$V_2 = 2350$ m/sec

The Mach number at point 2 is equal to:

$$M_2 = \frac{2350}{870} = 2.70$$

and

$$\overline{M} = \frac{1.25 + 2.70}{2} = 1.975$$

Using Figure 7.10, the required area ratio is obtained:

$A_2/A_1 = 49.5$

The results of this example and discussion comparing the three cases of expansion cooling during condensation heating are summarized below:

	Velocity at Point 2 m/sec	Static Temperature at Point 2 ^{o}K	Area Ratio Required A_2/A_1
Constant Mach No.	1625	3280	4.2
Constant Velocity	1090	4117	3.48
Constant Static Temperature	2350	1473	49.5

It is noted that, due to the high static temperature rise for the constant Mach number and the constant velocity cases, the condensate would have evaporated; therefore, there would not have been 20% condensation as assumed. The actual amount of condensate could be solved for by trial and error using the similar method as above.

The area ratio of the constant static temperature case is so great that a shock would probably be formed in the nozzle since the length of the condensation region is so short. For an optimum design of the nozzle, the condensation rate must be balanced with the length required for cooling of the condensate. It can therefore be concluded that the constant static temperature expansion cooling of the condensate would give the highest amount of condensate but would require a longer nozzle.

It should also be noted that the vapor-expansion cooling of the condensate at constant static temperature yields the highest exit velocity. This gain of velocity helps offset the requirement for a longer nozzle.

Cooling by Gas Injection

The injection of a non-condensing cooling gas in the condensing vapor region has been considered as a method of cooling. The gas would be injected into the nozzle at the point where the condensation is desired. The analysis of the nozzle upstream of the injection point would be done in a manner similar to the one above. The injected gas could be cooled very much below the temperature of the nozzle condensing gas and could be injected at high velocity. When the injected gas meets the condensing vapor, a very large fraction (perhaps all) of the condensate heat could be removed. This would mean that it could be possible to have all the gas condensing at once.

The choice of the injection gas is under study, but at present, helium and hydrogen seem the most promising because of the following reasons:

1. They have a high specific heat, which would release the amount of gas required.
2. They have a high ionization potential, helium 24.6 ev, hydrogen 13.6, compared to aluminum ionization energy of 5.98 ev. This means that they would not interfere with the charging of the aluminum colloidal particles if the ionization energy were kept below 13.6 ev (24.0 ev).
3. They have low molecular weight which means a high thermal acceleration is possible. Therefore, this injected gas would help increase the velocity of the droplets.

The decision between helium and hydrogen would depend on whether hydrogen would be reactive with the aluminum vapor or the walls of the nozzle. If hydrogen were not to react, it would probably be the best choice since it has higher specific heat and

and lower molecular weight than helium. Also hydrogen would be easier to store since its freezing point is higher.

There are several advantages and disadvantages of the gas injection system of cooling the condensate as compared with the vapor expansion systems. Table 7.1 compares the two methods of cooling the condensate.

There also is the possibility of using both the vapor expansion and the gas injection systems on the same nozzle. This would be done by first cooling the gas by vapor expansion (to save on the injection gas) and then using the gas injection systems. This type of analysis is being considered in the development of a computer code.

A computer code is being developed to handle analysis of the nozzle from the plenum through the condensation and colloidal particle growth. This code will give the nozzle contour required for a given exit velocity and condensate fraction. The code will be able to determine the colloidal particle size along the nozzle and its velocity. (More will be said about the particle velocity below.) Provision will be made in the code for gas injection at any point along the nozzle.

The colloidal particles would grow, due to vapor condensating on them and to collisions between the particles. As the particles grow, the velocity difference between the vapor molecules and the colloidal particles will increase. The method of analysis which will be used in the code is developed below:

RELATIVE VELOCITY BETWEEN THE CONDENSATE AND THE GAS

Theory

The drag force, F_D, acting on a spherical body with a velocity relative to a gas may be represented by:

$$F_D = C_D A \quad 1/2 \, \rho_V (\Delta v)^2 \qquad (7.23)$$

F = force acting on particle

C_D = drag coefficient

ρ_V = gas density

A = frontal area of condensate = πr^2

Δv = relative velocity between gas and particle = $v_g - v_c$

μ_g = viscosity of the gas

The acceleration of the particle is determined by the force acting on its mass:

$$F_a = ma = 4/3\pi\rho_s r^3 \ a = 4/3\pi\rho_s r^3 \frac{dv_c}{dt} \qquad (7.24)$$

ρ_s = density of particle, v_s it velocity
r = radius of particle
a = acceleration of particle = dv_c/dt

Equation (7.23) and (7.24)

$$4/3\pi\rho_s r^3 \frac{dv_s}{dt} = C_D \ A \ (1/2 \ \rho_V(v_g - v_s)^2$$

or

$$\frac{dv_s}{dt} = \frac{3C_D\rho_V}{8\rho_s r} \quad (v_g - v_c)^2 \qquad (7.25)$$

Since C_D is a function of $(v_g - v_c)$, its equation must be substituted into Equation (7.25) before it can be integrated. Example: for small velocity lags $R_e < 2$, Stokes Law can be used where:

$$C_D = 24/R_e \qquad (7.26)$$

Where the Reynolds Number, R_e is:

$$R_e = \frac{2(v_g - v_c) \ r}{\mu_g} \qquad (7.27)$$

substituting Equation (7.27) into (7.26):

$$C_D = \frac{12\mu_g}{(v_g - v_c) \ r} \qquad (7.28)$$

Substituting Equation (7.28) into (7.25):

$$\frac{dv_c}{dt} = \frac{9\mu_g}{2r^2} \ \frac{(v_g - v_c)}{\rho_s} \qquad (7.29)$$

Similarly, the drag coefficient can be written as a function for all Reynolds numbers. For example: if $2 < R_e > 5$, use Oseen's equation:

$$C_D = \frac{24}{R_e} + (1 + 3/16\ R_e)$$

Method of Iteration to be Used in the Code

If condensation starts at point 1, then at this point it is assumed $v_s = v_g$.

The radius, r, will change with time as the particle size increases. At point 1, the particle will have its critical radius, r*. It is also known that:

$$\frac{dv_c}{dt} \leq \frac{dv_g}{dt} \qquad (7.30)$$

Thus, at point 1, assume $\frac{dv_c}{dt} = \frac{dv_g}{dt}$:

Thus, since $\frac{dv_g}{dt}$ is known from the nozzle design, $(v_g - v_c)$ can be solved using either Equation (7.25) or (7.29) depending on the Reynold number. Using the value for $(v_g - v_c)$, the acceleration force on particle, F_a can be found. Compare this to the drag force on the particle, F_D. If $F_a > F_D$, reduce estimate of $\frac{dv_c}{dt}$ until $F_D = F_a$ using method below:

$$\frac{dv_c}{dt}_{\text{new}} = \left(\frac{dv_c}{dt}\right)_{\text{old}} \left(\frac{F_D}{F_a}\right)^{\alpha}_{\text{old}} \qquad (7.31)$$

Note that the value of α will be determined by the value which makes the code converge the fastest. This value will also depend on the rate of expansion of the nozzle. It is estimated that, α will have its best value between 0.25-0.50.

CONCLUSION AND FUTURE WORK

This report shows the fundamental principles involved in aluminum colloidal formation by homogeneous nucleation in a supersonic nozzle. The design theory and requirements are discussed from the plenum, where the solid aluminum would be vaporized, through the region of condensation. The following topics were discussed:

1. The theory of homogeneous nucleation
    a. Critical size of the aluminum colloidal particles.
    b. Rate of colloid formation of the aluminum colloidal particles and velocity of these particles.
    c. Length of the nozzle required for condensation.
2. Condensate heat removal
    a. The cooling of the condensate by the vapor expansion.
    b. The cooling of the condensate by gas injection.
3. The analysis of the velocity of the condensate compared to the vapor velocity.

The preliminary analysis of the design of the supersonic nozzle for aluminum colloid formation by homogeneous nucleation yielded the following conclusion.

The choice of the plenum temperature and pressure determine the velocity of the condensate and the initial rate of formation of the droplets. The stagnation temperature is the controlling parameter for the condensate velocity. If the stagnation temperature is too low, the condensate will start before the throat of the nozzle unless the pressure is very low. A higher plenum temperature would increase the velocity of the condensate, but too high a temperature would reduce the rate of formation unless balanced by an increase in plenum pressure.

The stagnation pressure has a very strong effect on the rate of droplet formation. If the pressure is too high, the condensate will take place too rapidly for efficient heat removal; if the pressure is too low, the condensate rate will be low and the nozzle will have to be very long to obtain a sufficient condensation fraction.

A preliminary estimate of the optimum choice of temperature and pressure for the nozzle design can be obtained from a study of Figures 7.6 and 7.7. Once the length of the nozzle required for the heat removal of the desired condensation fraction is determined, the use of Figure 7.7 will show the static temperature and pressure desired for the condensation process. Once the static temperature and static pressure are determined and the desired condensate velocity is known, the plenum condition can be determined by use of Equation (7.9) and (7.10). The flow rate, $\dot{m}$, desired for a design will also be known; using this flow rate the nozzle throat area can be determined by using Equation (7.11).

Two methods of removing the condensation heat were studied. These methods were the cooling of the condensate by vapor-expansion, and the cooling of the condensate by gas injection.

The vapor-expansion cooling of the condensate at constant static temperature was found to be more efficient than vapor-expansion cooling at either constant Mach number or at constant velocity. The constant static temperature process gave the highest condensation fraction and the highest velocity.

The gas-injected system for cooling the condensate would permit the nozzle to be smaller in the condensation region and to have a higher condensation fraction than would the vapor-expansion cooling. The advantages of the gas injection system must be evaluated, taking into account the weight and the reliability penalties paid for a more complicated system. It may be found that a combination of the vapor-expansion and gas-injection system might be the best design.

Future work on aluminum colloid formation by homogeneous nucleation will be directed toward the following goals:

1. Development of a more exact method of analysis in the condensation region of the nozzle. (This preliminary analysis assumed the vapor to be a perfect gas in the condensation regions.) The analysis of the nozzle condensation region design will be made by assuming the nozzle to be the summation of many small intervals. The analysis will then be made of the conditions existing in each interval and will optimize the design for each interval.
2. A detailed design will be made of a prototype suitable for testing in the CSU vacuum chamber.
3. A computer code is being developed to aid in tasks 1 and 2 above.

References

7.1. Mickelsen, W. R: Advanced Electric Propulsion Research, Annual Report for January 1, 1966 to December 31, 1966, prepared for National Aeronautics and Space Administration. Grant NGR06-002-032.

7.2. Shapiro, H. A.: The Dynamics and Thermodynamics of Compressible Fluid Flow, Volume 1, Ronald Press Company, 1953.

7.3. Shin, Y. W.: "Theoretical Analysis of Condensation of Pure Vapors in Supersonic Nozzles". Masters Thesis, Colorado State University, 1965.

TABLE 7.1

Comparison of Vapor Expansion System with the

Gas Enjection System of Cooling Condensate

ITEM	VAPOR EXPANSION	GAS INJECTION
Fraction of Vapor Condensation possible	probably less than 50% due to high weight and size penalty	100%
Additional equipment for operation of nozzle	None	Injection gas, gas storage tanks, pumps, heat exchanger, gas recovery mechanism

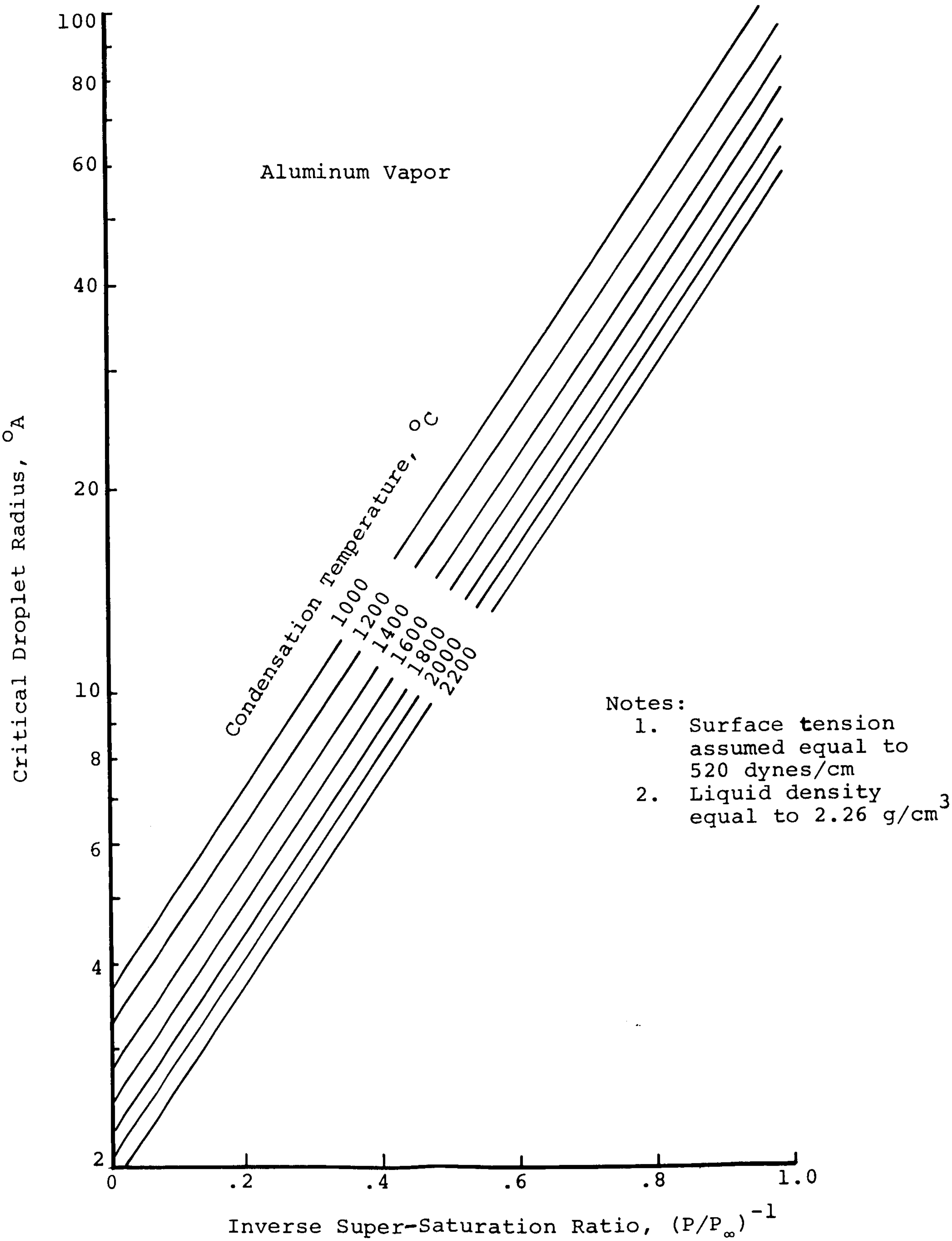

Notes:
1. Surface tension assumed equal to 520 dynes/cm
2. Liquid density equal to 2.26 g/cm^3

Figure 7.3. Critical Droplet Radius Versus Supersaturation Pressure and Temperature

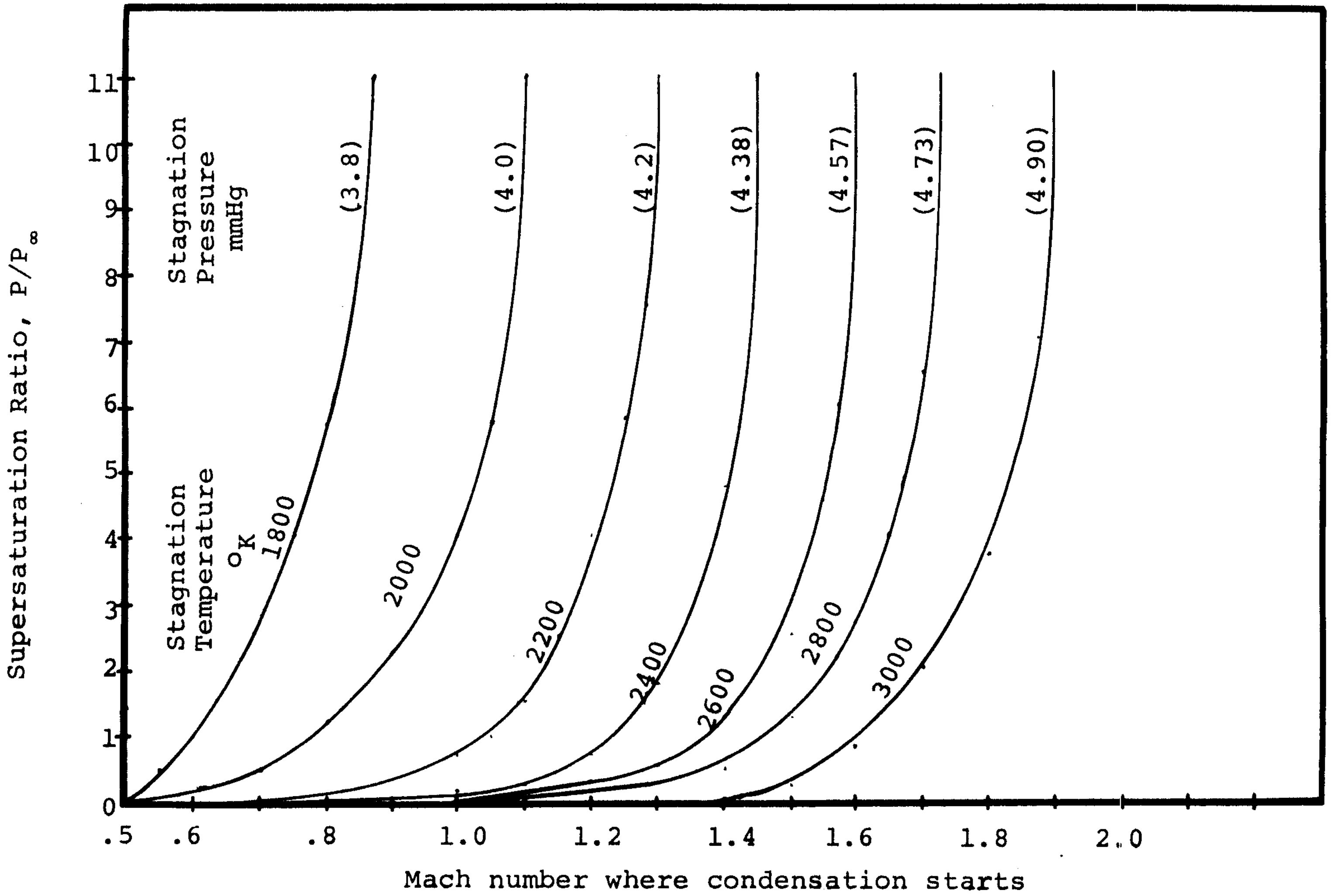

Figure 7.4. Mach Number Where Condensation Starts as a Function of Supersaturation Ratio, Stagnation Temperature and Stagnation Pressure.

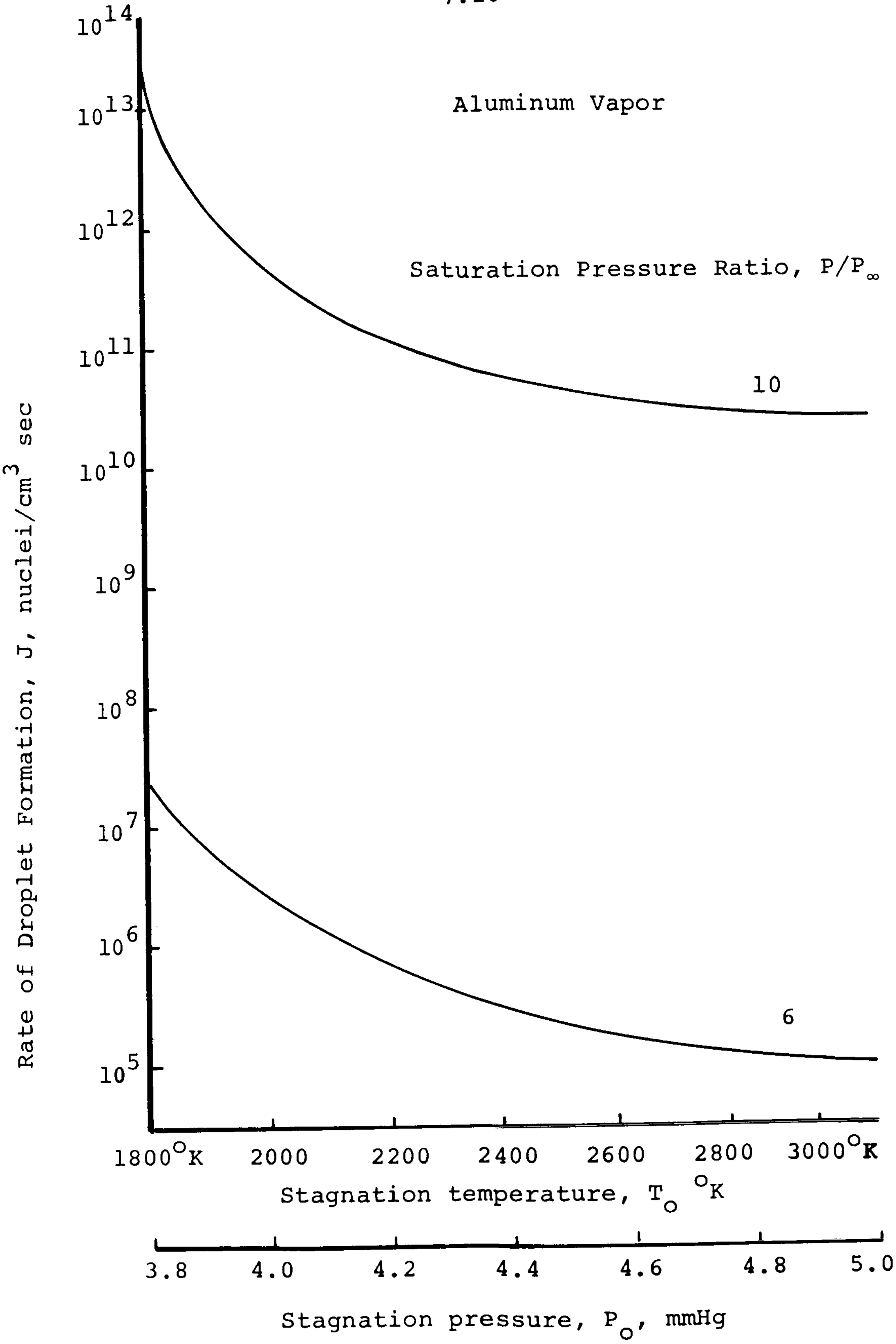

Figure 7.5. Rate of Droplet Formation as Function of Stagnation Temperature and Pressure as a Function of Saturation Pressure Ratios.

Numbers on the curves is static temperature, °C.

——— Rate of Droplet Formation

– – – – Critical Droplet Radius

Notes: 1. Aluminum Vapor
2. Surface tension assumed 520 dyne/cm^2

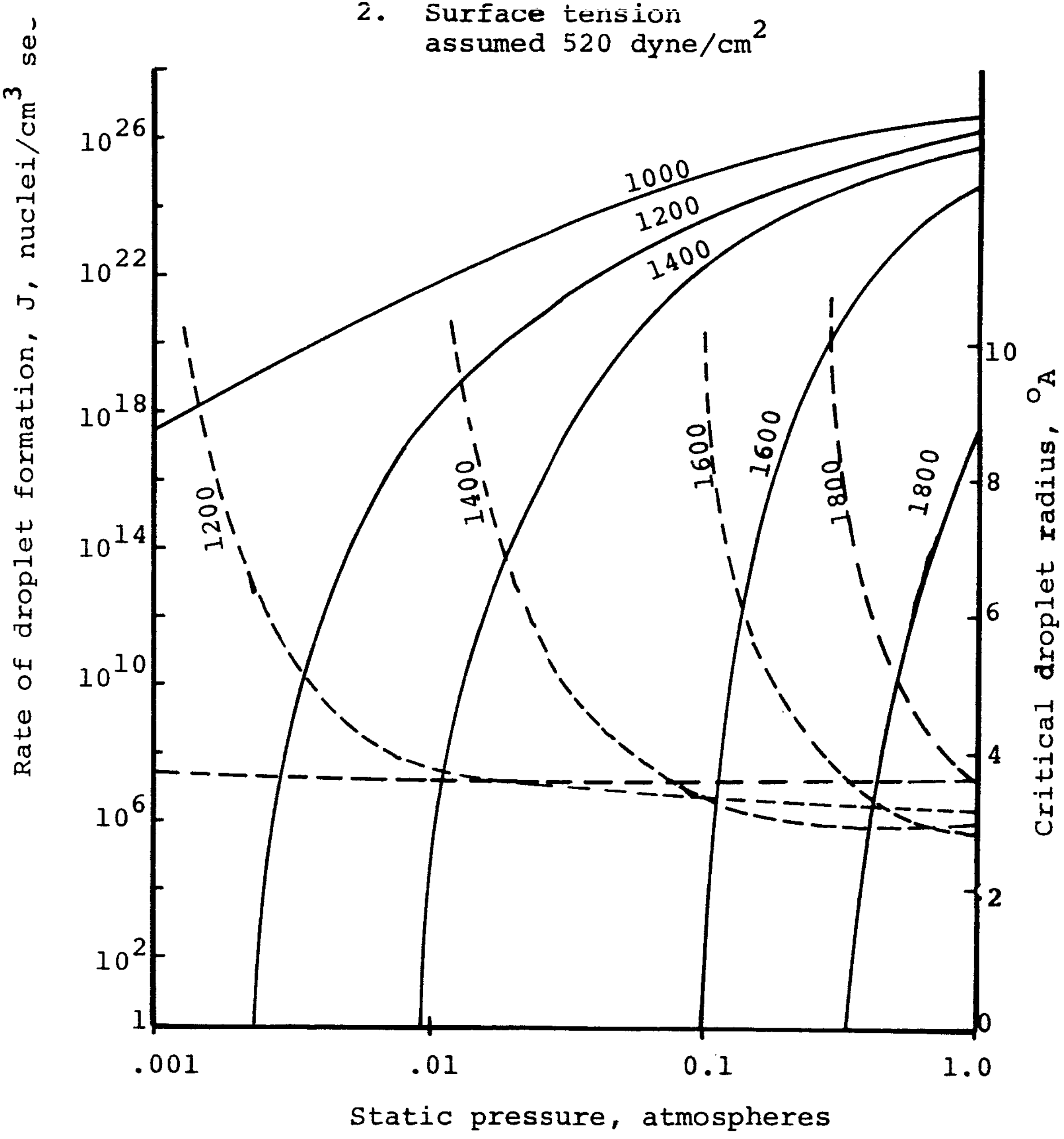

Figure 7.6. Rate of Nucleation and Droplet Radius As A Function of Pressure and Temperature

Notes:

1. Condensation rate used shown of Figure 7.6
2. Velocity of condensate was assumed to be 1000 m/sec

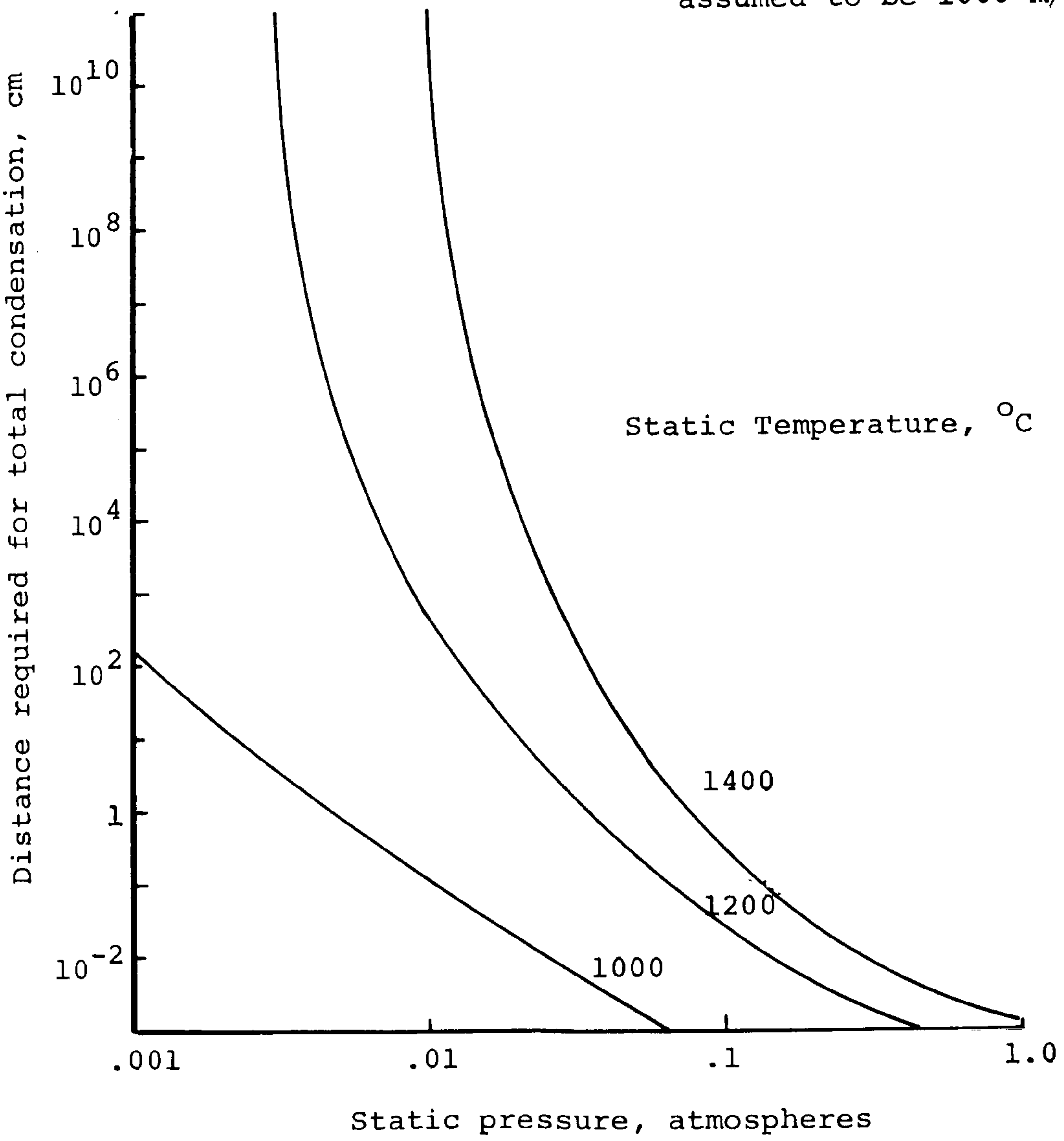

Figure 7.7. Distance Required for Total Condensation Aluminum Vapor Versus Pressure and Temperature.

Notes:

1. Specific heat ratio, $\gamma = 1.67$
2. Adiabatic heating
3. Perfect gas assumed

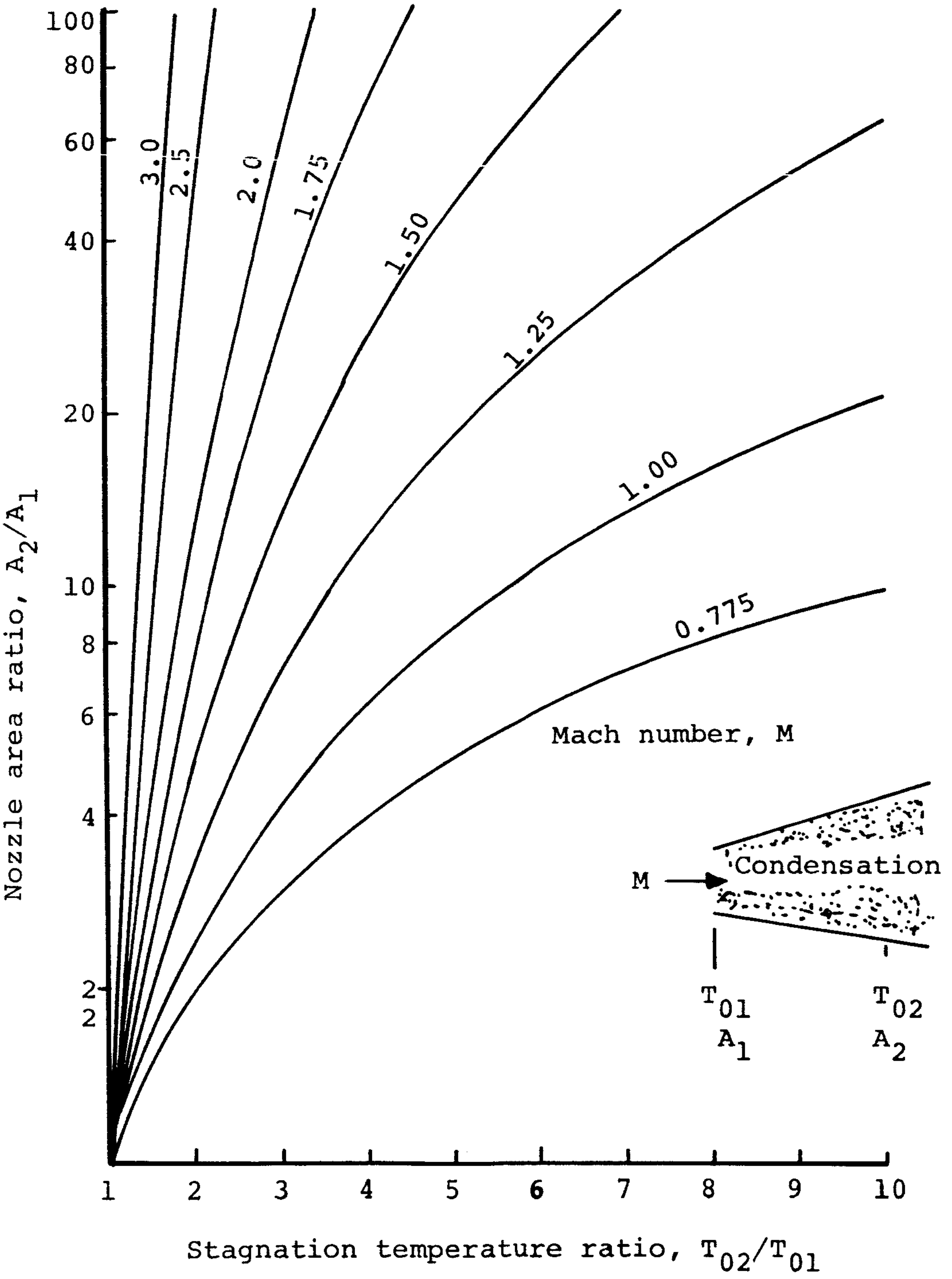

Figure 7.8. Nozzle Area Ratio Required to Hold Mach Number Constant During Condensation Heating as a Function of Stagnation Temperature Ratio.

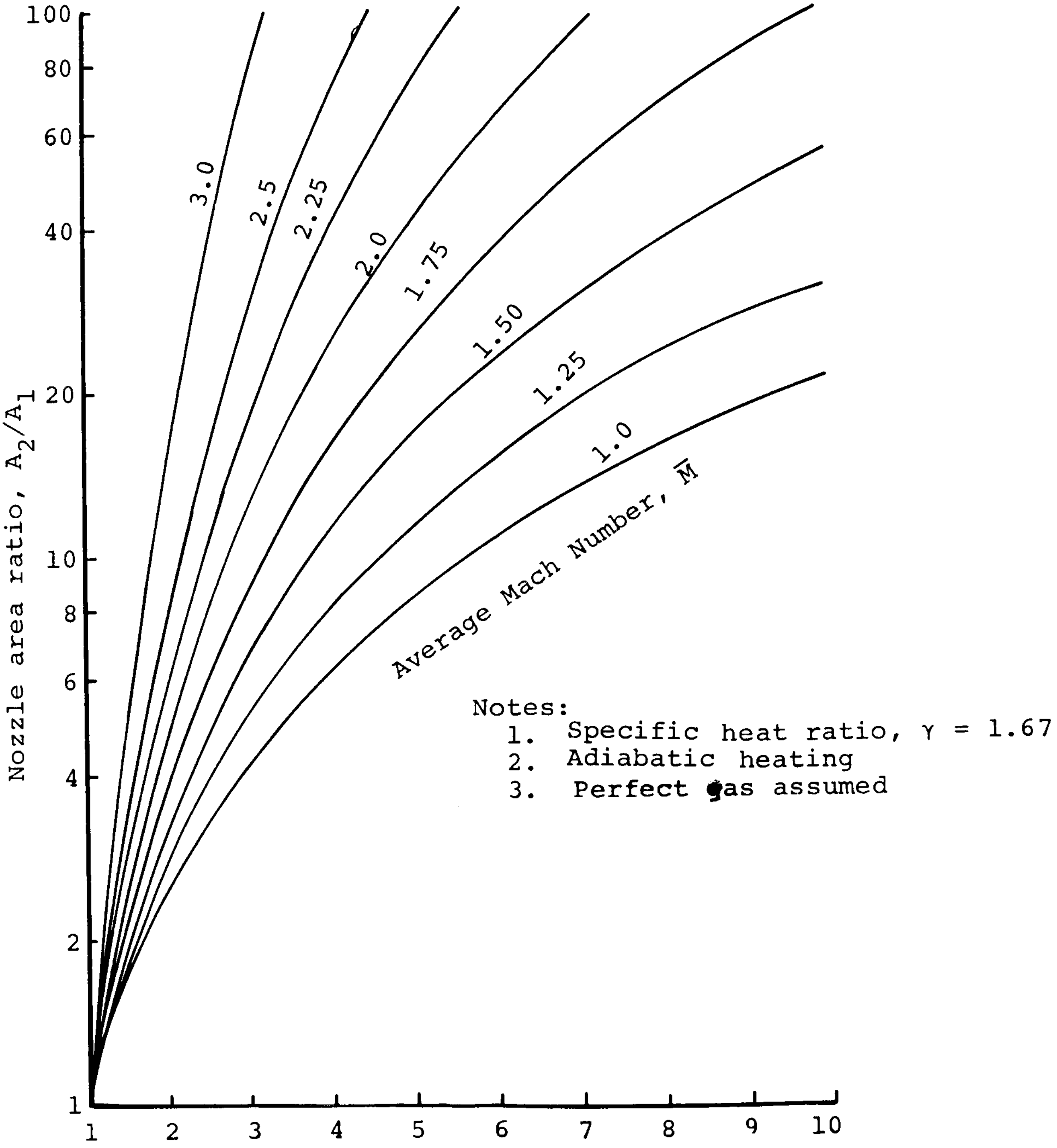

Figure 7.9. Nozzle Area Ratio Required to Hold Velocity Constant During Condensation Heating as a Function of Stagnation Temperature Ratio.

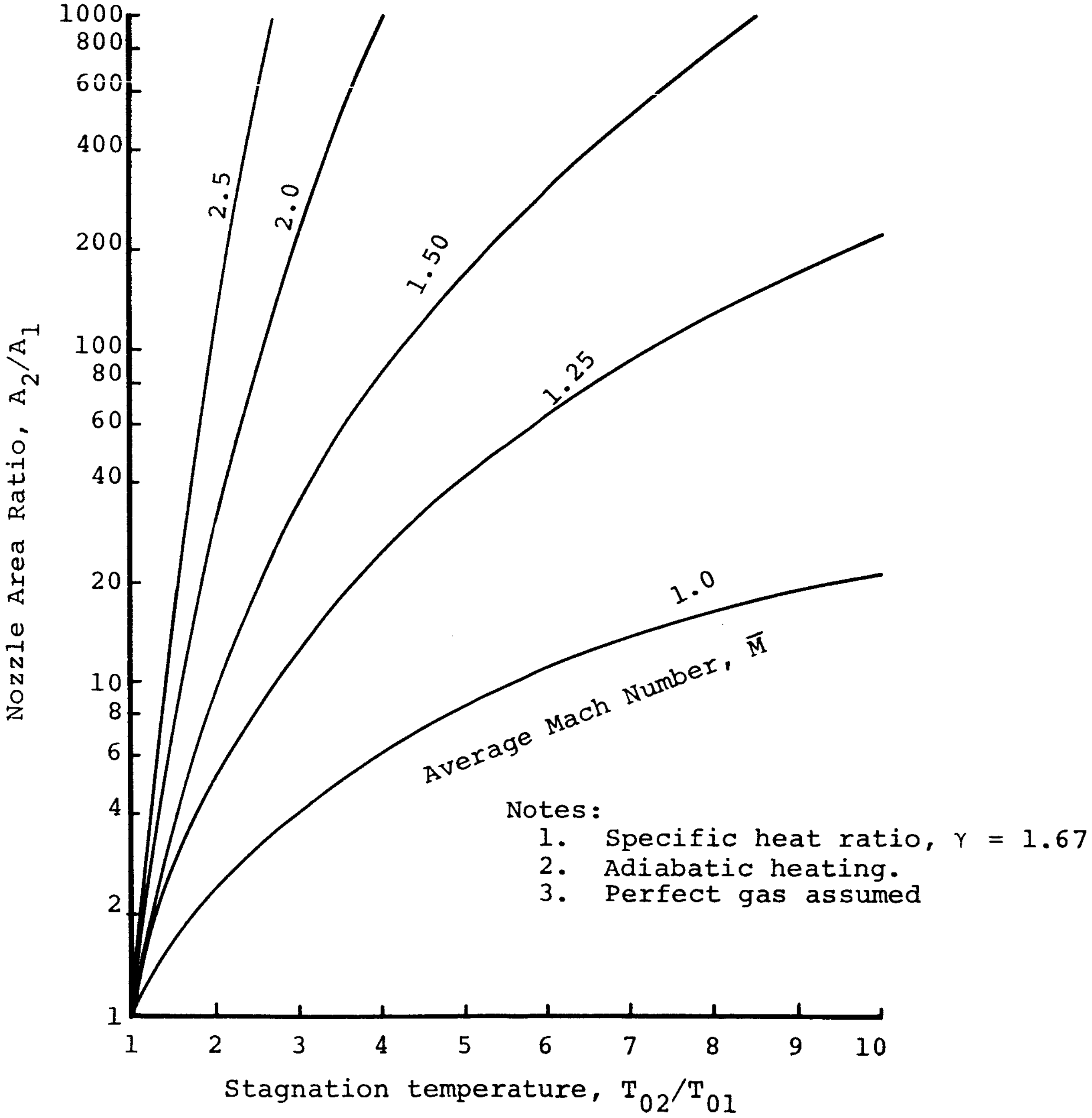

Notes:
1. Specific heat ratio, $\gamma = 1.67$
2. Adiabatic heating.
3. Perfect gas assumed

Figure 7.10. Nozzle Area Ratio Required for **T_o** Hold Static Temperature Constant During Condensation Heating as a Function of Stagnation Temperature Ratio

N67-36948

A DIRECT-CONVERSION DEVICE USING THERMALLY-ACCELERATED, CHARGED COLLOIDAL PARTICLES

by Harry I. Leon and William R. Mickelsen

INTRODUCTION

The direct conversion power generation system shown on Figure 8.1 is an advanced concept especially suitable for use with charged-particle electric thrusters. This design has no moving parts and is capable of producing high-voltage direct-current power without use of any power conditioner.

The design proposed, however, could be used equally well for any space or ground powerplant where direct current, high- or low-voltage is required. (The voltage output of this device is simply a function of the reactor temperature and the size of colloidal particles produced.)

DESCRIPTION OF THE POWERPLANT

A schematic diagram showing the essential parts of this powerplant is shown on Figure 8.1. The operation of the powerplant is as follows:

1. The working fluid is heated in a nuclear reactor to a superheated vapor.
2. The vapor is then expanded through a supersonic nozzle where the thermal energy is converted into kinetic energy.
3. At a point in the nozzle, the vapor reaches supersaturation and begins to condense. Section 7 of this report gives the theory involved in this condensation process.
4. The nozzle is shaped so that the condensate will grow to an optimum-sized colloidal particle.
5. The colloidal particles are then ionized by electron bombardment at the ionizer.
6. The kinetic energy of the ionized colloidal particle is then converted into direct current electrical energy by the generator. This will be explained in detail later.
7. The condensate is then returned to the reactor by means of a heat pipe and pump.

8. The heat generated due to inefficiency in the powerplant is removed by thermal radiation into space.

PRINCIPLES INVOLVED AND ANALYSIS

This section will contain the basic physics and chemistry involved in designing this powerplant, present some sample analyses, and show a parametric study for the design of a MW powerplant.

Reactor and Working Fluid

The reactor would be a fast reactor (to keep the size small) either consisting of many small circular pin-like fuel elements or a solid, homogeneous core with many small coolant holes. The coolant would enter as liquid and would be vaporized in the reactor. The coolant would enter the reactor at nearly vapor temperature since it would remove heat from the nozzle walls on its return to the reactor. Therefore the reactor would essentially add only the heat of vaporization to the coolant. Thus the coolant flow rate $\dot{w}$, required may be written as:

$$\dot{w} = \frac{P_{th}}{h_{fg}} \tag{8.1}$$

where P_{th} = reactor thermal power and h_{fg} = latent heat of vaporization.

Using Trouton's rule, the heat of vaporization can be approximated for most liquids. Trouton's rule states that the heat of vaporization is proportional to the boiling temperature, T_b of the liquid. This equation is given below:

$$h_{fg}\ (\text{cal/mole}) = 21\ T_b\ (K^{o}) \tag{8.2}$$

Using this equation the heat of vaporization was obtained for a large range of molecular weights and boiling points. The results of this estimate are shown on Figure 8.2.

The choice of the coolant from the standpoint of the latent heat of vaporization will involve a compromise. A low coolant mass flow rate is desired to help reduce the size of the reactor and nozzle. This means that a high heat of vaporization is desirable, or by Equation (8.2), a low molecular weight and high boiling point. The flow rate required to cool a 1-megawatt thermal reactor is shown on Figure 8.3 as a function of boiling point and molecular weight of the coolant. However, a high flow rate is required for high efficiency since the output of the device is a function of the mass flow rate, $\dot{w}$, of the coolant. Therefore, an optimization study must be made to determine the desired heat of vaporization.

The coolant must have a sufficiently large temperature range between the vaporization and solidification points so that there will be little possibility of forming the solid material during operation. Some of the other requirements of the coolant are listed below:

1. The coolant must be capable of being condensed into colloid particles, and subsequently charged.
2. The coolant must not react with the cladding of the reactor fuel elements or with the nozzle walls.
3. The boiling point must not be so high as to make a serious structural containment problem.
4. The coolant should not have a large fast neutron absorption cross-section nor become so highly radioactive as to be a radiation hazard. (This problem could be overcome by using a separate coolant to remove the heat from the reactor. The reactor coolant could be passed through a heat exchanger to heat the working fluid for the nozzle and generator.

Sizing of the Nozzle Throat

The sizing of the nozzle throat is one of the most important parameters of the design since all areas of the nozzle are related to the throat area. The area of the nozzle throat A*, depends on the flow rate, $\dot{w}$; stagnation pressure P_o and temperature T_o; the molecular weight M, of the fluid and its specific heat ratio γ, as given in the equation below:

$$A^* = \frac{W\sqrt{T_o}}{P_o}\left\{\frac{\gamma M}{R}\left[\frac{2}{\gamma + 1}\right]^{\frac{\gamma + 1}{\gamma - 1}}\right\}^{-1/2} \qquad (8.3)$$

The nozzle throat area was computed using Equation (8.3) for various values of the flow rate, molecular weight and stagnation pressure and a constant stagnation temperature of $3000^{o}R$. The results of these analyses are shown on Figure 8.4. The size of the throat of the device can now be easily determined by using Figures 8.3 and 8.4 together, illustrated by the example below: Example: To get idea of the nozzle area required, consider design of a 1 MW_t powerplant using a coolant that has a molecular weight, M, of 10, boiling point of $1500^{o}R$, at stagnation temperature, T_o, of $3000^{o}R$, and plenum pressure of, P_o = 10 PSIA.

The flow rate required for a 1 MW_t design, given by Figure 8.3 is 1100 lb/hr. Using this flow rate, go to Figure 8.4 and read a nozzle throat area of 5.0 in^2. This example not only shows how to use the parameterized graph but also gives an estimate of how compact a direct-conversion device of this type could be.

One of the coolants considered for the device is lithium. An analysis similiar to the one just mentioned was made to size the nozzle throat using lithium. The nozzle throat was computed for a range of stagnation pressures and reactor thermal outputs. The results of this analysis are shown on Figure 8.5. The relatively small change in nozzle throat area due to large changes in stagnation temperature should be noted on studying Figure 8.5. Although the stagnation temperature was found to make only a relatively small change in the throat area, a high temperature is very important for the efficiency of this machine. In Section 7 of this report, it is shown that the temperature is the most important parameter in determining the velocity at which condensation would occur for a given fluid.

Velocity and Size of Colloidal Particles and its Effect on Power Output

The velocity that can be obtained for an isentropic expansion can be written in the following form:

$$v_c = \sqrt{\frac{2\gamma}{\gamma - 1} \left(\frac{R}{M}\right) T_o \left[1 - \frac{P_c}{P_o}\right]^{(\gamma - 1)/\gamma}} \qquad (8.4)$$

Where v_c is the velocity obtained where condensation begins, and P_c is the static pressure at this point.

Methods were studied for increasing the exit velocity, v_e, of the colloids beyond the value of v_c. Some results of preliminary work for doing this are shown in Sections 3.1 and 7.1 of this report. For this preliminary study, however, $v_c \doteq v_e$ will be assumed. The power output P_j, of this machine can be written as:

$$P_j = 1/2\ \dot{w}\ v_e^2 \qquad (8.5)$$

The use of this device as a powerplant for a charged-particle thruster requires not only a high power output per unit weight but a high voltage output as well. (This voltage should be in the range of 10^4-10^6 volts.) The voltage, ϕ, that can be generated by a charged colloidal particle traveling through an electric field may be written as:

$$\phi = \frac{m\ v_e^2}{2q} \qquad (8.6)$$

Where m is the mass of the colloidal particles and q is the charge per colloidal particle. Thus, for a high output voltage, it is apparent from Equation (8.6) that a high mass of the colloidal particles and high velocity are required. To have high velocity, a high stagnation temperature and a low molecular mass coolant are required. (See Equation (8.4)). The coolant chosen should, therefore, have a low molecular weight yet be able to form large colloidal particles. The formation of colloidal particles depends on the surface tension of the coolant, the pressure, the temperature and the rate of removal of condensation heat as explained in Section 7.1 of this report. The voltage output of the generator was solved for a lithium-cooled device at various stagnation temperatures and colloidal particle sizes, and is shown on Figure 8.6. Since the temperature of this device is limited by the structure strength of the walls and the corrosion problem of high temperatures, it is clear that large colloidal particles will be required if high voltage is to be obtained.

The power output of this device is directly proportional to the product of the velocity squared and the mass flow ratio (see Equation (8.5)). Since v^2 is proportional to T_o/M, Equation (8.4) may be written as:

$$P_j \sim \frac{\dot{w}T_o}{M} \qquad (8.7)$$

Therefore, the maximum output power, the mass flow rate, $\dot{w}$, and temperature, T_o, should be high and the molecular weight, M, should be as small as possible. Studying Figure 8.3, it is noted that a low-boiling-point coolant would be desired. Furthermore, if the boiling point is low and the stagnation temperature is high, a high stagnation pressure would result. A high stagnation pressure would help reduce the nozzle size as shown by Equation (8.3) and Figure 8.4. However, the high stagnation pressure will require thicker walls. This is not too serious a problem since shielding would be required for the reactor anyway.

Study of Generator Design

The generator would consist of two electrode grids very close to one another and electrically connected to each other through the load. The electrode would build up a potential that would resist the flow of the charged colloidal particles through it. The flow of the charged particles would induce a current. This current would be limited by space charge as given by Child's law which can be written as:

$$J = 5.57 \times 10^{-12} \sqrt{q/m}\ \frac{\phi^{3/2}}{d^2} \qquad (8.8)$$

where:

J = current per unit area in amp/meter^2
q = change in coulomb
m = colloid mass in grams
ϕ = voltage generated
d = distance between electrodes in meters (deceleration length)

The power generated per unit area is equal to P_j/A which can be written as:

$$\frac{P_j}{A} = J\phi \qquad (8.9)$$

Equation (8.9) was solved for power density using Equation (8.8) and Figure 8.6 for various values of d, T_o, and particle mass to charge ratios. The results of these analyses are shown on Figure 8.7.

CONCLUSION AND DIRECTION FOR FUTURE WORK

This powerplant has an advantage over conventional types of powerplants for use with an electric colloidal thruster when high voltage is required since it could have a greater power to weight ratio. This design has a great weight saving since no heat exchanger, turbines, rotating generator, or power converter are necessary. Also, since the device has no moving parts, the reliability is potentially greater than that of a conventional powerplant.

This preliminary study has given a description of the device and the important parameters of each component of the system. Although a wide range of coolants could be used in this device, after studying the requirements for the working fluid on each component, it should be possible to make a wise selection. Based on this preliminary study, the coolant used should be of low molecular weight and a low boiling point but have a sufficiently high surface tension to aid in forming large colloids.

Continuing work on this concept is directed toward the following goals for the near future:

1. Selection of the actual fluid that will give the highest power to weight ratio.
2. A more detailed analysis of the colloidal particle formation and colloidal growing mechanism. A code is being developed to facilitate the study and aid in the nozzle design.
3. A study of the particle changing and the details in generator design.
4. A study of the waste heat removal and coolant recycle systems.

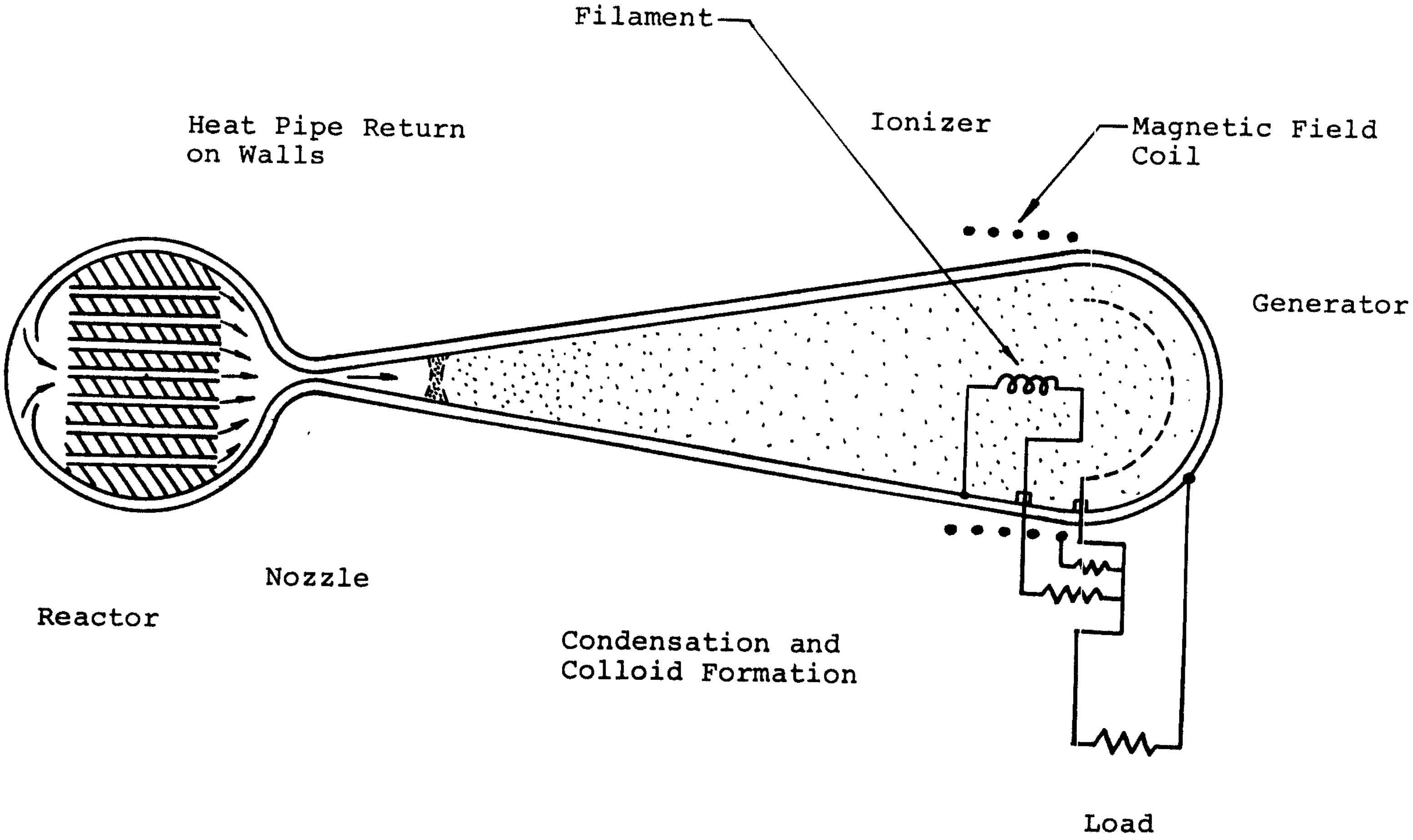
Filament
Heat Pipe Return
on Walls
Ionizer
Magnetic Field
Coil
Generator
Nozzle
Reactor
Condensation and
Colloid Formation
Load

Figure 8.1. Direct Conversion Using Thermally Accelerated Charge Colloid Particles

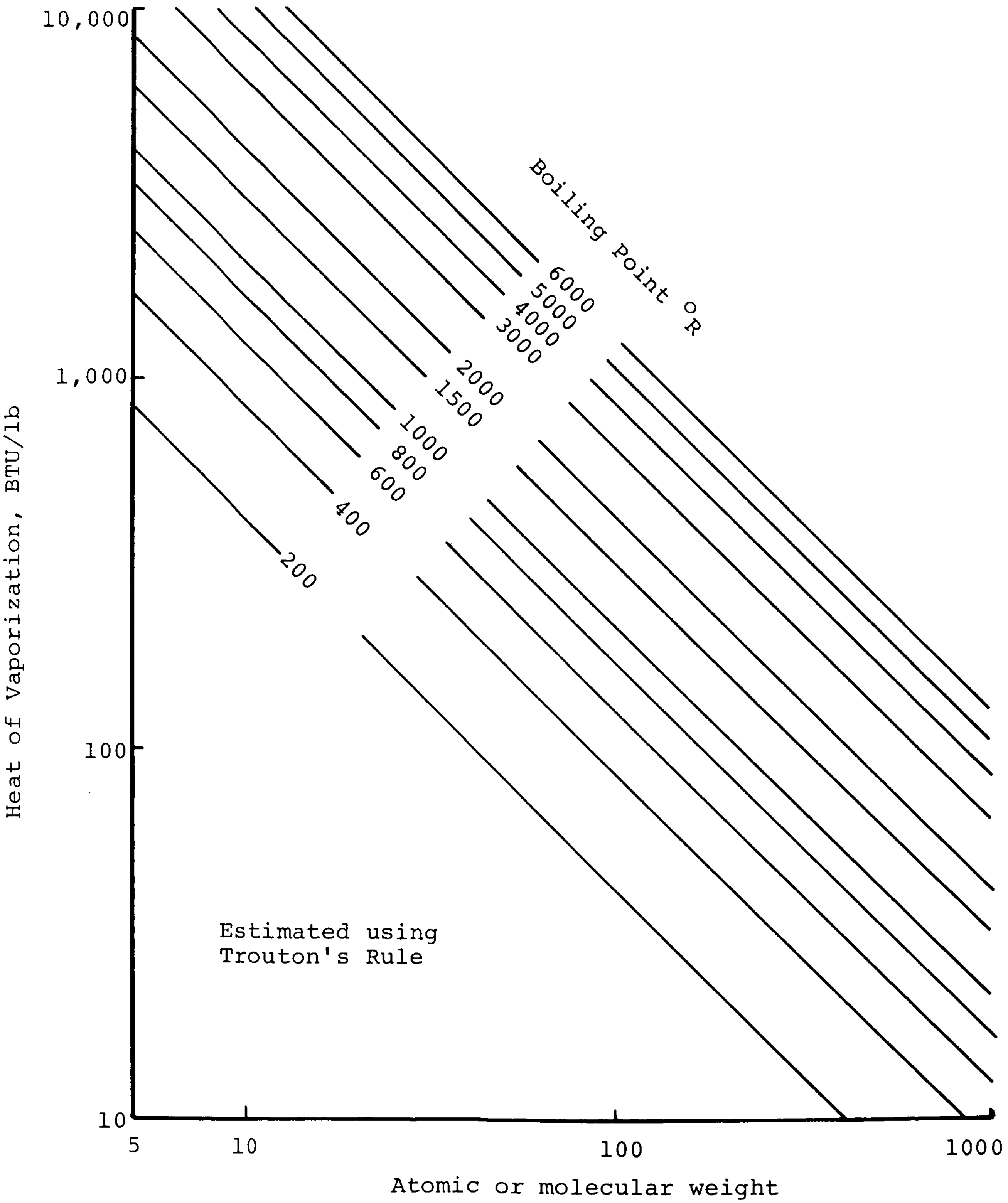

Figure 8.2. Latent Heat of Vaporization Versus Boiling Point and Molecular Weight.

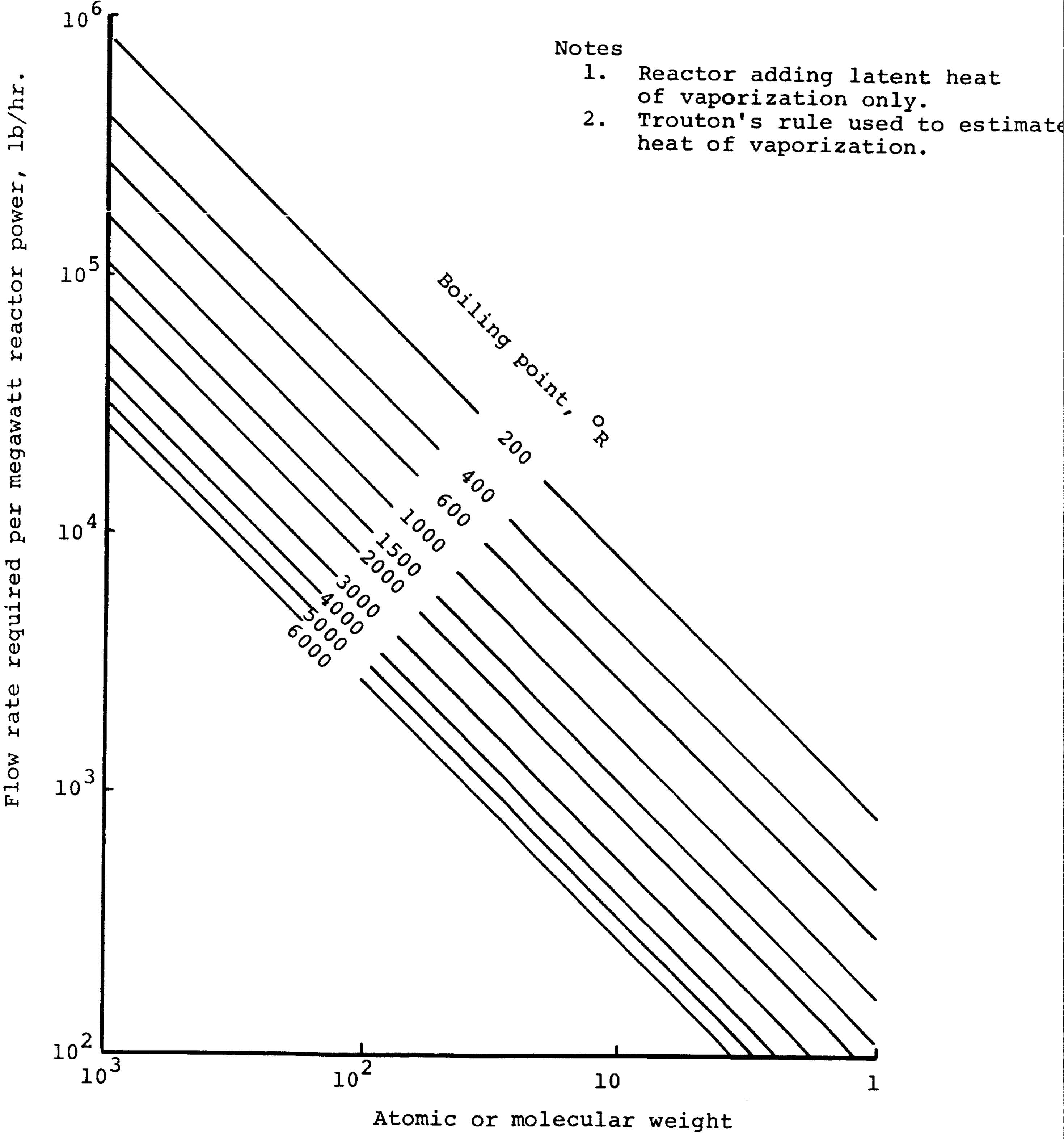

Figure 8.3. Reactor Coolant Flow Rate Versus Boiling Point and Molecular Weight.

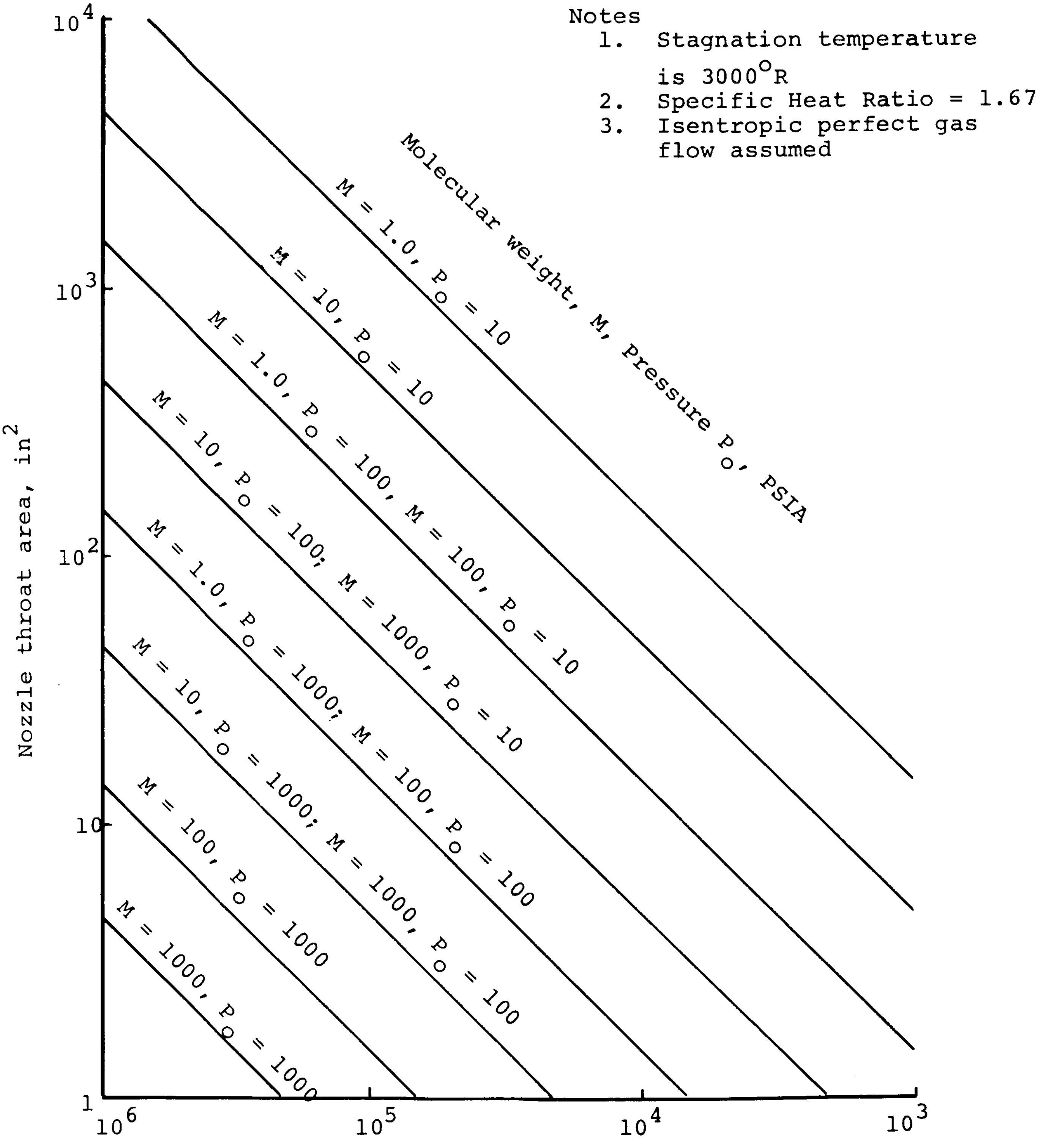

Figure 8.4. Nozzle Throat Area Versus Flow Rate Molecular Weight and Stagnation Pressure.

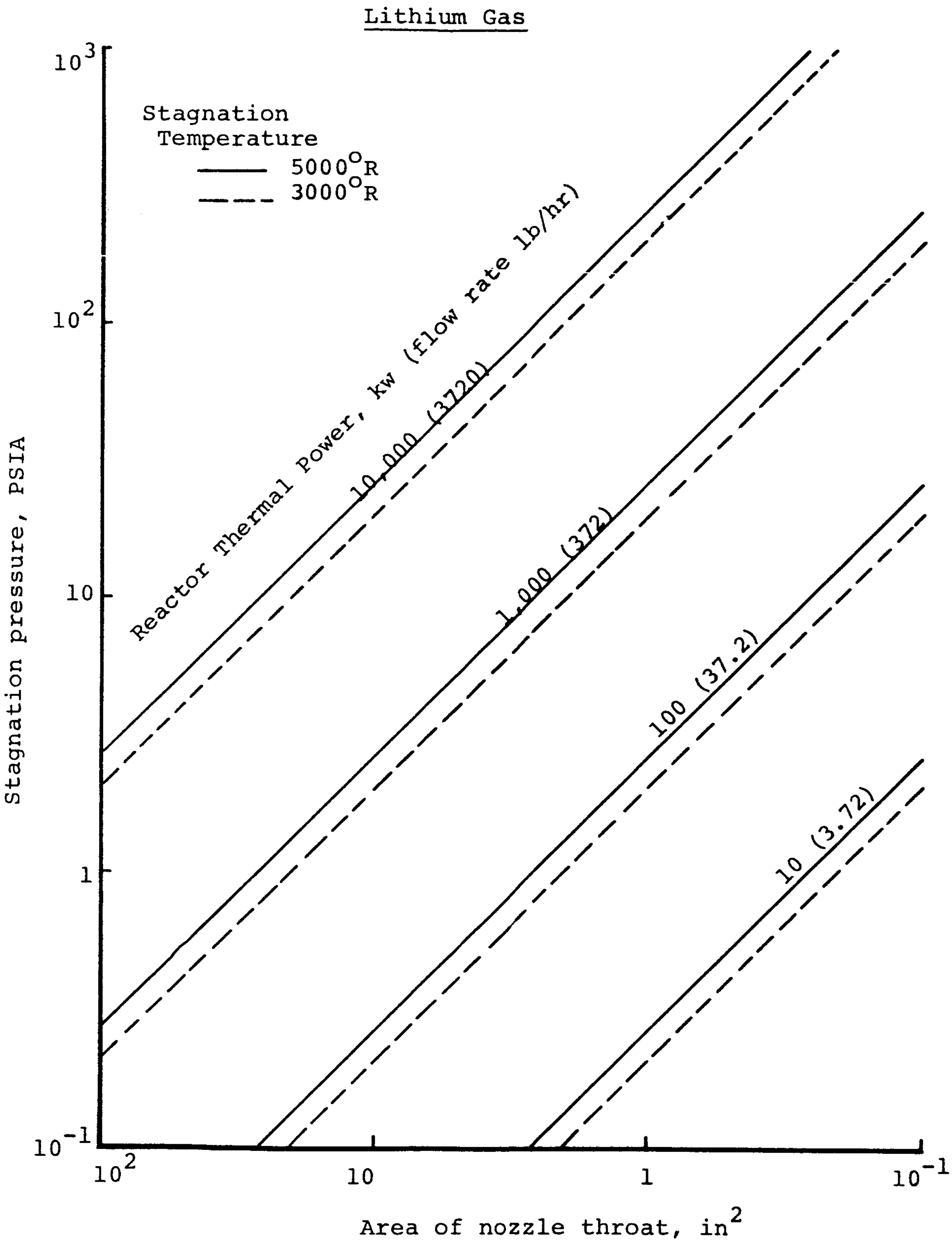

Figure 8.5. Area of Nozzle Throat Versus Thermal Power, Stagnation Pressure and Temperature.

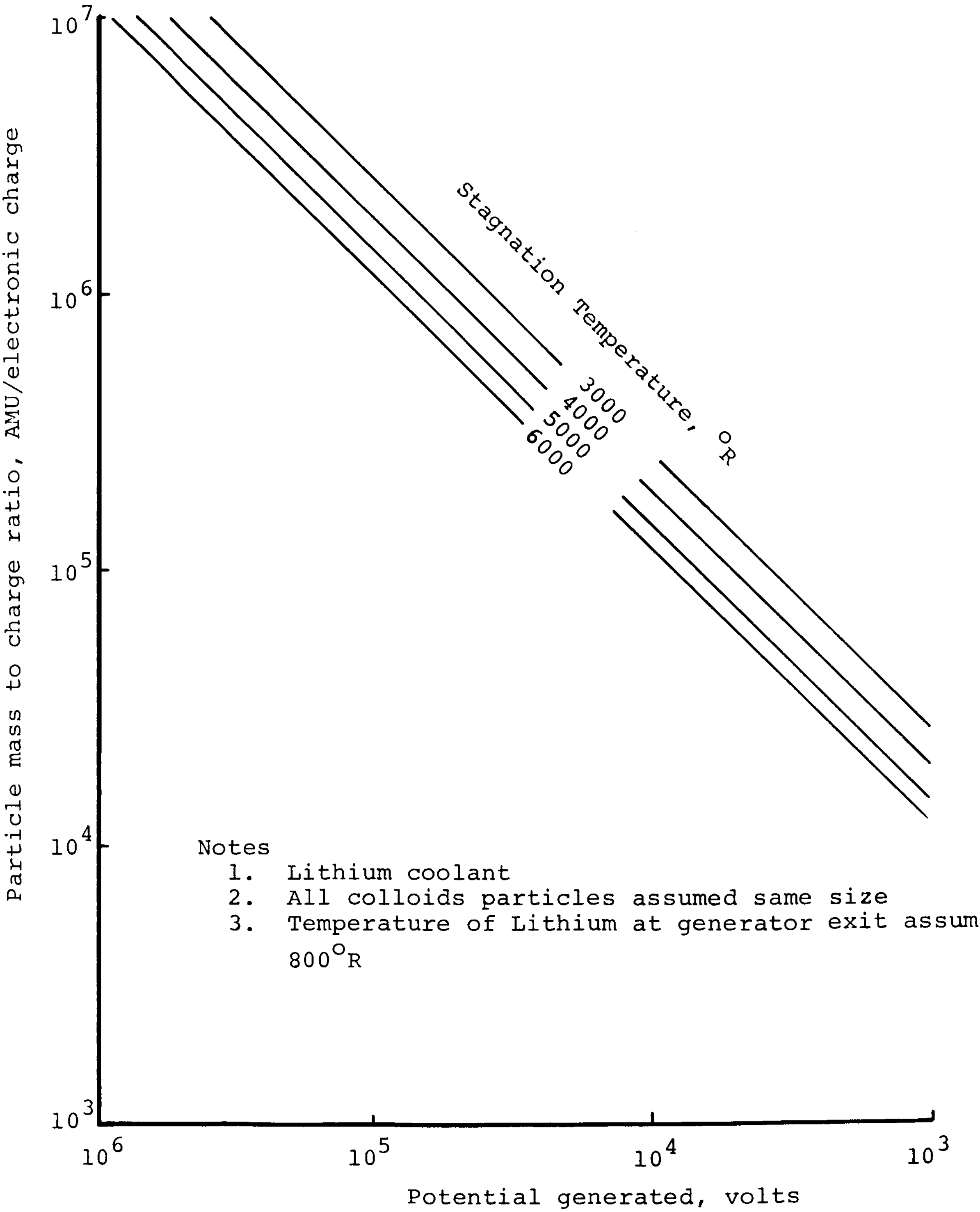

Notes
1. Lithium coolant
2. All colloids particles assumed same size
3. Temperature of Lithium at generator exit assumed 800°R

Figure 8.6. Maximum Output Voltage Versus Particle Mass to Charge Ratio and Stagnation Temperature.

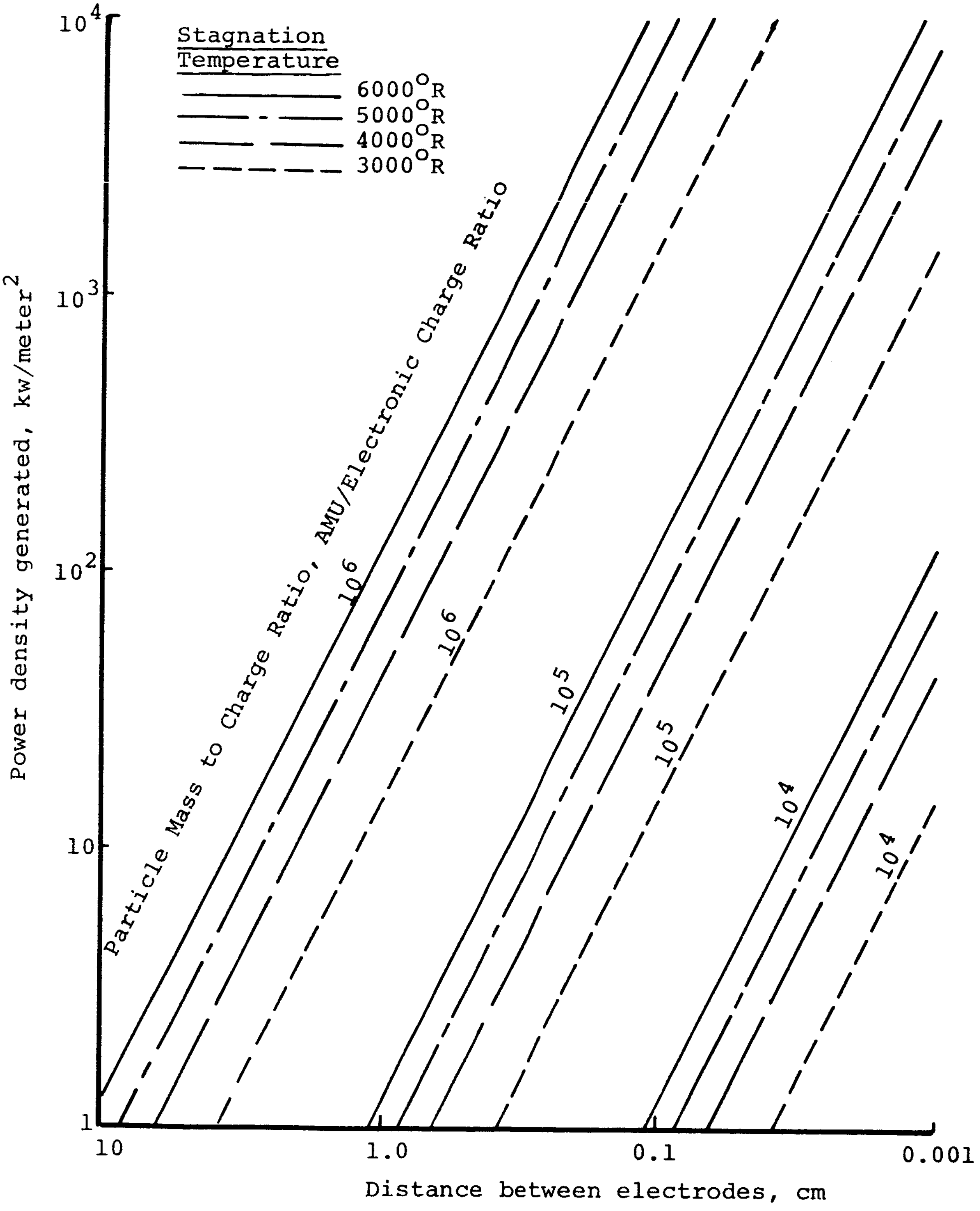

Figure 8.7. Generator Power Density as Function of Distance Between Electrodes and Particle Mass to Charge Ratio.

N67-36949

THE PRODUCTION OF CHARGED-PROTEIN MOLECULES BY ELECTROSTATIC SPRAYING

by Vivian Steadman and G. W. Tompkin, Jr.

The goal is to produce a charged colloid beam, the particles of which contain protein and, necessarily, a solvent. The specific charge desired is one greater than about 1000 coul/kg so that an I_{sp} in the neighborhood of 2000-5000 sec can be attained for accelerating voltages less than about 100 kv. (The I_{sp} range indicated is one in which the thruster efficiency using conventional ion sources is "intolerably low"[9.1].) In addition, the propellant should have a narrow specific charge distribution, so as to provide a high thruster efficiency[9.2].

The particular method of charged particle production now under consideration is that of induction charging. The charged droplets are created at the tips of a needle into which the propellant has been introduced and to which a high voltage (either positive or negative) has been applied. (A variation of this method is that of producing droplets at the rim of a spinning cup to which a high voltage has been applied[9.3].) The specific charge distribution of a colloid beam is most commonly determined from measurements using a simplified time-of-flight spectrometer; this type of spectrometer, in contrast to the quadrupole mass spectrometer, enables one to analyze the specific charge distribution for more than one jet of a given needle[9.4]. Furthermore, the jets do not get "lost" (due to some wandering in direction) when one is making measurements with the time-of-flight spectrometer[9.4].

A number of criteria have evolved as most conducive to the production of charged droplets having a narrow specific charge distribution by induction charging. These include:

(1) the needle geometry and, to a lesser extent, the needle material;

(2) the resistivity of the propellant;

(3) the propellant surface tension.

These three factors and the additional factors of mass flow rate, properties of the doping additive (including in particular the ease with which the ion of charge opposite to that on the expulsed droplet is neutralized at the needle tip[9.5]), and the potential difference between the needle and extractor determine the magnitude of the peak of the specific charge distribution. Increase in spraying potential, increase in doping additive concentration, and decrease in reservoir pressure each increase the specific charge of the propellant[9.5]. A few of the hypotheses which have been advanced to explain the origin of some of the observed dependencies of the specific charge distribution on the above mentioned factors are given below.

The wall thickness, the tip shape, the diameter of the tube, and the uniformity of the bore are the factors of the needle geometry which affect the specific charge distribution. The larger inner diameter tubes (8 mil I.D.) require larger spraying potentials to affect a given $\frac{Q}{M}$ distribution[9.1]. (The dimensions of the preferred standard needle at present are 8 mil O.D. by 4 mil I.D.[9.6].) Thick walls[9.1], non-uniform bores[9.6] and non-beveled tips[9.1,9.6] produce broad $\frac{Q}{M}$ distributions. An instance is known in which a Pt needle with a 90° tip performed successfully for 20 hours after which the needle efficiency dropped and considerable ion emission was detected from the by-then-glowing tip[9.6]. A suggestion as to why the bevel tip gives superior performance is that the spraying occurs at the edge of the concave liquid meniscus and the electric field gradient is more slowly changing along a bevel slope for the droplets being produced at the meniscus edge[9.1]. However, the question as to whether the meniscus is concave or convex is unsettled[9.5]. The material of the needle is less significant in affecting the $\frac{Q}{M}$ distribution[9.1], but variations in the slope of the increase of $\frac{Q}{M}$ with spraying potential which are dependent on capillary material have been noted[9.5].

The need for low resistivity of the propellant is related to the fact that the time for buildup of charge in any given cusp from which spraying is to occur should be short relative to the ejection time[9.3]. The following equations indicate the nature of the time dependencies involved:

$$t_{ejection} \approx \frac{1}{2} \frac{QV_a}{M} d^2 \qquad (9.1)$$

where d is some minimum distance for ejection[9.3].

$$Q_t = Q_\infty \left(1 - e^{-\frac{t}{\rho\varepsilon}}\right) \qquad (9.2)$$

where Q_t (Q_∞) is the charge in a cusp at time t (∞), ρ is the resistivity, and ε is the capacitivity[9.3]. From such equations one expects that solutions with very high resistivity will produce very low $\frac{Q}{M}$ ratios as well as broad specific charge distributions. At least the low $\frac{Q}{M}$ ratio result has been observed[9.5]. It has been found desirable in the propellants considered in the past to reduce the resistivity to the order of a few thousand Ω-cm's.

The ease of neutralization of the "non-expulsed" ion has been correlated with the failure of certain systems to spray electrohydrodynamically[9.5]. (The question as to whether there is actually a "non-expulsed" ion is unsettled[9.5].) There are at least two aspects to this problem, the first being that for an anion (cation) to be used in a solution for the generation of positive (negative) charged particles, the anion's (cation's) interfacial electron (hole) energy level must be less (greater) than the capillary work function; the second being the improvement in the specific charge distribution and the increase in the specific charge observed when the ion being neutralized had a higher mobility than the ion ejected from the capillary[9.5].

The maximum specific charge C_R (or C_{E_o}) that a droplet of radius r, density ρ, and surface tension γ can possess is determined by either the Rayleigh criterion

$$C_R = \frac{6 \quad \varepsilon_o \gamma}{\rho r^{\frac{3}{2}}} \qquad (9.3)$$

or the field emission criterion

$$C_{E_o} = \frac{3\varepsilon_o}{\rho r} E_o \qquad (9.4)$$

where E_o is the value of the field at which electron or ion emission occurs[9.5]. The Rayleigh criterion dominates in the lower specific charge range[9.5]. Such a dependence of the charge-to-mass ratio on surface tension has been observed, but a broader $\frac{Q}{M}$ distribution may also accompany the reduction in surface tension[9.5,9.6]. (It is possible to add a surface tension reductant which leaves the other parameters of the solution, including resistivity, specific gravity, and viscosity, essentially unchanged[9.6].)

Previously, the propellants utilized had been mainly low vapor pressure ($<10^{-6}$torr) organic compounds to which was added a doping agent belonging to one of the following classes of compounds: ionic salts, covalent salts, organic and inorganic acids, Lewis acids, organic and inorganic bases, and compounds having large quenching cross-sections for electrons[9.3]. The various aspects of induction charging discussed above were established using such propellants. How similar will the results be for protein solutions, possibly also doped? What other factors peculiar to proteins must be considered in induction charging? The latter question will be discussed below; the former, requiring a more precise theory, left to experiment.

Protein dissociation has been discussed from the point of view of producing subunits of larger molecules - these subunits themselves being suitable candidates for protein-based propellants[9.7]. However, the means of dissociation may be of critical importance as well in determining the specific charge which is obtainable from a protein in a given state of dissociation. (The term "dissociation" here includes both the reversible and irreversible processes by which a protein subdivides into smaller subunits. The nature of the particular subunits involved are such that they may be obtained by either reversible or irreversible changes in the state of the protein. An example of such subunits are the half- and quarter-molecules of hemoglobin since for neither is their production necessarily irreversible[9.8]. Denaturation phenomena include irreversible dissociations.)

It has been observed that in certain solvents the intrinsic viscosity of a denatured protein is much lower than in others[9.9]. The explanation for this variation is that the denatured protein is more tightly coiled in the solution of lower viscosity[9.9]. Indeed, this hypothesis is reasonable since the solution of lower viscosity also happens to be the one of lower solubility[9.9]. Two problems relevant to research on charged droplet generation using proteins emerge:

(1) How will denaturation affect the mobility of a protein in a given solvent system?

(2) How will the tightness of the protein coil affect the charging mechanism?

It would seem that the more intramolecular linkages there are, the lower the degree of fragmentation of the protein upon charging should considerable fragmentation occur.

Only recently have techniques been developed which enable one to study the randomness of a protein coil with some degree of certainty. (Previously, light scattering, the most informative of the earlier approaches, was useful only for particles of dimension greater than about 100Å [9.9]--appreciably larger dimensions than are characteristic of hemoglobin and its subunits, for instance[9.18].) One valuable new technique is ESR spin-labeling. Applied to the study of acyl enzyme, it was found that a "spin label" involving a nitroxide group when attached to the enzyme gave rise to a ESR spectrum indicating equilibrium between protein configurations in which the spin label was alternately "strongly immobilized" and "weakly immobilized"[9.10]. This equilibrium persisted even at relatively high urea concentrations (≤5M)[9.10]. (Urea at such concentrations is a protein denaturant.) But in the saturated urea solution, the spectrum was that of a "mobile" spin label and evidentally attached to a flexible coil[9.10]. The "strong immobilization" of the spin label, on the other hand, is most likely representative of the tightness of the coil of the protein. One cannot say, as formerly, that the high intrinsic viscosity found for denatured protein in urea solution is indicative of a system in which the protein is a completely random coil[9.9].

For quarternary proteins, there is a further complication in that there may be two immobilized spin label spectra--one corresponding to the undissociated protein and one to the tight coil situation. In such a case, the intensity of one of these signals *might* change with time due to alterations in the conformational constraints of the protein which accompany the transition of a protein to its denatured states. However, the spin label on the coil may not change its degree of "mobility" with the extent of dissociation. An instance of the latter situation is indicated by the fact that the ESR of the spin label nitroxide maleimide attached to hemoglobin is unchanged by the dissociation of the protein into symmetrical $\alpha\beta$ chains in 3N NaCl[9.11]. The particular constraints involved in the spin label "immobilization" are evidentially not altered.

The interplay of viscosity, the nature of the effects of the denaturant on the protein, solubility, and the tightness of the protein coil for a given solvent-protein system most likely affect the specific charge distribution in a complex fashion. Since, as the example of the acyl enzyme shows (and as is true for numerous proteins[9.8]), the viscosity of a given protein solution does not provide an accurate measure of the tightness of the protein coil, it would be worthwhile to make independent measurements of this protein characteristic.

In the event that the use of proteins of larger molecular weight would prove necessary in order to obtain a fragment having a specific charge in the region of interest (roughly 1000-100,000 amu particles), there are numerous quaternary proteins, i.e. ones which dissociate into half-molecules and then into quarter-molecules in a manner similar to hemoglobin. In fact, it appears that most proteins of molecular weight greater than 50,000 amu have quaternary structure[9.12]. Another possibility is the use of protein complexes, such as that between casein and hemoglobin[9.13]. The combined molecular weight of this particular complex is approximately 128,000 amu[9.13]. The complex is stable in electrophoresis fields[9.18].

The utilization of proteins in the formation of charged colloids having specific and narrow $\frac{Q}{M}$ distributions involves at least three further difficulties:

(1) Control of the rate of dissociation and/or denaturation of the protein.

(2) The limited number of solvents in which proteins are soluble and the limited solubility of a protein in a given solvent. Hemoglobin, for instance, has a maximum solubility in water at 25°C of 17 g/l[9.14]. If all the water at the needle tip were dispersed in charged droplets, this solubility would imply that on the average, each droplet contained only about 1.7% by weight hemoglobin, giving rise to droplets of 3.76×10^6 amu (specific charge of order 1). The solubility of Hb

in water at 25°C in the presence of 1.05 moles NaCl is 198 g/l[9.14], but it is not known how the presence of the salt will affect the charging mechanism. (Possibly, it will behave as a doping agent.) In general, the solubility of proteins in a given solvent is a function of its pH, ionic strength, and the dielectric constant[9.12]. Several other solvents besides water are known for proteins including dimethyl sulfoxide, formamide, dichloroacetic acid, and ethanol-water mixtures[9.14].

(3) The choice of solvent is also governed by its evaporation and freezing characteristics upon exposure to vacuum. Evaporation of solvent from a charged droplet interferes with the narrowness of specific charge distribution. It is critical in arcing problems in the neighborhood of the charging needle. The vacuum system to be utilized in our initial experiments on the Hb-water propellant system should have a sufficiently high pumping speed to maintain a hard vacuum at the site of the needle should particles of about .01 μ diameter be produced, with a mass flow rate of about 10^{-5} g, a value typical of earlier experiments employing doped glycerol solutions[9.15].

Should the high vapor pressure of water, nevertheless, present too many problems, one will need to consider other solvents. Formamide, for instance has a vapor pressure of only 1 mmHg at 70.5°C[9.17]. The experimental apparatus being used in the generation of charged colloid beams from hemoglobin is shown in Figure 9.1.

References

1. Hunter, R. E., and Wineland, S. H.: Charged Colloid Generation Research, Space Electronics Symposium, AAS Science and Technology Series V. 6, 1965, p. II-1.

2. Mickelsen, W. R. and Kaufman, H. R.: Status of Electric Thrusters for Space Propulsion, NASA TN D-2172. May, 1964.

3. Gignoux, D., Anton, H. F., and Shea, J. J.: Charged Colloid Generation Systems for Electric Propulsion, NASA CR-54049, Oct. 1963. Development of a Charged Colloid Source for Electrostatic Propulsion, NASA CR-54176, 1964.

4. Cohen, E.: Research on Charged Colloid Generation, APL TDR 64-75, June, 1964.

5. Wineland, S. H., Burson, W. C., and Hunter, R. E.: The Electrodynamic Generation of Charged Droplet Beams, AFAPL-TR-66-72. August, 1966.

6. Cohen, E., and Huberman, M. N.: Research on Charged Particle Electrostatic Thrusters, AFAPL-TR-66-94. September, 1966.

7. Tompkin, G. W.: Colloid Particle Formation for Biological Wastes, Advanced Electric Propulsion Research. NASA Grant NGR06-002-032, p. 8.1, January, 1967.

8. Simko, J. P., and Kauzmann, W.: The Kinetics of the Urea Denaturation of Hemoglobin. I. Beef Oxyhemoglobin. Biochemistry, *1*, 1005 (1962).

9. Kauzmann, W.: Some Factors in the Interpretation of Protein Denaturation. Adv. Protein Chem, *14*, 1 (1959).

10. Berliner, L. J. and McConnell, H.: A Spin-Labeled Substrate for α-Chymotrypsin. Proc. Nat'l Acad. Sci. U.S., *55*, 708 (1966).

11. Boeyens, J. C. A., and McConnell, H.: Spin-Labeled Hemoglobin. Proc. Nat'l. Acad. Sci. U.S. *56*, 22 (1966). Ohnishi, S., Boeyens, J. C. A., and McConnell, H.: Spin-Labeled Hemoglobin Crystals, *Ibid*., 809.

12. Mahler, H., and Cordes, E.: *Biological Chemistry* (Harper and Row, New York, 1966), p. 120.

13. Patton, A. R.: Private Communication, 1967.

14. Cohn, E. J.: Influence of the Dielectric Constant in Biochemical Systems. Chem. Rev., *19*, 241 (1936).

15. Cohen, E., Somol, C. J., and Gordon, D. A.: A 100-kv, 10-w Heavy-Particle Thruster. AIAA 65-377, July 1965.

16. Gayle, J. B., Egger, C. T., and Bransford, J. W.: Freezing of Liquids on Sudden Exposure to Vacuum. J. Spacecraft, *3*, 323 (1964).

17. Dow Chemical Company files, as reported in *Handbook of Chemistry and Physics* 41st ed. 1959-1960, Chemical Rubber Pub. Co., p. 2364.

18. Steiner, R. F.: *The Chemical Foundations of Molecular Biology*, Van Nostrand Co., 1965, p. 200.

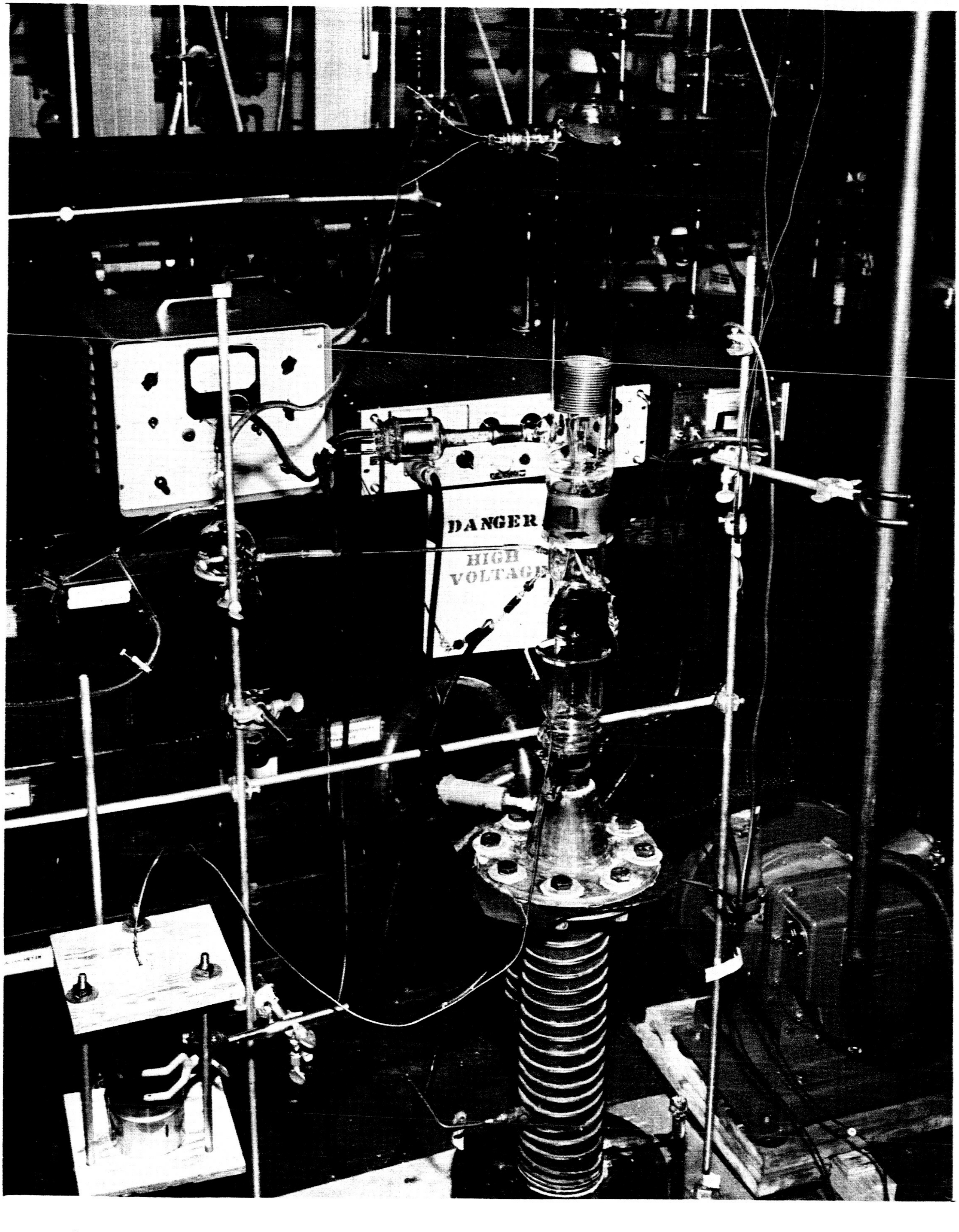
DANGER
HIGH
VOLTAGE

Figure 9.1. Apparatus for Electrostatic Spraying of Biowaste-Type Propellants.

FACILITIES AND EXPERIMENTAL EQUIPMENT

by Peggy J. Francis

During the past six months, work toward improvement of the NASA-CSU vacuum system has continued. An air pressurization system was installed in order to better control the atmosphere of the plastic-enclosed facility. The two high voltage power supplies previously obtained under the grant have been installed, and several low-voltage, high-current power supplies were built. A nitrogen leak detector has been put into the system to further assure safe operation of the facility.

The quadrupole mass filter (Figure 10.1) described in the previous grant report is nearing completion. The following components are ready for final test:

1. low frequency power amplifier
2. high frequency oscillation and power amplifier
3. power supplies and voltage regulator.

Components still under construction are the frequency monitoring equipment, automatic voltage amplitude control and the frequency to voltage converter.

Components for aluminum metal vaporizer shown in Figure 10.2 have been fabricated and assembled. Preliminary tests have been made in the vacuum chamber using the resistance heater. These preliminary tests show a large heat leak out the back end. Additional insulation is being added at the present time to reduce this heat leak. Future tests will include induction heating.

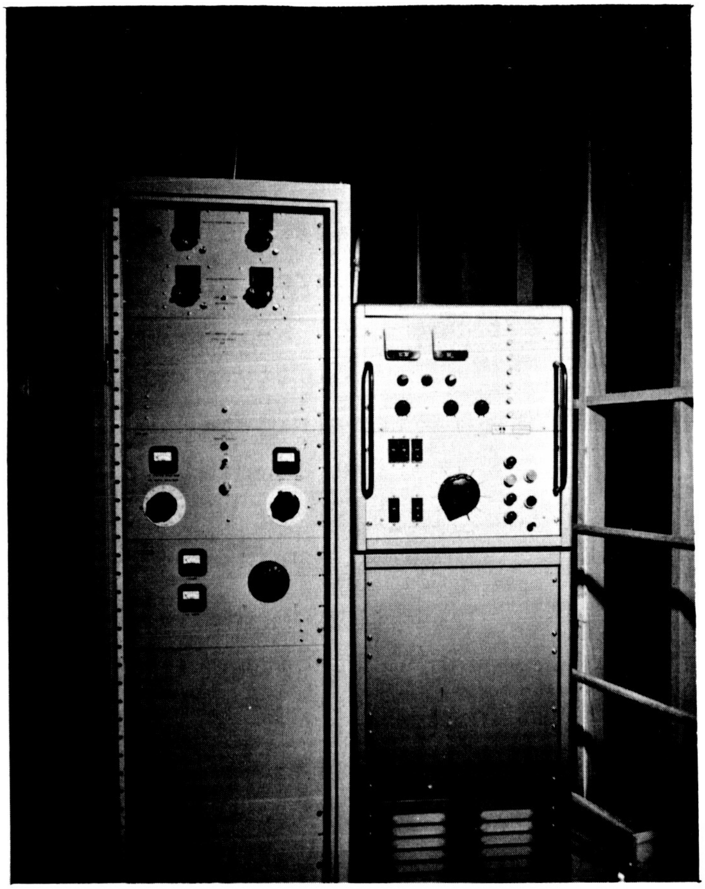

Figure 10.1 Electronics for Quadrupole Mass Filter.

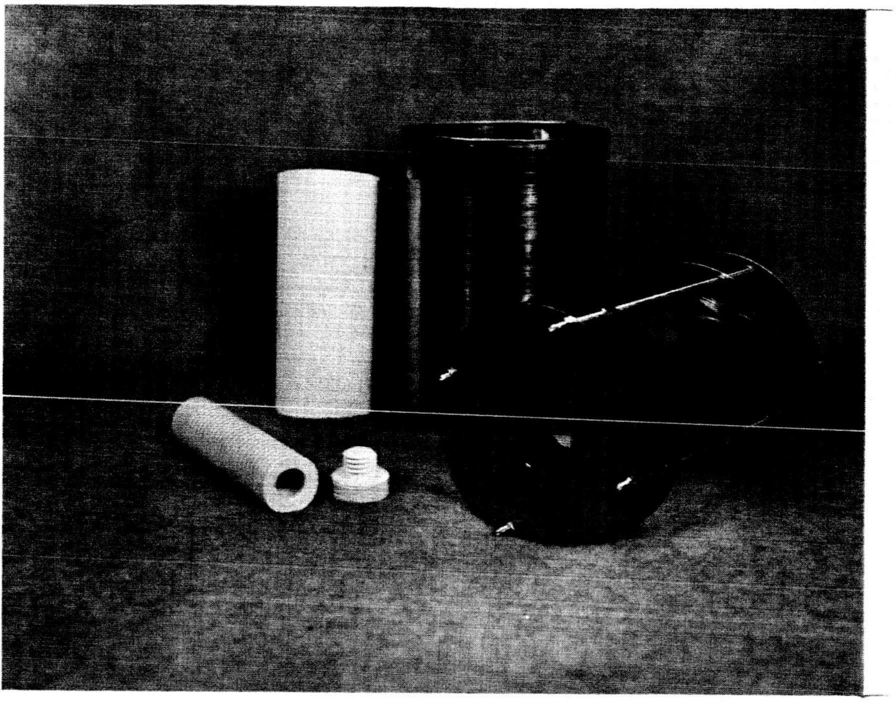

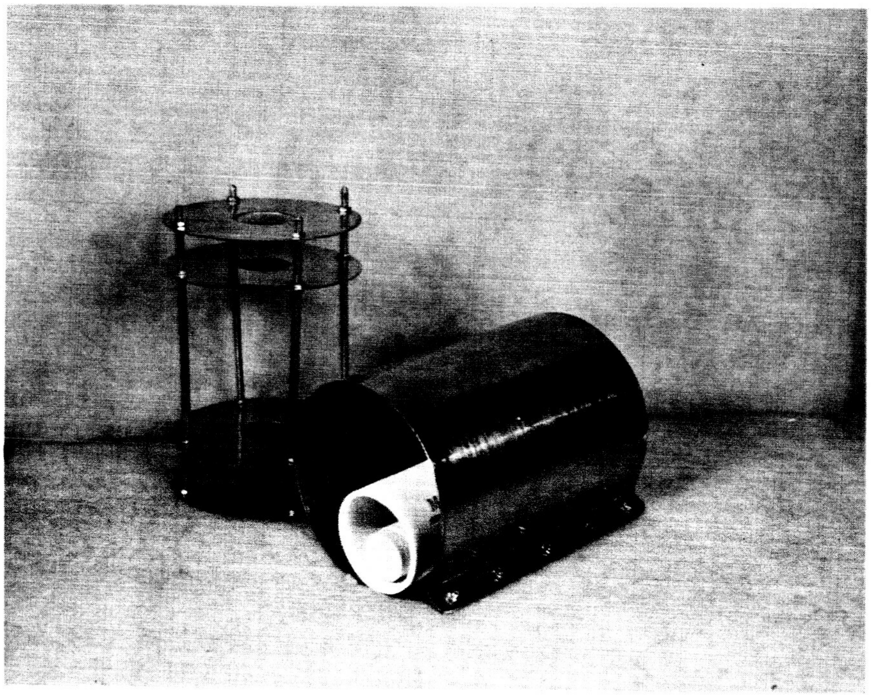

Figure 10.2 Components for Aluminum Metal Vaporizer.